The Construction, Development and Application of Potential Simulation Models to the Filling of Carbon Nanotubes by Molten Salts

Clare Louise Bishop

Chemistry Department

A thesis submitted to University College London
in the Faculty of Mathematical and Physical Sciences
for the degree of Doctor of Philosophy, January 2009

For Gary

I, Clare Louise Bishop, confirm that the work presented in this thesis is my own. Where information has been derived from other sources, I confirm that this has been indicated in the thesis.

Abstract

Inorganic nanotube structures (INTs) can be synthesised through the direct filling of carbon nanotube templates with molten salts. The resulting structures, usually rationalised in terms of known bulk crystal structures, are shown to be contained within a general set of structures classified in terms of folded sheets of infinite squares and hexagons.

A flexible model for the carbon nanotube is employed (using a Tersoff II potential), a significant development on previous work in which a rigid description was utilised. As a result, the nanotube is free to rotate, vibrate and translate within the simulation cell and analysis techniques are developed to account for this behaviour. Molecular dynamics simulations are performed using different molten salt models. These salt models are chosen so as to reflect different relative energetics of the underlying bulk crystal structures. In this context, a new model is developed and characterised in which key bulk structures have equal energies. The molten salts are observed to directly fill the carbon nanotubes which vary in diameter. The stability of novel key structures, which are characterised as having non-circular cross sections, are rationalised with reference to elliptical carbon nanotube distortions. For small diameter carbon nanotubes a preference for square net based INTs is observed.

The energy landscapes of the inorganic nanotubes, that are revealed by the molecular dynamics simulations, appear more complex than that of the carbon nanotubes themselves. The structures of larger inorganic nanotubes formed are dependent both on the nanotube diameter and the radius ratio of the ionic salt of choice. In contrast, the morphologies of small diameter inorganic nanotubes are dependent on the nanotube diameter only. A first principles analysis of the atomistic interactions is developed to explain this novel observation. The resulting theory is consistent with the ubiquitous nature of the rock salt nanocrystallites observed in experiment.

Acknowledgements

I would like to acknowledge the assistance of Dr. James Bray, whose guide to writing a thesis in latex has been invaluable to the writing-up process [12].

I am extremely grateful to the Chemistry department at University College London for the teaching assistantship which I held from 2004 until 2008. As a result, I have made many friends within the department (both staff and students) and I am very grateful for all the teaching experience that I have gained during this time. I would like to thank all the physical chemistry teaching staff that I have taught with; they have (without exception) been extremely helpful and a pleasure to work with. They have also made the many long hours I have spent in the teaching laboratories a much pleasanter experience! In particular, I would like to thank Dr. Wendy Brown and Mr. Crosby Medley for all their help with my teaching responsibilities.

I am indebted to my supervisor Dr. Mark Wilson for inspiration, encouragement and patience from the very beginning. I would like to thank him for always providing me with the clearest explanations at times of confusion, all his great advice and his endless enthusiasm for my ideas. I could not ask for a better supervisor.

I would like to thank Dr. Sobia Ashraf and Dr. Robert Palgrave for their friendship and always knowing where to find a good lunch. Thank you to all members of room 105 (past and present) for their companionship, entertainment and fun. In particular; Dr. J. Miguel Mora Fonz, Dr. Dimitrius Toroz, Dr. Theodorus Goumans, Mr. Davy Adriaens, Mr. Alan Lobo, Miss Sheena Dungey, Mr. Keith Butler, Mr. Hitesh Bhalla, Miss Yaliney Ramanan, Miss Sasja Steenvoorde and Miss Martina Miskufova. I am extremely grateful for the guidance, advice and friendship of the other members of the Wilson group; Mr. Bevan Sharma and Mr. Numaan Ahmed.

Thank you to all my friends who have encouraged me throughout my time at university and for being there when I needed to take time out and have some fun! In this respect, I would especially like to thank Mr. William Francis, Mr. Tom Robinson and Miss Sam McConnell for their friendship.

I am extremely lucky to have two wonderful families who have all supported and encouraged me throughout my studies. Thank you to all the Wakes, the Bishops, the Chapmans and the Gooches for always being there for me. Thank you mum and dad for your love and support (financial and otherwise!), I could not have done it without you.

Finally, thank you to my husband Gary. I now promise to do all the things that I have been putting off until "after I have finished my PhD". You have always been there for me, supporting me with encouragement, humour and, most of all, love.

Contents

List of Figures

List of Tables

Chapter 1

Introduction

1.1 Carbon Nanotubes

Evidence that carbon nanotubes were first synthesised in the 1970s alongside vapour grown carbon fibres exists in the form of transmission electron micrographs in which we appear to observe hollow graphite tubular structures on the nanoscale [67]. However, it was certainly the "rediscovery" of the carbon nanotube by Iijima in 1991 that caused an explosion in interest in this exciting new nanotechnology [38]. The credit for the discovery of the carbon nanotube may be controversial [60] but this is in regards to "multi wall" carbon nanotubes which consist of concentric graphite tubular structures. In contrast, the discovery of the "single-walled" carbon nanotube is not ambiguous and was first reported by two groups in 1993 [6, 39].

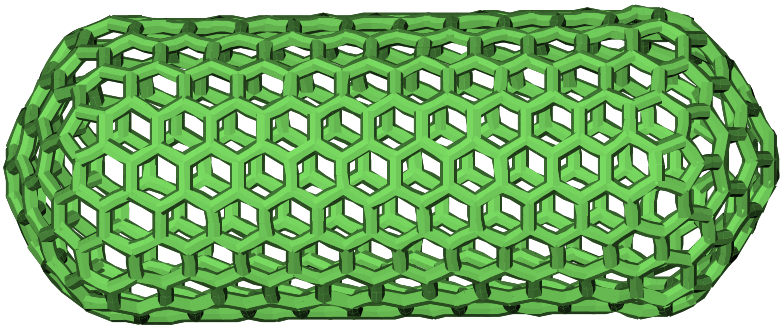

Figure 1.1: A model of a short single walled carbon nanotube which can be rationalised as a sheet of graphene "rolled up" into a cylindrical geometry. The ends are capped with a hemispherical fullerene consisting of both five and six membered rings. Single walled carbon nanotubes can routinely be grown to several millimetres long, the longest reported was 4 cm in length [121]. When this length scale is compared to the diameter (typically 1-2 nm for single walled nanotubes) we see that the carbon nanotube has an extremely large aspect ratio.

Conceptually, the single walled carbon nanotube is rationalised as an infinite graphene sheet that is rolled up to form a tubular structure (figure 1.1). The circumference of the cylinder corresponds to a chiral vector in the graphene plane which defines the nanotube morphology. The direction of this vector is indicated by the two integers n and m to give nanotubes of varying diameters denoted to be of (n,m) morphology (this nomenclature will be explained in further detail later in this thesis, for example in section 4.2). The direction of folding along the chiral vector determines the band structure and consequently the electronic properties of the nanotube; approximately one third of carbon nanotubes being metallic (where $n - m$ is a multiple of 3) and two thirds being semi-conducting in character [77]. The carbon nanotubes are observed to terminate with "caps" consisting of both five and six member carbon rings or hemispheres of fullerenes.

In reality, the synthesis of this metastable phase of carbon is actually performed via a range of methodologies rather than through the "folding" of a single graphene sheet. For example, laser vaporisation, carbon arc synthesis and chemical vapour deposition (specifically methane CVD, high pressure carbon monoxide decomposition, CO CVD, alcohol CVD and plasma-enhanced CVD) are the most widely utilised methods used to grow the nanotubes (for a review of synthetic methods see references [40, 77]). The emphasis in the literature is towards the development of high yield, high purity and highly diameter selective syntheses.

1.2 Inorganic nanotubes

Inorganic nanotubes (INTs) are analogous to the carbon nanotube, they are tubular structures on the nanoscale consisting of inorganic material. The first reported INT was the multi walled hollow WS_2 INT synthesised by Tenne *et al* in 1992 [98]. In the proceeding years there has been great interest in these cylindrical crystallites and a wealth of potential applications have been recognised. Initial investigations into the mechanical properties of WS_2 and MoS_2 are very promising, indicating they may be applicable to tribological and other high strength applications (for example bullet proof materials) [5]. Lithium ion cells have attracted great attention in the field of high-capacity batteries, lithium ions have been successfully intercalated within inorganic nanotubes and are cited for lithium ion storage in this battery technology [17]. The high surface area, stability and pore size of the MoS_2 [14], TiS_2 [15] and BN [47] inorganic nanotubes make them promising candidates for hydrogen storage.

Ion and molecular transport within the nanopore has attracted much interest, in particular nanodevices capable of allowing biological active molecules have been

created. For example, silica nanotubes have been shown to successfully facilitate the translocation of DNA within the nanotube pore [21]. The ion transport properties of TiO_2 nanotubes have made them excellent candidates for components in solar cells and hydrogen cells [81]; the change in electrical resistance on application of hydrogen (8.7 orders of magnitude) makes them the most sensitive known gas sensor to ever be tested [29].

The list of potential applications within this fast expanding nanotechnology field is effectively endless. It is therefore of general interest to observe if the unique reduced coordination environment within the cylindrical nanocrystallites exhibit any systematic novel crystal structure motifs or if there are any exceptional chemical and physical properties that are not seen in the crystal bulk environment. Our goal, therefore, is to work towards a more fundamental understanding of the properties of these materials, moving towards a less empirical appreciation of their potential usefulness.

1.2.1 INT synthesis

There are various methods of generating inorganic nanotubes (for a recent review see [5]) which consists of a wealth synthetic routes. A small selection will follow but the list is by no means exhaustive due to the very large number of reports of INT synthesis in the literature. WS_2 and MoS_2 nanotubes can be synthesised chemically from the reduction of the corresponding metal oxides by reaction with H_2S to form intermediate trisulphide molecules which go on to form the corresponding nanotubes [97]. Hydrothermal synthesis has been widely utilised in which thermal treatment of a suitable precursor results in the metal oxide nanotubes, for example SiO_2 [46], V_2O_5 [93] and ZnO [120] nanotubes. A recent novel approach to synthesise Fe_3O_4 nanotubes utilised an egg protein as a "nanoreactor." The ion affinity of the protein encourages nanoflakes to form, they then undergo a "rolling" mechanism to form the cylindrical nanotubes [27].

An alternative method (to a chemical route) of synthesising inorganic nanotubes is by the use of a template. For example, ZnO nanowires have been utilised for the epitaxial growth of GaN on the nanowire surface by chemical vapour deposition. The oxide is then removed by thermal decomposition to leave the hollow GaN nanotubes [28]. In this research, we will focus on the internal filling of a robust carbon nanotube template with molten ionic salts to form inorganic nanotubes. The confined environment within the carbon nanotube pore encourages charge ordering of the encapsulated ions to form highly order inorganic nanotube crystals. This method has proven very successful with many INT systems being formed via the

direct filling of such carbon nanotubes.

1.2.2 INTs via the direct filling of the carbon nanotube pore

Multi walled carbon nanotubes were the first nanotubes to be filled internally with metal oxides by Tsang *et al* in 1994 [104]. The nanotubes were opened by treatment with nitric acid, dried and then refluxed with a nitric acid solution containing a metal nitrate. This resulted in the insertion of cobalt, nickel, uranium and iron oxides.

The same procedure was found to be too harsh for the filling of single walled nanotubes because the acid reflux caused the destruction of the nanotubes. As a result, a new method of filling the nanotube via capillarity was developed and the first single walled nanotube to be filled with crystalline material was $RuCl_4$ [85]. The nanotubes were opened by treatment with hydrochloric acid and then filled by immersion in a saturated solution of $RuCl_3$. The resulting structure was then reduced by treatment with hydrogen to form Ru crystallites inside 2-5 % of the nanotube pores.

Subsequently, the opening step by acidification has proved unnecessary and a one step procedure has been developed [86]. The nanotubes are first ground with the ionic salt of choice by mortar and pestle and the mixture is sealed under vacuum within a silica quartz ampule. This is then heated to a temperature approximately 100 K over the system melting temperature, the salt is thought to open the nanotubes via attack of the fullerene caps. Recently experiments, in which an electrode potential is applied to single walled nanotubes, appear to show that it is indeed the nanotube tips rather than the sidewalls that are most electroactive [32].

The procedure relies on the melting temperature of the salt being less than approximately 900°C because at higher temperatures there is a risk that the carbon nanotube can become thermally damaged. Likewise, the nanotube must not be damaged by chemical attack by the filling material itself. The molten liquid must have a surface tension below the threshold value of approximately 100-200 mN m^{-1} in order that it can fill the pore via a capillary action [86]. One can achieve filling yields of 50-70 % by following this procedure [92].

Where the ionic salt proves unsuitable for filling via the one step procedure, modifications can be made. For example, single walled nanotubes can be filled with molten hydroxides via the standard one step procedure and then emptied by treatment with water [82]. The resulting opened nanotubes can then be refilled under milder thermal conditions, for example by treatment with uranyl acetate or uranyl nitrate solutions to form encapsulated UO_2 clusters and uranyl acetate molecules [101]. Treatment with steam is an alternative and unaggressive method for opening

single walled nanotubes which also has the advantage of removing remaining impurities from the carbon nanotube synthesis (such as catalyst and graphitic particles) [103].

A wide range of nanotube filling experiments have been reported via these methods. Oxides (such as NiO [104], UO_2 [104], FeO_2 [104], PbO [1], V_2O_5 [2], Sb_2O_3 [24], CoO_2 [104], MoO_3 [16]) and halides (such as CoI_2 [72], UCl_4/KCl [84], $LaCl_3$ [25, 118], AgCl/AgI [90], KI[57, 87], LiI [37], BaI_2 [89], HgI_2 [37]) have all been inserted into the carbon nanotube templates.

The confinement of the ions within the nanotube pore causes strict charge ordering despite the system temperature being above the melting point of the molten salts. Indeed, the ions in the liquid surrounding the carbon nanotubes remain in the liquid phase, whilst the ions forming the INT are highly ordered and can be considered to be crystalline in character.

Invariably, the structures of the crystallites formed within the nanotube by direct filling (or otherwise) are rationalised in terms of the bulk structure. Binary and ternary halides tend to form linked polyhedra in chains corresponding to known crystal environments, for example PbI_2 and $TbCl_3$ [88, 118]. The halides of MX stoichiometry exhibit coordination environments demonstrated in bulk crystal environments in the centre of the nanocrystal and reduced coordination environments at the surface of the nanocrystal. For example, the nanocrystallites of potassium iodide are rationalised in terms of sections of bulk rock salt structure [57, 87] and the hexagonal structure formed from a AgCl/AgI mixture in terms of the bulk wurtzite form [90]. However, there are also examples of nanocrystallites that cannot be rationalised in terms of known bulk structures, such as the binary halide BaI_2 nanocrystal [89]. This structure is formed of five and six coordinate linked polyhedra; such low coordination environments are unknown in any bulk crystal structures for this system. We argue that the popular approach of rationalising the crystals in terms of the bulk structures should be applied with caution. We will present a family of inorganic tubular structures for the 1:1 stoichiometry that contains the potassium iodide and AgCl/AgI nanocrystallite structures within its broader definition.

It has been noted by Sloan *et al* that crystallites of the alkali metal halides are predominately of the rock salt form, even when the radius ratio of the system predicts a twelve coordinate environment in the bulk (for example all RbI and KI INTs and 80 % of the CsI INTs). Where the rock salt structure is observed, the direction of growth is "almost always parallel to the $\langle 110 \rangle$ direction," or in other words, the chains of alternating ions run parallel to the nanotube axis. In addition, the authors note that the structure of the HgI_2 confined in very narrow multi-walled

nanotubes appears to consist of two chains of alternating ions forming a twisted "ribbon structure" within the pore; despite the stoichiometry predicted by the filling material [37, 91]. These observations (the preference for the rock salt structure despite the radius ratio, the direction of growth and the "ribbon" of alternating ion chains in the most confined pores) are all consistent with the theory that we present here in chapter 6.

1.3 Elliptical Deformations

The first experimental observation of an elliptical distortion in a filled carbon nanotube was on the insertion of cobalt iodide [72]. This was found to form an tetrahedral chain of Co_2I_4 units which formed a twisted chain along the nanotube pore. The images from transmission electron microscopy demonstrate a deviation of nanotube diameter that is commensurate with the rotational angle of the asymmetric internal structure (see figure 1.2).

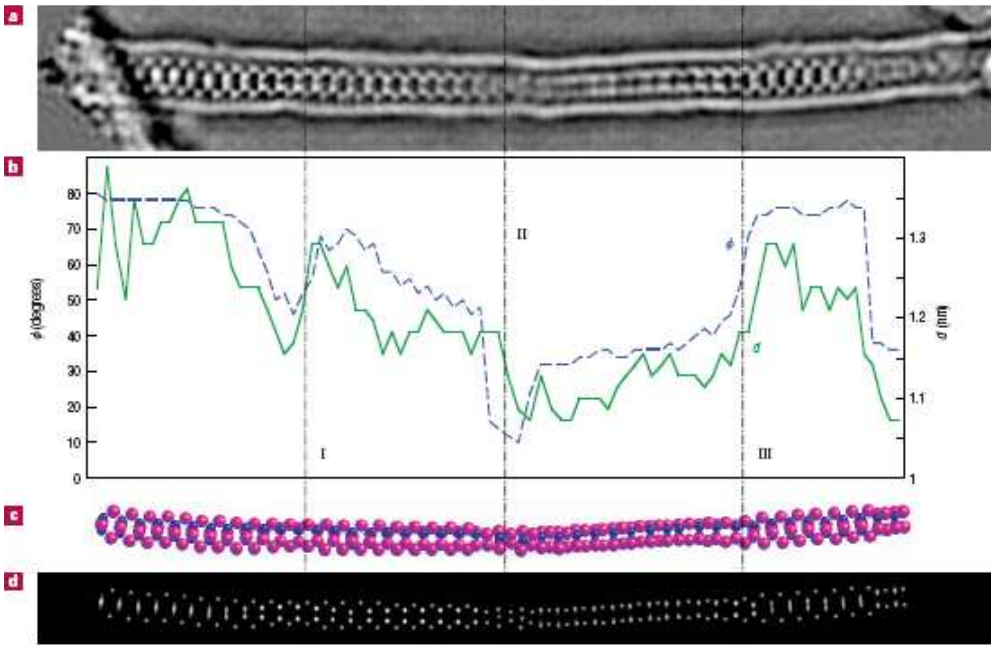

Figure 1.2: A: A transmission electron microscopy image of cobalt iodide with the carbon nanotube pore. B: The rotational angle of the internal twisted structure is commensurate with the deviations in nanotube diameter. C: A model of the encapsulated structure which consists of a twisted chain of tetrahedral Co_2I_4 units. D: A simulated image of the structure shown in C. Reprinted by permission from Macmillan Publishers Ltd: Nature Materials, see reference [72], copyright (2003).

Later, small diameter double-walled carbon nanotubes were not observed to fill with the asymmetric PbI_2 molten salt unlike their single walled counterparts [22].

The authors suspect that an elliptical deformation of the cobalt iodide type is hindered by the presence of the outer carbon nanotube in the former but is accommodated by the more flexible single walled nanotube in the latter.

High resolution transmission electron microscopy (HRTEM) shows a deviation of single wall carbon nanotube diameter along its length when filled with two chains of iodine atoms [30]. This deviation can be understood in terms of the helical structure of the iodine chains which gives rise to an elliptical distortion about its asymmetric cross section to minimise the iodine-carbon nanotube repulsion. The pitch of the helical distortion in the iodine chains shows a positive correlation with the helicity of the enclosing nanotube (see figure 1.3).

The time-dependent rotational dynamics of "peapod" nanostructures has recently been determined. $Sc_3C_2@C_{80}$ is encapsulated in a "zig-zag" chain arrangement within a single-walled nanotube and is observed via transmission electron microscopy to undergo distortions and thereby accommodate the rotational modes of the internal structure [106]. Elliptical cross sections of the carbon nanotube are accompanied by an expansion and contraction of the nanotube diameter which correlates with the internal fullerene motion.

Molecular dynamics simulations of carbon nanotubes immersed in molten AgI have also demonstrated elliptical distortions when filled with asymmetric "ribbon" like structures consisting of two chains of alternating silver and iodide ions [4].

1.4 Molecular dynamics simulations

The high resolution transmission electron microscopy (HRTEM) images produced from the filling experiments provide insight into the final product that resides within the carbon nanotube pore. Typically, the method of analysis is to produce simulated HRTEM patterns for likely candidates of the internal structure and to compare them with the experimental micrographs to locate a close match. However, there are difficulties that arise from this process of analysis. Firstly, the experimental data in the literature appears to show many regions of crystalline material that are not analysed in this way due to their complex nature and, understandably, often only the simplest HRTEM patterns within the micrograph are highlighted for analysis. Secondly, the HRTEM analysis of the final filled structures offer little insight into the mechanism of filling the carbon nanotube. Thirdly, it is difficult to develop a picture of the filling statistics for a given nanotube. It is likely, at the elevated temperatures used for filling, that both kinetic and thermodynamic factors are critical in determining the final filled structures.

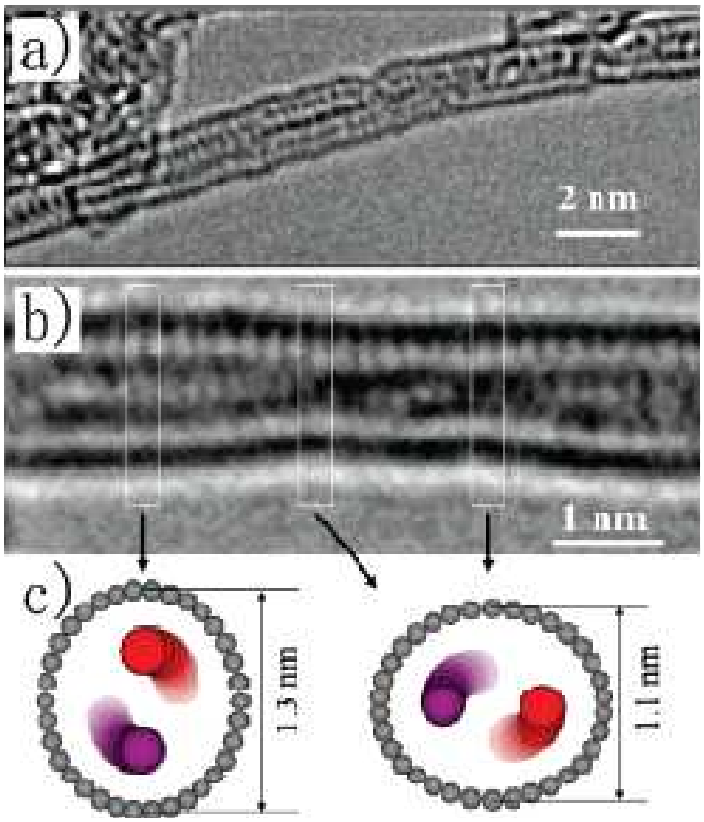

Figure 1.3: Reprinted with permission from Guan *et al* [30], copyright (2007) American Chemical Society. HRTEM showing two chains of iodine atoms enclosed in a single wall carbon nanotube. The change in diameter along the length of the nanotube is understood in terms of an elliptical distortion corresponding to the helicity of the iodine chains.

Molecular dynamics simulations (see chapter 2) of the filling of a carbon nanotube with an alkali halide were first performed by Wilson and Madden in 2001 [115]. The potassium iodide salt was modelled with a simple pairwise Born-Mayer potential [36] (see section 2.9) and the long range coulombic interactions were treated with an Ewald summation [20] (see section 2.10). The interactions between the ions and the nanotube were treated with a Lennard-Jones potential parametrised for isoelectronic noble gases interacting with a graphite surface [94] (see section 4.4). However, the carbon nanotube itself was held fixed and treated as a rigid entity. The procedure of the filling simulation was as follows. Firstly, an equilibrated configuration of molten potassium iodide ions was prepared and the ions residing in the cylindrical volume to be occupied by the carbon nanotube were then removed whilst maintaining charge neutrality in the system. The carbon nanotube (with ends capped with circular graphene sheets) was inserted into this empty volume and the liquid was allowed to equilibrate around the rigid nanotube. Finally, the graphene end caps were removed before continuing the simulation. The ions were observed to enter the nanotube pore

and, after approximately 48 ps, the tube appeared completely filled with crystalline material. The simulations were repeated with varying diameter carbon nanotubes. As observed experimentally, the structures corresponded to sections of the bulk rock salt structure, with growth occurring in the ⟨110⟩ direction (the alternating chains of cation and anions running parallel to the nanotube axis). This may be expected as the radius ratio of the potential model gives rise to a rock salt ground state crystal structure.

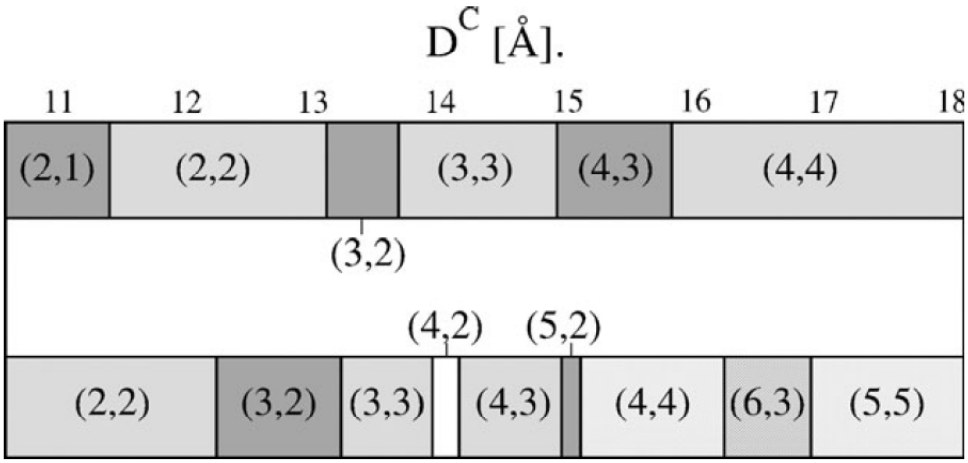

Figure 1.4: A "phase diagram" of the predicted INTs that will fill the carbon nanotube as a function of nanotube diameter, (reproduced from Wilson, 2007 by permission of The Royal Society of Chemistry [113]). The top panel indicates the morphology of INTs based on the folding of square net sheets, the bottom panel shows INTs formed from the rolling of hexagon sheets.

This early work has since been extended and a range of molten salts filling the nanotube have been simulated by varying the ion-cation interaction potential model used in order to probe the MX, MX_2 and MX_3 stoichiometries [108, 109, 110, 111, 112, 113, 114]. The research has progressed from a 'responsive' to a 'predictive mode' by the construction of INT "phase diagrams," such as the one shown in figure 1.4. These show the preferred structure that is predicted to form inside the nanotube pore as a function of tube diameter and potential model used for the MX stoichiometry. The model predicts that the INTs formed are based on the rolling of infinite planar sheets (formed of square nets or percolating hexagons) to form a cylindrical geometry in a manner exactly analogous to the geometry of the carbon nanotube itself (this will be explained in further detail in section 5.1).

At first glance, the proposition that the INTs of the alkali halides are based on the folding of infinite sheets may seem contradictory to the rock salt type structures observed experimentally. However, the $(2 \times 2 \times \infty)$ section of bulk rock salt structure observed to form with the insertion of KI [87] can also be interpreted as a

cylindrical INT based on the folding of square net sheets. Likewise, the $(3 \times 3 \times \infty)$ might actually correspond to a cylindrical square based INT with a chain of alternating ions running through the central channel [57]. Indeed, the authors report a distortion from the perfectly square cross section of this structure to a more radially "symmetric" one. In addition, a similar circular distortion is reported in theoretical calculations of a $(3\times3\times\infty)$ encapsulated in a (11,11) carbon nanotube [79]. Sloan *et al* state that the predominant structure observed to form from the alkali halide melts is based on the rock salt structure, generally growing in the $\langle 110 \rangle$ direction (chains of ions parallel to the nanotube axis) [37, 91]. We would argue that with a small distortion to a more circular cross section (as observed with the $(3 \times 3 \times \infty)$ crystallite), these can always be considered as concentric cylinders formed from square net sheets. The hexagon based "tunnel" wurtzite INT observed to form from the AgCl/AgI melt has been interpreted in terms of the bulk [90], yet this hollow (*i.e.* cylindrical) structure can also be interpreted through the folding of a sheet of percolating hexagons. In addition, more cylindrical based INTs may be uncovered by analysis of the more complex HRTEM patterns not yet examined. Simulating the HRTEM patterns of these "folded sheet" INTs predicted by simulation may result in a match with some of these more complex images.

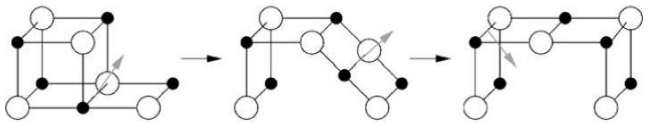

Figure 1.5: The "folding mechanism" observed during the molecular dynamics simulations of the potassium iodide system. The exploratory planar structure transforms to the $(2\times2 \times \infty)$ crystallite via this mechanism. (Reproduced from Wilson, 2007 by permission of The Royal Society of Chemistry [113]).

The filling simulations give us an insight into the filling mechanism which cannot be examined by the current experimental procedures. For example, the formation of the $(2 \times 2 \times \infty)$ rock salt nanocrystallite appears to proceed via a two step mechanism [113]. Firstly a "ladder" like structure of two chains of alternating ions explores the nanotube pore, an increasing number of ions enter the nanotube whilst maintaining charge neutrality. This planar exploratory structure then undergoes a "folding mechanism" (see figure 1.5) to form the bulk like crystallite that is observed to form experimentally within approximately 1.4 nm diameter carbon nanotubes [87].

Another exciting aspect of the molecular dynamics approach is that the simulations can be repeated with many different starting liquid configurations. The resulting structures can be used to construct a filling profile and provide an insight

into the statistics of filling for the system of interest. The relative thermodynamic stability of the various structures formed can be probed, such as the preference for the (n,n) square net structures formed in small diameter carbon nanotubes [11] (see chapter 6).

Recently, carbon nanotubes immersed in the molten AgI salt have been simulated by Baldoni *et al* who have also incorporated the carbon interactions into the model [4]. They have observed structures based on structures formed from an infinite plane of square nets for low diameter carbon nanotubes and those formed from hexagon sheets for the larger carbon nanotubes. This is consistent with the results we will present here in chapters 5 and 6.

1.5 The MX stoichiometry

In this thesis the results of molecular dynamics simulations of the filling of flexible carbon nanotubes with molten salts will be presented. Four potential models will be utilised for the description of the ionic salt used to fill the nanotube pore. These are typical Born-Mayer potentials [36] which describe ionic salts of the MX stoichiometry (see section 2.9). Potentials I and III in this work have been parametrised [26] to describe crystal systems in which the atomic radii predict tetrahedral (e.g. wurtzite or zinc blende) and octahedral (rock salt) bulk crystal phases respectively. Previous molecular dynamics simulations of carbon nanotube immersed in the KI melt have successively utilised potential III [115] for the description of the cation-anion interactions since it predicts a rock salt structure in the bulk. Later potential I was utilised in the molecular dynamics simulations for comparison with the AgCl/AgI experimental HRTEM images because a salt with a wurtzite bulk structure was required [109]. Potentials II and IV are modifications of potential I and will be constructed and characterised as part of this work. The parameters for potentials I, II, III and IV are given in table 4.6 and further details regarding the relative stability of the B3 and B1 crystal phases are given in section 5.1.

1.5.1 Crystal phase transitions of potential I

In order to understand the behaviour of the ions when encapsulated in the nanotube pore, it is clearly important to have a more general understanding of their behaviour in other known phases, in particular in the crystalline and liquid states. For example, the ionic radii of the MX salt described by potential I predicts that the wurtzite crystal system is only slightly lower in energy than its rock salt analogue. As a result, one might expect a relatively low pressure-driven phase transition between the low

density wurtzite and higher density rock salt structures. Phase transitions between the tetrahedral and octahedral coordination environments are extremely relevant to the characterisation of the system described by this potential (and potentials II and IV which are derived from it).

Molecular dynamics simulations were performed by Wilson *et al* in which the zinc blende phase of an MX crystal was pressurised and the transition to the rock salt phase were monitored [117]. The ion interactions were described using potential I and the simulation was performed in the isothermal-isobaric ensemble using a barostat which allowed anisotropic fluctuations of the simulation cell (see section 2.5 for further detail). It was found that the transition progressed via a two step mechanism. Firstly the cubic simulations cell underwent a tetragonal distortion to give a diatomic beta tin (d-β-Sn) intermediate. The system then underwent a shearing motion so that one of the cell angles increased to approximately 110°. On decreasing the relaxation time of the barostat (see section 2.5) the two-step mechanism remained unaltered but the final rock salt structure demonstrated grain boundary defects in which the layers of the structure contained stacking faults. Theoretically, the required pressure calculated from the zero Kelvin energy volume curves to drive this phase transition was 4.8 GPa; in the dynamic simulations pressures between 15 and 21 GPa were required. This "over pressure" is representative of the kinetic barrier to this transition.

The first step of this mechanism, in which the system transforms from the tetrahedral zinc blende phase, is analogous to a transition that is observed for the isostructural monotomic system; the diamond phase. Diffraction studies have shown, that at high pressure, the diamond phase of Si and Ge undergoes a tetragonal distortion to the monotomic beta tin structure (m-β-Sn) [53, 56]. The contraction of the lattice decreases the second nearest neighbour separations which, in turn, increases the coordination from four to six. Experimentally, studies monitoring the high pressure phase transitions of the tetrahedral diatomic systems have largely been performed for the group III-V and group II-VI semi-conductors. Historically, the diffraction studies were generally interpreted in terms of a d-β-Sn intermediate for systems of low ionicity and rock salt phases for the compounds of higher ionicity [61, 64]. However, there has been much debate in regards to these assignments leaving the existence of the d-β-Sn phase in much doubt [63]. Many of the proposed earlier occurrences of the d-β-Sn phase have been reassigned to the *Cmcm* structure; a lower symmetry relation of the rock salt structure with puckered, rather than planar, layers (figure 1.6). Indeed, density functional calculations have been performed for a broad range of the semi-conductors which indicate that a phonon mode within

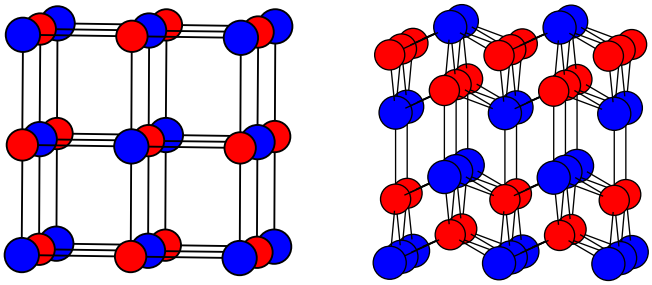

Figure 1.6: Left: The B1 structure (rock salt) with octahedral coordination of the ions (Space group $Fm\overline{3}m$). Right: The related, lower symmetry *Cmcm* structure with puckered layers.

the d-β-Sn structure becomes increasingly unstable with the compound's ionicity. It appears that this unfavourable phonon mode may be responsible for its apparent absence (and the favouring of the more distorted *Cmcm* structure) in the high pressure phases of the diatomic systems [68].

Energy-volume curves determined from density functional calculations of a wide range of possible candidates were calculated for GaP, InP and InAs which show that the d-β-Sn is favourable in a small pressure range for GaP [62]. In the other systems it lies close in energy (but is relatively unstable) to the other more favourable systems such as the *Immm* and *Cmcm* systems. It is therefore conceivable that it could be observed experimentally depending on the kinetic pathway of the system through the energy landscape. The disordered form of d-β-Sn has been observed as one of the high pressure phases of GaSb [13, 58, 105] and alongside the *Immm* structure (another relation of the rock salt structure) before transforming to the *Cmcm* phase in InSb [64]. However, in general the d-β-Sn structure is largely absent in the systematics of the high pressure phases of the group III-V and group II-VI semi-conductors [61].

In summary, the observation of the d-β-Sn structure as a high pressure phase of the zinc blende phase is extremely rare in practice and the *Cmcm* phase is widely observed. Wilson notes that the simple potential model used in the molecular dynamics simulations (Potential I) may not capture all of the electronic structure features of the semi-conductors. This may explain the observation of the elusive d-β-Sn structure in the molecular dynamics simulations [117]. The higher lever density functional calculations such as those by Mujica *et al* [62] are better equipped to describe, and discriminate between, the electronic structure of these materials.

1.5.2 Nanocrystallites in the MX stoichiometry

Potentials III and IV both predict rock salt structures in the bulk crystal system; the former has been specifically parametrised to model the potassium iodide salt[26]. Potassium iodide has been utilised in filling experiments and either the $(2 \times 2 \times \infty)$ or the $(3 \times 3 \times \infty)$ nanocrystallite was observed to form, depending on the diameter of the nanotube being filled [57, 87]. Evidence that nanocrystallites based on the rock salt structure predominate in small diameter nanotubes, regardless of the potential model used, will be presented in this thesis. Furthermore, the experimentally observed preference for rock salt based crystallites to grow along the $\langle 110 \rangle$ direction will be explained. Therefore, the experimental and theoretical observations of such crystallites are of great relevance to this work.

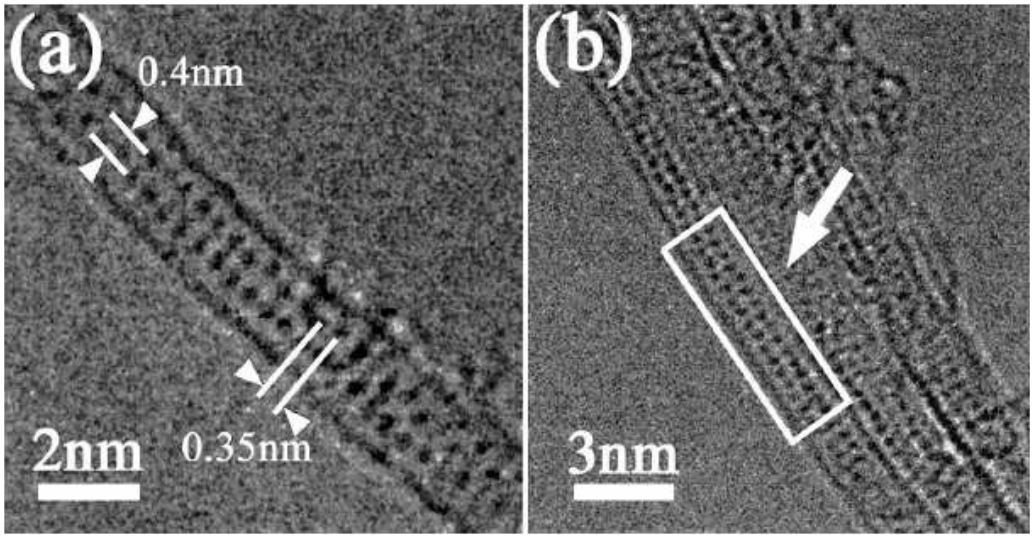

Figure 1.7: An HRTEM for a $(2 \times 2 \times \infty)$ nanocrystallite of KI encapsulated within a single walled carbon nanotube with diameter of 1.35 nm (similar to the diameter of a (10,10) carbon nanotube). The dark spots correspond to columns containing one potassium and one iodide ion. Reprinted from Chemical Physics Letters, Sloan *et al* [87], Copyright (2000), with permission from Elsevier.

Figure 1.7 shows an HRTEM image of a $(2 \times 2 \times \infty)$ nanocrystallite of KI encapsulated within a single walled carbon nanotube with diameter of 1.35 nm (similar to the diameter of a (10,10) carbon nanotube) [87]. It was noted that the crystal was anisotropic with the anion-cation separations perpendicular to the nanotube axis (0.398±0.003 nm) being larger than the spacings that run parallel to the nanotube axis (0.346±0.003 nm); a ratio of 1.15. The spacings parallel to the nanotube axis correspond more closely to the spacings observed in the bulk crystal (0.353 nm). The spacings perpendicular are significantly expanded in comparison. The coordination environment of all the ions in this crystallite is reduced from the

bulk (from six to four); all of the ions can be regarded as residing on the crystallite surface.

The first density functional calculations of KI encapsulated within a carbon nanotube assumed the experimental ion positions and therefore the assumed anisotropy of the system [119]. Charge transfer from the crystallite to the nanotube, corresponding to one in every four electrons, was observed in that study.

Later, density functional calculations were performed on finite units of KI crystallites encapsulated within a carbon nanotube [79, 80]. This approach had the advantage that the periodic boundary conditions did not impose a commensurate and potentially unphysical geometry on the crystallite. The anisotropy of the $(2\times2\times\infty)$ nanocrystallite is successfully predicted by these calculations both in the free crystallite and when encapsulated within various diameter nanotubes. Geometry optimisations of the free crystal give the cation-anion separations running along the length of the crystallite as 0.3388 nm, in good agreement with experiment. The cross section of the crystallite was found to be of rhombic (rather than of square) geometry and the cation-anion separations in the cross section were reported as 0.3416 nm. This separation compares less favourably with experiment in which an expansion in the cross section was observed from the bulk value. On encapsulation within the nanotubes, the separations running parallel to the nanotube axis remain largely unchanged. However, the crystal is compressed in the cross section with a reduction in the anion-cation separations perpendicular to the nanotube axis. This effect is most pronounced for the smallest diameter carbon nanotubes. In addition, the K-I-K angle in the rhombic cross section is found to increase with greater confinement. Unlike, the earlier theoretical study [119], a small amount of charge transfer is observed in which the carbon nanotube donates charge to the iodide ion. This effect is carbon nanotube diameter dependent, with the greatest transfer occurring in the smallest diameter nanotubes.

Density functional and Hartree-Fock calculations on free $(2 \times 2 \times \infty)$ nanocrystallites of LiF also demonstrate a rhombic geometry in the cross section with the anion anion separation being greater than that of the cation cation separation [8]. The authors suggest that this is due to two contributing factors; firstly the greater short range repulsion of the anions in comparison to the cations and secondly, the greater polarisation of the anions such that their induced dipoles screen the electrostatic repulsion between the cations [48]. Although these rhombic distortions have not been reported in the experimental results yet, this may be due to the limitations of the current experimental HRTEM resolution available. The calculations on the LiF $(2 \times 2 \times \infty)$ nanocrystallites also predict a contraction of the cation-anion sep-

arations running parallel to the crystallite axis. However, although the separations perpendicular to the crystallite axis are greater than those parallel, once again the results do not show the expansion relative to the bulk value that was observed in experiment.

A global model for the interpretation of the contraction of the cation-anion separations running parallel to the nanotube axis has been developed by Bichoutskaia *et al* [7] which will be explained in more detail in section 6.6. In this work, the energy of the $(n \times m \times \infty)$ crystallites is partitioned in terms of the energy of the chains of alternating ions running parallel to the nanotube axis and the energy of interaction between these chains. The inter-chain energy is much weaker than the intra-chain energy and as a result a contraction along the chains is observed. However, the predicted separations perpendicular to the crystallite axis are still significantly smaller than in experiment. We note that these calculations are in the absence of the encapsulating carbon nanotube.

The most recent density functional calculations of the $(2\times2\times\infty)$ nanocrystallites include the presence of the carbon nanotube [10]. The results were compared with the previous results for the free crystallite [7, 8] in order that any changes in the KI geometry could be assigned to the physical effects provided by the introduction of the encapsulating nanotube. Dispersive interactions between the nanotube wall and the crystallite were observed to increase the anion-cation separations perpendicular to the nanotube axis by a small amount. In addition, the effects of charge transfer were also analysed and significant charge transfer was observed to take place from the carbon nanotube to the anion, greatly affecting the carbon nanotube properties. When the charge transfer effects are accounted for, a greater expansion of the anion-cation separations is observed relative to the calculations in the absence of the nanotube. Further contraction along the anion cation chains running parallel to the nanotube axis is observed to take place with the charge transfer. The resulting geometry gives the best agreement with experiment to date.

1.6 Thesis structure

The synthesis of inorganic nanotubes is a new and expanding nanotechnology which has attracted much attention in the literature. Theoretical calculations (both semi-empirical potential based and high level density functional studies) have proved invaluable in determining the structures of these novel nanocrystallites. In particular, molecular dynamics simulations give insight into the filling mechanisms and the structural nature of the inorganic nanotubes formed. In this work we will present

an improved potential based model for the filling of carbon nanotubes with molten salts of the MX stoichiometry by incorporation of the carbon-carbon interactions. In addition we will develop a theory which aids our understanding for the prominence of the rock salt nanocrystallites in small diameter nanotubes.

The structure of the thesis will be as follows:

- In chapter 2 the computational procedures that are utilised in the model will be summarised. The technique of choice is molecular dynamics which allows us to model a relatively large number of particles in the system with relatively simple potential models.

- The parametrisation of a novel potential model will be performed in chapter 3 which describes a crystal of MX stoichiometry. The potential model describes a system which favours neither the tetrahedral nor the octahedral coordination in the bulk. The properties of the system in the crystal and liquid phases are discussed in preparation for its use in the filling simulations in the later chapters.

- The existing model for the filling of carbon nanotubes is developed in chapter 4 to incorporate the interactions of the carbon atoms. The application of a many body potential model allows the carbon nanotube to act as a flexible, rather than rigid, entity. The use of the this flexible model leads to technical complexity in the analysis methods, which are described. The flexible model is utilised within the carbon nanotube filling simulations, using four potentials of the MX stoichiometry to model the ion interactions. This includes the novel potential model parametrised in chapter 3. Simulations are performed for carbon nanotubes of varying diameter and the filling events are investigated.

- In chapter 5 structures that were found to form inside the carbon nanotubes are surveyed, for all four potential models. The analysis is performed by considering the underlying energy landscapes, which contain the possible INT structures. It is found that the energy landscape (which determines the morphology of the inorganic nanotubes) is highly dependent on the carbon nanotube diameter.

- A new model for the characterisation of inorganic nanotubes based on the folding of square net sheets is developed in chapter 6. This successfully explains the construction of the inorganic nanotube energy landscape at small diameters. It also accounts for both the ubiquitous nature and the direction of growth of the rock salt crystallites which have been observed in experiment.

Chapter 2

Computational Methods

A central aim of the present research is to improve the existing model for the filling of carbon nanotubes with molten salts to form inorganic tubular structures (INTs). The technique of choice for this work is molecular dynamics simulation in which the trajectory of the ions and atoms in such a system are predicted by integrating Newton's second law of motion. The classical technique allows us to model multi-component systems with a relatively large number of particles.

The inter-particle forces that must be determined during the process of the integration are determined from potential models of varying complexity. They have been designed to describe the physical properties of the system of interest, whether that is many-bodied but short-range effects of a molecular system (carbon for example) or the simple pairwise properties of an ionic salt where the long-range charge-charge interactions are of extreme importance.

In this chapter we will describe the techniques and algorithms used in molecular dynamics simulations of this type. All have been shown to be very successful in the modelling of ionic systems and will be utilised in later chapters in the modelling of the carbon nanotubes with molten salts.

2.1 The Lagrangian formalism of molecular dynamics

In a system of N ions with coordinates

$$\mathbf{q} = (\mathbf{q_1}, \mathbf{q_2}, \mathbf{q_3}, ...\mathbf{q_N}) \tag{2.1}$$

and momenta

$$\mathbf{p} = (\mathbf{p_1}, \mathbf{p_2}, \mathbf{p_3}, ...\mathbf{p_N}) \tag{2.2}$$

the Lagrangian function $\mathscr{L}(\mathbf{q}, \dot{\mathbf{q}})$ is:

$$\mathscr{L}(\mathbf{q}, \dot{\mathbf{q}}) = \mathscr{K}(\dot{\mathbf{q}}) - \mathscr{V}(\mathbf{q}) \tag{2.3}$$

where $\mathscr{K}$ is the kinetic energy given by

$$\mathscr{K}(\dot{\mathbf{q}}_i) = \sum_{i=1}^{N} \frac{1}{2} m_i \dot{\mathbf{q}}_i{}^2, \tag{2.4}$$

and $\mathscr{V}(\mathbf{q})$ is the potential energy of the system which is described by a potential energy function.

We can construct the fundamental Lagrangian equation of motion [3]:

$$\frac{\partial}{\partial t}(\frac{\partial \mathscr{L}}{\partial \dot{\mathbf{q}}}) - (\frac{\partial \mathscr{L}}{\partial \mathbf{q}}) = 0. \tag{2.5}$$

The force on the i^{th} ion is given by:

$$\mathbf{f_i} = \nabla_{\mathbf{q}} \mathscr{L} = -\nabla_{\mathbf{q}} \mathscr{V}, \tag{2.6}$$

and we find that

$$m_i \ddot{\mathbf{q}} = \mathbf{f_i}. \tag{2.7}$$

If we solve the second order differential equation 2.7 in three dimensions we can predict the ion trajectories as a function of time.

2.2 The Hamiltonian formalism of molecular dynamics

The Hamiltonian function $\mathscr{H}(\mathbf{q}, \mathbf{p})$ is:

$$\mathscr{H}(\mathbf{q}, \mathbf{p}) = \sum_{\mathbf{i=1}}^{\mathbf{N}} \mathbf{p}\dot{\mathbf{q}} - \mathscr{L}(\mathbf{q}, \dot{\mathbf{q}}). \tag{2.8}$$

The Hamiltonian equations of motion are given by

$$\frac{\partial \mathscr{H}}{\partial \mathbf{p}} = \dot{\mathbf{q}} \tag{2.9}$$

$$\dot{\mathbf{q}} = \frac{\mathbf{p}}{\mathbf{m}} \tag{2.10}$$

and

$$\frac{\partial \mathscr{H}}{\partial \mathbf{q}} = \nabla_{\mathbf{q}} \mathscr{L} = \dot{\mathbf{p}} \tag{2.11}$$

$$\dot{\mathbf{p}} = -\nabla_{\mathbf{q}} \mathscr{V} = \mathbf{f_i}. \tag{2.12}$$

Therefore, we can solve the first-order differential equations 2.10 and 2.12 to predict the trajectories as a function of time. This is preferable to solving the second order differential equation 2.7.

These equations generate trajectories that probe the canonical ensemble (NVE).

2.3 The Nosé-Hoover thermostat

In section 2.2, equations of motion were derived to explore the canonical ensemble, in which the number of particles N, the volume V and the system energy E are held constant. These equations of motions can be extended to probe the microcanonical (NVT ensemble) by coupling the system to a theoretical heat bath. The instantaneous temperature corresponding to the system's kinetic energy fluctuates about the average temperature which is determined by the thermostat.

Nosé defined an augmented Hamiltonian for constant-temperature dynamics based on time-scaled variables [65, 66]:

$$\mathscr{H}_{Nosé} = \mathscr{V}(q) + \sum_{i=1}^{N} \frac{\mathbf{p}_i^2}{2m_i s^2} + \frac{\mathbf{p}_s^2}{2Q} + (\chi + 1) k_B T \ln s, \tag{2.13}$$

where s is a time scaling variable and $\mathbf{p}_s$ is the conjugate momentum of s. These parameters describe the heat bath that the system is coupled to. χ is the number of

degrees of freedom of the system and T is the system temperature. Q is the thermal inertia parameter which has units $kg\ m^2$ and determines the extent of coupling of the system to the thermostat. Q can be related to a relaxation time, T, through

$$Q = \chi k_B T \tau^2. \tag{2.14}$$

The relaxation time τ must be chosen carefully to give an appropriate value of Q. A large value of Q gives a weak coupling between the heat bath and the system and so thermostating is not effective in the sense that changes in T imposed by the thermostat occur only on relatively long time-scales. Conversely, if Q is chosen to be small then the thermostat may dominate the equations of motion, leading to the those equations becoming "stiff" and giving rise to potential system instabilities.

Hoover simplified this approach by eliminating the time-scaling to give a new (non-Hamiltonian) conserved quantity for the system [33]:

$$\mathscr{H}'(\mathbf{p}, \mathbf{q}, \xi, \mathbf{p}_\xi) = \mathscr{V}(q) + \sum_{i=1}^{N} \frac{\mathbf{p}_i^2}{2m_i} + \frac{\mathbf{p}_\xi^2}{2Q} + \chi k_B T \xi \tag{2.15}$$

$$\tag{2.16}$$

with the following set of equations of motion:

$$\dot{\mathbf{q}} = \mathbf{p}/m \tag{2.17}$$

$$\dot{\mathbf{p}} = \mathbf{f} - \mathbf{p}\frac{p_\xi}{Q} \tag{2.18}$$

$$\dot{\mathbf{p}}_\xi = \Big[\sum_{i=1}^{N} \frac{\mathbf{p_i}^2}{m_i} - \chi k_B T\Big] \tag{2.19}$$

$$\xi = \frac{\mathbf{p}_\xi}{Q}. \tag{2.20}$$

Equation 2.20 which defines the friction coefficient ξ is included for completeness but is not necessary to update the ion trajectories.

2.4 Nosé-Hoover chains

It has been shown that the Nosé-Hoover method is not ergodic for small systems and therefore the correct distributions are not produced [51]. The fluctuations in the thermostat can be controlled by coupling it to yet another thermostat. In fact, we can utilise a chain of Nosé-Hoover thermostats to improve the ergodicity of the

system [51]. The conserved quantity for a chain of M thermostats becomes:

$$\mathscr{H}'_{chain}(\mathbf{p},\mathbf{q},\xi,\mathbf{p}_\xi) = \mathscr{V}(q) + \sum_{i=1}^{N}\frac{\mathbf{p}_i^2}{2m_i} + \sum_{i=1}^{M}\frac{\mathbf{p}_\xi^2}{2Q_i} + \chi k_B T\xi_1 + \sum_{i=2}^{M} k_B T\xi_i. \quad (2.21)$$

The corresponding equations of motion for the Nosé-Hoover chain are:

$$\dot{\mathbf{q}} = \mathbf{p}/m \quad (2.22)$$

$$\dot{\mathbf{p}} = \mathbf{f} - \mathbf{p}\frac{p_{\xi 1}}{Q_1} \quad (2.23)$$

$$\dot{\mathbf{p}}_{\xi 1} = \Big[\sum_{i=1}^{N}\frac{\mathbf{p_i}^2}{m_i} - \chi k_B T\Big] - p_{\xi 1}\frac{p_{\xi 2}}{Q_2} \quad (2.24)$$

$$\dot{\mathbf{p}}_{\xi j} = \Big[\frac{\mathbf{p_{j-1}}^2}{Q_{j-1}} - k_B T\Big] - p_{\xi j}\frac{p_{\xi j+1}}{Q_{j+1}} \quad (2.25)$$

$$\dot{\mathbf{p}}_{\xi M} = \Big[\frac{\mathbf{p_{M-1}}^2}{Q_{M-1}} - k_B T\Big] \quad (2.26)$$

$$\xi_i = \frac{\mathbf{p}_{\xi i}}{Q_i}. \quad (2.27)$$

In this work M has been taken to be 5, improving the ergodicity of the system yet without requiring too many extra equations of motion (which would affect the simulation speed).

2.5 Isothermal-Isobaric Molecular Dynamics

Hoover formulated a set of equations of motions that introduce a fixed external pressure and relaxation time in an extension of the Nosé-Hoover constant temperature molecular dynamics [33, 34]. However, Hoover pointed out that these equations of motions did not correctly generate the isothermal-isobaric ensemble and so various modifications have been suggested.

One such approach is a constant stress formalism which correctly generates the isothermal-isobaric ensemble [50] and that has been used in this work. The simulation cell is fully flexible and can change in volume as well as in shape so that the pressure fluctuates around an external pressure P_{ext}. The instantaneous pressure P_{int} is given by the virial theorem in which $< P_{int} >= P_{ext}$:

$$P_{int} = \frac{1}{3V}\Big[\sum_{i=1}^{N}\frac{\mathbf{p}_i^2}{m_i} + \sum_{i=1}^{N}\mathbf{q}_i\mathbf{F}_i - 3V\frac{\partial\phi(\mathbf{q},V,\overleftrightarrow{\mathbf{h}}_\mathbf{0})}{\partial V}\Big]. \quad (2.28)$$

The isotropic and anisotropic fluctuations are separated out for convenience so that simulations can be performed where the simulation cell can undergo isotropic fluc-

tuations only when necessary (i.e. the shape of the cell remains fixed). Unlike other formalisms [55], this constant stress approach has the advantage that the predicted trajectories do not depend on the original choice of lattice vectors.

The conserved quantity within this formalism is as follows:

$$\mathscr{H}' = \sum_{i=1}^{N} \frac{\mathbf{p}_i^2}{2m_i} + \frac{1}{2W_{g_0}} Tr[\overleftrightarrow{\mathbf{P}}_{\mathbf{g_0}}^{\mathbf{T}} \overleftrightarrow{\mathbf{P}}_{\mathbf{g_0}}] + \frac{P_\epsilon^2}{2W} + \frac{P_\xi^2}{2Q} + \phi(\mathbf{q}, V, \overleftrightarrow{\mathbf{h}}_{\mathbf{0}}) + P_{ext}V + (\chi + d^2)k_BT\xi, \tag{2.29}$$

where d is the number of dimensions (3 in this work), ϵ is the barostat friction coefficient and p_ϵ is the corresponding barostat momentum. W is the "mass" of the barostat, analogous to the thermal inertia parameter Q. The simulation cell shape is given by the tensor $\overleftrightarrow{\mathbf{h}}$ where $\overleftrightarrow{\mathbf{h}} = V^{\frac{1}{d}} \overleftrightarrow{\mathbf{h}}_{\mathbf{0}}$. The tensor $\overleftrightarrow{\mathbf{h}}_{\mathbf{0}}$ is the cell matrix which has the condition that $det(\overleftrightarrow{\mathbf{h}}_{\mathbf{0}}) = 1$. The corresponding set of equations of motion are:

$$\dot{\mathbf{q}}_\mathbf{i} = \frac{\dot{\mathbf{p}}_i}{m_i} + \frac{\overleftrightarrow{\mathbf{P}}_{\mathbf{g_0}}}{W_{g_0}} \mathbf{q}_i + \frac{p_\epsilon}{W} \mathbf{q}_i \tag{2.30}$$

$$\dot{\mathbf{p}}_i = \mathbf{F}_i - \frac{\overleftrightarrow{\mathbf{P}}_{\mathbf{g_0}}}{W_{g_0}} \mathbf{P}_i - \left(1 + \frac{d}{\chi}\right) \frac{p_\epsilon}{W} \mathbf{P}_i - \frac{p_\xi}{Q} \mathbf{P}_i \tag{2.31}$$

$$\dot{V} = \frac{dVp_\epsilon}{W} \tag{2.32}$$

$$\dot{p}_\epsilon = dV(P_{int} - P_{ext}) + \frac{d}{\chi} \sum_{i=1}^{N} \frac{\mathbf{P}_i^2}{m_i} - \frac{p_\epsilon}{Q} p_\epsilon \tag{2.33}$$

$$\dot{\overleftrightarrow{\mathbf{h}}}_0 = \frac{\overleftrightarrow{\mathbf{P}}_{\mathbf{g_0}} \overleftrightarrow{\mathbf{h}}_{\mathbf{0}}}{W_{g_0}} \tag{2.34}$$

$$\dot{\overleftrightarrow{\mathbf{P}}}_{\mathbf{g_0}} = V(\overleftrightarrow{\mathbf{P}}_{int} - \overleftrightarrow{\mathbf{I}} P_{ext}) - \frac{V}{d} Tr[\overleftrightarrow{\mathbf{P}}_{int} - \overleftrightarrow{\mathbf{I}} P_{ext}] \overleftrightarrow{\mathbf{I}} - \frac{p_\xi}{Q} \overleftrightarrow{\mathbf{P}}_{\mathbf{g_0}} \tag{2.35}$$

$$\dot{\xi} = \frac{p_\xi}{Q} \tag{2.36}$$

$$\dot{p}_\xi = \sum_{i=1}^{N} \frac{\mathbf{P}_i^2}{m_i} + \frac{p_\epsilon^2}{W} + \frac{1}{W_{g_0}} Tr[\overleftrightarrow{\mathbf{P}}_{\mathbf{g_0}}^{\mathbf{T}} \overleftrightarrow{\mathbf{P}}_{\mathbf{g_0}}] - (\chi + d^2)k_BT. \tag{2.37}$$

2.6 The Velocity Verlet Algorithm

The equations of motion may be integrated to predict the trajectories of the particles as a function of time. A finite difference approach truncates a Taylor expansion about time t in order to determine the position at a time $t + \delta t$.

$$\mathbf{q}(t + \delta t) = \mathbf{q}(t) + \delta t \dot{\mathbf{q}}(t) + \frac{1}{2}\delta t^2 \ddot{\mathbf{q}}(t) + \frac{1}{6}\delta t^3 \dddot{\mathbf{q}}(t) + ... \tag{2.38}$$

The value of the time-step δt must be small enough to maintain accuracy in the integration but large enough that a suitable timescale is used for the molecular dynamics simulation, resulting in a good exploration of the phase space. The velocity-Verlet algorithm [95] is one such approach where the positions ($\mathbf{q}$), velocities ($\mathbf{v}$) and accelerations ($\mathbf{a}$) are all saved at time t:

$$\mathbf{q}(t+\delta t) = \mathbf{q}(t) + \delta t \mathbf{v}(t) + \frac{1}{2}\delta t^2 \mathbf{a}(t) \tag{2.39}$$

$$\mathbf{v}(t+\delta t) = \mathbf{v}(t) + \frac{1}{2}\delta t \big[\mathbf{a}(t) + \mathbf{a}(t+\delta t)\big]. \tag{2.40}$$

Equation 2.40 is evaluated in two stages [3] by calculating the velocity at the time $t + \frac{1}{2}\delta t$ and then the forces at time $t + \delta t$:

$$\mathbf{v}(t+\frac{1}{2}\delta t) = \mathbf{v}(t) + \frac{1}{2}\delta t \mathbf{a}(t) \tag{2.41}$$

$$\mathbf{v}(t+\delta t) = \mathbf{v}(t+\frac{1}{2}\delta t) + \frac{1}{2}\delta t \mathbf{a}(t+\delta t). \tag{2.42}$$

This algorithm has been applied to the constant temperature and constant pressure ensembles by Martyna *et al* [50] by updating the friction coefficient ξ and barostat parameter ϵ in an analogous manner to the particle positions $\mathbf{q}$.

2.7 Periodic Boundary Conditions

The systems in this work are modelled using periodic boundary conditions in which the simulation cell is surrounded by an infinite periodic array of identical cells. As a result, there are images of all the particles in each of the identical cells. If the trajectory of a particle causes it to travel over the simulation cell boundary into an adjoining cell then an image of the particle will enter the central simulation cell at the opposite boundary, thus conserving the number of particles in the simulation cell (as can be seen in figure 2.1). The use of periodic boundary conditions means that surface effects are eliminated. However, the system must be large enough that the effect of the imposed periodicity is limited. In particular, we must account for this periodicity when analysing long-range properties such as disorder in the amorphous phases.

2.8 Minimum Image Convention

The interaction of a particle with its nearest mirror images only is the minimum image convention. The simulation cell (with cell lengths L_x, L_y, L_z) can be thought

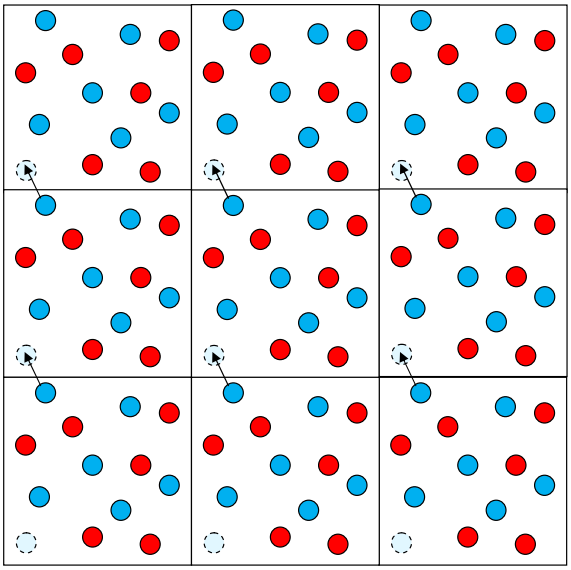

Figure 2.1: As a particle crosses the simulation cell boundary, its mirror image can be seen to enter the simulation cell at the opposite boundary.

of as being recentred onto a given particle so that all other particles (or their mirror image) lie within a distance of $L_{x,y,z}/2$ in the x, y and z directions. The truncation

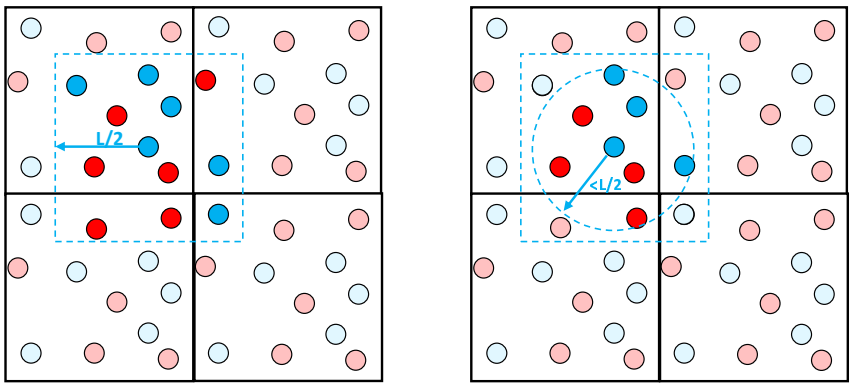

Figure 2.2: Left: In the minimum image convention the particles interact with the nearest $N-1$ mirror images. Right: A spherical truncation of the cutoff is used for the short-range contributions to the potential energy.

of the short range contributions to the potential energy cannot be based solely on the minimum image convention which which does not have a spherical cutoff. Therefore, a spherical truncation cutoff is used which must be less than $L_{x,y,z}/2$ to comply with the minimum image convention but at a distance great enough that the energy contribution of particles at a greater distance is insignificant, as can be seen in figure 2.2.

2.9 Ion-Ion interaction potentials

The ion-ion interactions in this work are modelled using a rigid ion model in which the ions are modelled as charged hard spheres. In this model a pairwise Born-Mayer potential [36] is utilised which has been parameterised for the alkali halides by Fumi and Tosi [26]. A comprehensive review of the suitability of these potentials for the alkali halides is provided by Sangster and Dixon [78] in which they state that these are the standard potentials of choice for the alkali halides, equivalent to the Lennard-Jones potential for the rare-gas systems. The proven ability to model the ionic halide systems and the simplicity of the model makes it an ideal choice for this work. The simple pairwise potential takes the form:

$$U(r) = B_{ij}e^{-a_{ij}r} + \frac{z_i z_j}{r} - F_C(r)\frac{C_{ij}}{r^6} - F_D(r)\frac{D_{ij}}{r^8}. \tag{2.43}$$

The first term in this equation gives the short-range repulsive contribution to the potential energy which describes the repulsion on overlap of the electronic wave-functions by an exponential decay. The parameters B_{ij} and a_{ij} give the height of the repulsive wall and the rate of decay of the repulsion respectively. The constant B_{ij} describing the repulsive wall is dependent on the ion radii σ_i and σ_j:

$$B_{ij} = A\exp\Big[(\sigma_i + \sigma_j)/\rho\Big] \tag{2.44}$$

$$\equiv A\exp\Big[a_{ij}(\sigma_i + \sigma_j)\Big]. \tag{2.45}$$

The constant A is specific to the crystal structure of the system.

The coulombic interaction in equation 2.43 has the functional form of r^{-1}. z_i and z_j are the charges on the ions i and j and the long range term $\frac{z_i z_j}{r_{ij}}$ is treated using an Ewald summation (see section 2.10).

The van der Waals constants C_{ij} (dipole-dipole parameter) and D_{ij} (dipole-quadrupole) were calculated by Mayer [52] from the UV absorption spectra of various alkali halides and describe the system dispersion. This is the attractive force that arises from correlations in the instantaneous fluctuations in the electron densities of the ions. The dipole-dipole parameter can be linked to the ion polarisabilities (α) via the Slater-Kirkwood formula [83]:

$$C_{ij} = \frac{(3/2)\alpha_i\alpha_j}{(\alpha_i/P_i)^{1/2} + (\alpha_j/P_j)^{1/2}}, \tag{2.46}$$

where P_i and P_j are the electron numbers of the ions i and j (the effective number of electrons contributing to the ion polarisability) [73]. Mayer found that the dipole-

quadrupole parameter D_{ij} was between 10 and 20% of the dipole-dipole parameter for the alkali halides and has not been included in this work [52].

The functions $F_C(r)$ and $F_D(r)$ are Tang-Toennies damping functions [96] which are required to account for the behaviour of the dispersion terms at small values of r. At low r overlap effects act to reduce the dispersion terms with respect to their idealised power-law values. The form of the function is designed to fall from a scaling factor of 1 at larger r (where the dispersion effects are observed to have a simple power law dependence) and then to fall to zero as $r \to 0$. For example, the dipole-dipole damping is modelled using a function of the form

$$F_C(r) = 1 - \exp(-f_c r) \sum_{k=0}^{6} \frac{(f_c r)^k}{k!}. \tag{2.47}$$

2.10 Treatment of the long range forces

Due to the ionic systems being modelled, it is necessary to perform a treatment of the long range coulombic terms in equation 2.43 that arise from the charged ions. Since the interaction is long-range (r_{ij}^{-1}) the minimum image convention and a simple short range cutoff cannot be used since the interactions of separations greater than $L/2$ are significant. In this work the Ewald summation [20] is used to calculate these long range charge-charge interactions which has been widely reviewed in the literature [3, 23, 76].

In order to account for the more long range interactions, the central simulation cell is surrounded by a periodic system of identical simulation cells that have been arranged into a sphere. The potential energy of an ion interacting with all other ions within a periodic system is

$$U^{long} = \frac{1}{2} \sum_{\mathbf{n}}^{\infty\ \prime} \Big[\sum_{i=1}^{N} \sum_{j=1}^{N} \frac{z_i z_j}{|\mathbf{r}_{ij} + \mathbf{n}|^{-1}} \Big]. \tag{2.48}$$

The summation over $\mathbf{n} = (n_x L, n_y L, n_z L)$ accounts for interactions outside the central simulation cell where n_x, n_y, n_z are integers. The prime indicates that when $\mathbf{n} = 0$ the interaction does not include $i = j$ (the central ion does not interact with itself). When $\mathbf{n} \neq 0$ and $i = j$ the ion is interacting with its image in a surrounding box.

This summation however, fails to converge, which is the motivation for reconstructing it into two summations that converge more rapidly. The first summation can be thought of physically as a neutralisation in which each point charge is screened with a Gaussian distribution of charge equal in magnitude, but opposite in sign, to

give a summation in real space

$$U_{real}^{long} = \frac{1}{2}\Big[\sum_{i=1}^{N}\sum_{j=1}^{N}\sum_{\mathbf{n}}^{\infty\ \prime} z_i z_j \frac{erfc\big[\kappa|\mathbf{r}_{ij}+\mathbf{n}|\big]}{|\mathbf{r}_{ij}+\mathbf{n}|}\Big], \tag{2.49}$$

where $erfc$ is the complimentary error function

$$erfc(x) = \frac{2}{\sqrt{\pi}}\int_{x}^{\infty} exp(-t^2)dt. \tag{2.50}$$

The value of κ is chosen so that only terms with $\mathbf{n} = 0$ (ions in the central simulation cell) contribute to the summation.

The effect of the screening point charges must be accounted for and a summation in reciprocal space is required to cancel the screening charges with Gaussian distributions with opposite sign

$$U_{recip}^{long} = \frac{1}{2}\sum_{k\neq 0}\Big[\sum_{i=1}^{N}\sum_{j=1}^{N}\frac{4\pi}{k^2L^3}z_i z_j exp\Big(\frac{k^2}{4\kappa^2}\Big)cos(\mathbf{k}\cdot\mathbf{r}_{ij})\Big] \tag{2.51}$$

where $\mathbf{k} = 2\pi\mathbf{n}/L^3$ are the reciprocal vectors.

The interaction of each of the Gaussian screening distributions with the corresponding point charge has been included with equation 2.49 and must be subtracted from the total energy:

$$U_{Gauss}^{long} = \frac{\kappa}{\sqrt{\pi}}\sum_{k=1}^{N} z_i^2. \tag{2.52}$$

Finally, a surface charge at the surface of the sphere of simulation cells corresponding to the $\mathbf{k} = 0$ vector must be accounted for

$$U_{corr}^{long} = \frac{2\pi}{3L^3}|\sum_{i=1}^{N} z_i\mathbf{r}_i|^{\ 2}. \tag{2.53}$$

The total long range contribution to the potential energy is therefore:

$$U^{long} = U_{real}^{long} + U_{recip}^{long} - U_{Gauss}^{long} + U_{corr}^{long}. \tag{2.54}$$

Chapter 3

A parameterised Born-Mayer Potential Model

Previous filling simulations of carbon nanotubes have shown that the internal structure formed is highly dependent on the nature of the ionic melt utilised [111, 112]. In this work it was shown that the ionic melt obtained using a potential which favours a tetrahedrally coordinated crystal system resulted in inorganic structures which could be rationalised in terms of the folding of infinite hexagonal sheets. In contrast, ionic melts obtained using a model which favours octahedral ion coordination gave rise to nanotubes rationalised in terms of the folding of infinite square net sheets. Clearly, the nature of the underlying (thermodynamically favoured) crystal phase plays an important role in the energetics of the pseudo one-dimensional tubular phase.

As a result, the underlying energetics which lead to the ionic melt must be well characterised in order that the results of the filling simulations can be understood. In this chapter, we develop a new ionic potential model with novel thermodynamic and entropic properties. The properties of both the tetrahedral and octahedral crystal phases are investigated as well as the pressure-driven phase transition between the two. The melting points from the two crystal structures are determined and the properties of the liquid phase discussed.

This new potential will be utilised in the carbon nanotube filling simulations. It is hoped that it will provide a bridge in our understanding between the tetrahedral and octahedral crystal systems. Analysis of the new potential model's energetics will develop our understanding of how the potential parameters effect the physical properties of the ionic melt and in turn, the internal structures that are formed within the carbon nanotube.

3.1 The parameterisation of a new potential model

A range of ionic melts will be investigated in the carbon nanotube filling molecular dynamics simulations. It is of interest to investigate how varying the potential parameters of simple pairwise potentials alters the physical properties of the system and specifically, the inorganic pseudo-one dimensional structures that are formed inside the carbon nanotubes.

The interactions between the ions in the molten salts utilised in this work were modelled using a Born-Mayer potential (section 2.9) in which the magnitude of the short-range repulsions are dominated by the ionic radii (equation 2.45).

The Fumi-Tosi parameters [26] for the LiCl system predict a tetrahedral structure in the bulk crystal (see table 3.2 where it is referred to as potential I). This tetrahedral coordination environment can be in the form of the B3 (zinc-blende) or B4 (wurtzite) structures which differ only in the stacking sequence of the layers and are therefore energetically near equivalent (see the centre and bottom structures in figure 3.1). The favouring of the tetrahedral morphology contradicts experiment where the octahedral B1 (rock salt) structure is found to be the stable phase of LiCl (upper panel in figure 3.1). This is because the ion compressibility of the chloride anion is not accounted for in this rigid ion model in which the ionic radii remain fixed in all environments. On placing a gas-phase ion in an environment in which it is surrounded by cations there are two costs to the short-range energy. Firstly, the repulsion due to the overlap of the wavefunctions and secondly the energy due to the compression of the electron density in the confined environment in comparison to the gas phase. Both of these contributions are dependent on the coordination environment of the anion. The compressibility of the chloride ion is also responsible for the stability of the eight fold coordination environment in CsCl, despite the radius ratio of the system predicting an octahedral coordination [74]. The correct eightfold coordinated phase of CsCl is only predicted on inclusion of the "rearrangement energy" which is the energy cost when compressing the anion by converting it from a gas phase to a crystal environment.

This compressible ion effect is most apparent for alkali-earth oxides where the compressibility of the oxide ion is very significant and a Compressible Ion Model (CIM) has been developed for their treatment [48, 116]. In contrast, the phenomenon is small for the alkali halides and can normally be ignored without detriment. However, in the case of LiCl, where the B1 and B3 (or B4) polymorphs lie closer together in energy than the other halides, the omission of the anion compressibility means

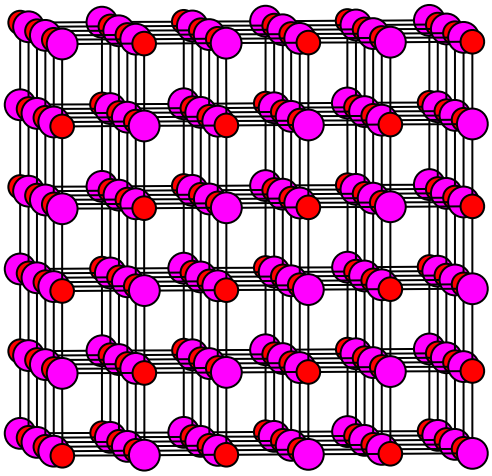

(a)

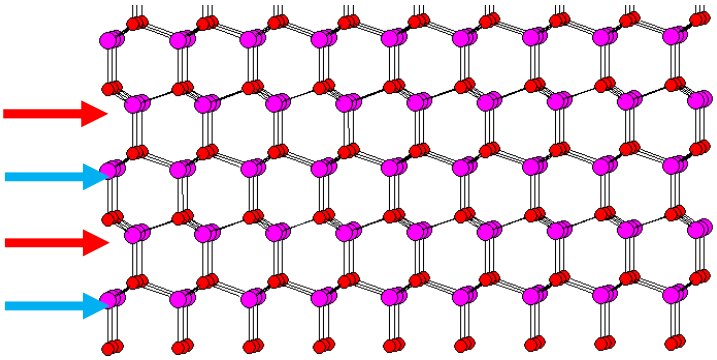

(b)

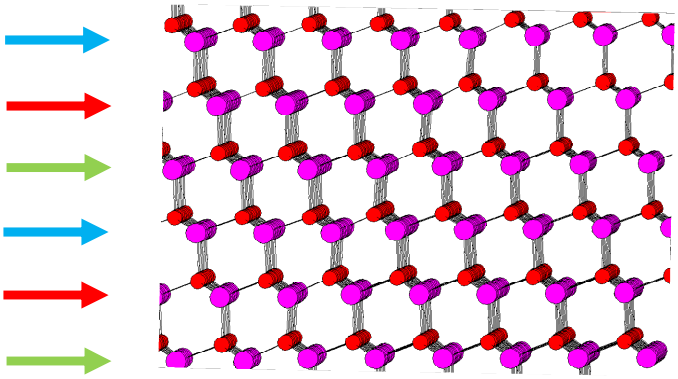

(c)

Figure 3.1: Top: The cubic B1 (rock salt) structure in which the ions are octahedrally coordinated. Centre: The hexagonal B4 (wurtzite) structure in which the ions are tetrahedrally coordinated. The puckered layers have an ABABAB ordering. Bottom: The closely related cubic B3 (zinc blende) structure in which the anions are also tetrahedrally coordinated but the puckered layers have an ABCABCABC ordering. This is a diatomic form of the diamond crystal structure. For a comprehensive description of these crystal structures see Nelmes *et al* [64].

that the tetrahedral coordination environments are unrealistically favoured over the octahedral environment [117].

Despite this limitation in the ability of the potential to model the true stable phase of LiCl, we can view this as a generalised "MX" potential in which we can tune the parameters to our advantage and investigate the physics of the system. This original potential will be referred to as potential I in this work. In particular we can alter the value of B_{ij} effectively varying the cation-anion radius ratio of this metal halide. On increasing the value of B_{ij} (and therefore the radius ratio of the system) we are increasing the size of the cation, making the octahedral coordination environment more favourable with respect to the tetrahedral coordination. The effect of varying B_{ij} of this potential model can be observed by calculating the zero point energy of each crystal phase at different volumes, as can be seen in figure 3.2.

minimum radius ratio	**coordination**	**polyhedral environment**
0.732	8	cube
0.414	6	octahedron
0.225	4	tetrahedron

Table 3.1: The coordination environment predicted by the radius ratio rules [70].

We find that as the radius ratio increases (a larger cation and therefore larger values of B_{ij}), the volume of both the crystal phases is increased and the B1 phase becomes relatively more stable. Pauling calculated the theoretical radius ratios at which various coordinations are favoured [70]. As the radius ratio increases and the cation becomes larger, an increase in the packing of the anions around it is allowed (table 3.1).

Potential I	**M-X**	**M-M**	**X-X**
B_{ij}	8.68	0	61.66
a_{ij}	1.55	1.50	1.55
C_6	2.09	0.0763	115.987
Potential II	**M-X**	**M-M**	**X-X**
B_{ij}	12.938	1.1456	61.66
a_{ij}	1.50	1.50	1.50
C_6	2.09	0.0763	115.987

Table 3.2: The parameters used for potential I (Fumi-Tosi [26]) and the modified potential II in atomic units.

The parameter B_{ij} was modified until the B1 and B3 energy curve minima were equal which occurred when B_{ij} was equal to 12.938 E_h, as can be seen in the bottom of figure 3.2. This means that the internal energy of the two crystal systems are

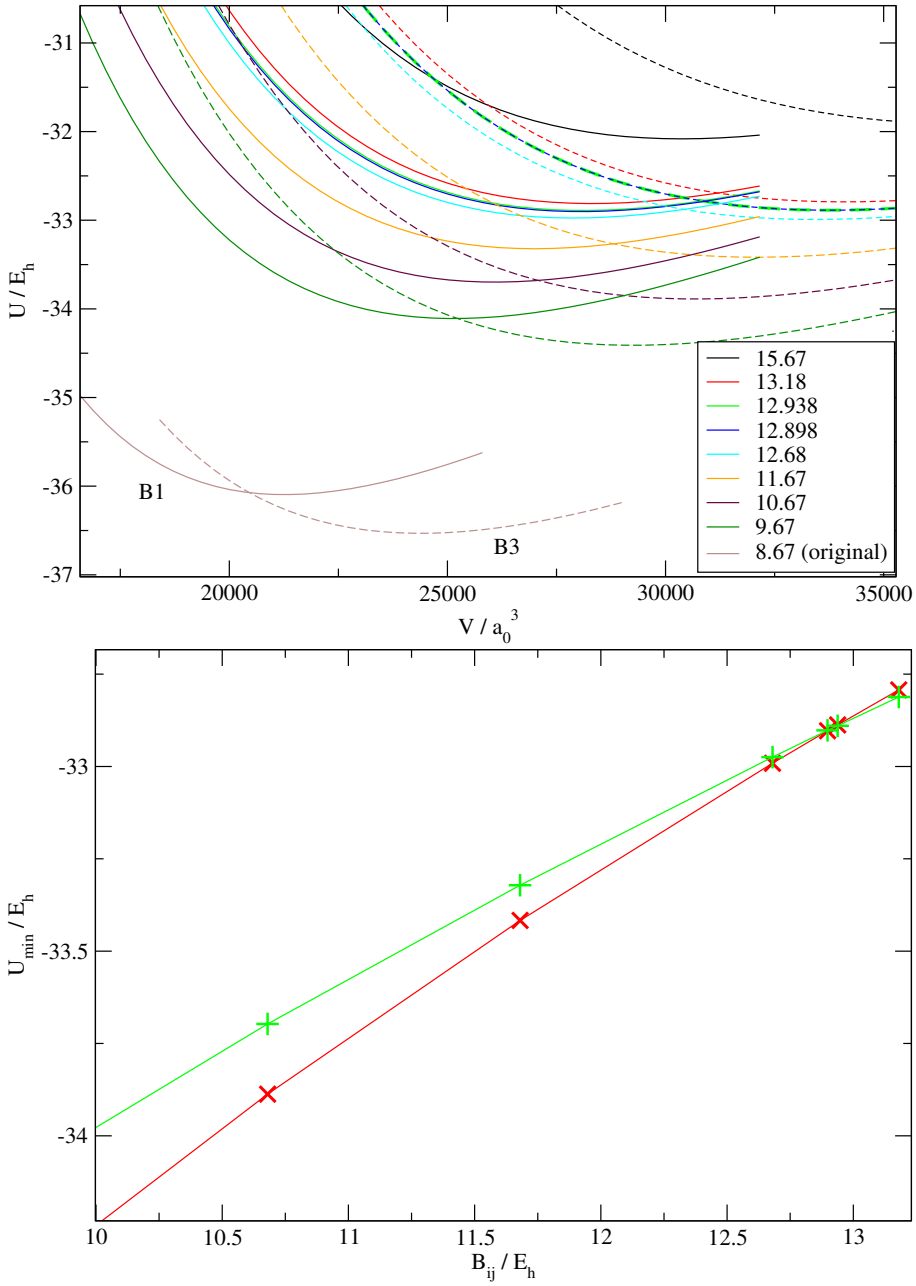

Figure 3.2: Top: The effect of varying the parameter B_{ij} (each colour represents a different value of B_{ij} which is listed in the figure caption in atomic units) on the relative stability of the B1 (rock salt) and B3 (zinc blende) crystal phases. The B1 phase is shown with the unbroken lines and the B3 phase is shown with the dashed lines. The relative energy of the U, V minima of the B1 crystal phase increases with the radius ratio. Bottom: The minima plotted as a function of B_{ij} (B3 shown in red, B1 shown in green). At $B_{ij} = 12.938$ E_h the two crystal systems are equally favoured.

equally favoured for the corresponding radius ratio. This novel case will be referred to as potential II in this research. The crystal system of this interesting potential model is investigated with respect to the crystal and liquid phases.

3.2 Thermodynamic properties of potential II

At the melting temperature (T_{B3}) and melting pressure (P_{B3}) of the B3 crystal the liquid and crystal phases are in thermodynamic equilibrium. Therefore, the Gibbs free energy of the B3 crystal and the liquid are equal at this state point.

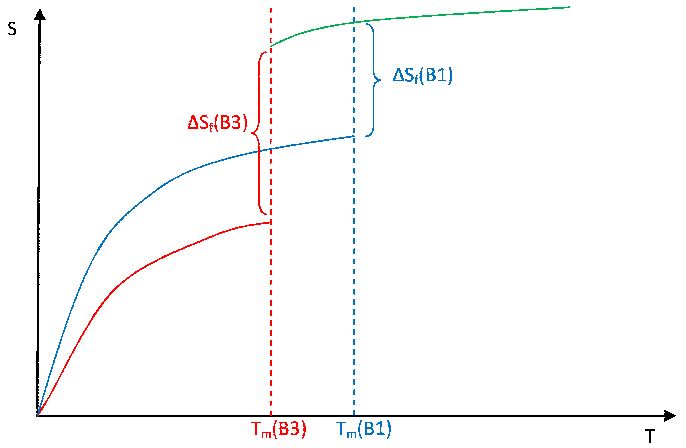

Figure 3.3: red: entropy of the B3 Crystal. blue: entropy of the B1 crystal. green: entropy of the liquid. A schematic to show how the entropy varies with temperature. The melting temperatures of the two crystal systems are dependent on the ratio of the entropies of fusion.

$$G_{B3}(T_{B3}, P_{B3}) = G_{liq}(T_{B3}, P_{B3}) \tag{3.1}$$

and

$$\begin{aligned} &H_{B3}(T_{B3}, P_{B3}) - T_{B3}S_{B3}(T_{B3}, P_{B3}) = \\ &H_{liq}(T_{B3}, P_{B3}) - T_{B3}S_{liq}(T_{B3}, P_{B3}). \end{aligned} \tag{3.2}$$

An equivalent expression is

$$\begin{aligned} &U_{B3} + P_{B3}V_{B3}(T_{B3}, P_{B3}) - T_{B3}S_{B3}(T_{B3}, P_{B3}) = \\ &U_{liq} + P_{B3}V_{liq}(T_{B3}, P_{B3}) - T_{B3}S_{liq}(T_{B3}, P_{B3}). \end{aligned} \tag{3.3}$$

Similarly when the B1 crystal and the liquid are at equilibrium we have

$$\begin{aligned} U_{B1} + P_{B1}V_{B1}(T_{B1}, P_{B1}) - T_{B1}S_{B1}(T_{B1}, P_{B1}) &= \\ U_{liq} + P_{B1}V_{liq}(T_{B1}, P_{B1}) - T_{B1}S_{liq}(T_{B1}, P_{B1}) &\quad . \end{aligned} \tag{3.4}$$

We recall that potential II was designed so that the internal energy of the B1 crystal U_{B1} was equal to that of the B3 crystal, U_{B3} (see section 3.1). If, in addition, we also assume that the liquid consists of one phase (i.e. the liquid is not polyamorphic) we can subtract equation 3.4 from equation 3.3 to give

$$\begin{aligned} P_{B3}V_{B3}(T_{B3}, P_{B3}) - P_{B1}V_{B1}(T_{B1}, P_{B1}) - T_{B3}S_{B3}(T_{B3}, P_{B3}) + T_{B1}S_{B1}(T_{B1}, P_{B1}) &= \\ P_{B3}V_{liq}(T_{B3}, P_{B3}) - P_{B1}V_{liq}(T_{B1}, P_{B1}) - T_{B3}S_{liq}(T_{B3}, P_{B3}) + T_{B1}S_{liq}(T_{B1}, P_{B1}) & \end{aligned} \tag{3.5}$$

At zero pressure we have:

$$\begin{aligned} T_{B3}S_{B3}(T_{B3}, 0) - T_{B1}S_{B1}(T_{B1}, 0) &= \\ T_{B3}S_{liq}(T_{B3}, 0) - T_{B1}S_{liq}(T_{B1}, 0) &\quad . \end{aligned} \tag{3.6}$$

We find that the origin of the difference in melting temperature at zero presure between the two crystal systems is purely entropic, which is to be expected since the internal energies are equal. In fact the ratio of the melting temperatures gives us an insight into the entropy of melting the two crystals.

$$T_{B3}\Big(S_{B3}(T_{B3}, 0) - S_{liq}(T_{B3}, 0)\Big) = T_{B1}\Big(S_{B1}(T_{B1}, 0) - S_{liq}(T_{B1}, 0)\Big) \tag{3.7}$$

$$\frac{T_{B3}}{T_{B1}} = \frac{\Delta S_f^{B1}}{\Delta S_f^{B3}} \tag{3.8}$$

There is an inverse relationship between the melting temperature and the entropy of fusion ΔS_f^x; the smaller the entropy of fusion, the higher the melting temperature.

Figure 3.3 shows the purely entropic dependence of the melting points of the two crystal systems. Unlike other potential models, the difference between the two melting points is dependent only on the entropy of the systems. Therefore, it is of interest to determine the entropic and melting properties of this system (see sections 3.4 and 3.3 respectively).

3.3 The melting temperature of the parametrised potential

The melting point of this unusual system has thermodynamic consequences since the difference in melting points arises for purely entropic reasons (see section 3.2, figure 3.3). The nanotube filling simulations must be performed at a temperature greater than the crystal melting point so that the ions outside of the carbon nanotube are in the liquid phase. Both these points provide motivation for the calculation of the system melting temperature.

At the melting temperature of the ionic salt, the free energy of the liquid and crystalline phases are equal. In this work the crystal-liquid interface was simulated allowing the melting temperature to be determined. At the melting temperature the crystal-liquid interface is stable and both phases can coexist in equilibrium. At a temperature above the melting temperature the crystal melts at the interface and the liquid region grows. Conversely, at a system temperature below the melting temperature the crystal phase grows at the interface and the liquid region is sacrificed.

Molecular dynamics simulations were performed for 48 ps using potential II in the isothermal-isobaric ensemble with a cubic simulation cell containing 108 molecular units to equilibrate the B1, B3 and liquid phases. The volume was allowed to change isotropically by constraining the barostat to the isotropic fluctuations only (see section 2.5). The liquid phase simulation was pressurised for a further 6 ps until the cell volume was comparable to that of the crystal systems.

The interface was prepared by joining the crystal and liquid configurations from the ends of these equilibrating runs to form a tetragonal cell. A short molecular dynamics run was performed at constant volume with frequent temperature rescaling to 100 K so that the ions at the interface in unphysical configurations could adjust. The resulting configuration was allowed to equilibrate at 100 K in the isothermal-isobaric ensemble for 12 ps where the volume could adjust so that the two phases could reach their equilibrium densities.

The resulting interface was used as the starting configuration for isothermal-isobaric molecular dynamics simulations at various temperatures. The interface was monitored to see if the crystal phase or the liquid phase was growing and therefore if the average system temperature was below or above the melting temperature. The crystallisation and melting events were monitored by calculating the coordination number of the ions in different regions of the simulation cell. The coordination number of an ion was calculated by calculating the number of ions of opposite charge

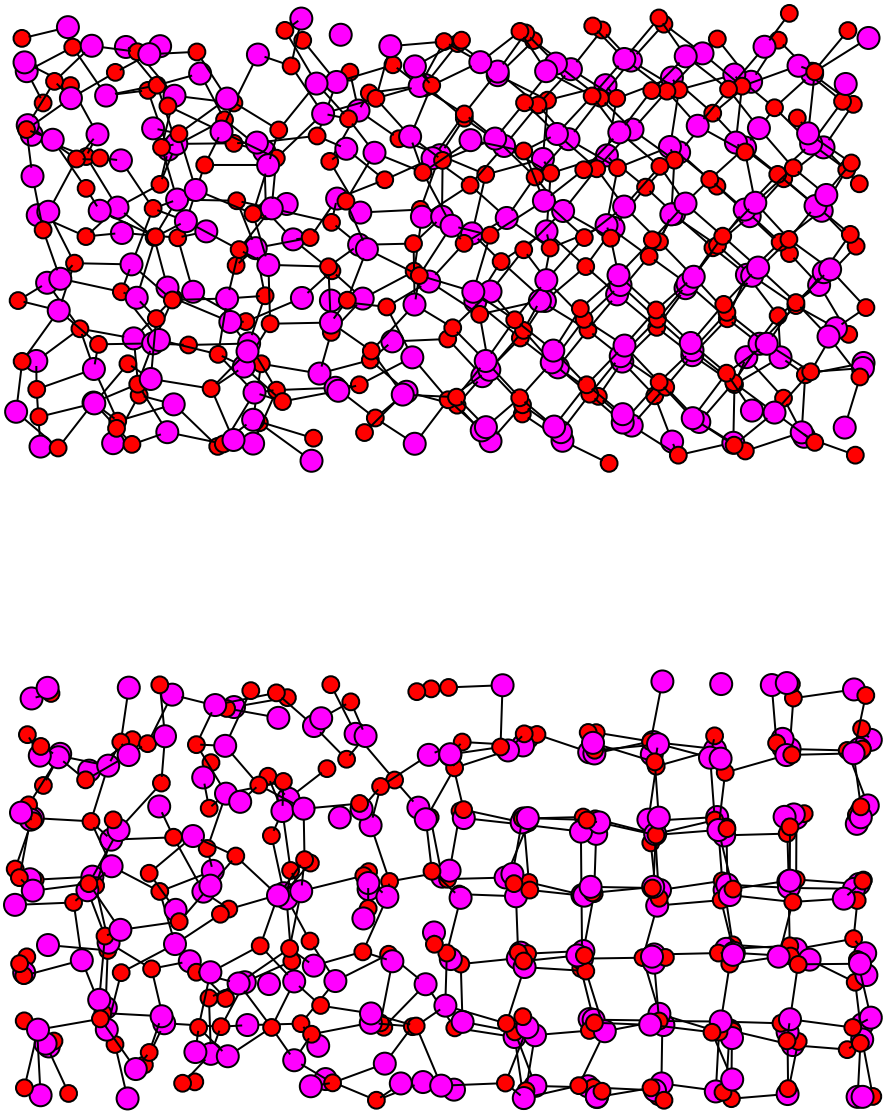

Figure 3.4: Snapshots of the interface simulation cells from the molecular dynamics simulations (Top: B3-liquid Bottom: B1-liquid). These consist of liquid and crystalline regions separated by an interfacial region.

residing at a distance less than the defined cutoff from itself. Periodic boundary conditions (see section 2.7) were accounted for when calculating the cation-anion separations. The cutoff used was taken to be 7 a_0 which is the upper bound for the first anion-cation peak in the liquid radial distribution for this system. Since the coordination number is expected to vary over the length of the simulation cell (depending if the ion is in the liquid, interfacial or crystal region) the simulation cell was divided into "bins" along the longest cell length of the tetragonal cell. The number of ions of a given coordination number that resided in each "bin" was calculated resulting in a density profile along the length of the cell. Density profiles were calculated at various times during an interface simulation such as can be seen for the crystallisation of the B3 interface at 600 K in figure 3.5.

The melting temperatures were determined to be 763 ± 13 K for the B1 phase and 612 ± 13 K for the B3 phase at zero pressure. This difference in temperature is very significant since we recall that the internal energy of the two crystal systems is identical for potential II. The difference in the melting temperature is purely entropic in origin. The higher melting temperature of B1 indicates a lower entropy of formation of the liquid phase from the B1 crystal phase (see figure 3.3). Using the melting temperatures in equation 3.8 we can quantify this at 80 % of the value of the formation of the liquid phase from the B3 crystal phase.

B3	
Pressure (a.u.)	**melting point (K)**
0.00000	$600 < T_m < 625$
0.00001	$625 < T_m < 650$
B1	
Pressure (a.u.)	**melting point (K)**
0.00000	$750 < T_m < 775$
0.00005	$1085 < T_m < 1100$
0.00010	$1425 < T_m < 1450$
0.00015	$1550 < T_m < 1575$
0.00030	$1900 < T_m < 1925$
0.00030	$2400 < T_m < 2425$

Table 3.3: The melting temperatures of the B1 and B3 crystal phases as determined by the interface calculations.

The analysis was repeated at different system pressures so that a region of the phase diagram could be determined. It was not possible to examine the phase diagram at negative pressures since at all negative pressures the system went past the point of mechanical stability. Only a small part of the B3 crystal-liquid coexistence line could be determined as at pressures greater than 0.00005 atomic units the system

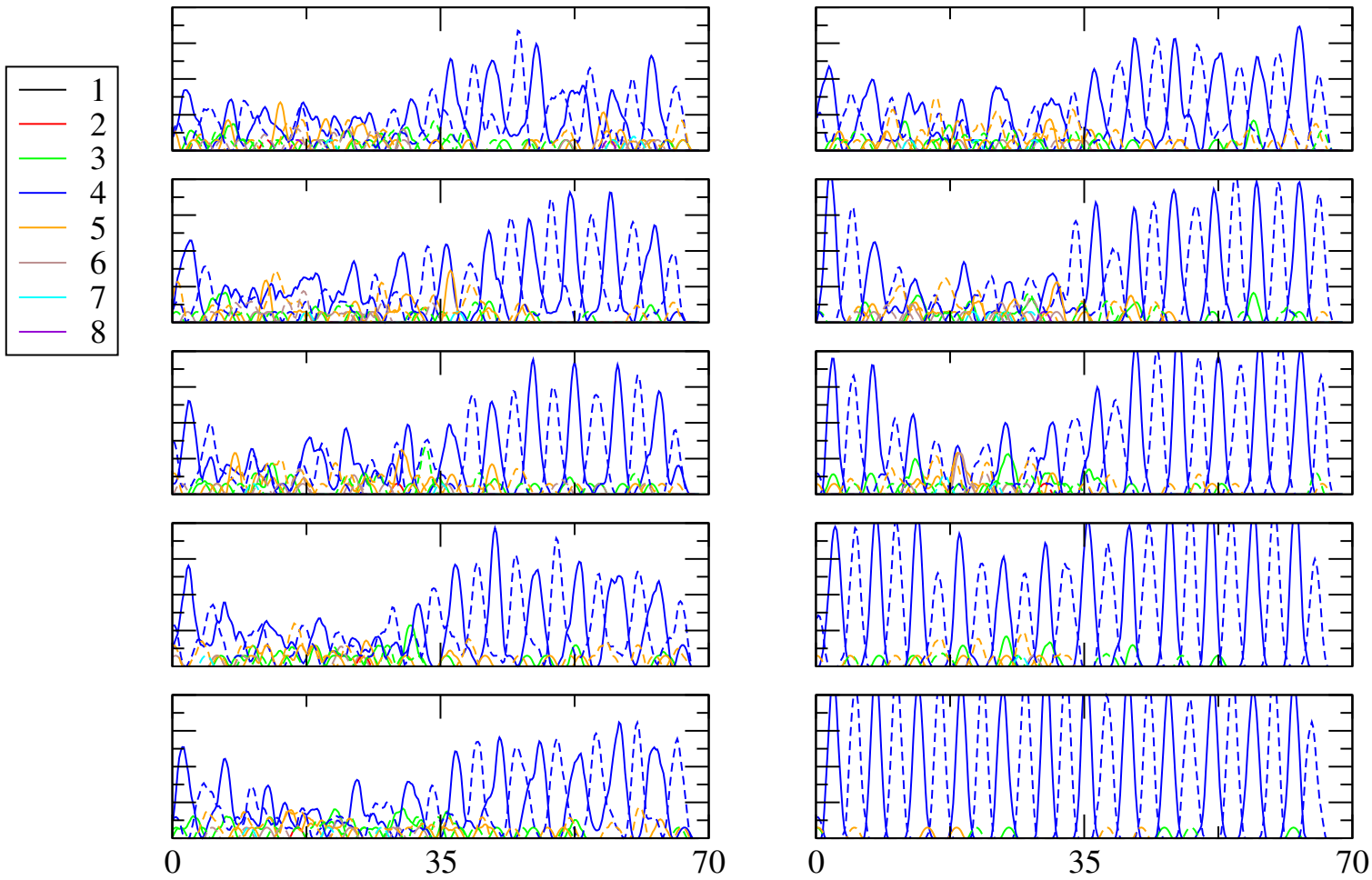

Figure 3.5: The density profiles along the simulation cell as a function of coordination number. Each successive graph is averaged over the next 0.15 ps. The dashed lines indicate the coordination number of the anions and the unbroken line the coordination environment of the cations. As the simulation progresses the interface moves into the liquid region. The onset of crystallisation can be recognised by the discrete peaks in the density profile and the uniform coordination number of four, indicating a tetrahedral coordination environment. The average temperature of the system is found to be below that of the melting temperature.

undergoes a phase transition to the B1 crystal phase (see section 3.5). It appears that the inclusion of the interface also lowers the activation barrier to the phase transition (as well as removing the hysteresis for melting) on comparison with the over-pressure that was determined for the crystal simulations (1.71×10^{-4} atomic units, see section 3.5).

It was possible to determine the B1 crystal-liquid coexistence line up to 0.001 atomic units. At greater pressures the large fluctuations of the barostat and thermostat meant that the varied instantaneous temperatures onset melting or freezing events that may not correspond to the true system equilibrium. The outcome of these simulations therefore varied close to the melting temperatures and were not reliable.

Figure 3.6 summarises the P-T phase diagram that was produced for potential II. Figure 3.6 shows that for the B1 phase $\frac{dT}{dP}$ decreases with increasing temperature.

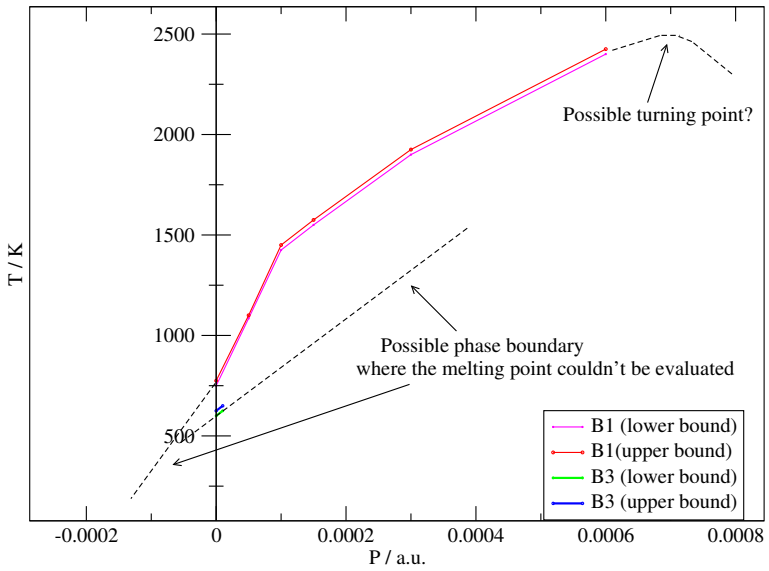

Figure 3.6: The determined melting temperatures (interface calculations) and predicted solid-liquid coexistence lines for the two crystal systems.

If in fact there is a turning point in the liquid-crystal coexistence line then this may be an indication that there is a pressure induced amorphic (PIA) phase transition in the liquid phase [54]. Such PIA are associated with a negative melting slope in which the liquid phase is more dense than the crystal, indicating the possible presence of high and low density liquid phases. The properties of the liquid phase will be investigated in section 3.10.

3.4 The vibrational density of states

The difference in the melting point of the two crystal systems is purely entropic in origin. It is therefore of interest to determine the entropy of the crystal systems. In this section we will calculate the entropy from the vibrational density of states.

We can approximate the ions in the system as an ensemble of simple harmonic

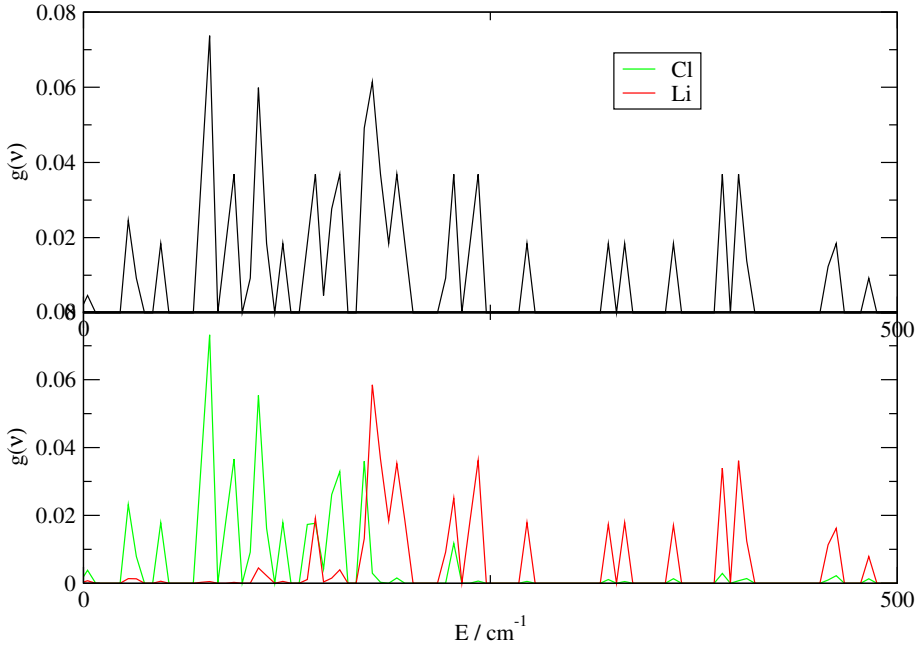

Figure 3.7: The density of states for the B1 crystal system using potential II. The top panel shows the total density of states and the bottom panel show the spectra for both the cations and anions.

oscillators. The harmonic approximation gives the energy of the i^{th} vibrational energy level as

$$\epsilon_i = (n + {}^1/_2)h\nu. \tag{3.9}$$

Summing over these energy levels, the partition function for vibrational motion is therefore

$$q = \frac{e^{-h\nu_i/2k_BT}}{1 - e^{-h\nu_i/k_BT}}. \tag{3.10}$$

The Helmholtz Free Energy (A) is given by

$$A - A_0 = U - TS \tag{3.11}$$

$$= -k_BT\ln(q), \tag{3.12}$$

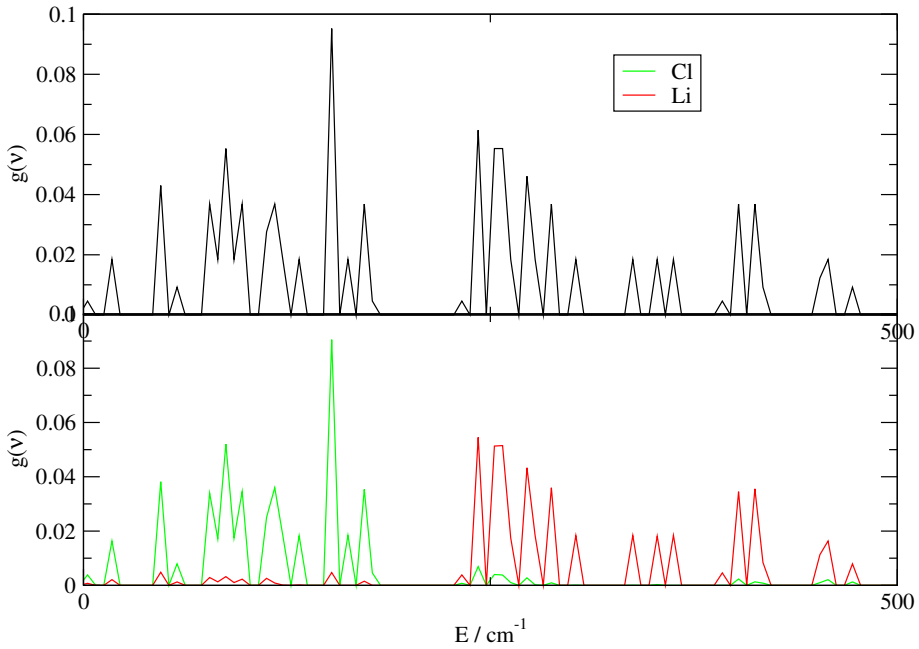

Figure 3.8: The density of states for the B3 crystal system using potential II. The top panel shows the total density of states and the bottom panel show the spectra for both the cations and anions.

where q is the partition function. Therefore, for a system of simple harmonic oscillators we have

$$A - A_0 = \sum_i -k_B T ln \left[\frac{e^{-h\nu_i/2k_BT}}{1 - e^{-h\nu_i/k_BT}} \right] \tag{3.13}$$

$$= \sum_i \frac{h\nu_i}{2} + k_B T \ln \left[1 - e^{-h\nu_i/k_BT} \right]. \tag{3.14}$$

The entropy of the system is given by the partial derivative

$$S = -\left(\frac{\partial A}{\partial T} \right)_V \tag{3.15}$$

$$= -\frac{\partial}{\partial T} \left(\sum_i \frac{h\nu_i}{2} + k_B T \ln \left[1 - e^{-h\nu_i/k_BT} \right] \right)_V \tag{3.16}$$

$$= \sum_i -k_B \ln \left[1 - e^{-h\nu_i/k_BT} \right] + \frac{h\nu_i}{T \left[e^{h\nu_i/k_BT} - 1 \right]}. \tag{3.17}$$

Therefore, we can evaluate the following integral to evaluate the entropy as a function of temperature

$$S(T) = \int_0^{\nu_{max}} \left(-k_B \ln \left[1 - e^{-h\nu/k_BT} \right] + \frac{h\nu}{T \left[e^{h\nu/k_BT} - 1 \right]} \right) g(\nu) \partial\nu, \tag{3.18}$$

where $g(\nu)$ is the vibrational density of states. The vibrational density of states was constructed by determining the dynamical matrix for both the B1 and B3 crystal systems. The ions in a system of 108 molecular units of LiCl were individually displaced from their ideal lattice sites (denoted using mass-weighted Cartesian co-ordinates) by $\pm 0.003\ a_0$ in the x, y and z directions. The $3N$ elements of the matrix $\left(\frac{\partial F}{\partial r}\right)$were determined by taking the differential of the force on the i^{th} ion with respect to the direction α, after the displacement of the ion in the β direction:

$$\mathbf{D}_{\alpha,\beta}(i) = \left(\frac{\partial^2 U(i)}{\partial r_\alpha \partial r_\beta}\right) \tag{3.19}$$

where α and β is the x,y or z direction. On diagonalising this matrix, the eigenvalues corresponding to the vibrational frequencies and the eigenvectors corresponding to the phonon modes were obtained. The resulting vibrational density of states can be seen in figures 3.7 and 3.8. As expected the density of states consists of discrete peaks corresponding to the phonon modes of the crystals.

The respective density of states were used to calculate the entropy of the B1 and B3 crystals as a function of temperature using equation 3.18 and is shown in figure 3.9. There is only a small difference in entropy between the two crystal systems. This can be attributed to the vibrational entropy contribution arising from the different local environments of the ions in the two crystal systems. In the region of the system melting points (section 3.3), the entropy of B1 is higher than that of the B3 system. This small difference in entropy accounts for the differing melting points of the B1 and B3 crystal systems using potential II.

3.5 The transition from the B3 crystal to the B1 crystal system using potential II

The energy/volume relationships between the B3 and B1 crystal polymorphs indicate that, as pressure increases, the higher density B1 structure will become thermodynamically more favourable and so a (pressure-driven) phase transformation may occur. It is of interest, therefore, to attempt to drive this transition.

A cubic cell of 108 molecular units of LiCl was constructed for the B3 crystal system. A short molecular dynamics run using the modified potential II of 1000 steps (0.6 ps) was performed with temperature rescaling in order that the ions were displaced slightly from their ideal lattice sites.

Molecular dynamics simulations were then performed in the NPT ensemble at various pressures. A timestep of 25 atomic units (0.6 fs) was found to conserve energy

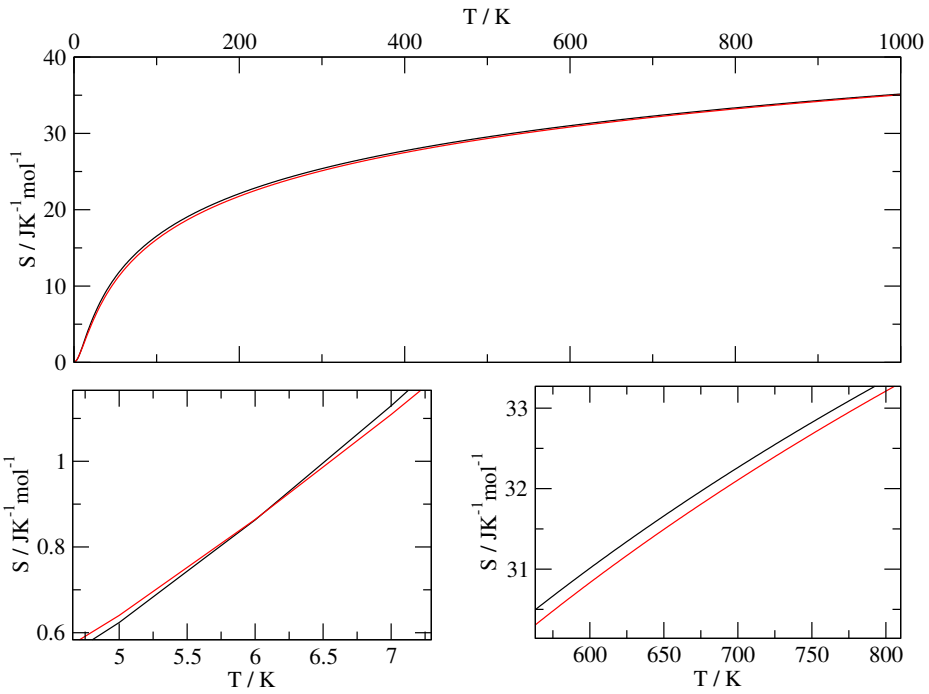

Figure 3.9: Top: How the entropy of the crystals vary with temperature which is calculated from the density of states (B1 shown in black and B3 shown in Red) At all but the lowest temperatures the B1 crystal has greater entropy than the B3 crystal. Bottom left: The intercept of the two entropy curves occurs at 6.05 K and 0.8 $JK^{-1}mol^{-1}$. Bottom Right: The entropy of the systems in the region of interest (close to their melting points). The entropy of the B1 crystal system is slightly higher than that of the B3 crystal in this region.

and be sufficiently long enough to explore phase space. The Nosé-Hoover thermostat (see section 2.3) and both anisotropic and isotropic barostats (see section 2.5) were utilised; all with a relaxation time of $\tau = 10000$ atomic units (0.24 ps). The system was allowed to equilibrate for 18 ps before any pressure was applied.

It was found that the system underwent a first order phase transition to the denser B1 crystal system when the system was pressurised to $1.71(\pm 0.01) \times 10^{-4}$ atomic units (5.0 GPa). This is considerably less than the 15-21 GPa reported for the unmodified potential I by Wilson *et al* [117]. Theoretically the phase transition should occur at zero pressure due to the fact that the potential was parameterised so that the internal energy of the structures was equal. In practise a pressure must be applied for the transition to occur. This "over-pressure" enables the system to overcome the activation barrier to the phase transition mechanism.

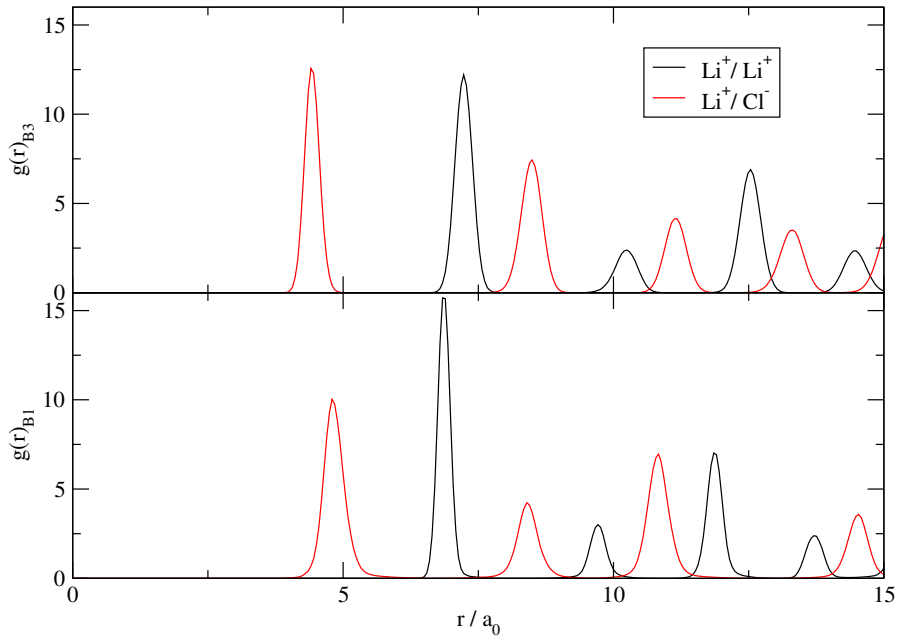

Figure 3.10: The radial distribution function $g(r)$ for the two crystal systems as calculated by equation 3.20. Top: Before the transition took place, the B3 crystal system. Bottom: B1 crystal system, after the transition took place.

The radial distribution function, $g(r)$, of a system indicates the coordination environment of an ion, as a function of distance from that ion. Experimentally, this function is constructed by performing a Fourier Transform from the reciprocal space neutron or X-ray scattering function to give $g(r)$ in real space. Theoretically, the distribution can be calculated directly from the ion-ion separations on examining the ion configurations. The function compares the density of the coordinating ions with that of an ideal gas where the density of the particles is uniformly distributed

through space:

$$g(r) = \frac{1}{x_{norm}} \sum_{i=1}^{N} n_{r_{ij}} \tag{3.20}$$

$$x_{norm} = \frac{4\pi N^2}{6V}[(r + \delta r)^3 - r^3], \tag{3.21}$$

where $n_{r_{ij}}$ is the number of ions with separation r_{ij} and x_{norm} is a normalisation factor. The summation over $n_{r_{ij}}$ is determined by calculating a histogram with a class-interval smaller than the ion-ion separations themselves. The function $g(r)$ is therefore the ratio of the number of ions lying at a separation r_{ij} within a small spherical interval $(r + \delta r)$ with respect to the number of ions with separation r_{ij} lying in the equivalent spherical interval for an ideal gas, given by the normalisation factor x_{norm}. Therefore, x_{norm} is derived by taking the number density (N/V) multiplied by the number of ion sites multiplied by the volume of the spherical shell. Double counting is also accounted for with the factor of a $\frac{1}{2}$. The resulting function $g(r)$ consists of discrete peaks for a crystalline environment due to the ordered arrangement of ions in the crystal. For amorphous systems, the function is continuous and analysis of the deviations from $g(r) = 1$ are invaluable in examining mid to long range order, as they indicate ion-ion correlations.

The radial distribution of this crystal system prior to the pressure application is distinctly different to that generated after the phase transition has taken place as can be seen in figure 3.10. As one expects, the distribution consists of discrete peaks indicating a highly ordered crystal system. It is noted that the nearest neighbour anion-cation separation increases as the pressure is applied. This is evidence of the pressure-distance anomaly where the nearest neighbour increases despite the reduction in system volume due to the increase in coordination number as more cations are packed around the central cation. The coordination number changes from 4 to 6 as the transition takes place.

Further evidence that the transition has occurred from the B3 to the B1 crystal system can be gleaned from calculating the radius ratio (r_{+-}/r_{++}) from the first peaks of the radial distribution functions. In the B3 crystal system the ratio of the first peaks is 0.61 which compares favourably with the theoretical value of $\sqrt{6}/4$. After, the transition has occurred the radius ratio is 0.69 which is close to the theoretical value of $\sqrt{2}/2$ in the B1 system.

The phase transition occurred in two stages as can be seen in figures 3.11 and 3.12. The mechanism of the transition is examined further in section 3.7. The first indication of change was that the cubic cell underwent a tetragonal distortion, with

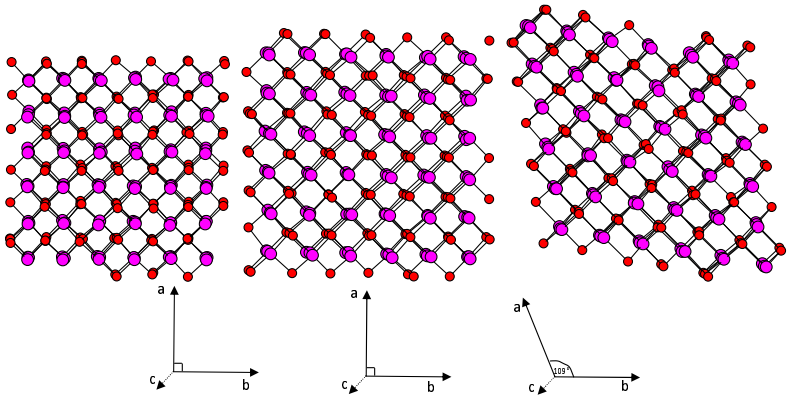

Figure 3.11: The simulation cell viewed towards the (100) plane. The a and b cell lengths can clearly be seen to increase before the cell undergoes a shearing mechanism.

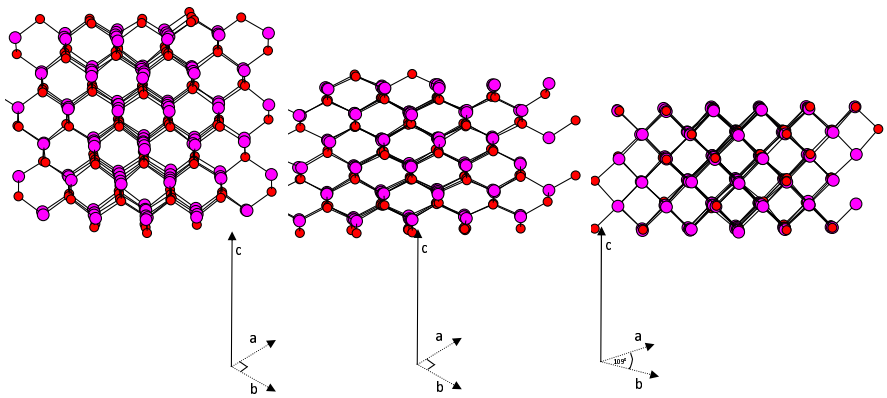

Figure 3.12: The simulation cell viewed towards the (110) plane. The cell undergoes a compression along the c axis before the shearing motion occurs.

two cell lengths increasing by 3 % and the other reduced by 7 %. After 420 fs the cell then underwent a shearing motion with one angle increasing to 109°, with a further 25 % reduction of the shortest cell length and a 13 % increase of the others.

3.6 The effect of the anisotropic barostat on the transition between the B3 and B1 crystal system

It is clear that the mechanism by which pressure is applied may be critical in determining the nature of the phase transformation. The relatively small numbers of ions in a typical simulation cell means that the pressure fluctuations are large by experimental standards and may play a role in the phase transitions. As a result, we will here determine the the effect of changing the barostat relaxation time (and hence changing the rate at which the pressure changes are applied).

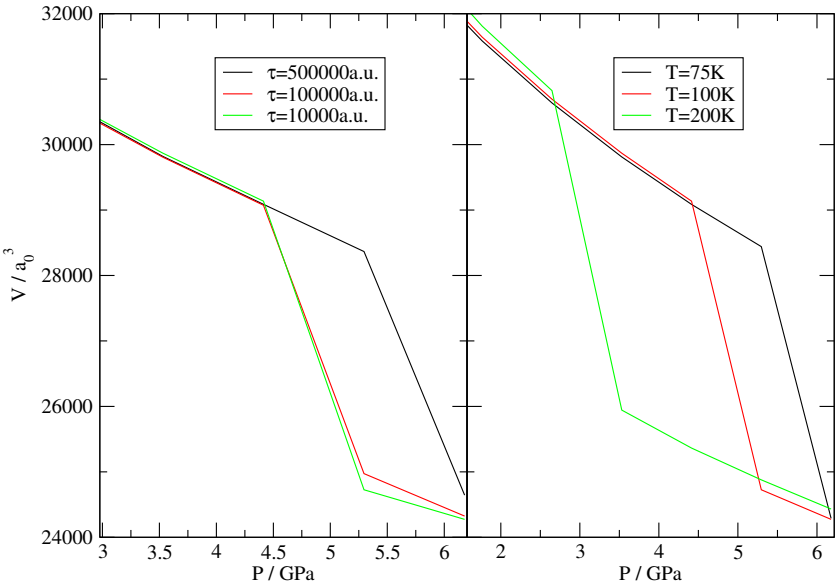

Figure 3.13: Left: The effect of the barostat, how the over pressure varies with the barostat relaxation time, τ. Right: The effect of temperature on the over pressure.

The molecular dynamics simulation was repeated using a value of $\tau = 500000$ atomic units (12 ps) and $\tau = 100000$ atomic units (2.4 ps) for both the anisotropic and isotropic barostats. It was found that the over-pressure increased with increasing τ as can be seen in figure 3.13. When τ was reduced below 10000 atomic units the system failed to conserve energy and hence the simulation broke down. This is due to the relatively large modification to the equations of motion (as can be seen in

equations 2.14 and 2.18) by a small value of τ.

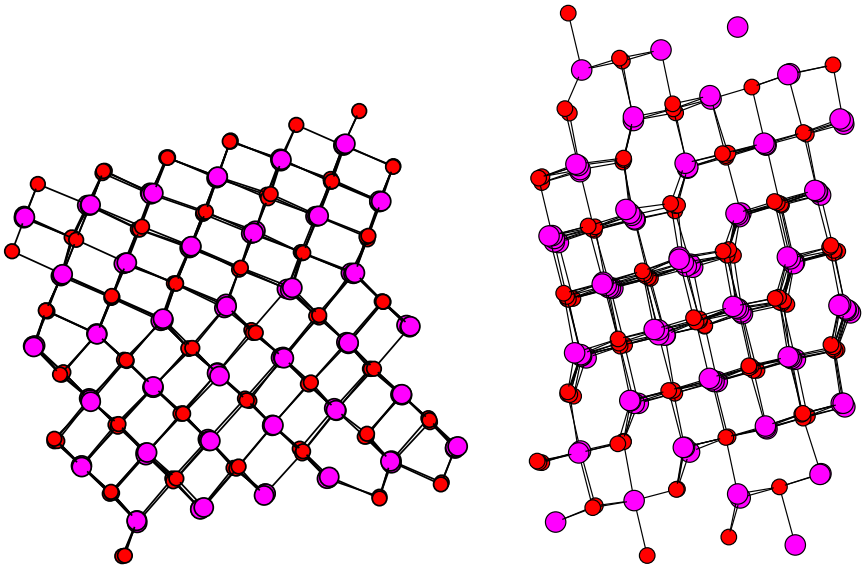

Figure 3.14: Left: Grain boundary defect in the resulting B1 crystal from the molecular dynamics simulation using $\tau = 100000$. There is a fault in the stacking of the layers forming the crystal due to the less concerted movement of the ions in the phase transition when a larger value of τ is used. This persisted to the end of the simulation. Right: A similar fault formed during the simulations with $\tau = 500000$ atomic units but this was eliminated by the end of the simulation.

The reason that the over-pressure increases with τ is that the mechanism relies on a concerted movement of the ions during the tetragonal distortion and shearing motion as described in section 3.7. The larger modification of the equations of motions by a smaller τ promotes such a concerted motion. Defects are observed in the structures when a large value of τ is used ($\tau = 100000$ and $\tau = 500000$ atomic units). A grain boundary defect was formed during the simulation using $\tau = 500000$ atomic units but was then eliminated by the end of the simulation. A defect was also formed in the simulation where $\tau = 100000$ atomic units which persisted on the timescale of the simulation, both of these can be seen in figure 3.14. These stacking faults are created as the movement of the ions during the transition using a "weaker" barostat are less concerted due to a smaller modification of the equations of motion. Further evidence of the defect can be observed by monitoring the system energy; we note that the simulation containing the persistent grain boundary defect ends at a higher energy than the others in figure 3.15. This increase in system energy in the molecular dynamics run with $\tau = 100000$ atomic units points to a defect energy of the order of 10^{-3} E_h per ion.

Similarly the over pressure is also reduced by increasing the system temperature and can be seen in figure 3.13. The increase in kinetic energy of the ions reduces the

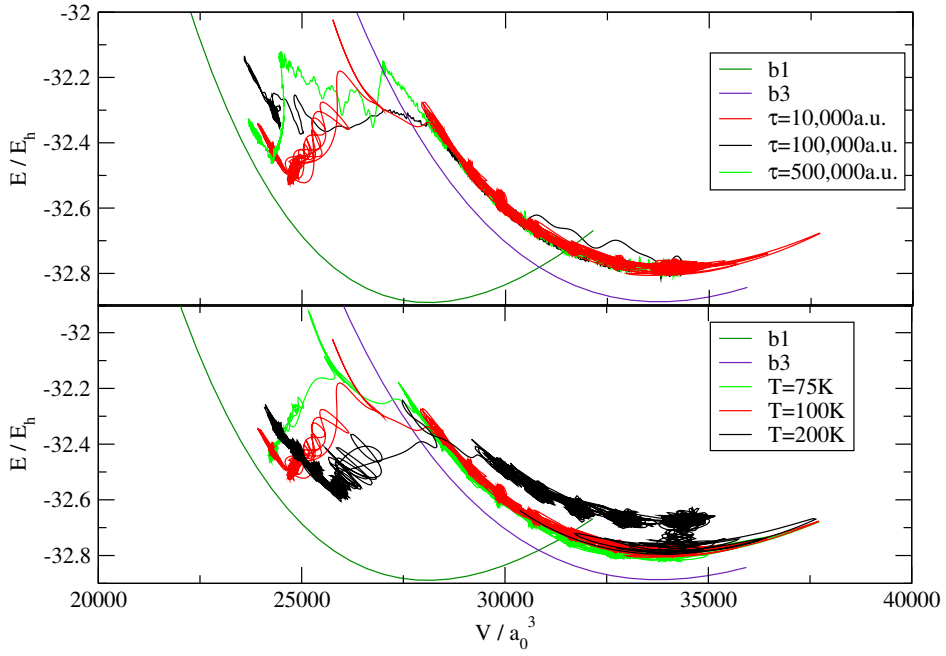

Figure 3.15: The energy versus volume during the phase transition in comparison to the 0K energy volume curves. Top: Varying the barostat parameter τ. The simulation where $\tau = 500000$ atomic units ends at a higher energy than the systems using the other relaxation times. This is due to the persistent grain boundary defect shown in figure 3.14. Bottom: Varying the system's kinetic energy.

system hysteresis by providing additional thermal energy which assists in overcoming the activation energy barrier for the transition mechanism.

The difference in the way that the system explores the energy landscape according to the varying barostat and system temperature can be observed in figure 3.15. There is further evidence that the ion movement is less concerted as τ is increased since the pathway does not appear to become trapped in the potential energy well of an intermediate and explores more diverse regions of the landscape between the two crystal systems.

3.7 Structure of the intermediate in the transformation of the crystal from B3 to the B1 system

A NPT molecular dynamics simulation was performed at 100 K with the pressure being ramped by 0.00003 atomic units (0.88 GPa) every 12.1 ps. The Nosé-Hoover thermostat, anisotropic and isotropic barostats were used with a relaxation time of 0.24 ps. The system underwent a phase transition from the B3 to the B1 crystal

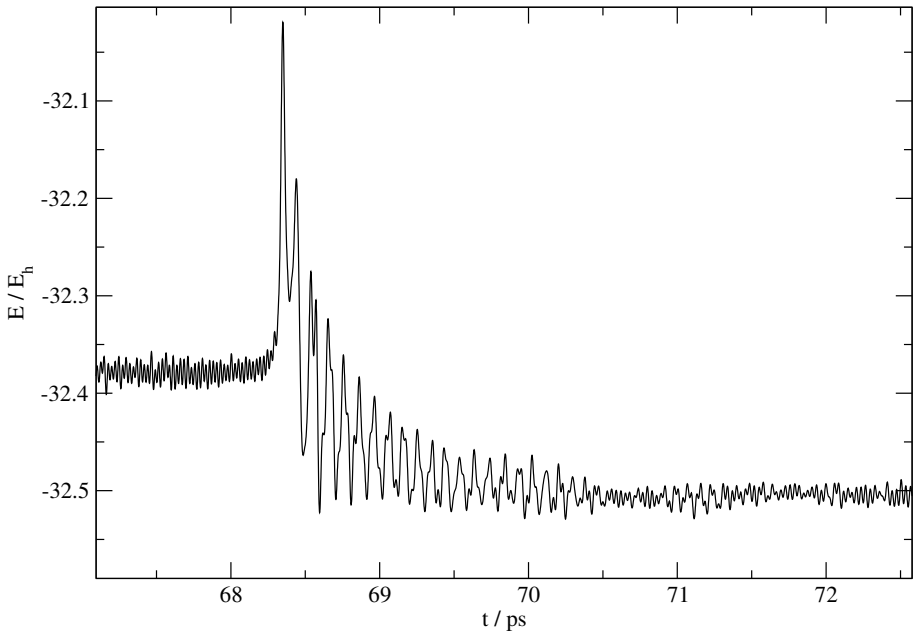

Figure 3.16: The energy of the system increases at the time corresponding to the phase transition. At this region of high potential energy, do we have a stable intermediate?

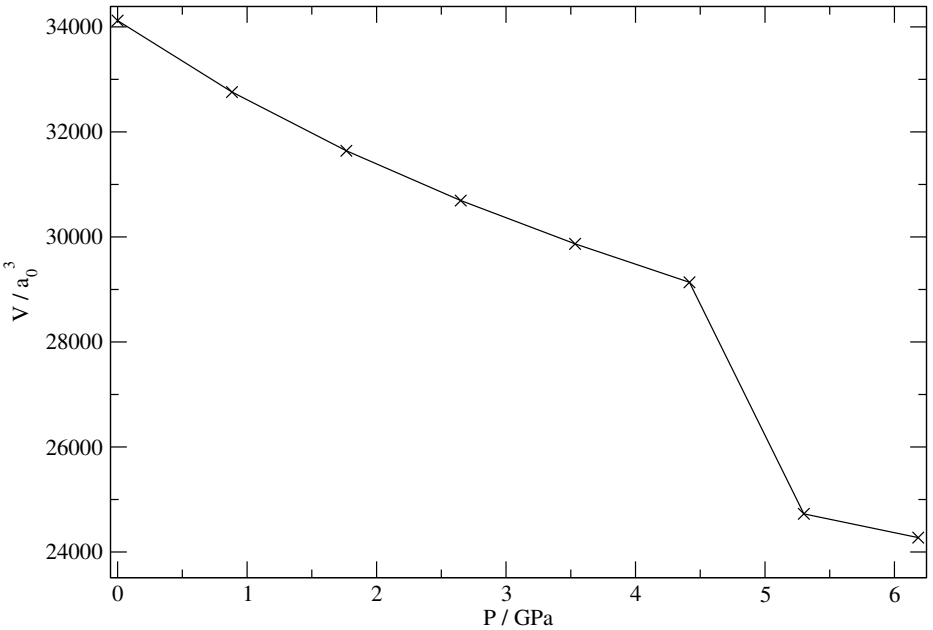

Figure 3.17: The system undergoes a first order phase transition corresponding to the increase in energy observed in figure 3.16.

structure when the pressure reached 0.00018 atomic units (5.3 GPa).

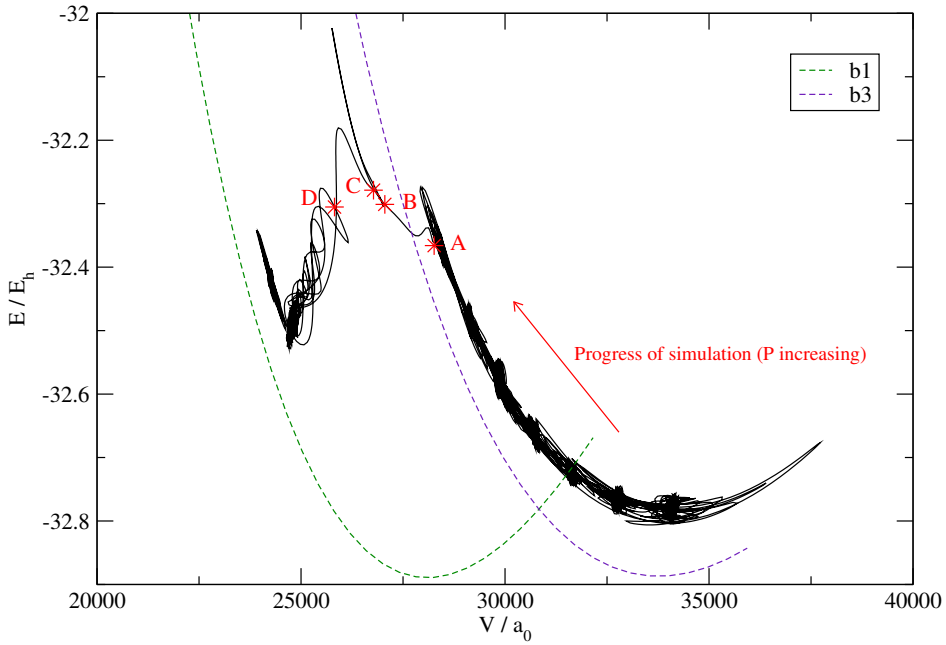

Figure 3.18: How the energy varies with volume as the simulation progresses. The system explores the local energy landscape between the B1 and B3 energy volume potential wells (dashed lines). The reference points in time A,B,C and D are determined from this graph.

On monitoring the potential energy of the system during the transformation from the B1 to the B3 crystal structure we see that there is a sharp increase in the energy. This suggests that the system goes through a high energy intermediate corresponding to the discontinuity that is observed in the pressure versus volume profile.

On observing the relationship between the system's potential energy and the cell volume we find further evidence of an intermediate. As the system explores the local energy landscape between the B1 and B3 potential energy/volume curves, the shape of the profile seems to indicate that the system is occupying the well of another distinct potential energy curve. The reference points A,B,C and D in figure 3.18 have been chosen to distinguish between these events of the simulation. From the beginning of the simulation until time A, the system can clearly be seen to lie in the potential energy/volume curve of the B3 crystal structure. As the pressure increases, the potential energy increases but the system remains "trapped" in the B3 energy well. Between times A and B the system starts to leave this part of the energy landscape and no longer is lies in the B3 crystal well. Between B and C the shape of the profile shows evidence of the system lying in the well of an unknown intermediate. From time C until D the system seems to be exploring

another region of the energy landscape which is distinct from either the B1 or B3 potential energy well. Finally from D until the end of the simulation, the potential energy decreases and can be seen to occupy the B1 crystal energy/volume well in the energy landscape. These reference points in time can be linked with the change

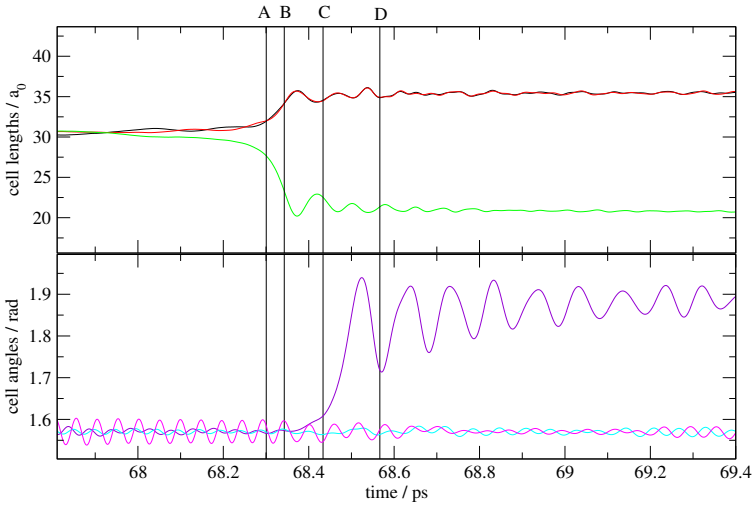

Figure 3.19: How the cell parameters evolve between time A and D. The cell undergoes a tetragonal distortion before shearing to the hexagonal symmetry.

in cell parameters as the system undergoes the phase transition. Figure 3.19 shows how the cell lengths and cell angles change as the simulation progresses.

The mechanism of the phase transition is two step from the perspective of the cell parameters. The geometry of the cubic cell is conserved until time A when the cell lengths start to deviate. We find that the one cell length shortens as the others increase after time A until the system is tetragonal by time B. The cell angles remain at $\pi/2$ radians until time C when the shearing of the cell commences and the angles distort to the hexagonal symmetry of the B1 system at time D.

A possible intermediate structure is the diatomic beta tin (d-β-Sn) which is trivially related to the B3 structure as can be seen in figure 3.20. We recall from section 1.5.1 that the role of d-β-Sn as an intermediate has been of much debate in the literature [63]. It is largely absent in the systematics of the high pressure phases of the group III-V and group II-VI semi-conductors [61]. The energy volume curves of d-β-Sn with various c'/a' ratios were constructed using tetragonal cells and can be seen in figure 3.21. The energy versus volume profile between time B and time D from figure 3.18 was compared with the energy landscape formed by the various d-β-Sn energy volume potential energy wells. It is found that the intermediate structure appears to lie in the region where this family of potentials energy curves reside.

When constructed in a tetragonal (rather than the typical cubic) cell the B3 system has a c'/a' ratio of $\sqrt{2}$ as shown in figure 3.20. In particular the dynamical

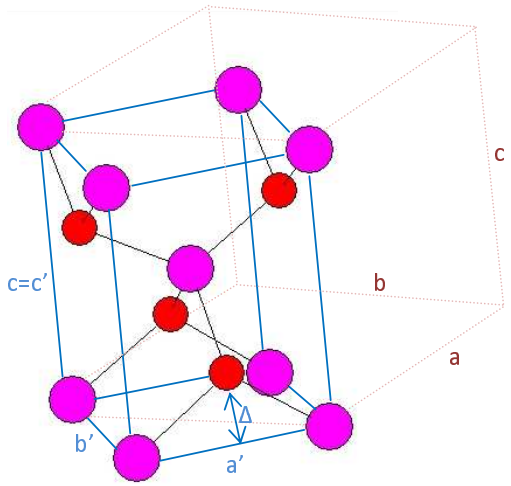

Figure 3.20: The tetragonal unit cell of the d-β-Sn structure. The unit cell is shown in blue. $\delta = 0.25$ in all d-β-Sn structures (including the B3 system). When the c'/a' ratio is $\sqrt{2}$ the structure is equivalent to the B3 crystal system. The higher symmetry of the B3 crystal means that it can be constructed in a cubic unit cell which is shown in dashed red. We see that the c axis is equivalent in both symmetries and the other cell parameters take the ratio $a = a'\sqrt{2}$ and $b = b'\sqrt{2}$ in the tetragonal cell.

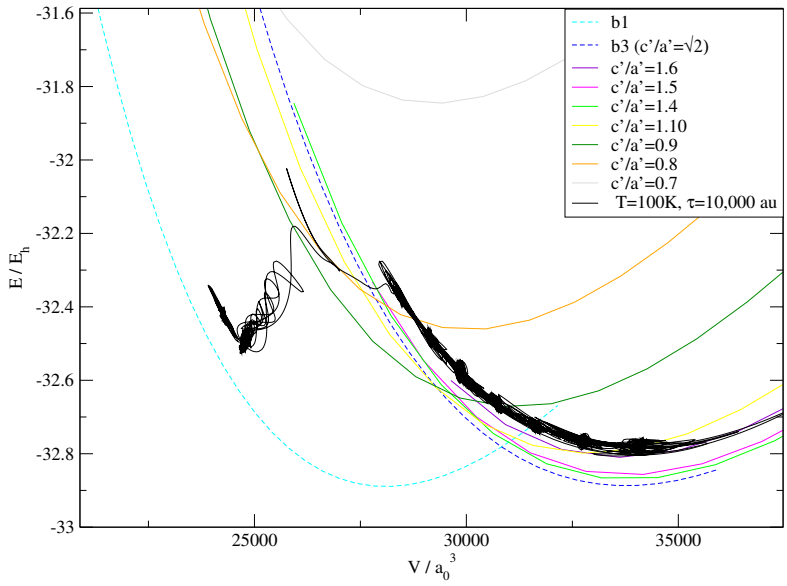

Figure 3.21: Calculated potential energy curves for various c'/a' (tetragonal cell) ratios compared with the dynamical data from the molecular dynamics simulation. The system explores the region of the energy landscape where the family of d-β-Sn structures lie.

data from the molecular dynamics simulation seems to correlate most closely with the $c'/a' = 0.8$ and $c'/a' = 0.9$ curves (tetragonal cell).

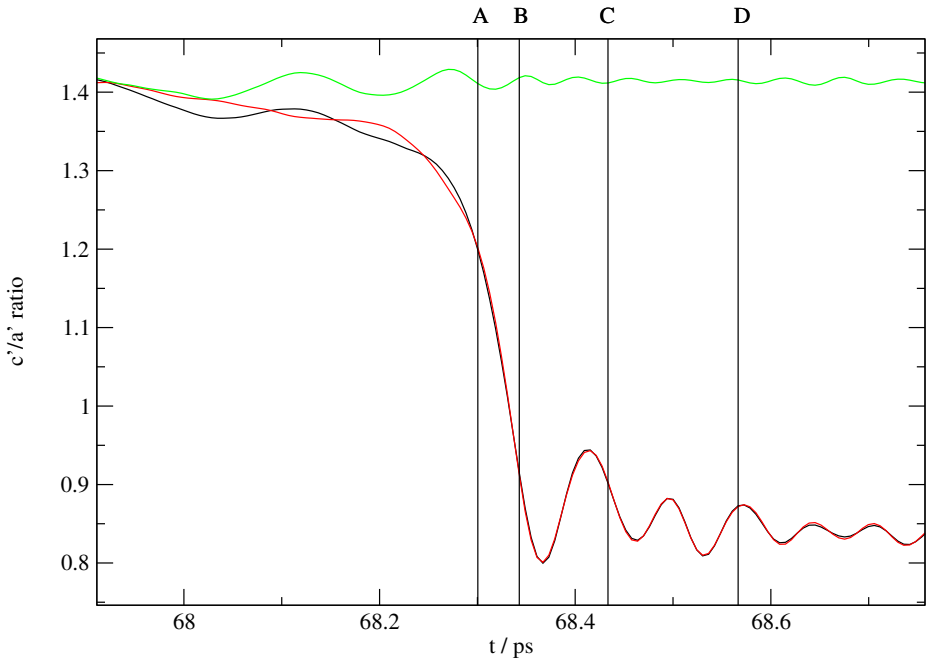

Figure 3.22: As the system undergoes the tetragonal distortion between time A and C the c'/a' ratio reaches a minimum of 0.8. The ratio then increases to 0.94 before the system undergoes the shearing part of the mechanism.

Further indication of this ratio can be found by plotting the c'/a' ratios as a function of time in figure 3.22. Between reference points B and C the system fluctuates between a c'/a' ratio of 0.80 and 0.94 which gives further evidence that the system is exploring the potential energy landscape provided by the family of d-β-Sn curves in figure 3.21

The mechanism of the tetragonal distortion can be further understood by plotting the average radial distribution functions for the time periods between the reference points A,B,C and D as can be seen figure 3.23. The radial distribution for the region B to C (shown in red) is consistent with a tetragonal distortion to the d-β-Sn structure.

On viewing the bottom panel of figure 3.23 which corresponds to the anion-cation interactions we see that the on compression along the c axis the nearest neighbour bond length remains constant. The peak does not exhibit any broadening or change amplitude which may have indicated the nearest neighbour environment splitting into two environments or a change in local coordination number. This is consistent with the d-β-Sn structure since the nearest neighbour environment is still a tetrahedral coordination of four cations around each anion. The peak does not shift with the compression since the vector of the nearest neighbour bond lies in the

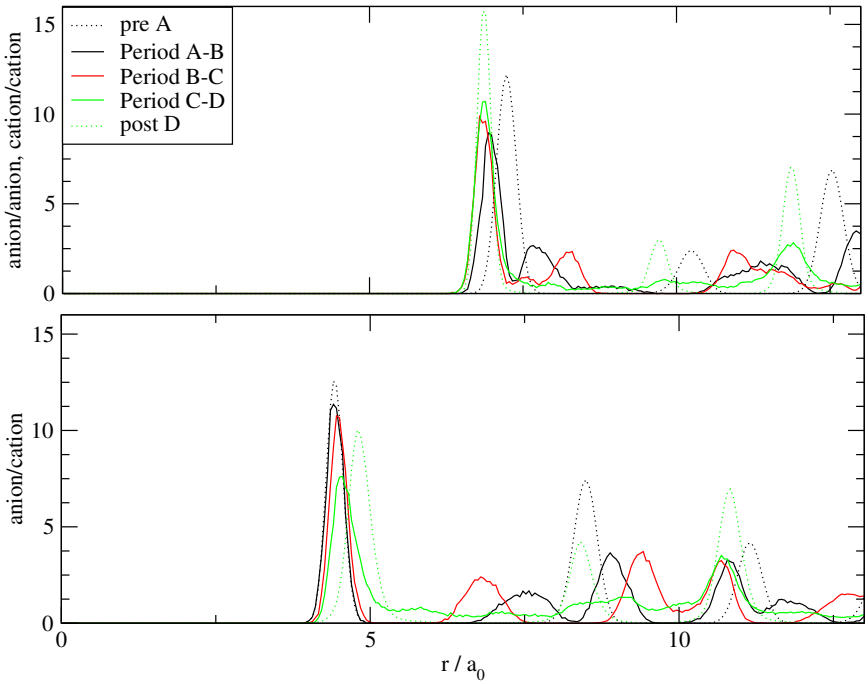

Figure 3.23: The top panel shows the radial distribution function $g(r)$ like-like interactions for the system at various time periods of the transition. The bottom panel shows the radial distribution function for the unlike interactions (MX interactions). The time period of particular interest is shown in red which corresponds to time period B to C when the system undergoes a tetragonal distortion.

plane of the c and the a' (or b') cell vectors. Since the c undergoes a shortening as the a' parameter extends the bond length remains near constant.

The second nearest neighbour corresponding to the next peak in the radial distribution at is also consistent with the d-β-Sn structure. The peak at 8.5 a_0 splits into two peaks either side at 6.8 a_0 and 9.4 a_0, the latter being of greater amplitude. This is due to the fact that the vector from the central anion to the second nearest cation neighbours lie in two environments; four lying in the plane perpendicular to the c axis and two have a component along the c axis. Before the distortion the vectors are of equal length and the two environments are equivalent. However, on compression along c and expansion along a' and b', the two environments become distinct.

The top panel of figure 3.23 shows the radial distribution for the anion-anion and cation-cation interactions. As with the previous example, the first peak in this distribution remains largely unchanged in terms of position and amplitude. This is because the component vectors lie along the direction of the compression and expansion respectively and so the resultant vector remains relatively unaltered in magnitude with only a small decrease overall.

However, the second nearest anion neighbours to the central anion lie at 11 a_0 either along a vector parallel to the c axis or perpendicular to it. On compression along c the anions in the former environment have the distance significantly reduced to form a second coordination shell at a distance only slightly greater than the nearest neighbour cation. Therefore the ions that lie along a vector parallel to the c axis shifts to form a shoulder to the nearest neighbour peak at 8.2 a_0. The ions that lie perpendicular to the c axis shift to a higher value of r comparable to that of the next cation coordination shell, causing that peak to broaden and increase in magnitude.

Finally figure 3.24 shows snapshots from the molecular dynamics simulations before the transition and during the time period B to C. We see that the transition clearly consists of a compression along c but that the positions of the ions within the unit cell are unchanged. All of this evidence points to an intermediate with the d-β-Sn structure.

The energy volume curves in figure 3.21 show that this is a metastable structure since the curves lie above those of the B1 and B3 crystal systems for all c'/a' ratios between the B1 and B3 curve minima. The modified potential parameters have not resulted in an increase in the d-β-Sn structure for any c/a' ratio with a stability lower than that of the B1 and B3 crystals. Therefore, despite the modification it is still a metastable intermediate.

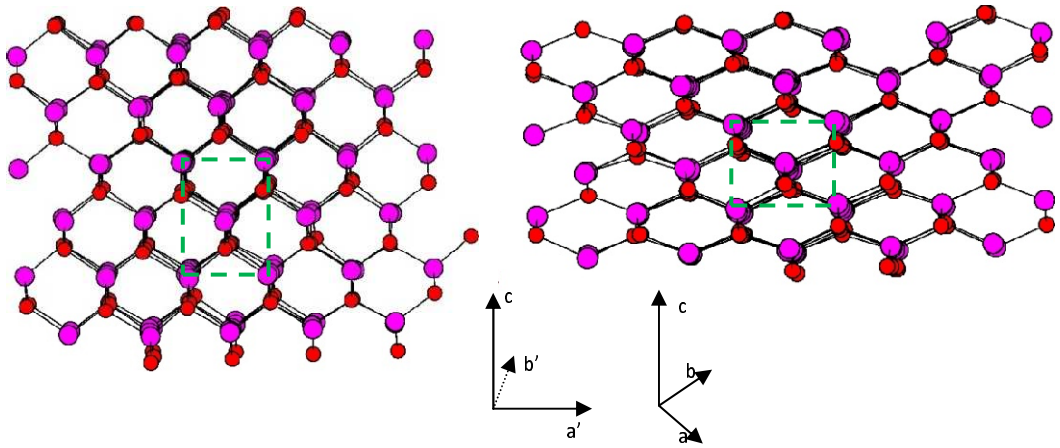

Figure 3.24: Snapshots of the simulation cell from the molecular dynamics simulations graphics. Left: Before time A. Right: A snapshot between reference point B and C. The tetragonal unit cell in the $c - a'$ plane is shown with green dashed lines. The symmetry remains tetragonal with a compression along the c axis as the transition starts to take place.

3.8 The effect of the isotropic barostat on the transition between the B3 and B1 crystal system

Since the second stage of the mechanism of the phase transition consisted of a shearing action of the simulation cell it was of interest to consider whether the transition would be hindered using an isotropic barostat only. The isothermal isobaric equations of motion (section 2.5) were constrained to allow isotropic fluctuations only. The simulation cell therefore remained cubic throughout the transition.

It was found that the transition did occur isotropically at 0.0008 atomic units (23.5 GPa) at 100K using a barostat with $\tau = 0.24$ ps as can be seen in figure 3.25.

The radial distribution function $g(r)$ was calculated for each of the time periods A (B3 structure), B, C and D (B1 structure) and can be seen in figure 3.26. It appears that the intermediate structure during time periods B and C is highly disordered since $g(r)$ oscillates about the ideal gas value of 1 and has no distinct, sharp peaks characteristic of a crystalline system. Further evidence of this amorphous phase is evident on viewing snap shots from the molecular dynamics graphics as shown in figure 3.27.

It would seem that the mechanism of the phase transition is quite different from that observed in the anisotropic phase transition. We can compare the energy versus volume profile of the molecular dynamics to show the different pathway through the energy landscape as in figure 3.28. We find that that the isotropic barostat pre-

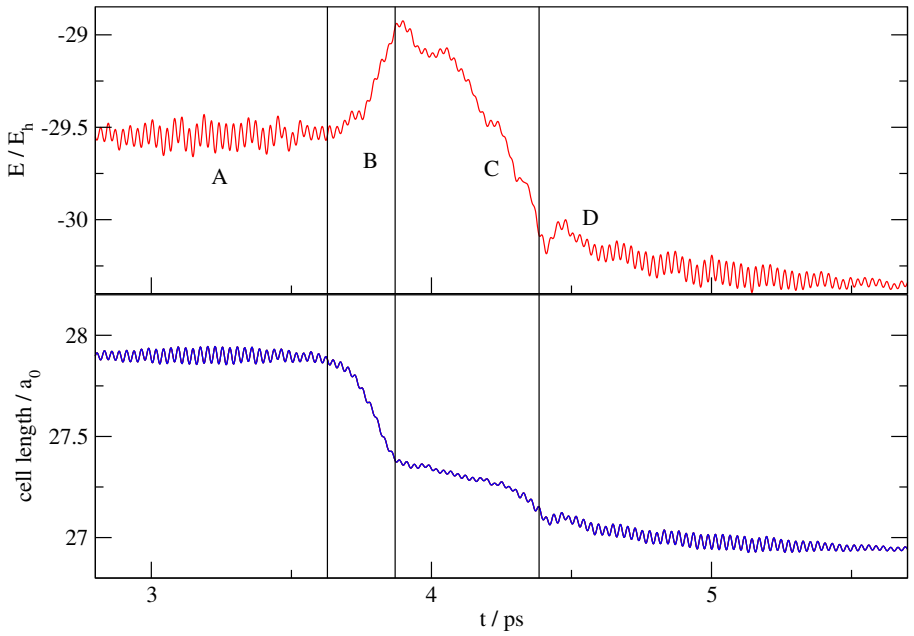

Figure 3.25: The isotropic transition from the B3 to the B1 structure. Evidence of the transition is given by the lowering in potential energy of the system and the reduction in cell parameters to the more dense B1 structure. The time periods A,B,C and D have been assigned in order that the intermediate structure can be investigated.

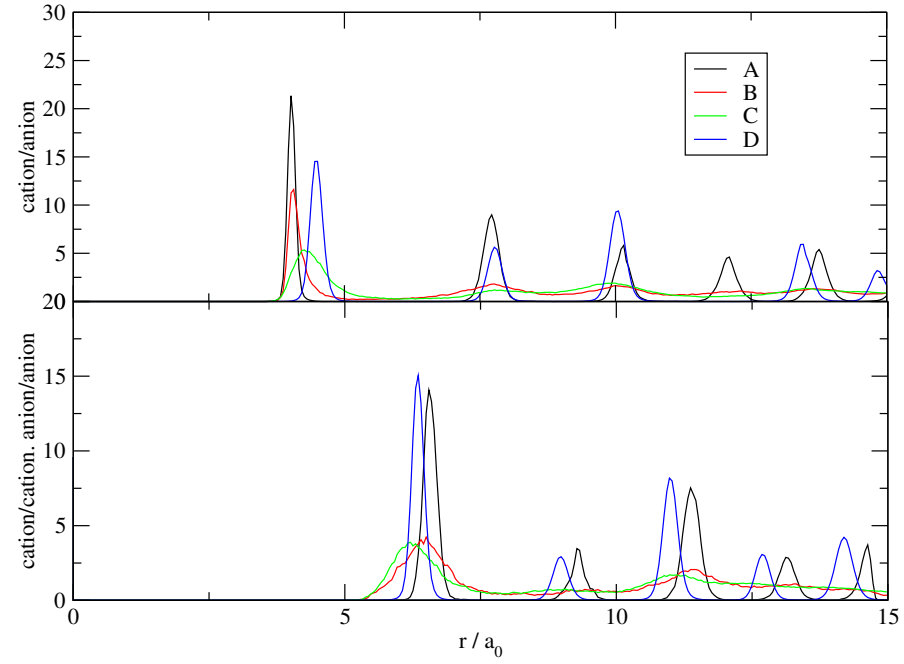

Figure 3.26: The radial distribution function $g(r)$ for the four time periods in the isotropic phase transition from the B3 to the B1 structure. The intermediate structure does not consist of distinct peaks, oscillating around the ideal gas value of 1. It appears to be amorphous.

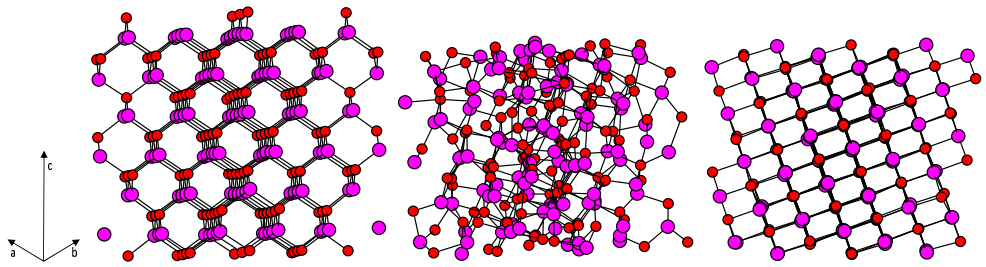

Figure 3.27: Left: The 110 plane of the B3 structure is shown in the cubic cell. This corresponds to time period A of the isotropic transition. Centre: The simulation cell viewed in the same direction during time period C. The system appears amorphous. Right: Time period D. The system has transformed to the denser B1 crystal structure.

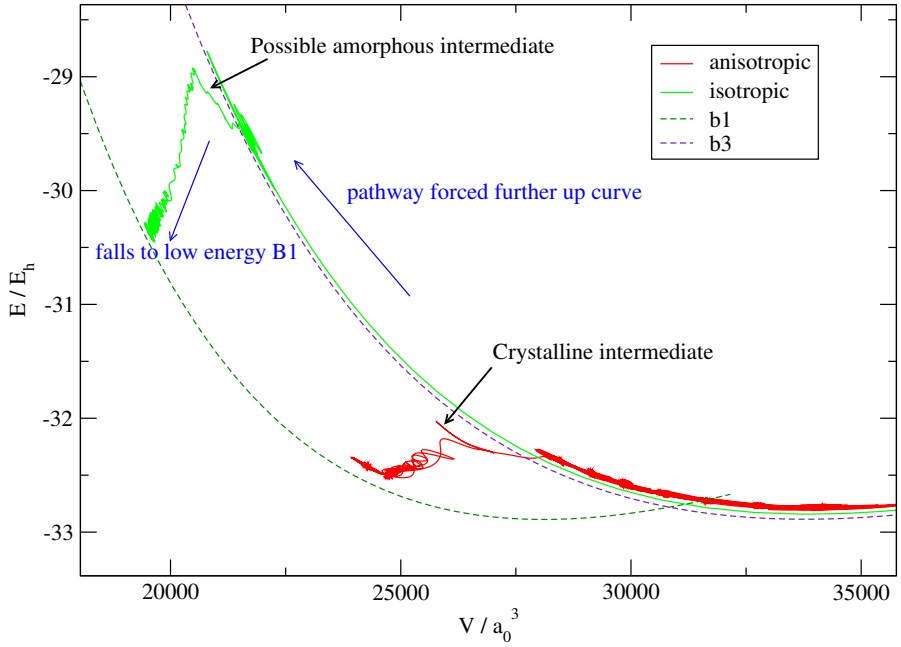

Figure 3.28: The dynamical pathway from the molecular dynamics simulations. The red pathway shows the anisotropic pathway when the system passes through the d-β-Sn intermediate. The green pathway shows the higher energy isotropic pathway in which the system passes through an amorphous intermediate state.

vents the cubic system passing through the lower energy mechanism, (a tetragonal distortion to the d-β-Sn intermediate structure followed by the shearing motion). The cubic symmetry imposes an increased system hysteresis. Instead the B3 crystal becomes increasingly unfavourable as the pressure forces the system higher up the potential energy curve. The crystal eventually becomes unstable, in this highly constrained environment, with respect to the underlying amorphous structure and a pressure-induced amorphisation transition is observed. Finally, the crystallisation transition from this amorphous state to the B1 crystal can be accommodated in the cubic cell and the system lowers in potential energy to occupy the B1 crystal potential energy well.

3.9 The transition from the B1 to B3 crystal structure

A simulation cell containing 108 molecular units in the B3 (zinc-blende) phase was equilibrated for 12 ps at 100 K, zero pressure with $\tau = 0.24$ ps. The pressure was reduced to -1.9 GPa (-0.000065 atomic units) and no transition was observed. This suggests that there is a hysteresis in the reverse mechanism as with the transition from the B3 to the B1 crystal phases.

However, when the pressure was reduced to more negative pressures in order that the barrier to the transition would be overcome, the forces on the ions took the system beyond the point of mechanical stability and the simulation failed. Effectively, the negative pressure pulled the crystal apart. The relatively large (by experimental standards) pressure fluctuations which result from the use of typical simulation cell sizes makes transitions near phase diagram spinodals difficult to perform.

The simulations were run at higher temperatures in the hope that the system could overcome the activation barrier of the transition more easily. However, the increased temperature also promoted the mechanical instability before the transition could be observed. Similarly the value of τ was increased in the hope that the more concerted ion motions would promote the reverse transition. However, this also promoted the point of mechanical instability and these simulations also failed.

3.10 Properties of the liquid phase

A simulation cell containing 216 molecular units was prepared by equilibrating in the isothermal-isobaric ensemble the end configuration of a crystal/liquid interface simulation in which the system fully melted. The equilibration was performed at

1700 K and zero pressure for 12 ps. The barostat was constrained so that only isotropic fluctuations were permitted and the geometry of the simulation cell was held fixed. The system was gradually pressurised by ramping the external pressure

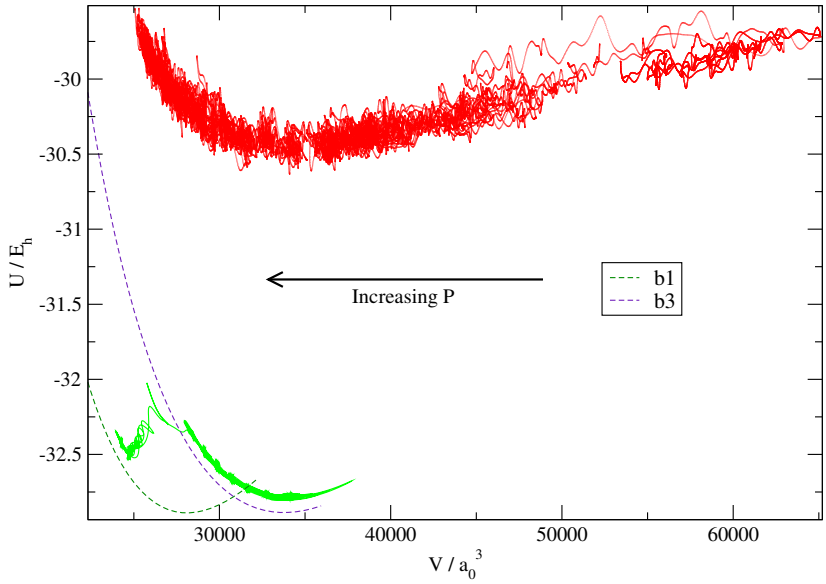

Figure 3.29: The energy pathway of the system as it is pressurised shown in red. For comparison the B1 and B3 energy volume curves are shown and the respective energy pathway for the crystal phase is shown in green.

by 0.00001 atomic units every 3.5 ps until it reached 0.00011 atomic units. The system was monitored during this pressurisation to see if the liquid underwent any structural changes. In particular, the possibility of a polyamorphic first order phase transition was investigated.

On monitoring the energy pathway of the liquid system as a function of pressure (figure 3.29) and comparing it to the crystalline systems, we find that the liquid system lies at a higher energy and greater volumes as expected. As the simulation is compressed we see that the system follows a relatively well defined pathway to lower volumes. We can envisage that there exists a family of liquid energy-volume curves (analogous to the crystalline ones) lying in this region of the phase diagram, providing an energy pathway for the system to explore. If it is the case that there are two polyamorphic phases of the liquids, we might expect that each polymorph results in a family of curves lying in slightly different regions of the phase diagram. The instantaneous energy volume pathway (shown in red in figure 3.29) appears to lie in two distinct regions of the landscape, possibly transferring from one polymorph curve to another.

The volume was measured as a function of pressure and can be observed in figure 3.30. The increasing external pressure results in a compression as one would expect.

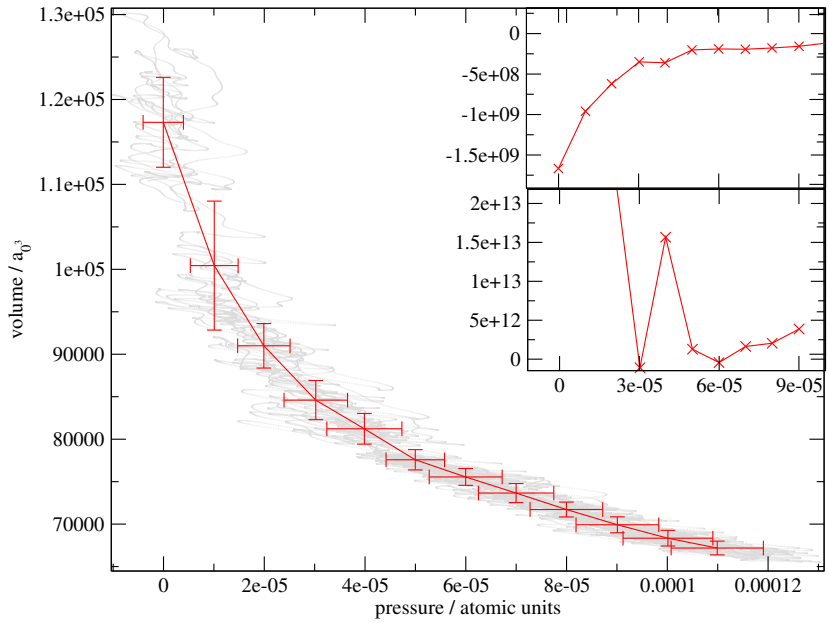

Figure 3.30: The volume as a function of pressure. The grey points correspond to the instantaneous system pressures/volumes as the simulation progresses. Average values are shown in red. Top Inset: The differential of the function shows a discontinuity at 0.00004 atomic units. Bottom Inset: The second differential also points to unsmooth behaviour at this pressure.

Both the average pressure and the instantaneous system pressures are shown for each pressure ramp. The differential of the function (inset, top) and second differential (inset, bottom) suggest that the volume change may not be continuous. This is very significant as if this is the case then it is an indication of a polyamorphic phase transition. The slight discontinuity occurs at a pressure between 0.00004 and 0.00005 atomic units, indicating a structural change within the liquid and possible liquid-liquid phase transition at this pressure.

Other properties of the liquid are investigated in terms of the coordination environment in order to locate any underlying polyamorphic transition. The mean average coordination number of the ions was calculated in the liquid phase at each pressure. It was found that the average coordination increased from 3/4 to an average coordination environment of 5. The increase in average coordination is not completely smooth as can be seen in figure 3.31. Here the increase in coordination number is larger between 0.00004 and 0.00005 atomic units providing further evidence of a possible liquid-liquid phase transition between these pressures.

Further characterisation of the coordination environment is provided by analysing the first coordination shell in terms of X-M-X angles. Figure 3.32 shows how the average angular distribution changes as a function of pressure. The transition is a smooth one, changing from the 4 coordinate to the bimodal 5 coordinate

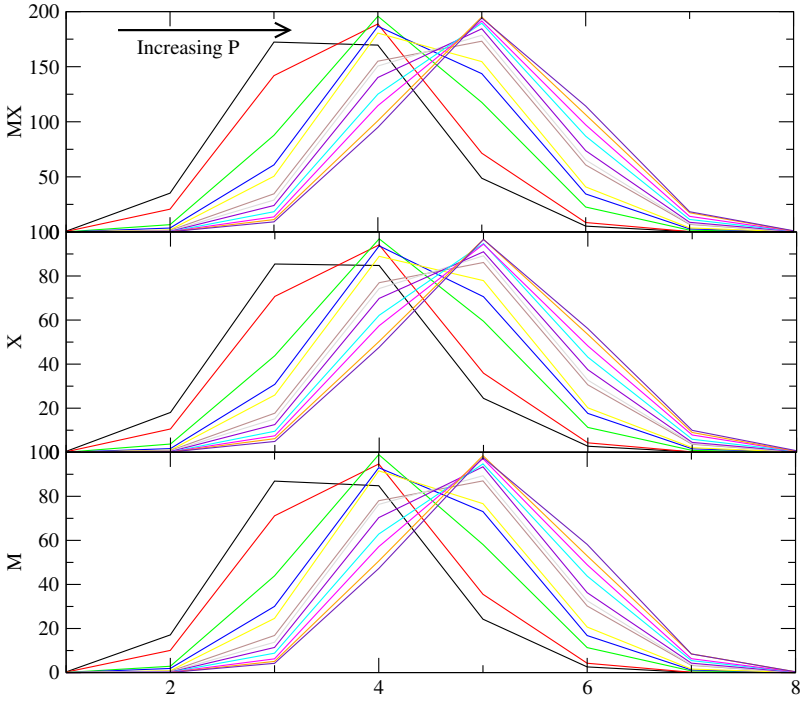

Figure 3.31: The average coordination number of the ions in the liquid phase. Each successive distribution corresponds to an increase in pressure of 0.00001 atomic units. The progression of the curves between the coordination number of 4 and 5 is not completely smooth. The largest increase in coordination occurs between 0.00004 (yellow) and 0.00005 atomic units (brown).

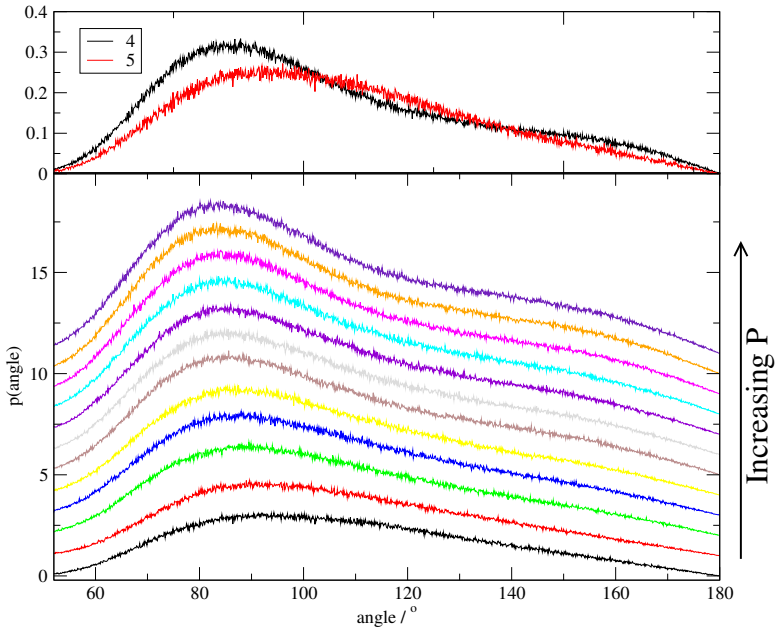

Figure 3.32: Top: The angle distribution for one coordination number only red: 4 coordinate ions only black: 5 coordinate ions only. Bottom: The total X-M-X angle distribution as a function of pressure. As the pressure increases the modal peak shifts to lower angles and the distribution becomes bimodal in character. This is consistent with a change from four to five coordination environments.

distribution. As one would expect the modal peak shifts to a lower angle consistent with a change from a near tetrahedral to pyramidal type geometry.

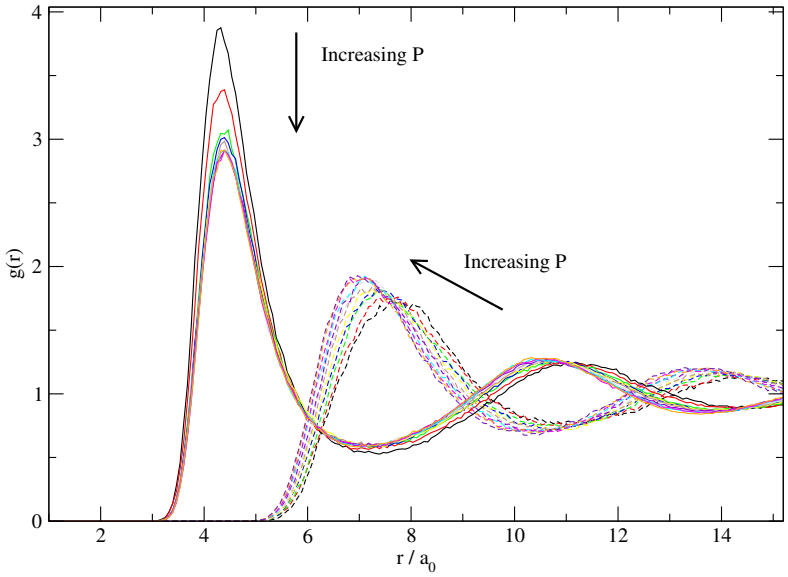

Figure 3.33: The radial distribution functions for the liquid phase. Black: 0.0000 atomic units. Each successive curve corresponds to an increase in pressure of 0.00001 atomic units. The dashed line corresponds to the cation-cation distances and the solid corresponds to the anion-cation separations. The cation-cation peak shifts in a smooth progression. The possible phase transition occurs between 0.00004 and 0.00005 atomic units (yellow and brown respectively) but there is no evidence of this here.

The radial distribution function $g(r)$ was calculated at each pressure using equation 3.20 and can be seen in figure 3.33. Unlike the radial distributions for the crystal phases, this distribution is continuous without the discrete peaks and zero probabilities of finding an ion at certain separations. The first peaks in the anion-anion and cation-cation distribution was found to shift to shorter separations with an increase in pressure. The ratio r_{+-}/r_{++} therefore increased from 0.57 to 0.63. This increase is analogous to the increase of 0.61 to 0.69 of the ratio r_{+-}/r_{++} which was observed in the crystal phases (see section 3.5). The shorter cation-cation separations on compression of the liquid is due to the increased packing of the ions around the central anions. However, although the radial distribution functions indicate a change in coordination environment, the shift in the radial distribution peaks appears as a smooth transition and therefore provides no evidence for a polyamorphic phase transition around 0.00004 atomic units.

Further insight into the coordination environment can be gleaned by breaking the radial distribution function down further according to coordination environments in a process called "colouring" the radial distribution function [31]. Figure 3.34 shows

the coloured radial distributions for the pressures near to the suspected polyamorphic phase transition. Unlike, the total radial distribution function, there is some evidence that the transition is not completely smooth particularly in the case of the 3 coordination colouring. $g_{33}(r)$ shows a peak shift in the second coordination shell between the pressures of interest (0.00004 and 0.00005 atomic units). There is a similar, though less pronounced shift in the $g_{34}(r)$ colouring in which the pair distribution between the three and four coordinate ions are investigated. The second coordination shell of three coordinate ions moving closer to the first coordination shell is most likely an indication of a clustering of the lower coordinate ions in the same region of the simulation cell.

The case for a polyamorphic first order phase transition is inconclusive. Clearly the parameterisation of this potential to favour the two coordination environments in the crystal phase has introduced a predisposition for such behaviour in the liquid phase and the curvature in the slope of the liquid-solid coexistence line calculated from the interface calculations supports this hypothesis. The liquid exhibits both four and five coordinate environments and there is a hint that this transition is not entirely continuous. The behaviour of the parameterised potential in both the crystal and liquid phases covers a range of coordination environments. The energy landscape in which the carbon nanotube filling simulations are performed using this parameterised potential will be complex and interesting, providing a bridge between the tetrahedral and octahedral systems that will also be used in the filling simulations.

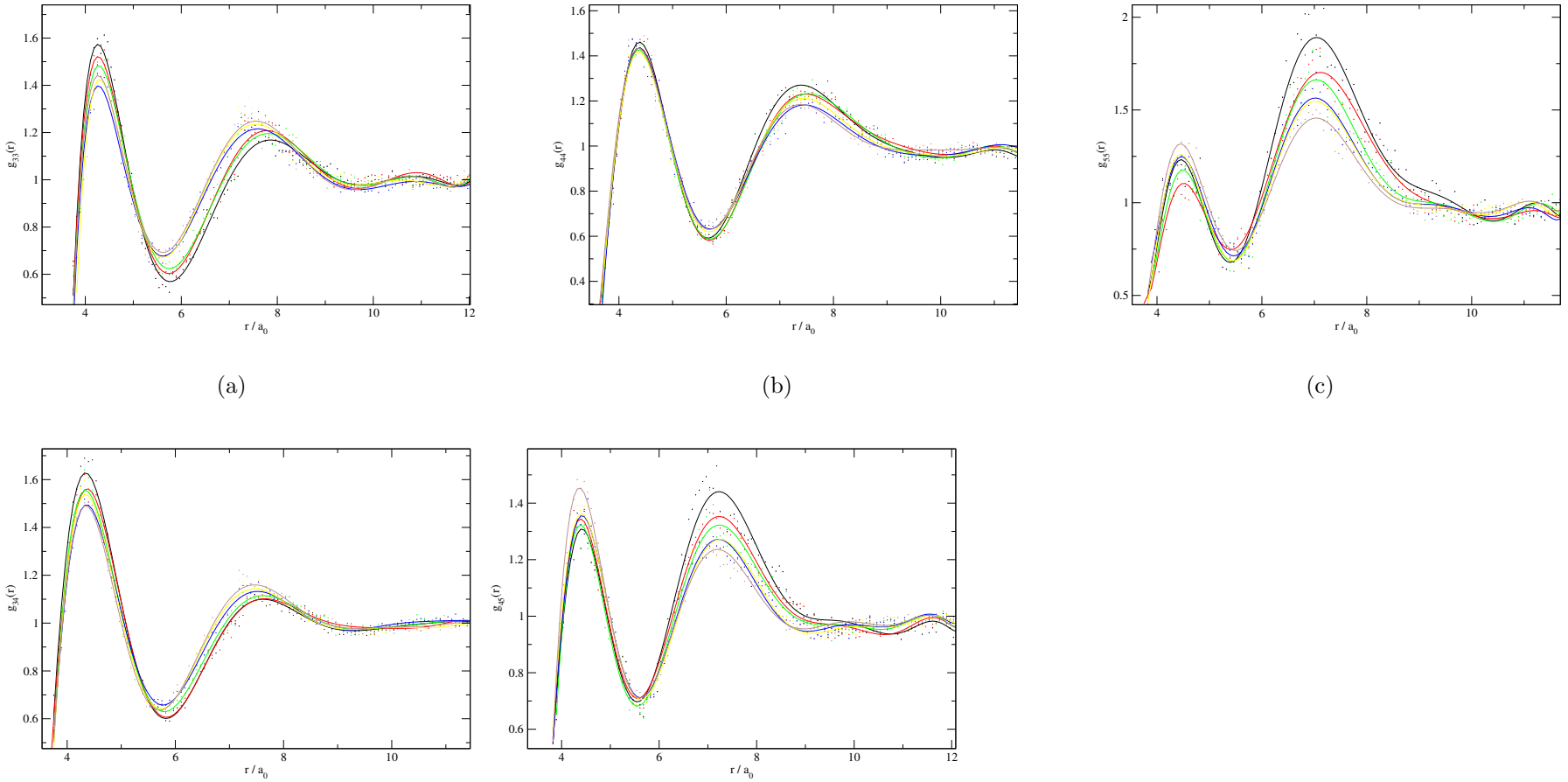

Figure 3.34: The coloured radial distribution functions ($g_{xy}(r)$ for two ions separated by r_{xy} which have a coordination number of x and y respectively) as a function of pressure. (black: 0.00002, red:0.00003, green: 0.00004, blue: 0.00005, yellow: 0.00006, brown: 0.00007 atomic units). The functions shown have been fitted with a polynomial and the raw data is shown by the individual points. This is due to the noise of the raw data which occurs due to the small number of ions to sample from when performing a colouring. The possible polyamorphic phase transition is thought to occur between 0.00004 and 0.00005 atomic units (green and blue respectively).

Chapter 4

A flexible carbon nanotube

A range of ionic systems have been utilised in molecular dynamics simulations of the filling of carbon nanotubes in which inorganic crystalline structures have been observed to form in the nanotube pore [108, 109, 110, 111, 112, 113, 114, 115]. Previously, the carbon nanotube has been modelled as a rigid entity which cannot change position, volume or geometry in any way.

In this chapter, the molecular dynamics simulations are improved by incorporating the carbon-carbon interactions into the system. The Tersoff II potential which has been parameterised for carbon [99] will model these interactions and will be tested in terms of both stable and metastable carbon phases. The metastable carbon nanotube phase is investigated in isolation and also as part of a multi-component system, the filling of carbon nanotubes with molten salts. As a result of the incorporation of the carbon-carbon forces, the carbon nanotube can be expected to translate, rotate and undertake deformations (such as molecular vibrations).

The novel ionic system described in chapter 3 will be one of four ionic systems that will be utilised in the molecular dynamics simulations. The flexible carbon nanotubes are found to fill directly from the ionic melts and the filling events are discussed.

4.1 The Tersoff II potential

The energy of interaction between a system of particles is given by

$$\phi = \phi_2 + \phi_3 + \phi_4 + ...\phi_n + ..., \tag{4.1}$$

where ϕ_n is the n-body interaction of n particles. In a pairwise potential model this series is truncated after ϕ_2 and the many-body terms are ignored. The Lennard-Jones and Born-Mayer potentials [36] are both examples of a pairwise potential of this form.

Pairwise interactions may be the most significant contribution to the energy of interaction and for closed shell systems this may be sufficient for accuracy. Nevertheless, in systems with covalent character the three-body forces are much more significant. For example, Si and C exist in various polymorphs with differing coordination environments in each and so any potential model used must be capable of modelling the three-body character accurately. In other words, the energy should incorporate an angular dependence and therefore depend on the energy of triplets of atoms.

Three-body potential models can be organised into two classes (ϕ_I and ϕ_{II}) [19]. Firstly, the two and three body terms can be incorporated into one function that describes both the two and three-body character:

$$\phi_I = \phi_{2,3} = \sum_{i<j:k} U_{ij:k}. \tag{4.2}$$

Alternatively, the potential model can consist of a sum of two separate functions in which the two and three body interactions are treated separately:

$$\phi_{II} = \phi_2 + \phi_3 = \sum_{i<j} U_{ij} + \sum_{i<j<k} W_{ijk}. \tag{4.3}$$

Carbon-carbon interactions in this work were modelled using the Tersoff II potential model [100] which has been parameterised for carbon [99]. This is a three-body potential model and was chosen so that the directional bonding (both sp^3 and sp^2 type interactions) could be satisfied. It falls into the first class of three-body potential in which the two and three body interactions are treated within the same functional form.

The energy of each individual carbon atom is taken to be half that of the bonding

pair:

$$U_{ij:k} = \sum_i U_i = \frac{1}{2} \sum_{i,j \neq i} f_c(r_{ij}) \big[f_R(r_{ij}) + b_{ij} f_A(r_{ij}) \big]. \tag{4.4}$$

f_R and f_A are the repulsive and attraction terms respectively, given by

$$f_R = \alpha_1 e^{-\lambda_1 r_{ij}} \tag{4.5}$$

$$f_A = -\alpha_2 e^{-\lambda_2 r_{ij}}. \tag{4.6}$$

b_{ij} is the bond order of the interaction between i and j. As one expects from empirical observations it is a monotonically decreasing function of coordination, as the coordination increases the bond order decreases:

$$b_{ij} = (1 + \beta^n \xi_{ij}^n)^{\frac{-1}{2n}}. \tag{4.7}$$

The effective coordination number ξ_{ij} depends on the distance of the coordinating carbons from the central carbon atom. It also has an angular dependence which means that the different coordination environments within the polymorphs of carbon can be accounted for:

$$\xi_{ij} = \sum_{k \neq i,j} f_c(r_{ik}) g(\theta) \tag{4.8}$$

$$g(\theta) = 1 + \frac{c^2}{d^2} - \frac{c^2}{[d^2 + (h - cos\theta)^2]}. \tag{4.9}$$

The Tersoff potential acts over a short range and smoothly decays due to the cutoff function:

$$f_c(r_{ik}) = \begin{cases} 1, & r < R - D \\ \frac{1}{2} - \frac{1}{2} sin[\frac{\pi}{2}(r - R)/D], & R - D < r < R + D \\ 0, & r > R + D \end{cases}. \tag{4.10}$$

This potential was first parameterised for silicon [100] but was later adapted for carbon [99] and the parameters can be seen in table 4.1.

The Tersoff II potential was incorporated into the molecular dynamics code during this research and can be used to model covalent systems such as carbon and silicon which exist in various coordination environments. The force functions for the Tersoff II potential which were derived as part of this process are included in the Appendix (section A-2). With the molecular dynamics code the carbon systems can be modelled independently or as part of a larger system along side other potential models. For example, the molecular dynamics simulations of the carbon

Parameter	Tersoff value
α_1	51.214
α_2	12.742
λ_1	1.8457
λ_2	1.1705
β	$1.5724\text{x}10^{-7}$
c	38049
d	4.3484
h	-0.57058
n	0.72751
R	3.685
D	0.283

Table 4.1: The Tersoff II parameters in atomic units.

nanotubes filling consist of a system of three interaction types; carbon-carbon (Tersoff II), ion-ion (Born-Mayer) and ion-carbon (Lennard-Jones).

4.2 The polymorphs of carbon

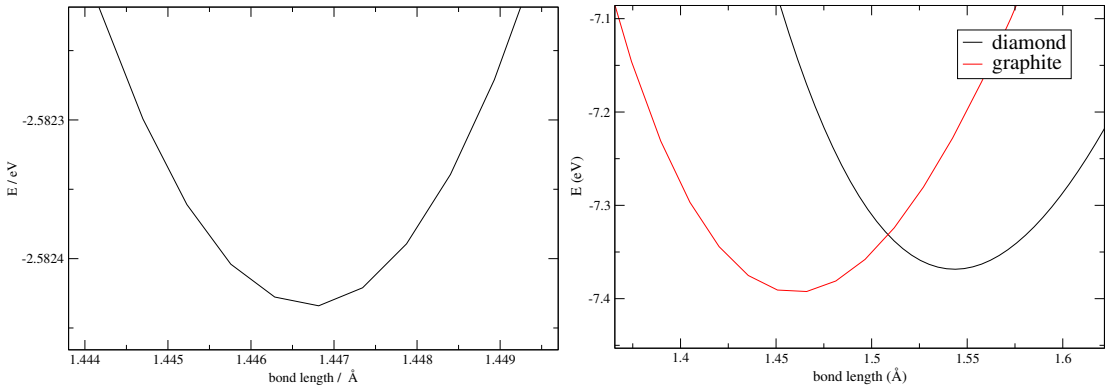

Figure 4.1: Right: The potential energy of a carbon-carbon dimer interacting as a function of bond length. Left: The energy volume curves for diamond and graphite. The graphite phase is correctly predicted to be the stable phase of carbon.

Simulations were performed of various systems consisting of carbon interactions only. Firstly the carbon-carbon dimer was found to perform well and conserve energy within the molecular dynamics code. The potential energy was calculated as a function of bond length and can be seen in figure 4.1. It predicts a bond length of 1.447 Å and potential energy of 2.582 eV, which compares with the experimental values 1.2425 Å and 4.26 eV respectively [35]. Both values are in poor agreement with experiment in this regime where there is a coordination of one but the strength

of the potential lies in the description of higher coordination environments where three-body effects are of importance.

Diamond and graphite phases were also modelled using the Tersoff potential and the energy volume curves can be seen in figure 4.1. Graphite is correctly predicted as the more stable phase by 0.024 eV per atom than diamond which is the correct energy difference between the polymorphs at zero Kelvin [49]. The model predicts a graphite bond length of 1.46 Å and 1.54 Å for diamond, which compare very favourably with the experimental values of 1.42 Å and 1.54 Å respectively [77]. The Tersoff II model appears transferable to both the sp^2 and sp^3 environments of carbon.

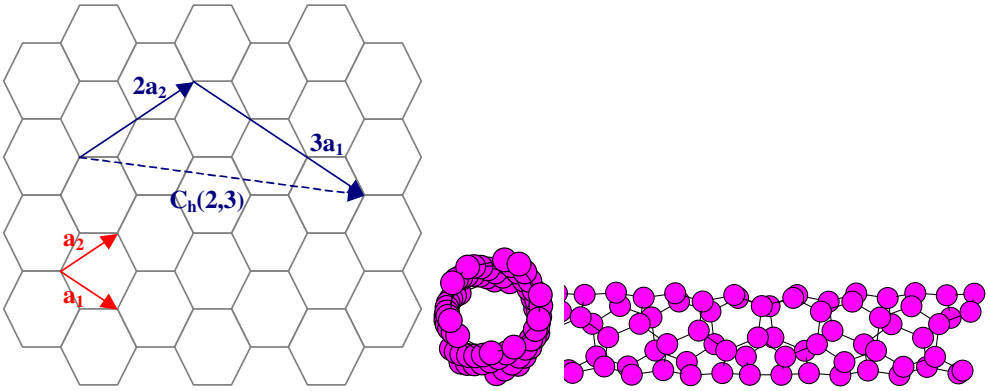

Figure 4.2: The carbon nanotube can be rationalised in terms of the folding of a graphene sheet. The unit vectors $\mathbf{a_1}$ and $\mathbf{a_2}$ are defined (left) and form the component vectors of the chiral vector $\mathbf{C_h}$. Here we have $\mathbf{C_h} = 3\mathbf{a_1} + 2\mathbf{a_2}$ which forms the circumference of the (3,2) carbon nanotube on folding.

A further polymorph of carbon is the metastable carbon nanotube phase which is a member of the fullerene family of carbon structures. Various diameter carbon nanotubes were also investigated using the Tersoff II potential model. Although not synthesised in this manner, the structure of carbon nanotubes can be rationalised in terms of a graphene sheet which is rolled up into a cylinder to form a carbon nanotube.

The direction in which the graphene sheet is folded into a cylinder determines the carbon nanotube morphology and therefore the physical properties of the nanotube. The chiral vector C_h forms the circumference of the carbon nanotube on folding and is defined by the linear combination of two component unit vectors $\mathbf{a_1}$ and $\mathbf{a_2}$ (see figure 4.2):

$$\mathbf{C_h} = n\mathbf{a_1} + m\mathbf{a_2}. \tag{4.11}$$

where n and m are the integers which define the nanotube morphology (n, m).

Due to the quantisation of the chiral vector length $|\mathbf{C_h}|$, enforced by the linear combination of unit vectors n and m, only certain values of nanotube diameter are permitted. Nanotubes of the morphology (n, n) are referred to as "armchair nanotubes" and those that are of $(n, 0)$ morphology are "zig-zag" nanotubes due to the shape of their cross section. All other morphologies are referred to as "chiral nanotubes" since (n, m) has the corresponding isomer, the (m, n) nanotube (figure 4.3).

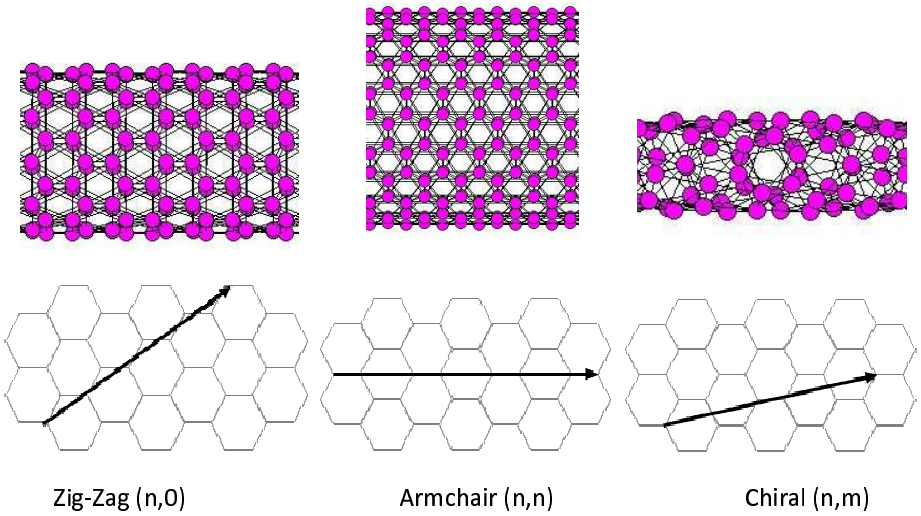

Figure 4.3: The three classes of carbon nanotube which are defined by their (n, m) morphology.

Coordinates of infinite carbon nanotubes were generated of varying morphologies in all three classes of nanotube. A value of 1.46 Å (the bond length predicted in bulk graphite) was used as the carbon-carbon bond length within the graphene sheet prior to the transformation to the cylindrical geometry. The nanotube was stretched to varying diameters and the potential energy above that of the graphite sheet (E_h) was monitored as a function of diameter as can be seen in figure 4.4.

A *ln-ln* analysis of the curve minima shows that the energy has a r^{-2} dependence for all the nanotube morphologies. This is consistent with the elastic continuum model in which the potential energy of the carbon nanotube is taken as the sum of the energy of the graphite sheet with the strain energy required to fold the sheet into the cylinder. The strain energy is given by

$$\begin{aligned} U_{strain} &= \frac{Eh^3A}{24r^2} \\ U_{strain} &= \frac{C_{strain}}{r^2}, \end{aligned} \tag{4.12}$$

where E is the elastic modulus, h is the thickness of the folded sheet and A is the area

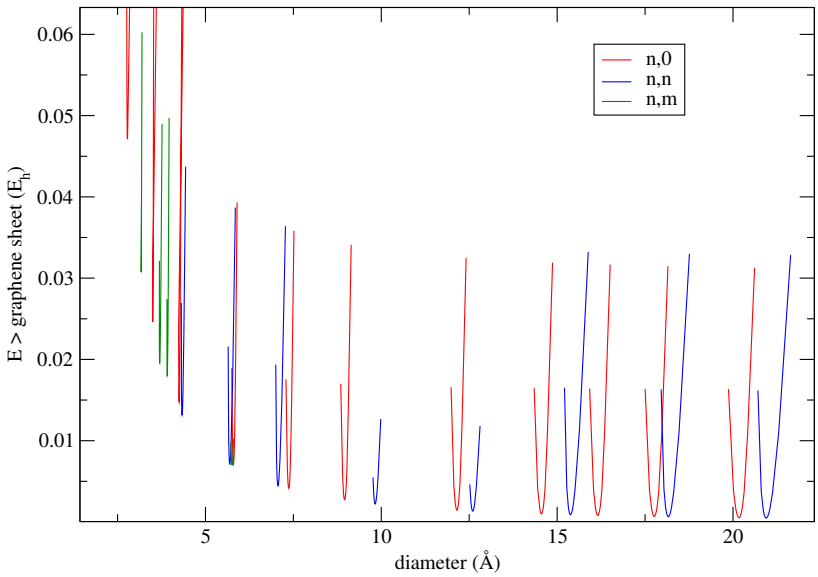

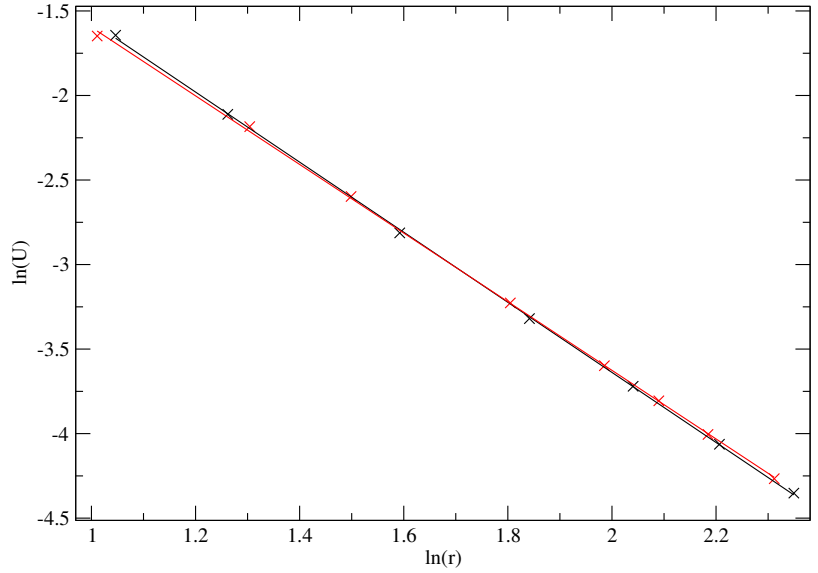

(b)

Figure 4.4: Top: Energy diameter curves for tubes of various chirality and diameter. Bottom: The curves show a $\frac{1}{r^2}$ dependence seen by linear regression of the natural log of the energy minima versus the log of the radius, which has a gradient of -2.

of the tube [59, 102]. For carbon nanotubes with radii above 5 a_0 the linear regression of the ln-ln plot gives the function $\ln(u) = -2.07(\pm 0.01)\ln(r) + 0.51(\pm 0.02)$ eV Å^2 for the (n,n) morphology and $\ln(u) = -2.03(\pm 0.01)\ln(r) - 0.43(\pm 0.03)$ eV Å^2 for the (n,0) morphology. The values of C_{strain} (the intercept of the linear regression) are much lower than those predicted by density functional calculations [71, 75] in which C_{strain} was found to be 2.00 eV Å^2. The increased strain in those calculations may be attributed to the explicit inclusion of the π-bonding interactions with the density functional calculations in comparison to empirical potential models [59, 75]. We note that in the high level density functional calculations, a subtle dependence on nanotube morphology was observed [44].

4.3 The radial breathing mode

Experimentally, by far the most characterised spectroscopic mode of vibration is the radial breathing mode of the carbon nanotube. The cross section of the cylindrical tube expands and contracts in a highly symmetrical fashion. This spectroscopic mode has traditionally been used to characterise the diameter of the nanotubes synthesised experimentally since there is a simple functional relationship between the diameter and energy of the radial breathing mode:

$$E_{rbm} = \frac{C_{rbm}}{d} + C'_{bundle}, \tag{4.13}$$

where d is the nanotube diameter and C_{rbm} is a constant [41]. The constant C'_{bundle} is zero for an isolated single-walled nanotube.

The radial breathing mode was located for various carbon nanotubes using the Tersoff II potential model and was found to conform to this model. The process of locating the radial breathing mode for a given nanotube was as follows. Firstly, the dynamical matrix $\left(\frac{\partial F}{\partial r}\right)$ was determined by displacing the atoms from their ideal sites and determining the change in force on that atom after the displacement:

$$\mathbf{D}_{\alpha,\beta}(i) = \left(\frac{\partial^2 U(i)}{\partial r_\alpha \partial r_\beta}\right), \tag{4.14}$$

where α and β is the x, y or z direction. The matrix was diagonalised and the vibrational density of states was calculated as in section 3.4 from the eigenvalues produced (figure 4.5). The radial breathing mode was determine by locating the corresponding eigenvectors with no component along the nanotube axis.

The radial breathing mode for each of the carbon nanotubes located in this manner can be seen in figure 4.6 and the vibrational energy of this mode is seen

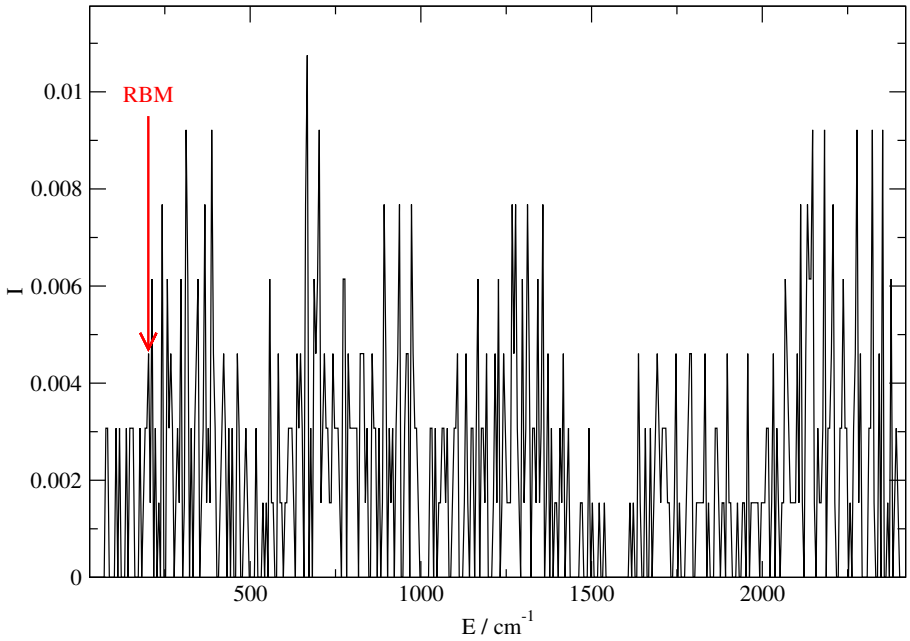

Figure 4.5: The density of states for the (9,9) carbon nanotube. The eigenvalue corresponding to the radial breathing mode is highlighted and was located by searching for eigenvalues with corresponding eigenvectors which possess a zero component along the nanotube axis.

to increase at lower radii due to the increased number of cross-tube carbon-carbon interactions. As is consistent with experiment, the value of C_{rbm} tends to a limiting value for nanotubes with diameter larger than 6 Å. Again, the anomalous behaviour at small radii can be explained by the more complex cross nanotube carbon-carbon interactions at this length scale.

The value of C_{rbm} tends to 2540($\pm$10) Å cm^{-1} which is slightly higher than the value accepted in the literature 2025($\pm$5) Å cm^{-1} [41, 43]. The increased energy of vibration for a given diameter is due to the overly stiff carbon-carbon bonds modelled with the Tersoff II potential model.

In summary, the Tersoff potential has been successfully incorporated into the molecular dynamics code and is found to be capable of modelling carbon only systems successfully in a range of coordination environments. In particular, the energetics of the carbon nanotubes are successfully modelled using this potential and are rationalised successfully via an elastic continuum model. Both the radial breathing mode and strain energy are a function of nanotube radius but they are both independent of nanotube chirality (for carbon nanotubes with diameter larger than 6 Å).

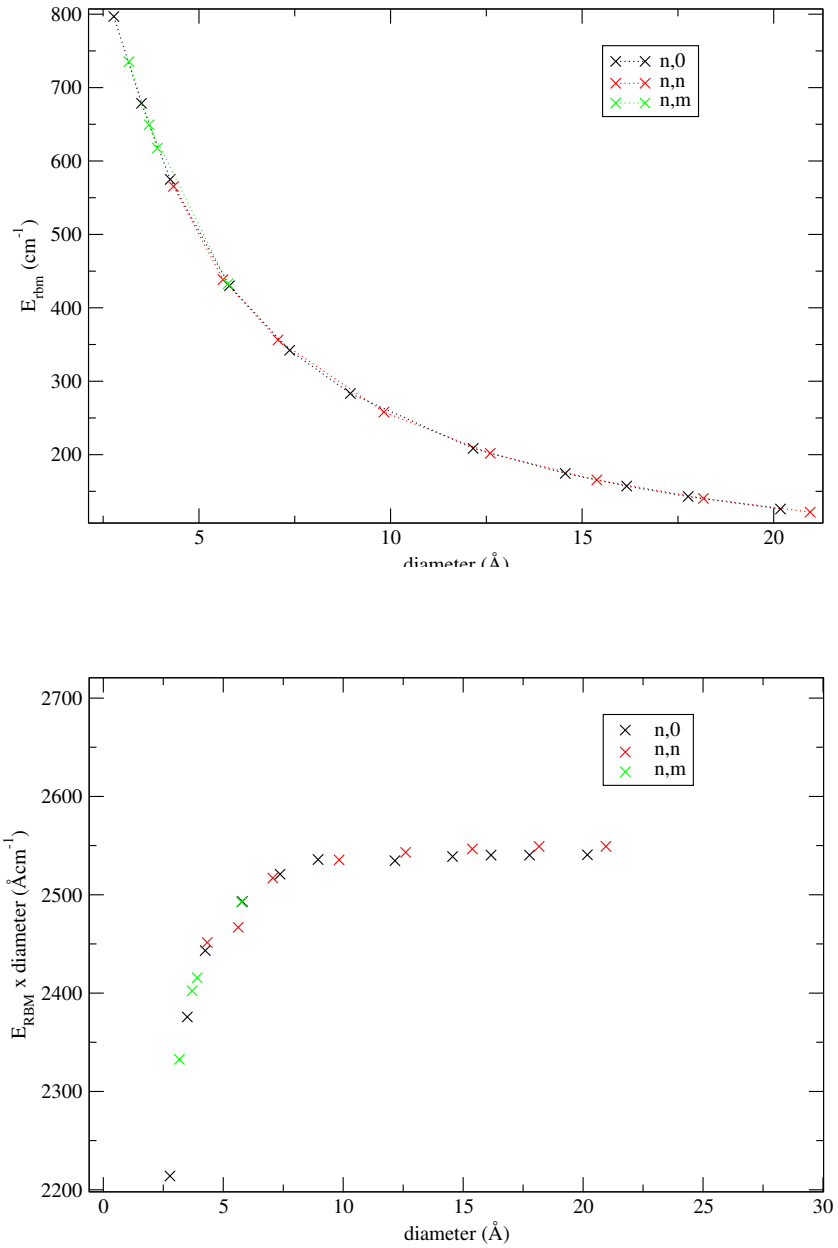

Figure 4.6: Top: The energy of the radial breathing modes for carbon nanotubes of varying diameters. Bottom: The energy of the radial breathing mode multiplied by the diameter (C_{rbm}) tends to a constant value of 2540($\pm$10) Å cm^{-1}.

4.4 The Tersoff II potential within a multi-component system

The Tersoff II three body potential was successfully incorporated into the molecular dynamics code for carbon only systems. In an advancement of this work, the Tersoff II potential model can be used alongside other potentials in multi component systems. One such multi-component system is that of a carbon nanotube immersed in a molten ionic salt. In this system there are three classes of interactions that must be considered, which all require their own potential model. Firstly, the carbon-carbon interactions are modelled using the Tersoff II potential model, as was utilised in the single component carbon systems. Secondly, the ion-ion interactions are modelled using a suitable pairwise additive potential model for the ionic salt of choice, such as a Born-Mayer potential [36]. Finally, the carbon-ion interactions are modelled using a simple pairwise additive Lennard-Jones potential:

$$U(r_{ic}) = 4\epsilon_{ic}\left[\left(\frac{\sigma_{ic}}{r_{ic}}\right)^{12} - \left(\frac{\sigma_{ic}}{r_{ic}}\right)^{6}\right]. \tag{4.15}$$

The parameters in table 4.2 are obtained from Lorentz-Berthelot mixing rules of a carbon graphite surface with isoelectronic noble gases as described by Steele *et al* [94]. The potential predicts an equilibrium anion-carbon dimer separation of 7.922

Lennard Jones	**C-M**	**C-X**
ϵ	57.9	79.4
σ	3.4025	3.735

Table 4.2: The parameters used for the carbon-ion Lennard Jones parameters in this work. The well depth ϵ is given in Kelvin and the zero energy separation σ is in Ångströms.

a_0 and a cation-carbon dimer separation of 7.217 a_0 as can be seen in figure 4.7.

Single point energy calculations were performed for an ion above a graphene sheet to locate the equilibrium graphene-ion distance for both the anions and cations using the Lennard-Jones potential. Two sites of adsorption were chosen; directly above a carbon atom and directly above the centre of a hexagon (so that it is equidistant from its six nearest neighbour carbons in the graphene sheet) which are shown with a dashed and solid line respectively in figure 4.8. The equilibrium separation is reduced in comparison to that of the preferred ion-carbon equilibrium distance in figure 4.7 for both the adsorption sites. If the ion resides at the equilibrium separation from its nearest neighbour carbon atom, the next nearest neighbours carbons will lie at a distance greater than this equilibrium separation. At this position in the potential

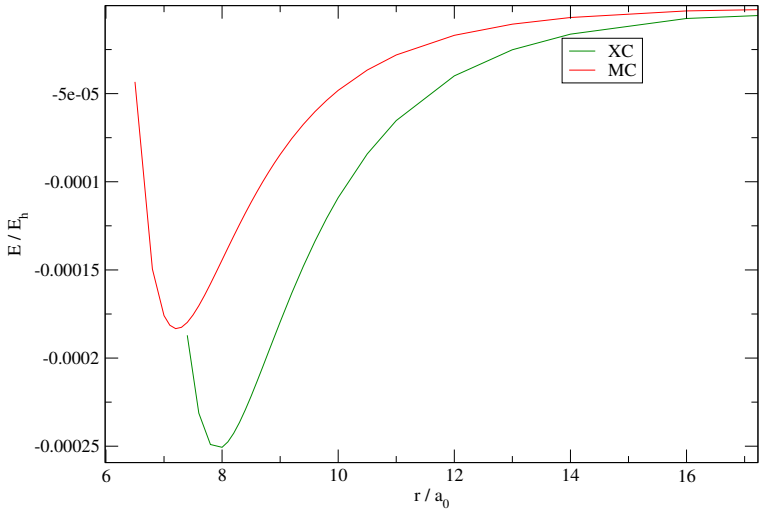

Figure 4.7: The Lennard Jones pairwise potential energy function $U(r_{ij})$ for the parameters used in this work (see table 4.2).

energy well, these carbon atoms will exert an attractive force on the ion pulling the ion closer to their preferred equilibrium separation.

In an extension of these single point calculations the equilibrium separation between a square net ionic sheet and a graphene sheet was calculated. Clearly, the separation will have some dependence on the infinite number of adsorption sites of the ion sheet on the graphene sheet. However, the results from the single ion adsorption show only a slight deviation according to the location of the adsorption leading us to assume that the deviation is of a similar magnitude for the ion sheet-graphene sheet calculations. As one might expect, we find that the equilibrium separation lies between that of the cation-graphene and anion-graphene separations at a distance of 6.84 a_0.

The results of these single point calculations are also given in table 4.3.

	X	**M**
ion with single carbon	7.922	7.217
ion over carbon (infinite carbon sheet)	6.55	7.20
ion over centre of hexagon (infinite carbon sheet)	6.40	7.10
square net sheet + infinite carbon sheet	6.84	

Table 4.3: Summary of equilibrium separations calculated from the single point energies in figure 4.8. The separations are given in atomic units (a_0).

Inclusion of the Tersoff II potential is a significant development to the previous filling simulations of carbon nanotubes with ionic salts that have been performed. Until now the carbon nanotube was modelled as a rigid, stationary entity which acted purely as a fixed template for the inorganic nanotubes. In other words, this is

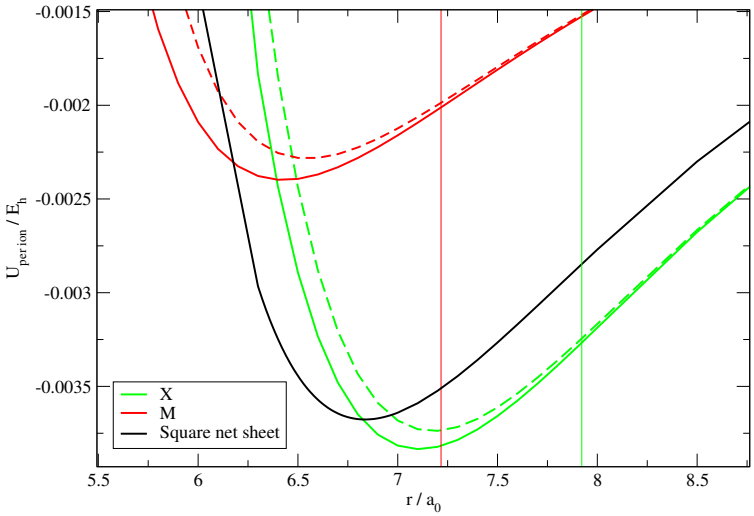

Figure 4.8: Single point energy calculations for various ionic species adsorbed onto a graphene sheet. The energy is the average energy per ion. The vertical lines show the ion-carbon dimer equilibrium separations from figure 4.7. red: Cation-graphene interaction. (solid above hexagon, dashed directly above carbon) green: Anion-graphene interaction. (solid above hexagon, dashed directly above carbon) Black: ionic square net sheet - graphene.

the first time that carbon-carbon interactions are included in the molecular dynamics simulations of the formation of inorganic nanotubes from the melt.

	Previous work	**Current Work**
ion-ion	Born-Mayer / Ewald summation	Born-Mayer / Ewald Summation
ion-carbon	Lennard-Jones	Lennard-Jones
carbon-carbon	none (rigid tube)	Tersoff II

Table 4.4: A comparison of the potential models used for the system interactions between the current and previous work [108, 109, 110, 111, 112, 113, 114, 115].

4.5 Filling simulations

Simulations were performed within the multi-component system in order that inorganic nanotubes could form directly through the filling of carbon nanotubes from the melt. A section of the nanotube was taken that was 5 unit cells in length and a circular graphene sheet was placed over each end so that the tube was effectively closed. A short molecular dynamics run of 73 fs was performed with temperature rescaling every 0.7 fs so that the system had the kinetic energy corresponding to the system into which it was to be theoretically immersed. An equilibrated configuration of the liquid consisting of 1728 ions within a cubic cell (corresponding to the

potential of choice) was taken and the rescaled nanotube configuration was placed inside the same cell. Any ions that lied within the region that the nanotube occupied (or that were positioned unphysically close) were removed whilst maintaining overall charge neutrality. A new molecular dynamics run was performed which allowed the liquid to equilibrate around the newly immersed closed nanotube (figure 4.9). This consisted of a 8.7 ps molecular dynamics run in the isothermal-isobaric ensemble. The barostat was constrained so that isotropic fluctuations were allowed only and a relaxation time of $\tau = 10,000$ atomic units (0.24 ps) was used for the thermostat and barostat.

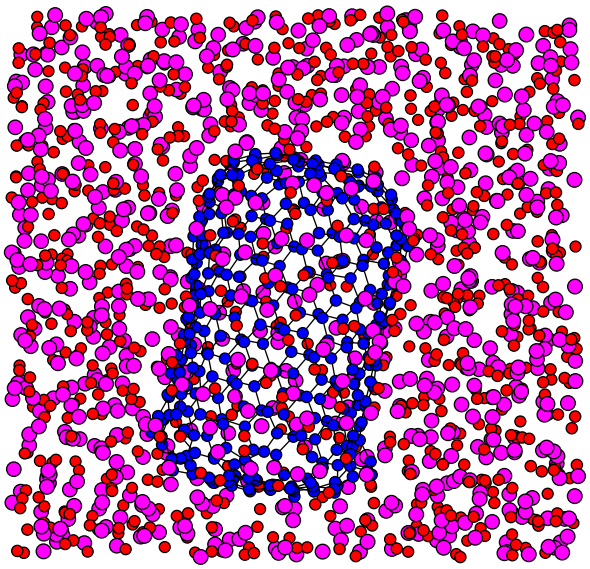

Figure 4.9: A snapshot from the molecular dynamics simulation in which the molten salt is equilibrating around the carbon nanotube. The carbon nanotube has its ends capped with circular sections of graphene sheets and is shown in blue.

After this equilibration period the run was continued in the same manner except that the graphite sheets at the ends of the nanotube were removed. This effectively meant opening it to the ions which were then free to start entering the nanotube.

The equilibration runs and filling simulations were performed at temperatures above the melting point of the ionic crystal by using a temperature range of 800-1000 K. The higher temperatures on this scale were used to promote the rate of filling near the beginning of the simulations and the lower temperatures were used once the tube had filled in order to limit the thermal fluctuations from the equilibrium structures.

Simulations were performed using both armchair $\big((9,9),(13,13),(15,15)\big)$ and zig-zag $\big((15,0),(22,0),(25,0)\big)$ configurations. These nanotubes were chosen as their diameters lie between 12 Å and 22 Å (comparable to the nanotubes utilised in

experiment) and so that there were three pairs of zig-zag and armchair nanotubes of similar diameter (see table 4.5).

Morphology	no of nanotube carbons	no of cap carbons	diameter
15,0	300	80	22.87
9,9	255	80	23.76
22,0	352	158	33.54
13,13	364	158	34.33
25,0	400	206	38.11
15,15	420	218	39.61

Table 4.5: The carbon nanotubes used in the filling simulations. The diameter is give in atomic units (a_0).

4.6 Analysis of the nanotube

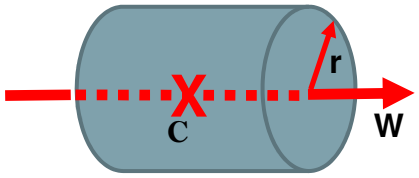

Figure 4.10: The coordinates of the carbon nanotube are fitted to the surface of a perfect cylinder which is defined by seven parameters. These parameters are a point lying on the cylinder axis (C_x, C_y, C_z) (conveniently a point close to the centre of mass of the nanotube), the nanotube radius r and a vector pointing along the nanotube axis $\mathbf{W} = \begin{pmatrix} \mathbf{w_x} \\ \mathbf{w_y} \\ \mathbf{w_z} \end{pmatrix}$. The error function in equation 4.17 is minimised using a steepest descent algorithm in which these parameters are obtained.

In order to monitor the nanotube dynamics and capture the filling events within them, a method of nanotube analysis has been developed. An integral part of this process is to define what constitutes an ion to be located inside the nanotube cavity. Previously, with the non-flexible nanotube, this consisted of observing if the ion coordinates entered the fixed region of space where the nanotube had been defined to be at the start of the simulation. However, in the current work the newly incorporated dynamics of the nanotube mean that the region enclosed by the nanotube is constantly changing. The nanotube is able to translate through the cell and the major axis of the nanotube can rotate with respect to the cell axes. The molecular vibrations of the nanotube mean that the encapsulated region can change in volume and deformations from the perfect cylindrical shape can occur. In contrast to the work with the rigid carbon nanotube, defining an ion to be inside

the nanotube is no longer a trivial problem. As a result of the nanotube dynamics the first step of the analysis must therefore be to calculate the region encapsulated by the carbon atoms.

It is assumed that the nanotube can be approximated by a perfect cylinder and the Cartesian coordinates of the carbon atoms are points in space that lie on the surface of this perfect cylinder. A method of fitting a set of 3D points that approximately lie on the surface of a cylinder has been developed for computer gaming graphics [18] and is applied to the carbon nanotube coordinates in this work.

The perfect cylinder surface is defined by seven parameters; the Cartesian coordinates of a point that lies on the cylinder axis (C_x, C_y, C_z), the unit vector that points along the axis of the nanotube $\mathbf{W} = \begin{pmatrix} \mathbf{w_x} \\ \mathbf{w_y} \\ \mathbf{w_z} \end{pmatrix}$ and the radius of the nanotube (r) which can be seen in figure 4.10. For any given point χ that lies exactly on the surface of a perfect cylinder then the following relation holds:

$$(\chi - C)^T \frac{(I - \mathbf{W}\mathbf{W}^T)}{r^2}(\chi - C) = 1. \tag{4.16}$$

Therefore, a sum over the N carbon atoms with Cartesian coordinates χ_i in our nanotube gives us an error function representing the deviation from the perfect cylindrical form of the nanotube:

$$E(C, \mathbf{W}, r) = \sum_i^N \Big(\big(\chi_i - C\big)^T \frac{(I - \mathbf{W}\mathbf{W}^T)}{r^2} \big(\chi_i - C\big) - 1 \Big)^2. \tag{4.17}$$

The error function 4.17 used in the fitting of the carbon positions is for an infinite cylinder. Since the carbon nanotube in this work is finite, it was also necessary to calculate the positions of the two defined ends of the nanotube. For each carbon coordinate, the corresponding coordinate is projected onto the cylinder's central axis along a vector which lies perpendicular to the cylinder axis. From these projected coordinates, the two most extreme points on the axis are taken to be the ends of the nanotube. The carbon nanotube length is taken to be the distance between these two points.

During the molecular dynamics simulations the positions of the atoms and ions were recorded every 29 fs (100 timesteps). For each of these recorded configurations, the error function was minimised by the method of steepest descent in order to obtain the perfect cylinder parameters $\mathbf{W}$, C and r. The initial parameter values for a given set are the minimised parameters $\mathbf{W}$ and r from the previous set of positions and the current calculated centre of mass is used for the initial value of

C. This allows quicker convergence of the new parameters. The reason that the previously minimised value of C is not used for the next initial guess is that the the minimised Cartesian coordinates of C are simply a point that lies on the central axis of the nanotube. It was found that over many minimisations point C might move away from the centre of the axis and cause non-convergence of the fitting process if the point C went past the defined ends of the carbon nanotube. If the nanotube moved across the boundary of the simulation cell then the cell boundary was moved according to the periodic boundary conditions so that the nanotube was positioned centrally in the cell prior to the minimisation. This was necessary for the convergence of the error function which cannot take into account periodic boundary conditions.

An ion was defined to be inside the carbon nanotube if its Cartesian coordinates satisfied two conditions. Firstly, if the distance of the ion from the central nanotube axis (defined by the minimised $\mathbf{W}$ and C) was less than that of the minimised radius r. Secondly, when the coordinate of the ion was projected onto the central nanotube axis along a vector perpendicular to the axis (defined by the minimised $\mathbf{W}$ and C), the point must lie between the two ends of the carbon nanotube tube. These criteria can be viewed in figure 4.11.

4.7 Averaging the positions of the nanotube and contents

When analysing the final structure of the inorganic structure inside the filled tube it is important to account for the thermal fluctuations that cause deviations from the perfect equilibrium structure. In previous work the underlying structure was found by averaging the coordinates over several time steps. This approach was successful since the nanotube was fixed in space, holding the enclosed inorganic structure in place. However, in this work, the nanotube is free to translate and rotate through the simulation cell. As a result the averaging of the coordinates no longer results in an accurate underlying structure. The introduction of the nanotube dynamics in the current model results in nanotube rotation and translations. Therefore the process of averaging causes the average structure (particularly the nanotube size) to vary in an unphysical way.

To prevent this inaccuracy and account for the introduction of nanotube dynamics, the mean positions were calculated after a geometric transformation of the nanotube and the contents. This transformation consisted of two components and can be seen in figure 4.12. Firstly, a rotation of the nanotube was performed so that

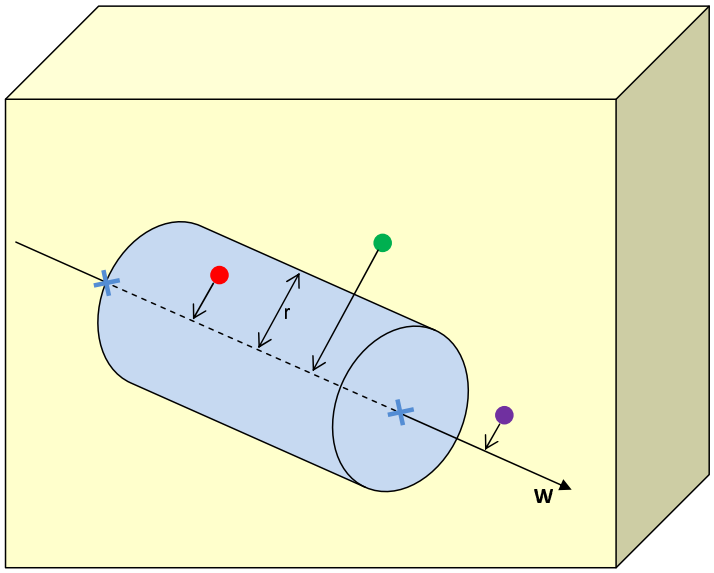

Figure 4.11: A schematic diagram to show the criteria used to decide if an ion is residing with the carbon nanotube. Firstly, the simulation cell boundaries must be redefined so that the nanotube in not intersected by them. The cylinder is then characterised by the seven parameters obtained from the steepest-decent fitting of the carbon coordinates to the cylinder surface via a minimisation of the error function in equation 4.17. The ions are monitored to see if they are located within the nanotube by testing the coordinates against two criteria. Green ion: The ion is not inside the nanotube as it fails on the first criterion. The distance from the central nanotube axis is greater than the cylinder radius r. Purple ion: The ion is not inside the nanotube as it fails on the second criterion. When projected onto the central axis along a vector perpendicular to **W** it does not lie between the two ends of the nanotube (shown with blue crosses). Red ion: The ion is inside the nanotube as it satisfies both the above criteria.

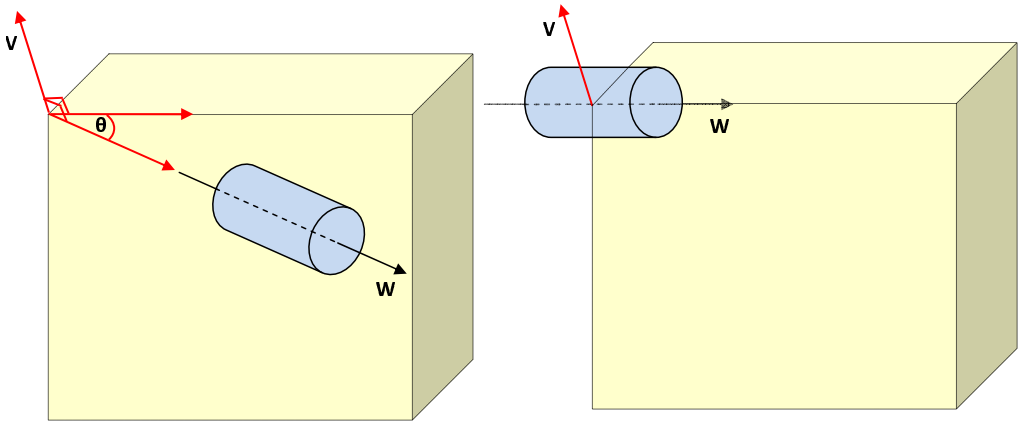

Figure 4.12: The geometric transformation performed before the averaging of the particle coordinates. The transformation consists of a rotation about the vector **V** by an angle θ so that it points along the z axis. The nanotube is then translated so that the centre of mass lies at the cell origin.

it pointed along the z axis (taken to be the c axis if the simulation cell), which is described by the rotation $M(\mathbf{V},\theta)$. The rotation matrix $\mathbf{M}$ used for this rotation of the carbons atoms and ions in the tube was performed about the vector $\mathbf{V} = \begin{pmatrix} \mathbf{v_x} \\ \mathbf{v_y} \\ \mathbf{v_z} \end{pmatrix}$ which is perpendicular to both the z axis and the minimised nanotube vector $\mathbf{W}$. The angle of rotation θ was the angle that $\mathbf{V}$ made with the z axis.

$$M(\mathbf{V},\theta) = \begin{pmatrix} cos\theta + (1-cos\theta)v_x^2 & (1-cos\theta)v_xv_y - (sin\theta)v_z & (1-cos\theta)v_xv_z + (sin\theta)v_y \\ (1-cos\theta)v_yv_x + (sin\theta)v_z & cos\theta + (1-cos\theta)v_y^2 & (1-cos\theta)v_yv_z - sin\theta)v_x \\ (1-cos\theta)v_zv_x - (sin\theta)v_y & (1-cos\theta)v_zv_y - (sin\theta)v_x & cos\theta + (1-cos\theta)v_z^2 \end{pmatrix} \tag{4.18}$$

Following this rotation, the coordinates of the carbon nanotube were translated so that the centre of mass of the tube lay at the origin. Performing this two-step transformation at each configuration before taking the mean coordinate positions proved successful in showing the underlying structure of the nanotube itself and also the ions inside the tube.

4.8 A cylindrical radial distribution function

The coordination environment within a crystal is often probed via a radial distribution function as described in equations 3.20 and 3.21. We must account for the reduction in dimensionality from the three-dimensional crystal system to the cylindrical nanotubular environment when probing the internal nanotube environment.

The new distribution function $g^{cyl}(r)$ is constructed in a similar manner to the original $g(r)$, except that the sum over $n_{r_{axis}}$ now corresponds to the number of ions in an interval $r+\delta r$ within a cylindrical volume (as opposed to a spherical volume):

$$g^{cyl}(r) = \frac{1}{x^{cyl}_{norm}} \sum_{i=1}^{N} n^{cyl}_{r_{axis}} \tag{4.19}$$

$$x^{cyl}_{norm} = \frac{\pi N h}{V}\big[(r+\delta r)^3 - r^3\big], \tag{4.20}$$

where h is the nanotube length. The parameter $n_{r_{axis}}$ is the number of ions with perpendicular shortest separation (r_{axis}) between the i^{th} ion and the central nanotube axis (as defined by the minimised parameters C and $\mathbf{W}$). The normalisation is taken over a cylindrical shell in which the number density radiating out from the central nanotube axis is compared to the hypothetical number density of an ideal gas of uniform distribution.

The cylindrical radial distribution $g^{cyl}(r)$ provides a useful tool for examining

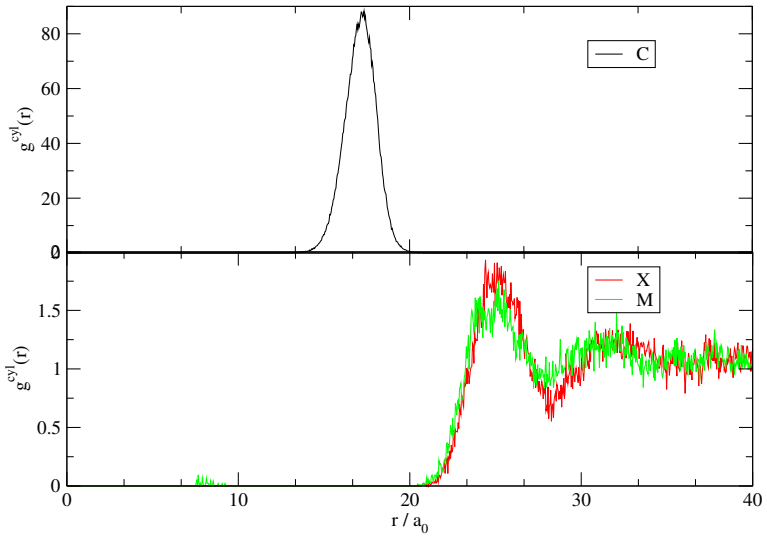

(a)

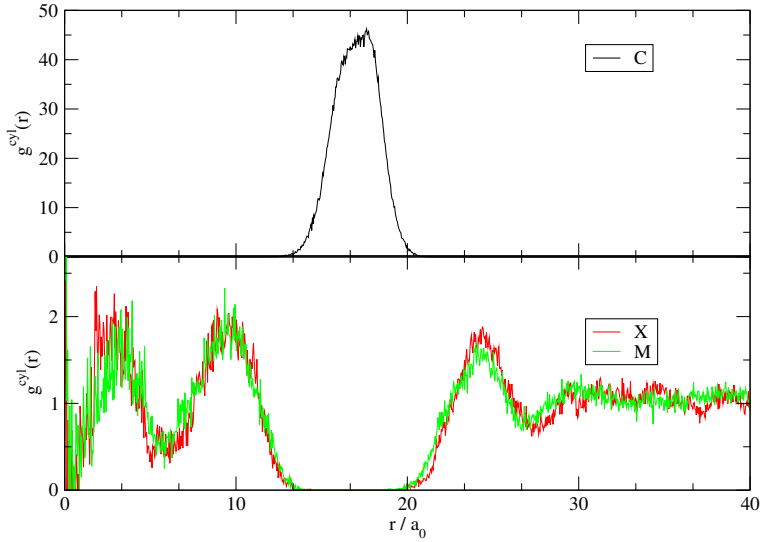

(b)

Figure 4.13: Top: The cylindrical radial distribution function $g^{cal}(r)$ for a nanotube filling simulation. Note the difference in scale of $g^{cyl}(r)$ for the carbon density in comparison to the ion density. This is due to the function being normalised with respect to an ideal gas with uniform density across the cylindrical shell volume. In comparison to this, the molecular structure gives a very high probability of finding a carbon atom at a distance r from the central axis. Top: Averaged over 17.4 ps near the commencement of the simulation. This is for the (13,13) nanotube using potential III (see table 4.6. The ion density remain outside the nanotube only. Bottom: Averaged over 17.4 ps near the end of the simulation. There is ion density between the central nanotube axis $r = 0$ and the carbon nanotube wall as it has filled. The ions have formed a double-walled internal structure indicated by the two (near) discrete peaks.

the internal structures of the carbon nanotubes and the structure of the liquid surrounding the carbon nanotube. An example is shown in figure 4.13 for a nanotube prior to and after a filling event.

4.9 The dynamics of the carbon nanotube

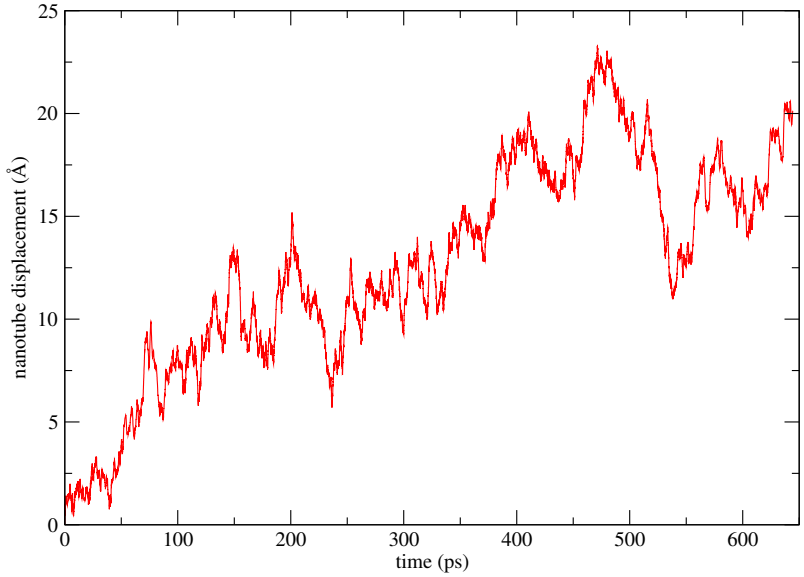

Figure 4.14: The carbon nanotube is observed to translate through the cell when the displacement of the nanotube's centre of mass is monitored. This graph relates to the (22,0) carbon nanotube using potential II.

The successful incorporation of the Tersoff potential into the model allows the nanotube to translate and rotate throughout space. The dynamics of the nanotube can be monitored via the minimised parameters $\mathbf{W}$, C and r as described in section 4.6. For example, the diffusion of the nanotube is observed by monitoring the displacement of the nanotube's centre of mass at time T from the position of the centre of mass at the commencement of the molecular dynamics simulation. The diffusion coefficient D is obtained from a mean square displacement plot, such as for the (22,0) nanotube in figure 4.14. The diffusion coefficient of this nanotube is found to be 2×10^{-6} cm s^{-1}.

The rotational motion of the nanotube can also be observed by calculating the angle that the nanotube axis vector $\mathbf{W}$ makes with the cell axes. For example, we can see the rotational motion for the (15,15) carbon nanotube in figure 4.15.

During the filling simulations the parameters obtained from the steepest descent minimisation of the perfect cylinder were monitored such as the error function $E(\mathbf{W}, C, R)$, the nanotube radius r and nanotube length. The evolution of these

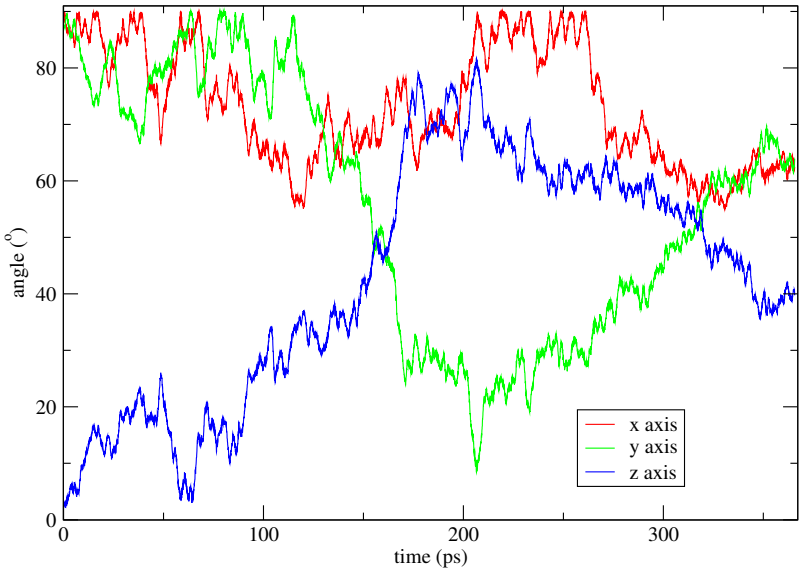

Figure 4.15: The angle that the nanotube axis vector **W** makes with the cell x, y and z axes, as a function of time for the (15,15) carbon nanotube using potential II.

variables gives us further insight into how the newly incorporated tube dynamics have advanced the model. Of particular interest is whether the parameters indicate if the nanotube has undergone any deformations during the filling events. A selection of these time evolutions are presented in figures 4.16 and 4.17.

The time evolutions demonstrate how the dynamic properties of the carbon nanotube fluctuate throughout the simulation. For example, the error function $E(C, \mathbf{W}, r)$ is a measure of deviation of the topology of the carbon nanotube from that of a perfect cylinder. This function would be equal to zero for carbon coordinates that lie precisely on the surface of a perfect cylinder. It is observed that $E(C, \mathbf{W}, r)$ fluctuates above zero, suggesting deviation of the geometry from that of a perfect cylinder.

Often, it is observed that the largest fluctuations in the time evolutions of $E(C, \mathbf{W}, r)$ are accompanied by an increase in the radius r. This correlation may due to the carbon nanotube deforming to an elliptic cylinder (figure 4.18). Such deformations during the filling events are instantaneous and are sometimes accompanied by an increase in the Tersoff energy due to the increased strain.

It is inconclusive if these elliptical deformations are directly related to the mechanism of filling. In some cases the elliptical deformations have been observed to coincide with the time when the filling rate was the greatest (for example the (15,15) nanotube with potential II, figure 4.17c). However, such fluctuations are also absent at the time of filling during the majority of the filling simulations. In fact these large instantaneous elliptical deformations were observed to occur before, during

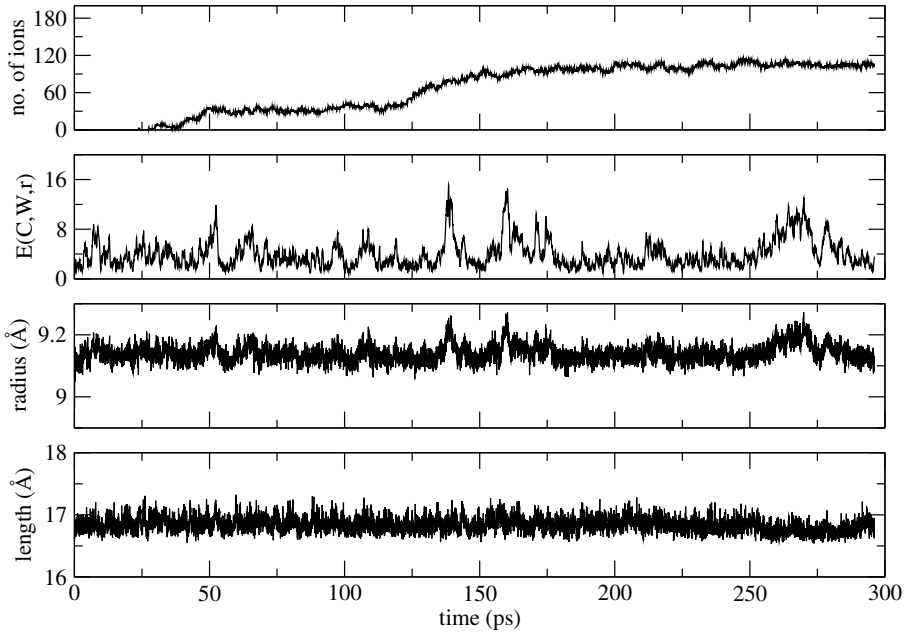

(a)

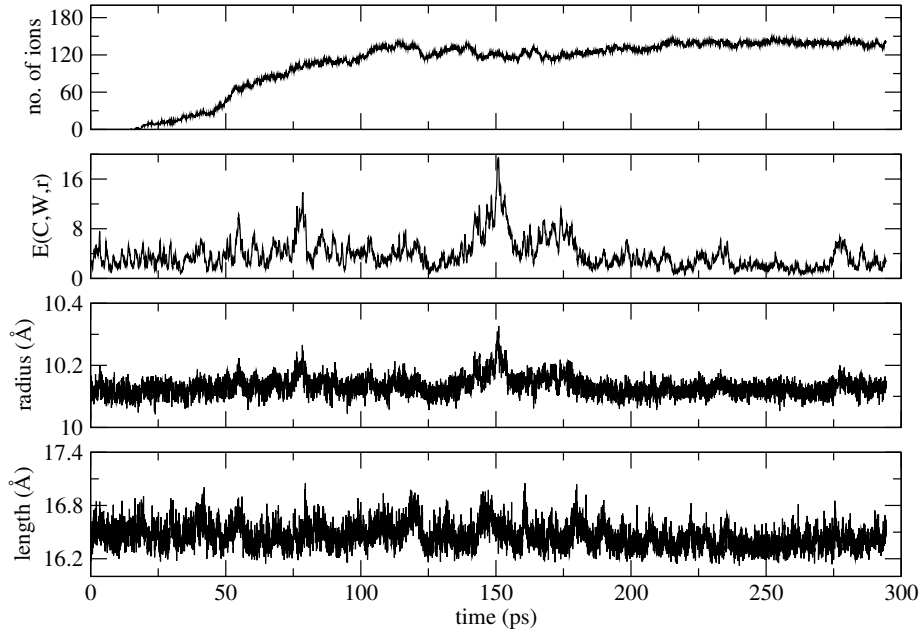

(b)

Figure 4.16: Evolution of the number of ions in the nanotube using potential I, the error ($E(C, \mathbf{W}, r)$), the radius and tube length as defined in section 4.6. (a): (13,13) carbon nanotube. (b): (25,0) carbon nanotube.

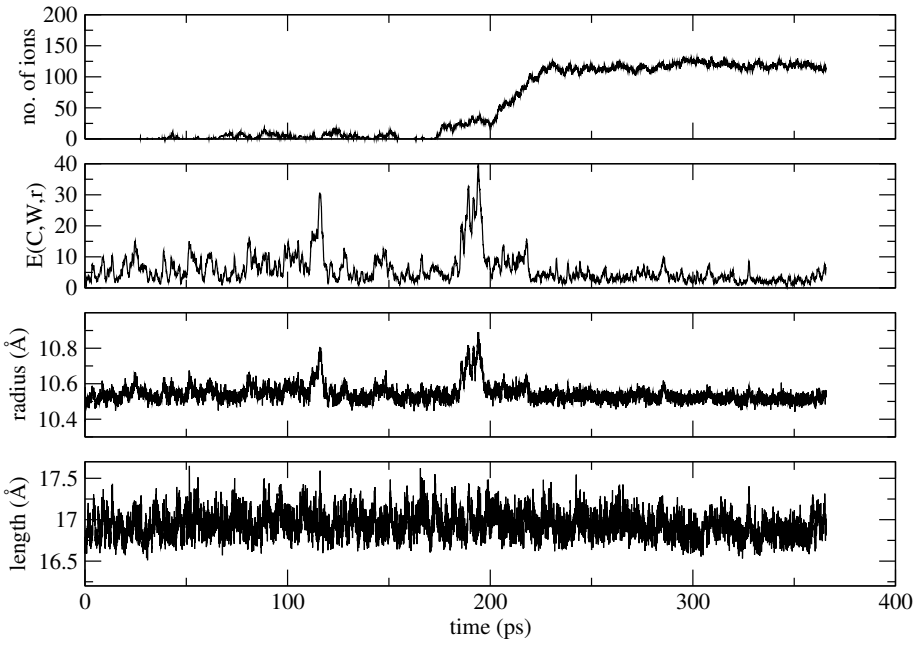

(a)

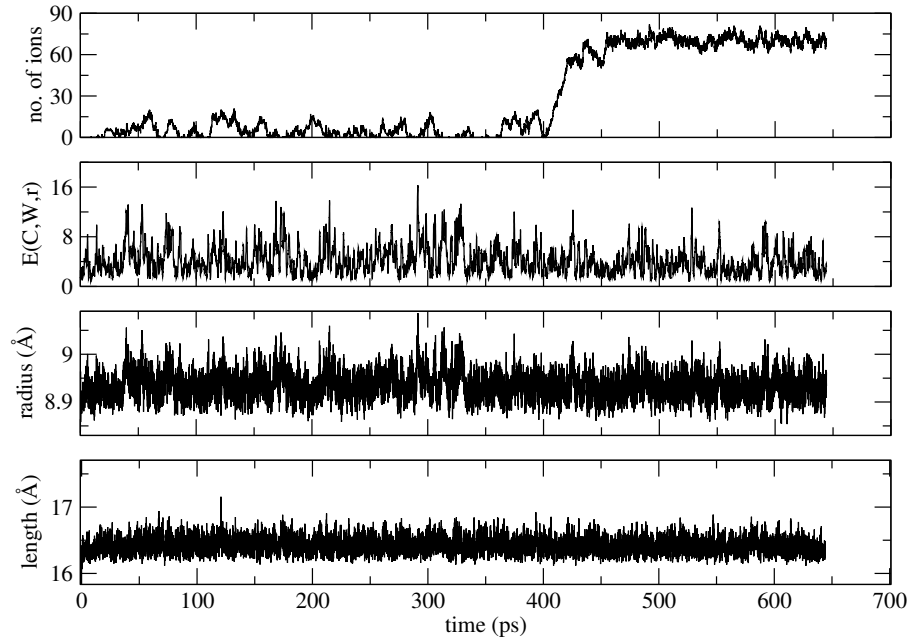

(b)

Figure 4.17: Evolution of the number of ions in the nanotube using potential II, the error ($E(C, \mathbf{W}, r)$), the radius and tube length as defined in section 4.6. (a): (15,15) carbon nanotube. (b): (22,0) carbon nanotube.

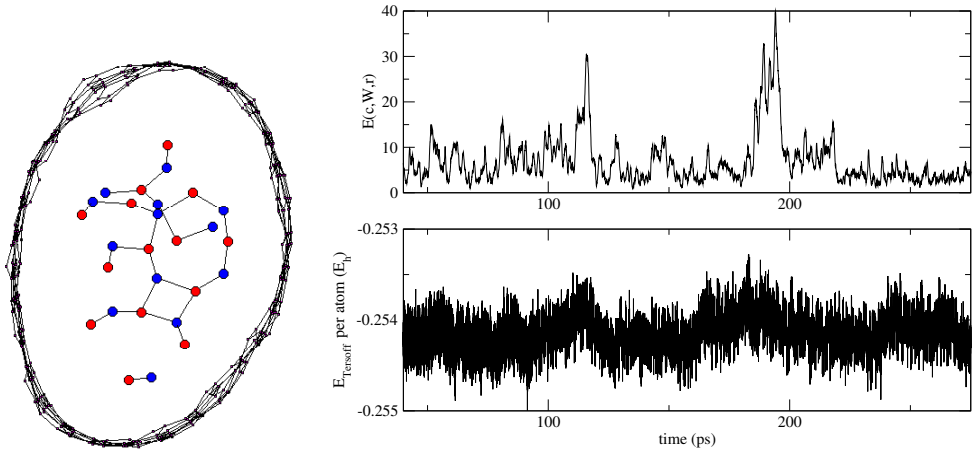

Figure 4.18: A snapshot of the (15,15) carbon nanotube using potential II at the time of the large fluctuation in $E(C, \mathbf{W}, r)$. The time corresponds to the greatest rate of filling (see figure 4.17a.) The instantaneous elliptic deformation causes the increase in $E(C, \mathbf{W}, r)$ and the calculated radius r. It is also apparent in the increased Tersoff energy due to an increased strain energy (right).

and after the filling events.

4.10 Filling Events

Simulations were performed as described in section 4.5 using four different parameterised Born-Mayer potential models, corresponding to four different ionic melts. Potential I predicts a tetrahedral B3 structure parametrised for the lithium chloride radius ratio and is described in section 3.1. Potential II is a modification of Potential I and was parameterised in section 3.1 in order that the tetrahedral B3 and octahedral B1 systems were equally favoured in the bulk crystals. Potential III has been parameterised for the potassium iodide radius ratio and has been used extensively for previous nanotube filling simulation work, in which a rigid nanotube was utilised [108, 109, 111, 113, 115]. This potential model predicts the octahedral B1 crystal system in the bulk. Finally, potential IV is another modification of potential I, in which the parameter B_{ij} has been increased (even more than for potential II), corresponding to an even larger anion than for potential I and II. This means that it also favours the octahedral B1 crystal system in the bulk crystal. However, although the radius ratio of the potentials are similar, the resulting crystals are more dense than those predicted by potential III. Due to the similar preference for the octahedral system by potentials III and IV in the bulk, we predict that the results of the filling simulations using these potentials will also be closely related. The parameters used for these potential models are summarised in table 4.6

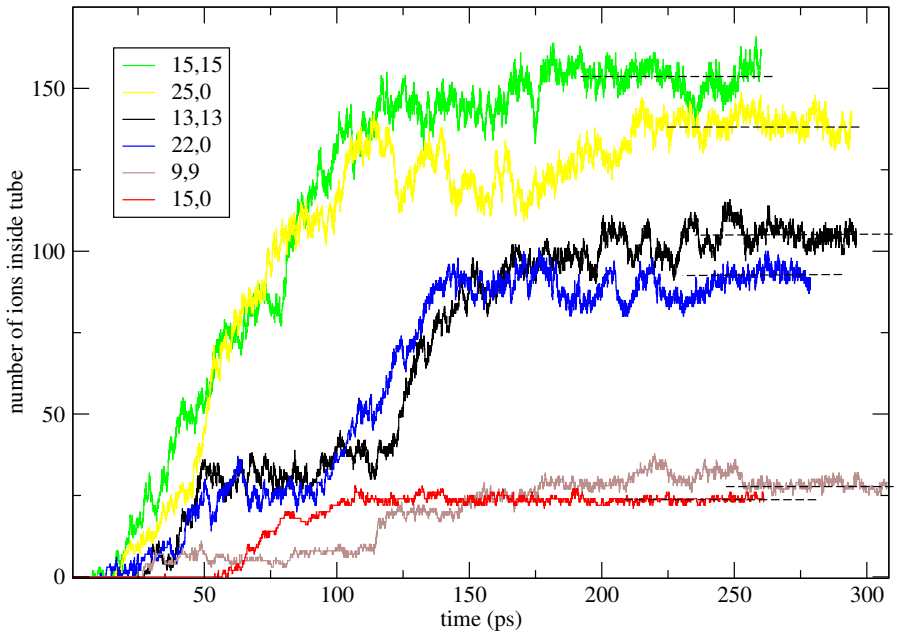

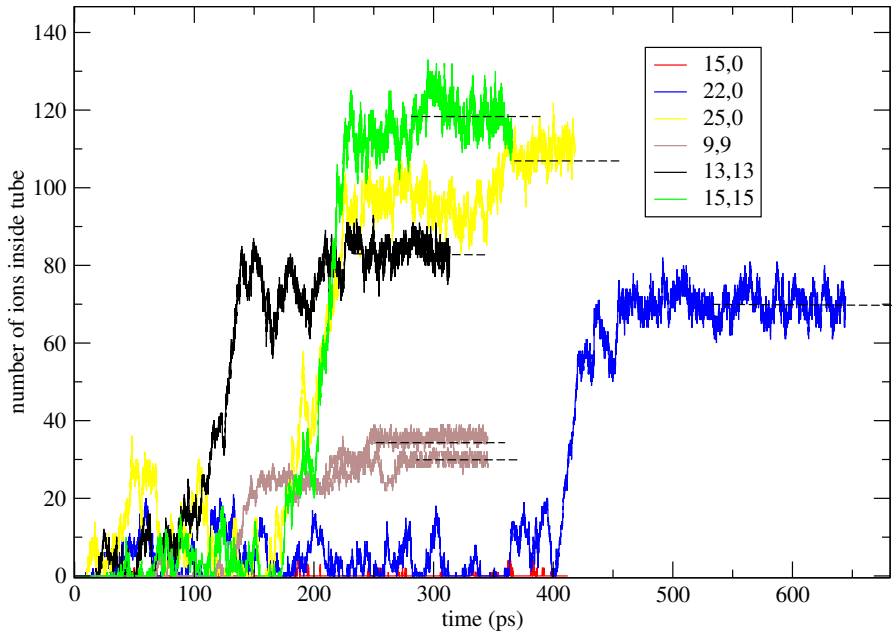

(b)

Figure 4.19: How the nanotubes filled with time. Top: Potential I. It can be seen that all 6 nanotubes were observed to fill. The dashed lines show the average number of ions residing in the nanotube once filled. Bottom: Potential II. Five tubes were observed to fill. Two filling events are shown for the (9,9) carbon nanotube.

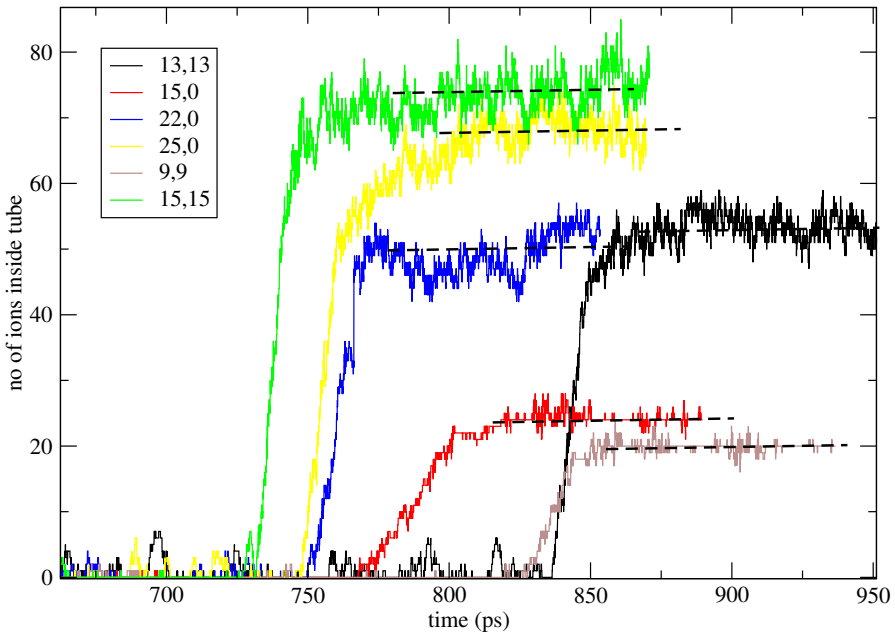

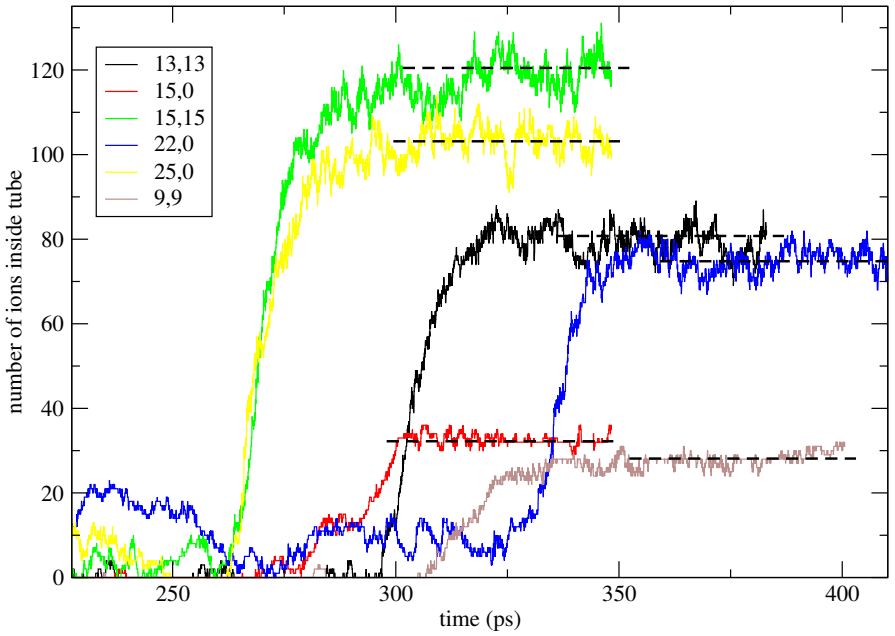

(b)

Figure 4.20: How the nanotubes filled with time. Pressure was required to fill the nanotubes with potential III and IV. The time after pressure is applied is shown in these evolutions. The dashed lines show the average number of ions residing in the nanotube once filled. Top: Potential III. It can be seen that all 6 nanotubes were observed to fill. Bottom: Potential IV. All six tubes were observed to fill.

Potential I, B3: tetrahedral			
	M-X	**M-M**	**X-X**
B_{ij}	8.68	0	61.66
a_{ij}	1.55	1.50	1.55
C_6	2.09	0.0763	115.987
Potential II, B3/B1			
	M-X	**M-M**	**X-X**
B_{ij}	12.938	1.1456	61.66
a_{ij}	1.50	1.50	1.50
C_6	2.09	0.0763	115.987
Potential III, B1:Octahedral			
	M-X	**M-M**	**X-X**
B_{ij}	102.88	0	269.52
a_{ij}	1.491	0	1.491
C_6	107.64	0.0763	624.76
Potential IV, B1:Octahedral			
	M-X	**M-M**	**X-X**
B_{ij}	19.938	1.1456	61.66
a_{ij}	1.50	1.50	1.50
C_6	2.09	0.0763	115.987

Table 4.6: The four potential models used for the filling simulations which are of the Born-Mayer construction. All values are given in atomic units.

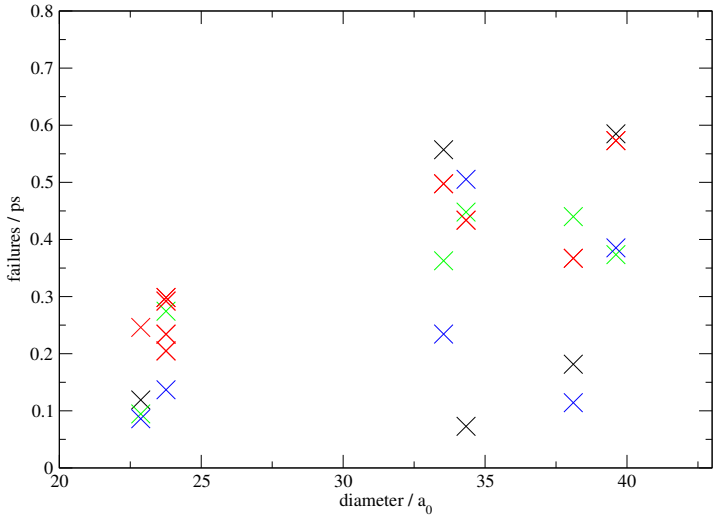

Figure 4.21: The rate of failed filling events as a function of nanotube diameter for all four potential models. Black: Potential I. (The failure rate here is averaged over a shorter timescale since this system filled much more quickly than the other potentials.) Red: Potential II. Green: Potential III. Blue: Potential IV.

Filling simulations were performed using all four ionic systems. It was observed that all the nanotubes were filled using potentials I and II on the timescale of this work, except the smallest diameter carbon nanotube (15,0) when using potential II. Potential II predicts a larger cation-anion equilibrium distance than for potential I and so it is possible that the nanotube was too small for any inorganic structure to fit inside. Potentials III and IV required a small application of pressure (0.00002 atomic units, 0.58 GPa) to instigate the filling events after which all the nanotubes filled. Filling profiles which show the number of ions residing in the nanotube pore as a function of time can be seen in figures 4.19 and 4.20.

The commencement of filling varied even within the same ionic melt for different carbon nanotubes. For example, the (22,0) carbon nanotube using potential II took considerably longer to start filling than the other nanotubes. In fact, the nanotube did not start to fill until many of the other carbon nanotubes using the same ionic melt had completed their filling process at 400 ps.

Failed filling events prior to successful event	**time filling commenced (ps)**	**failures (ps^{-1})**	**max number of ions in nanotube prior to filling**
37	123.997	0.2984	7
82	350.165	0.2342	12
98	478.265	0.2049	7
88	301.141	0.2922	18

Table 4.7: Four filling events for the (9,9) carbon nanotube using potential II. The rate of failed events is consistent despite the differing timescales prior to the commencement of the successful filling.

Not every occurrence of an ion entering the nanotube resulted in a filling event and prior to the filling events one can observe "failed filling events". These "failed filling events" occurred when one or more ions entered the nanotube at a time t but then at a time $t + \delta t$ the ions exited the nanotube so that it was completely empty again. In the case of the (22,0) carbon nanotube using potential II (which we recall took 400 ps before the commencement of the successful filling events), there were 200 failed filling events observed.

Potentials III and IV (which did not fill on the timescale of the simulations at zero pressure) also underwent many failed filling events prior to the carbon nanotube filling. This suggests that the difficulty in the filling did not arise due to the transportation of an ion to the nanotube entrance or due to the activation energy to enter the nanotube. In contrast, it points to an activation barrier to the filling mechanism which is overcome with the application of pressure to the system. Once the pressure was applied to these systems, very few failed filling events were observed

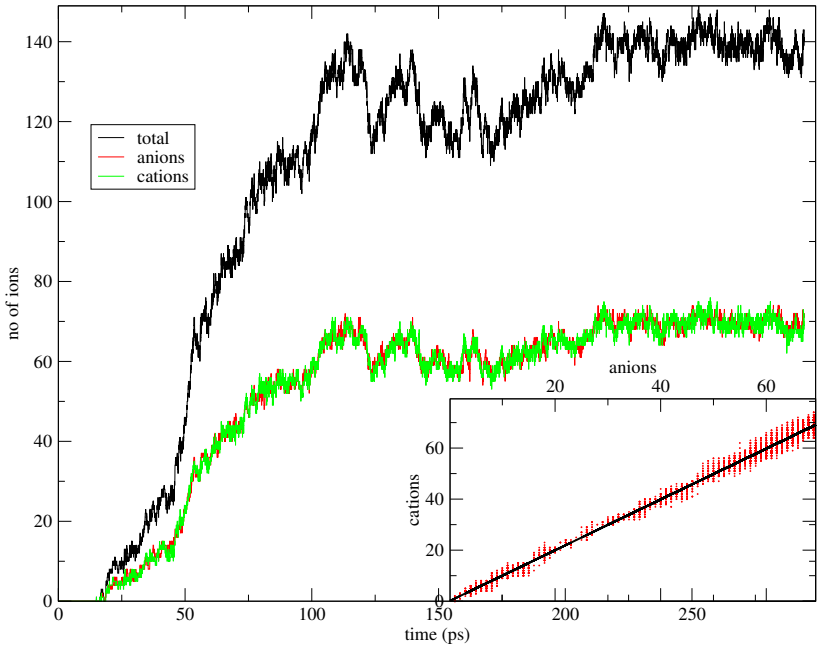

Figure 4.22: Time evolution for the potential I molten salt filling the (25,0) carbon nanotube. The inset shows the number of cations versus the number of anions in the nanotube at a given time. The functional form of the function in the inset indicates charge neutrality ($y = x$).

prior to the successful filling events.

Figure 4.21 shows the rate of failed filling events for all the potential models as a function of diameter which vary between 0.07 and 0.58 failures/ps and there appears to be some correlation between diameter and rate of failure. The filling of the (9,9) nanotube with potential II was repeated using different starting configurations and the rate of failed filling events is consistent for each simulation. This is despite the fact that they were averaged over different total times due to the successful filling event occurring on different timescales (see table 4.7).

Charge neutrality was maintained throughout the process of filling as can be observed by looking at the time evolution of the number of cations and ions entering the nanotube as in figure 4.22. This suggests that charge ordering plays an important role in determining the filling mechanism and resulting ionic structures that form inside the nanotube.

Regression analysis of the number of cations versus the number of anions in the nanotube was performed. A gradient of 0.995 was observed, confirming strict charge neutrality. Charge ordering proves to be the driving force in the formation of the inorganic tubular structures discussed in chapters 5 and 6. In particular, this is observed during the formation of the ionic chains of alternating ions in which ion-ion repulsion is minimised. Such interactions are prominent in the final inorganic

nanotubular structures observed and during the mechanism of filling, in which the tubular structures grow inside the nanotube pore from alternating ion chains.

Chapter 5

The formation of inorganic nanotubes

In the previous chapter a model for the filling of carbon nanotubes with molten salts, utilising a flexible representation for the carbon nanotube, was developed. Four potential models were considered for the MX stoichiometry which differed in their radius ratios (and hence, in the energetics of the underlying bulk crystal structures), including the novel potential that was characterised in chapter 3.

In this chapter, the resulting structures that formed within the carbon nanotube pore will be analysed in terms of the underlying energy landscape. It is found that the structures of the formed inorganic nanotubes can be rationalised in terms of the folding of infinite sheets which consist of percolating square or hexagonal nets. The details of the energy landscape are dependent on both the carbon nanotube diameter and the radius ratio of the molten salt being modelled. Three regimes of filling are identified in terms of the carbon nanotube diameter. The filling mechanisms and the role of the flexible nanotube in stabilising anisotropic inorganic nanotubes will be discussed.

The inorganic nanotubes formed within the small nanotube radius regime (such as the experimentally observed, rock salt nanocrystallite [87]) provide motivation for the theory developed in chapter 6.

5.1 The Energy Landscape

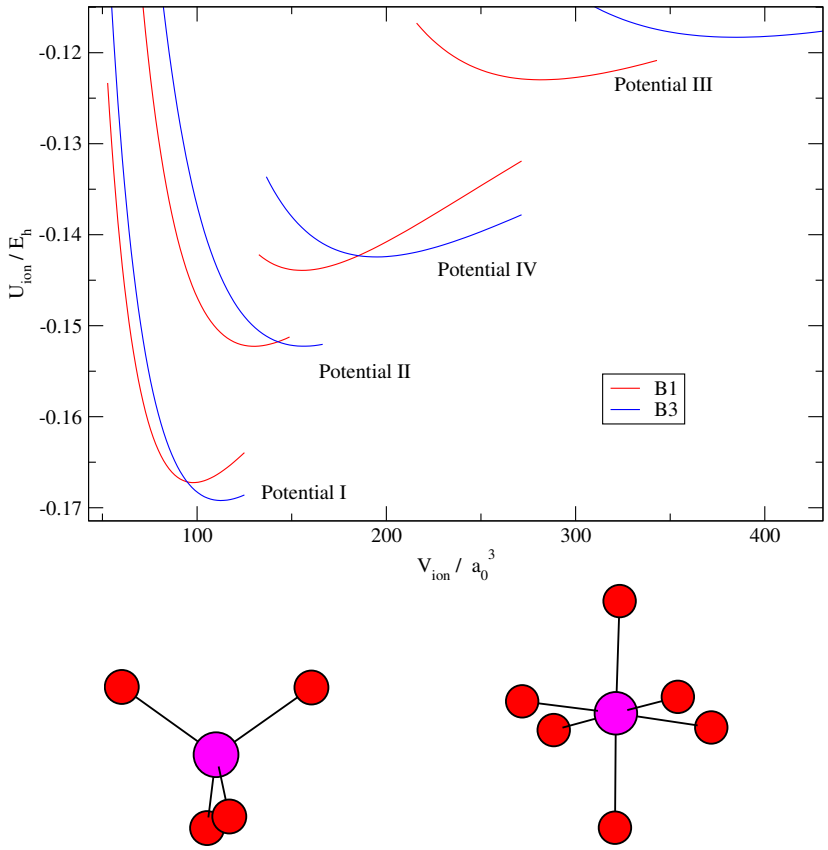

Figure 5.1: Top: Energy-volume curves calculated for the three dimensional crystal systems B1 and B3 using the four different potential models (energy and volume are calculated per ion). Potential one favours a tetrahedral co-ordination (B3). Potential two favours both polymorphs equally due to the parametrisation described in section 3.1. Potentials three and four both favour an octahedral coordination in the bulk due to their radius ratios. However, the systems predicted by potential four are more dense than those predicted by potential three. Bottom left: The tetrahedral environment experienced by an anion in the B3 structure. Bottom right: The octahedral environment experienced by an anion in the B1 structure.

In Chapter 4 molecular dynamics simulations were described in which flexible carbon nanotubes were found to fill directly with the inorganic molten salts in which they were immersed. Four ionic systems were used in these filling events and the potential parameters were given in table 4.6. The resulting internal structures that were formed inside the carbon nanotube were analysed in order that they could be identified. It was found that the structure of the ionic salt used determined the final structure formed, for the majority of the ionic tubular structures.

The differing potential parameters of the repulsive part of the pairwise potential model determines the relative energetics of the bulk crystal polymorphs. A table

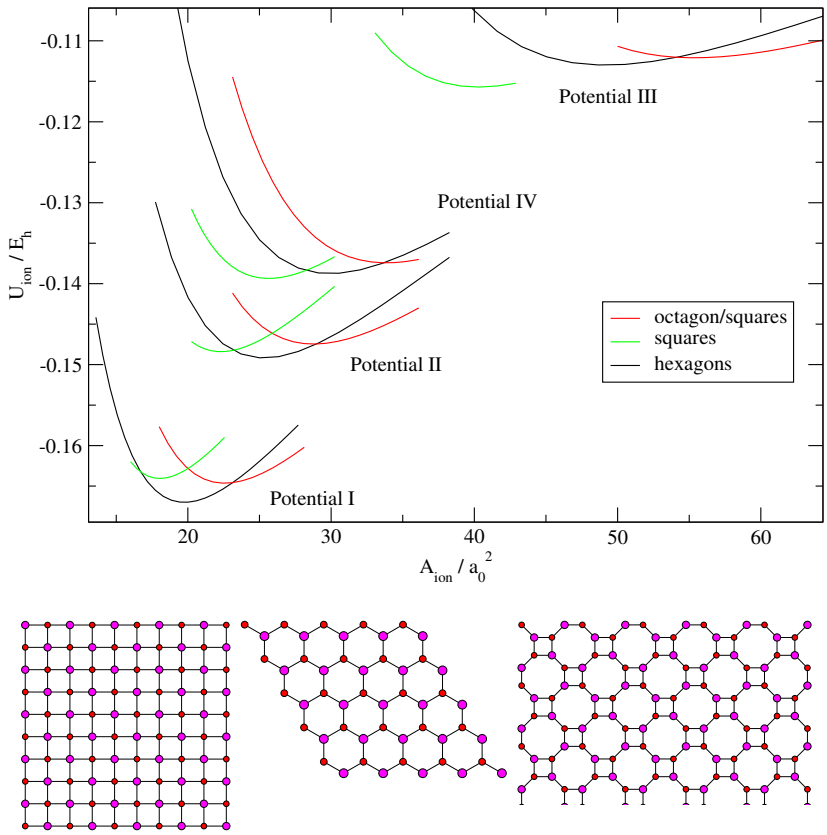

Figure 5.2: Top: Energy-area curves for the two dimensional polymorphs shown below. These were determined via single-point potential energy calculations at different areas (energy and area calculated per ion). The calculations have been performed using all four potential models. Potentials one and two favour infinite sheets based on the folding of tessellating hexagons. Potentials three and four favour infinite sheets based on the folding of square nets. Bottom left: The infinite square net sheet. Bottom centre: The infinite hexagon sheet (the binary form of graphene). Bottom right: The infinite sheet of tessellating squares and octagons.

containing the potential parameters and the implications of the varying radius ratios were discussed in section 4.10. In figure 5.1 the single point potential energies of the B1 and B3 crystal systems at 0K is calculated as a function of system volume and is summarised for all four potential models. The curve minima correspond to the crystal structure with the ideal M-X separation corresponding to the radius ratio of the given potential model within the given coordination environment (the tetrahedral B3 system or the octahedral B1 system). As expected, at the ideal M-X separation, the octahedral environment is more dense than the tetrahedral environment for all four potential models due to the increased packing of anions around the central cation. The parameters for potential I define a radius ratio which favours the tetrahedral coordination environment. The central cation is relatively small and so the anions can pack closely around it. Therefore, the curve minimum for the B3 tetrahedral system is lower in energy than that of the B1 octahedral environment. As the potential parameters predict successively larger cations (potential II, potential IV and then potential III), the tetrahedral environment becomes increasingly unfavourable. In contrast, the denser octahedral environment becomes increasingly favoured. In the B1 crystal system, the anions pack more densely around the central cation but at a slightly larger separation corresponding to a greater radius ratio. We can see that the B1 minimum is favoured for potential IV and strongly favoured for potential III in which the radius ratio predicts the largest central cation. Potential II was parameterised to favour neither the B1 or B3 phase and therefore their curve minima occur at the same internal energy.

On reduction of dimensionality from the three to two dimensional systems, the differing radius ratios also predict the relative energetics of related two dimensional polymorphs (figure 5.2). An infinite square net sheet of alternating ions is taken as the two dimensional analogue of the B1 or "rock salt" (octahedral environment) crystal system. Similarly, an infinite sheet of tessellating hexagons is taken as the two dimensional analogue of the B3 or "zinc blende" (tetrahedral environment) crystal system. Finally, a third two-dimensional polymorph is investigated which consists of tessellating octagon and squares. This polymorph is chosen as it has been observed as an intermediate structure in previous molecular dynamics simulations [112]. It is related closely to the infinite hexagon sheet since the anions are coordinated by three cations in both structures. However, the hexagon sheet polymorph is more dense than the octagon/square net infinite sheet for a given M-X bond length.

The single point energy of these two-dimensional polymorphs is calculated as a function of area and can be seen in figure 5.2. The relative energies of these infinite sheets mirrors that of the three dimensional crystal systems. That is, potential

I (which predicts a tetrahedral bulk system) favours the three coordinate hexagonal environment in the infinite sheet. In contrast, potentials III and IV (which predict the octahedral bulk structures) favour the tessellating square net sheet in two-dimensions. The energy difference between the polymorphs is quite small for potential IV, whereas potential III strongly favours the square net environment. For the novel potential II, (which we recall has been parametrised to favour neither the tetrahedral nor the octahedral crystal systems in the bulk) we have an intermediate situation in two-dimensions. The difference between the two sheet polymorphs is slight, with the hexagon environment slightly favoured over the square net sheet.

How do the relative energies of these polymorphs alter when we introduce a further reduction in dimensionality to the pseudo-one dimensional inorganic structures that are formed inside the carbon nanotube? The internal structures can be rationalised in terms of rolling the infinite sheet to form a cylindrical structure consisting of tessellating hexagons or square net sheets. In fact the rolling of the tessellating hexagons is exactly analogous to the folding the graphene to give the carbon nanotube itself. Therefore, the hexagon inorganic nanotubes are the binary analogue of the carbon nanotubes.

These cylindrical structures can therefore be classified using the same nomenclature to the carbon nanotubes [111]. A chiral vector is defined in terms of two component unit vectors $\mathbf{a_1}$ and $\mathbf{a_2}$ as with the graphene sheet (see figures 5.3 and 5.4). Again, since the chiral vector forms the circumference of the inorganic nanotube, the diameters of the internal structures are quantised. The inorganic nanotubes (INTs) will be defined by the following nomenclature from here on. The INTs formed from from the rolling of an infinite square net sheet will have the subscript sq so that the $(n,m)_{sq}$ is the INT_{sq} formed when the chiral vector

$$\mathbf{C_h^{sq}} = n\mathbf{a_1} + m\mathbf{a_2} \tag{5.1}$$

is folded to form the circumference of the INT_{sq}. Likewise, the INTs formed from the rolling of an infinite sheet of tessellating hexagons will have the subscript hex so that the $(n,m)_{hex}$ is the INT_{hex} formed when the chiral vector

$$\mathbf{C_h^{hex}} = n\mathbf{a_1} + m\mathbf{a_2} \tag{5.2}$$

is folded to form the circumference of the INT_{hex}.

Various properties of nanotubes such as the length of the chiral vector and the nanotube diameter can be calculated in terms of the integers n and m which determine the nanotube morphology. These properties have previously been derived for carbon nanotubes in the literature [77]. Since both carbon nanotubes and INT$_{hex}$s

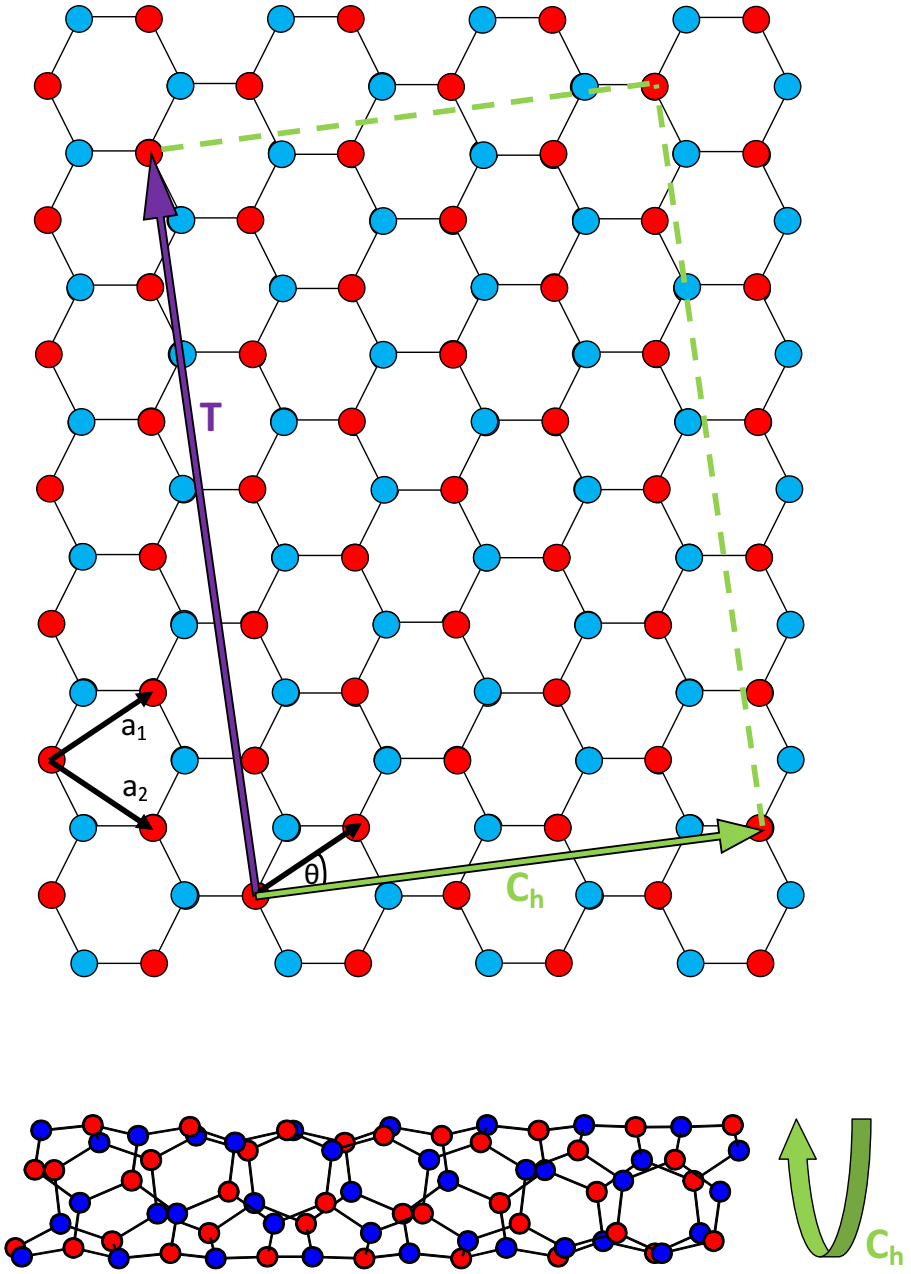

Figure 5.3: The folding of an infinite sheet of tessellating hexagons to form an inorganic nanotube. These INTs are the binary form of the carbon nanotubes themselves. The inorganic nanotube is defined by the chiral vector $\mathbf{C_h}$ which, on rolling the sheet, forms the circumference of the nanotube. The chiral vector $\mathbf{C_h}$ is the vector sum of the component unit vectors $\mathbf{a_1}$ and $\mathbf{a_2}$. In this example, the $(3,2)_{hex}$ inorganic nanotube is shown (bottom) and is defined by the green chiral vector $\mathbf{C_h} = 3\mathbf{a_1} + 2\mathbf{a_2}$ (top). The unit cell of the INT_{hex} is the rectangle enclosed by $\mathbf{C_h}$ and the perpendicular translational vector $\mathbf{T}$. The angle θ is the angle that the unit vector $\mathbf{a_1}$ makes with the chiral vector $\mathbf{C_h}$.

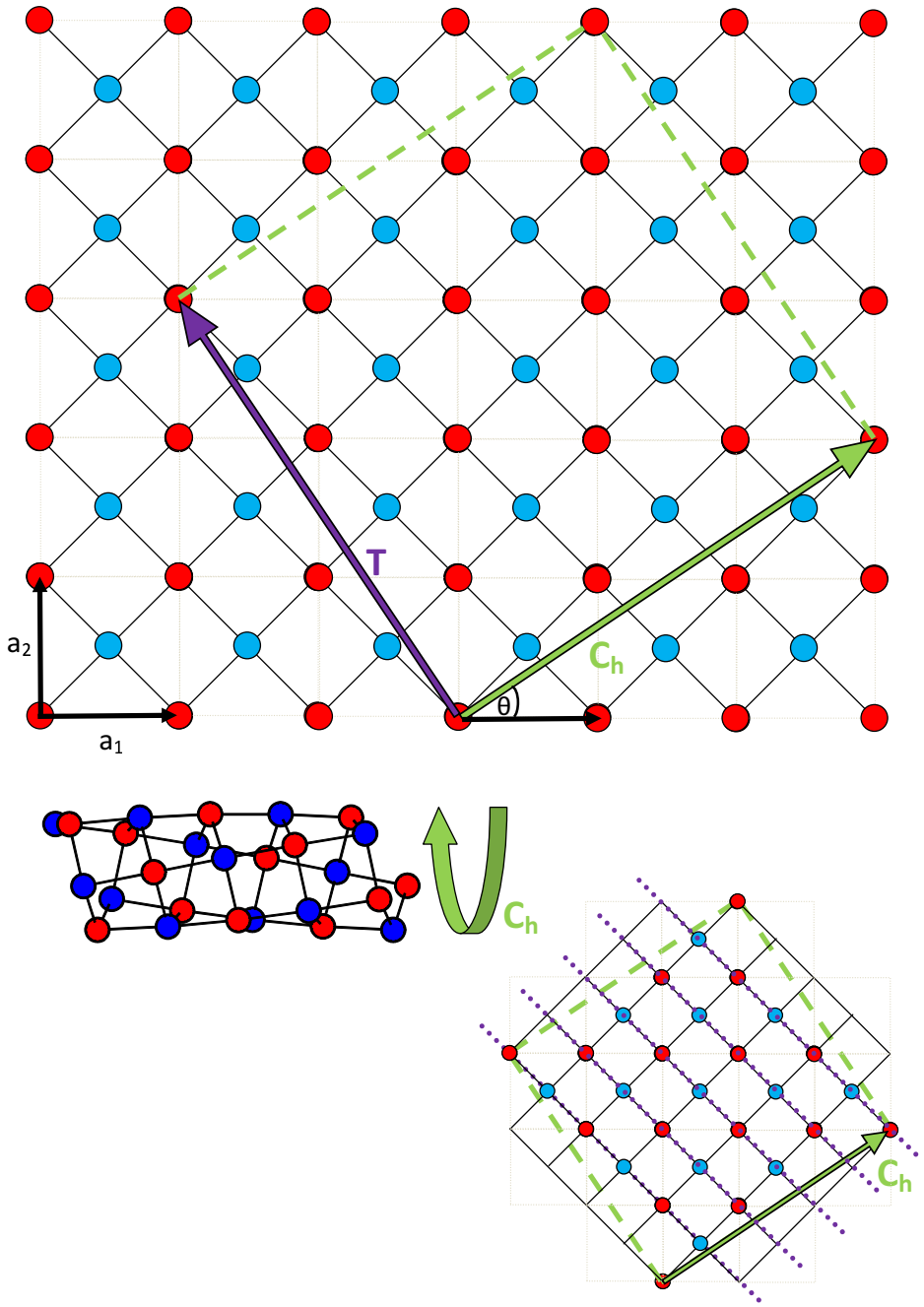

Figure 5.4: The folding of an infinite square net sheet to form an inorganic nanotube. The inorganic nanotube is defined by the chiral vector $\mathbf{C_h}$ which, on rolling the sheet, forms the circumference of the nanotube. The chiral vector $\mathbf{C_h}$ is the vector sum of of the component unit vectors $\mathbf{a_1}$ and $\mathbf{a_2}$. In this example, the $(3,2)_{sq}$ inorganic nanotube is shown (bottom) and is defined by the green chiral vector $\mathbf{C_h} = 3\mathbf{a_1} + 2\mathbf{a_2}$ (top). The unit cell of the INT_{sq} is the rectangle enclosed by $\mathbf{C_h}$ and the perpendicular translational vector $\mathbf{T}$ shown in purple. The angle θ is the angle that the unit vector $\mathbf{a_1}$ makes with the chiral vector $\mathbf{C_h}$. The bottom right figure shows the unit cell of the $(3,2)_{sq}$ INT. The five chains of alternating ions that run down the length of the INT are highlighted in purple. The number of alternating chains of ions in the INT_{sq} proves to play an important role in the INT_{sq} energetics and is given by $(n+m)$ as can be seen in table 5.1.

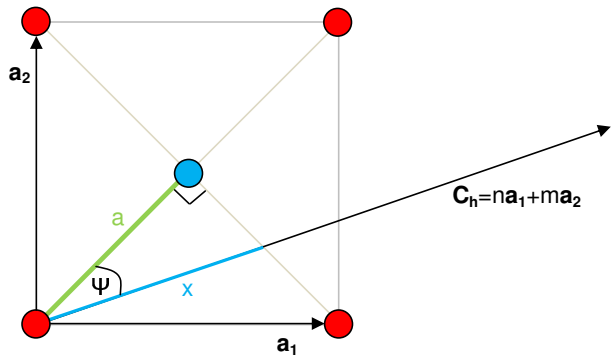

Figure 5.5: The number of chains running down the length of the nanotube is an important quantity and is given by $n + m$. This is derived using equation 5.6 by taking the cosine of angle ψ in order to determine the length x.

are based on the folding of infinite sheets of tessellating hexagons, the results can be applied to the INT_{hex} and are shown in table 5.1. The corresponding properties have been derived for the INT_{sq}s in this work and are also given in table 5.1. Later we will see how the formation of alternating chains of cations and ions plays an important role in the formation and energetics of the INT_{sq}s. Therefore, the number of chains in the INT_{sq} is a significant quantity. Figure 5.5 shows the angle ψ which is a function of the chiral vector $\mathbf{C_h}$. We see from this figure that

$$\cos\psi = \frac{r_{MX}}{x} \tag{5.3}$$

$$= \frac{\sqrt{2}(n+m)}{2\sqrt{n^2+m^2}}. \tag{5.4}$$

The number of chains is given by the length of the chiral vector ($|\mathbf{C_h}|$) divided by the length of x. Therefore the number of chains is

$$\frac{|\mathbf{C_h}|}{x} = \sqrt{2}r_{MX}\sqrt{n^2+m^2}\frac{\sqrt{2}(n+m)}{2r_{MX}\sqrt{n^2+m^2}} \tag{5.5}$$

$$= n + m. \tag{5.6}$$

We recall from section 4.2 that the potential energy of a carbon nanotube is taken to be the energy of a graphene sheet plus the strain energy required to roll the sheet into a cylinder. According to the elastic continuum model the potential energy of the carbon structures was therefore proportional to r^{-2} (equation 4.12). We can hypothesise that the same is true for the folding of the infinite two dimensional structures into the INT_{sq}s and the INT_{hex}s. However, this hypothesis proves to be a poor approximation for the energies of at least one class of INT, as we will see in chapter 6.

Property	$\mathbf{INT}_{hex}$	$\mathbf{INT}_{sq}$
Length of unit vector (a_0)	$\sqrt{3}r_{MX}$	$\sqrt{2}r_{MX}$
Chiral vector ($\mathbf{C_h}$)	$n\mathbf{a_1} + m\mathbf{a_2}$	$n\mathbf{a_1} + m\mathbf{a_2}$
Circumference ($\lvert\mathbf{C_h}\rvert$)	$a_0\sqrt{n^2+m^2+nm}$	$a_0\sqrt{n^2+m^2}$
Diameter (D)	$\frac{a_0}{\pi}\sqrt{n^2+m^2+nm}$	$\frac{a_0}{\pi}\sqrt{n^2+m^2}$
Translational vector ($\mathbf{T}$)	$t_1\mathbf{a_1} + t_2\mathbf{a_2}$	$t_1\mathbf{a_1} + t_2\mathbf{a_2}$
t_1	$\frac{2m+n}{d_R}$	$\frac{-m}{d_R}$
t_2	$-\frac{2n+m}{d_R}$	$\frac{n}{d_R}$
Length of nanotube ($\lvert\mathbf{T}\rvert$)	$\frac{a_0\sqrt{3}}{d_R}\sqrt{n^2+m^2+nm}$	$\frac{a_0}{d_R}\sqrt{n^2+m^2}$
Cosine of chiral angle ($\cos\theta$)	$\frac{2n+m}{2\sqrt{n^2+m^2+nm}}$	$\frac{n}{\sqrt{n^2+m^2}}$
Surface area of unit cell ($\lvert\mathbf{C_h}\rvert\lvert\mathbf{T}\rvert$)	$\frac{\sqrt{3}\lvert\mathbf{C_h}\rvert^2}{d_R}$	$\frac{\lvert\mathbf{C_h}\rvert^2}{d_R}$
Number of hexagons/squares per unit cell (N)	$\frac{2(n^2+m^2+nm)}{d_R}$	$\frac{(n^2+m^2)}{d_R}$
Number of chains of alternating ions along length	n/a	$n+m$

Table 5.1: Properties of the inorganic nanotubes in terms of the nanotube morphology defined by the integers n and m. The properties of the INT_{hex}s are from [77] and the corresponding properties for the INT_{sq}s are now derived. r_{MX} is the anion-cation distance in the infinite sheet of squares/hexagons, the angle θ is defined in figures 5.4 and 5.3 and d_R is the highest common factor of the integers n and m. The number of chains running down the length of the INT_{sq} is demonstrated bottom right in figure 5.4 where this important quantity takes the value of 5 for the $(3,2)_{sq}$ INT.

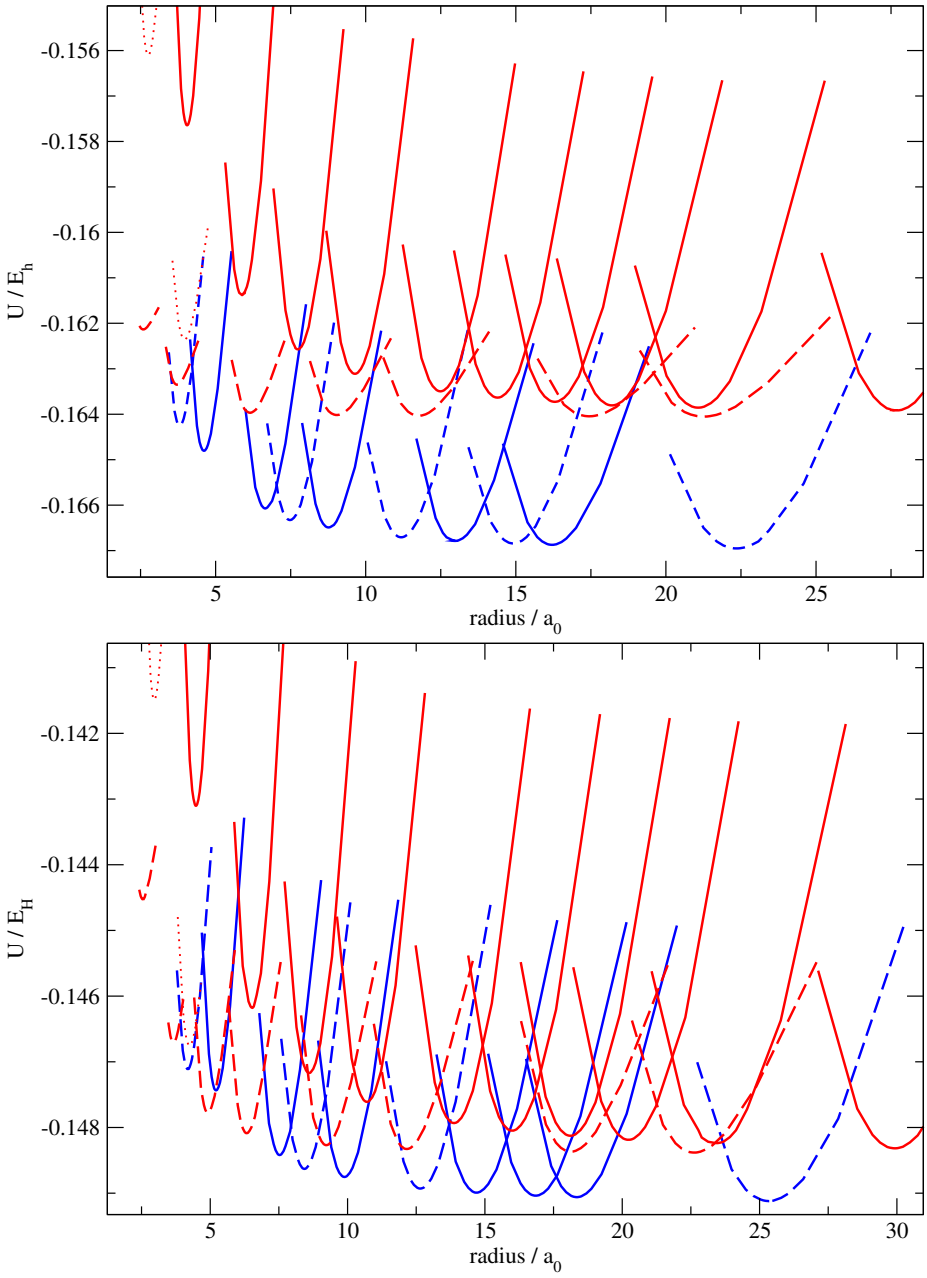

Figure 5.6: Energy versus radius curves for inorganic nanotubes of varying morphology using potential one (top) and potential two (bottom). The energy is calculated per carbon atom. A relaxed structure was stretched to various diameters by a scaling factor applied to the nanotube cross section. Blue dashed lines: $(n,n)_{hex}$. Blue solid line: $(n,0)_{hex}$. Red dashed lines: $(n,n)_{sq}$. Red solid line: $(n,0)_{sq}$. Red dotted line: $(n,m)_{sq}$.

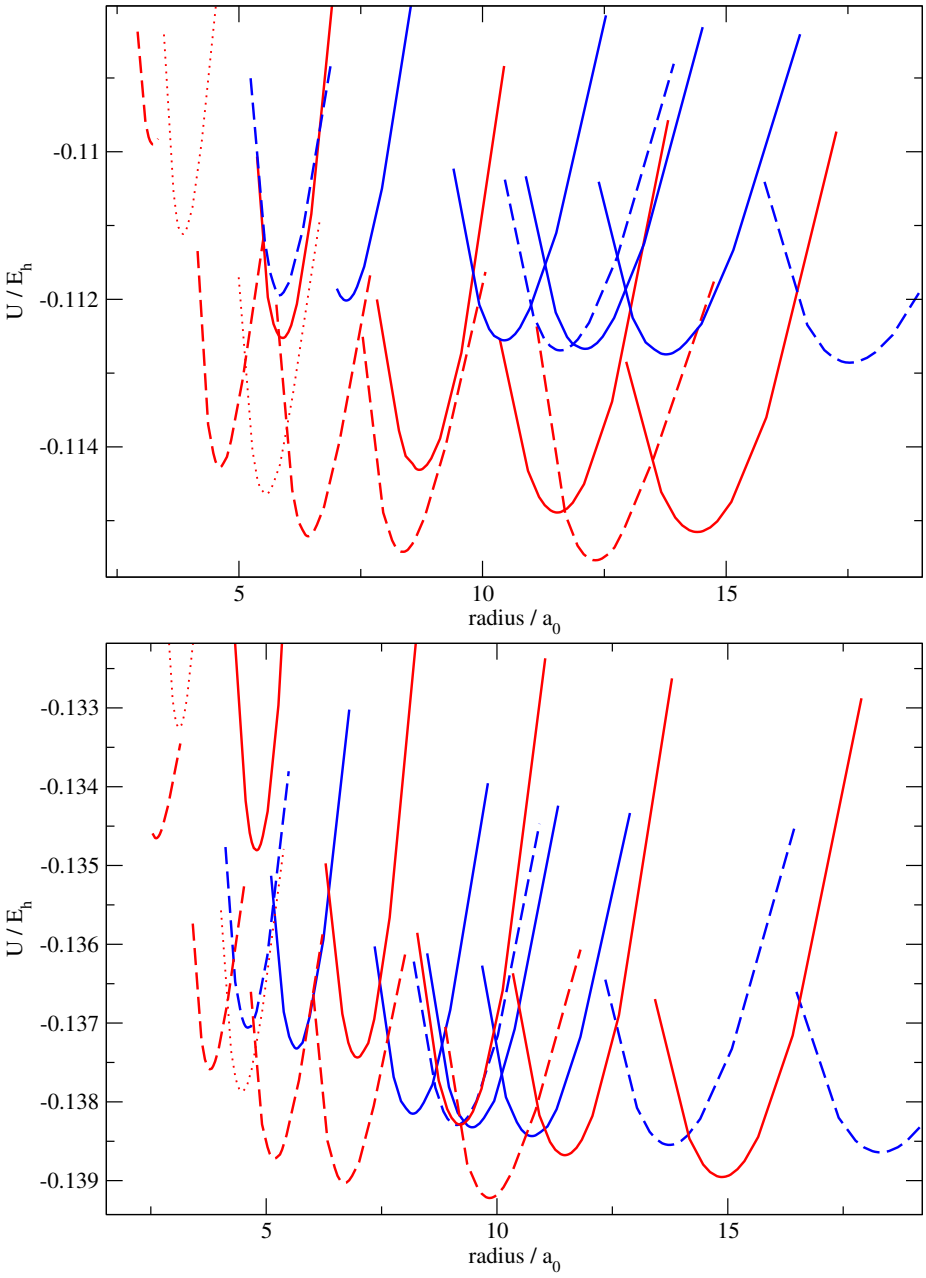

Figure 5.7: Energy versus radius curves for inorganic nanotubes of varying morphology using potential three (top) and potential four (bottom). The energy is calculated per carbon atom. A relaxed structure was stretched to various diameters by a scaling factor applied to the nanotube cross section. Blue dashed lines: $(n,n)_{hex}$. Blue solid line: $(n,0)_{hex}$. Red dashed lines: $(n,n)_{sq}$. Red solid line: $(n,0)_{sq}$. Red dotted line: $(n,m)_{sq}$.

The potential energy of the INTs were calculated from single point energies using INTs of varying diameter. The coordinates of these INTs were generated as follows. Firstly, the perfect INT was formed from the rolling of the lowest energy infinite sheet from the energy-area calculations into a cylinder of the desired morphology. The INT was then "relaxed" via a steepest descent algorithm (see appendix A-3) to optimise the anion-cation bond lengths in the structure. Finally a scale factor was applied through the cylinder cross section in order to produce configurations of varying diameter.

The resulting energy-diameter curves can be seen in figures 5.7 and 5.6. The minima of these curves represent the ideal configuration for the INT in question, with optimised bond lengths. We observe that for all four potential models, the energy landscape formed by the array of energy-diameter curves is complex. Unlike the carbon nanotubes, the minimum energy structures are dependent on the nanotube morphology with the optimised $(n,n)_{sq}$ INTs demonstrating a different functional form to that of the $(n,0)_{sq}$ INTs. Clearly, the energetics of the INTs require a more sophisticated treatment than the elastic continuum model; in fact a new model is successfully derived in chapter 6 which explains this observation.

As a result of these complex energy landscapes, the observed internal structures fall into two regimes. When considering larger radii INTs, the favoured structures are determined by the two-dimensional energy area curves in figure 5.2. That is, potential I and potential II form larger INTs consisting of cylinders constructed from an infinite sheet of tessellating hexagons. Conversely, potentials III and IV consist of INTs based on the folding of infinite square nets. In other words, the ionic system's radius ratio determines the morphology of the large radii INTs.

However, a new result is observed for the small radii INTs which is true for all four potential models, regardless of the system radius ratio. The small radii INTs are based on INT_{sq}; moreover the $(n,n)_{sq}$ INTs are the lowest energy structures at small radii. Again, this preference for the $(n,n)_{sq}$ is rationalised through the theory developed in chapter 6.

In the remainder of this chapter the INTs that were found to form inside the carbon nanotubes are surveyed. It is observed that in general, the structures from the dynamical simulations correspond to the lowest energy static structure given in the energy landscapes in figures 5.7 and 5.6 for the "preferred diameter". The preferred diameter is determined by the templating carbon nanotube diameter itself and also the ion-carbon equilibrium separation controlled by the Lennard-Jones ion-carbon potential model (table 4.3). We recall that the optimum ion-carbon distance is of the order of 6.84 a_0 for an infinite ion sheet and a graphene sheet in two

dimensions.

5.2 The (15,0) carbon nanotube

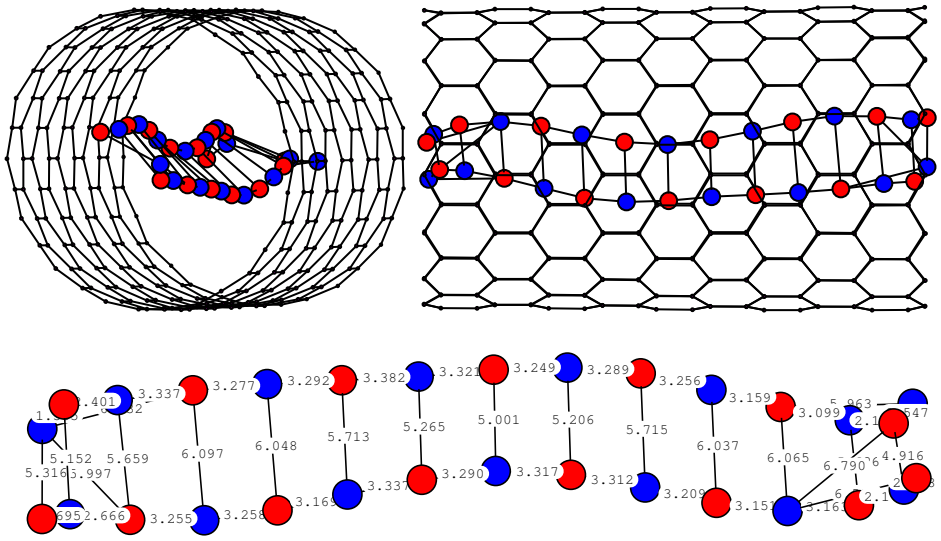

Figure 5.8: Time averaged structure (section 4.7) formed inside the (15,0) carbon nanotube using potential I. The bond lengths are shown in the $(1,1)_{sq}$ INT observed to form. Notice the shorter cation-anion bond lengths along the nanotube axis in comparison to the longer cation-anion bond lengths perpendicular to the axis. The structure appears to contract along the alternating chains of ions.

The (15,0) carbon nanotube was the smallest of the nanotubes used in the molecular dynamics simulations with a diameter of 22.9 a_0. It was only filled successfully at zero pressure using potential I on the timescale of this work; all the other three ionic systems required an application of pressure to instigate the filling process (0.00002 atomic units, $\equiv$ 0.58 GPa). Potential I corresponds to the most dense ionic system. The larger ionic radii of the other potential models may have hindered the onset of filling in this small diameter carbon nanotube.

5.2.1 Potential I

For potential I, the final structure observed inside the nanotube resembles a (1×2) square net or a "ladder like" structure which is the $(1,1)_{sq}$ INT structure using our standard nomenclature. A similar structure has been observed in the previous work using a rigid nanotube, during the filling process. In that work the structure underwent a folding mechanism into the $(2,2)_{sq}$ INT consisting of four chain of alternating ions [113]. However, this transformation was not observed in this work

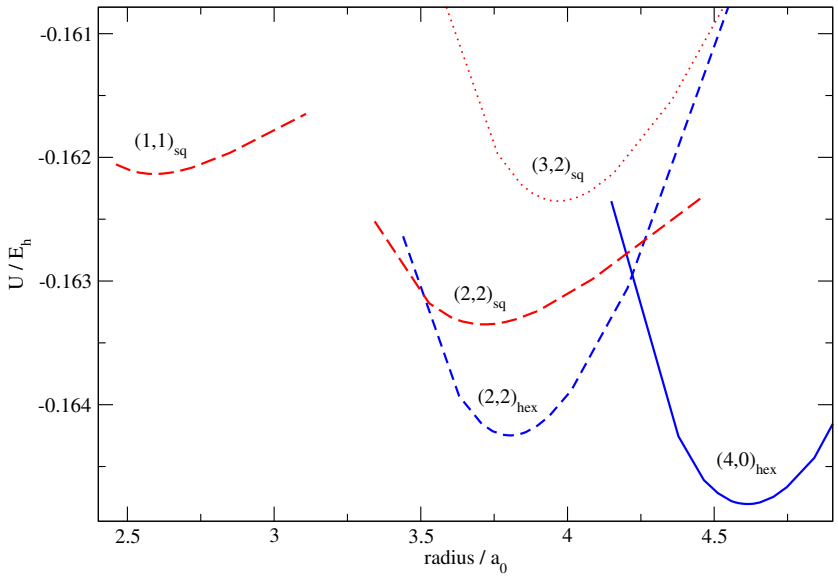

Figure 5.9: The lowest radii region of the energy landscape for potential I. The preferred radii suggests that the $(2,2)_{hex}$ would be the favoured structure in the (15,0) carbon nanotube. However, the $(1,1)_{sq}$ is observed to form and it does not transform to the $(2,2)_{hex}$.

utilising the flexible carbon nanotube, on the timescale of the simulations. In section 5.8 we will see how the deformations in the carbon nanotube itself may stabilise structures such as the $(1,1)_{sq}$ INT which have an anisotropic cross section.

In chapter 6 a theory is developed in which we find that small radii nanotubes favour structures consisting of chains of alternating cations and ions being formed down the length of the nanotube pore. The stability of these structures (the $(n,n)_{sq}$ INTs) is confirmed by the energy-diameter curves shown in figures 5.6 and 5.7. The ladder $(1,1)_{sq}$ structure is an example of one such stable structure and it consists of two chains of alternating ions. A contraction of anion-cation bond length is observed parallel to the nanotube axis due to the string interactions down the length of the INT. This can also be rationalised using the chain theory derived in chapter 6. The contraction is observed by monitoring the bond lengths of the time-averaged structure, as can be seen in figure 5.8. The mean anion-cation separation along the ion chains is 3.2 a_0 compared with the mean of 5.6 a_0 perpendicular to the nanotube axis.

The templating effect of the carbon nanotube with diameter of 22.87 a_0 and ion-carbon separation of 6.84 a_0 indicates that an INT structure of a radius approximately 4.6 a_0 would lie in the preferred region of the energy landscape. Figure 5.9 shows an expanded view of the energy landscape shown in figure 5.6 around this radius. We find that the $(1,1)_{sq}$ lies at a radius, slightly smaller than expected (where the INT radius is taken to be half the cross section of the INT which in the case of

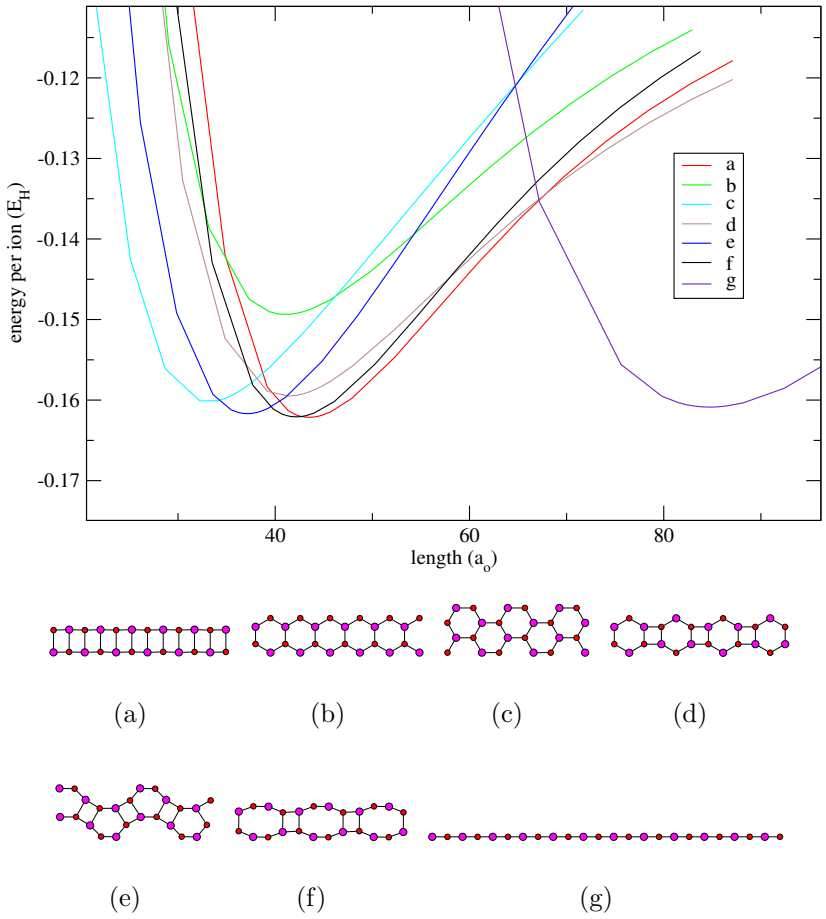

Figure 5.10: Potential energy versus length of a chain which contains 24 ions. The chain of squares (a) is most stable and the chain of hexagons (b and c) are significantly less stable.

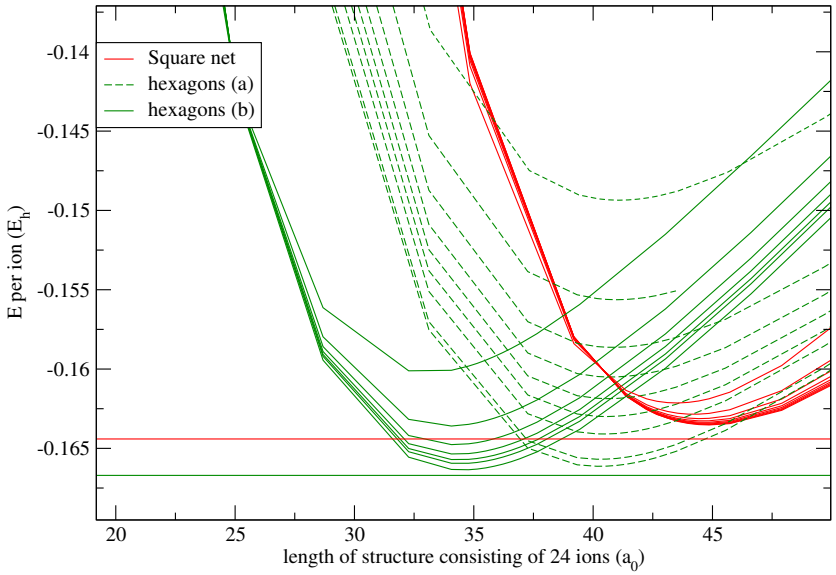

Figure 5.11: Stabilisation of the chains structures as the chains are layered. The horizontal lines show the limiting values for an infinite hexagonal sheet (green) and infinite square net sheet (red). The dashed green line is the build up of the structure shown in figure 5.10b and the complete green line is for the structure shown in figure 5.10c.

the $(1,1)_{sq}$ INT is equivalent to half the cation-anion separation perpendicular to the nanotube axis). A mean radius of 2.8 a_0 is observed from the bond lengths of the average structure seen in figure 5.8. We might expect that as more ions enter the nanotube, accessing the larger radii region of the landscape, the $(2,2)_{hex}$ INT might form since it is the lowest energy structure in the preferred region. However, it appears that there is a barrier to the transformation between these square-based and hexagon-based structures. It therefore remains in the $(1,1)_{sq}$ region of the landscape.

Since we are constrained to structures of the INT_{sq} and INT_{hex} morphologies in the static energy-diameter calculations, a range of chain structures were investigated as candidates for small radii INTs. It was found that on relaxing a chain of hexagons via a steepest decent algorithm (Appendix A-3), the structure always transformed into a more stable one, based on a chain of squares. The structures of these lower energy chains were determined by the length scale or stretch factor of the original chain of hexagons. This is consistent with the chain theory developed in chapter 6.

To help understand the relative energetics of these low diameter structures, potential energy calculations in the absence of the carbon nanotube were performed for a range of one-dimensional structures. Figure 5.10 shows the energies of these structures (as well as snapshots of the structures themselves) as a function of structure length (each containing 24 ions). The simple linear arrangement of hexagons (structure b) was unfavourable in comparison to all the other structures. The lowest

energy structure was found to be structure a which was the $(1,1)_{sq}$ INT structure observed to fill the (15,0) carbon nanotube. Figure 5.10 also highlights that an alternate arrangement of hexagons, in which successive hexagonal units are arranged in a non-linear fashion (structure c), are energetically favoured over the linear arrangement (structure b).

Layers (m)	a	b	c
1	-0.16214	-0.14915	-0.15981
2	-0.16284	-0.15528	-0.16359
3	-0.16312	-0.15809	-0.16476
4	-0.16326	-0.15973	-0.16535
3	-0.16335	-0.16083	-0.16570
6	-0.16342	-0.16163	-0.16594
4	-0.16346	-0.16224	-0.16635

Table 5.2: Energy per ion (E_h) for an ion in sheet containing m layers of structure a, b or c.

Further potential energy calculations are performed by building up layers of structure a, b and c and the calculated energies are as shown in figure 5.11 and table 5.2. The sheets are constructed by increasing the number of layers of structure a, b and c perpendicular to the major axis, keeping the added layer in the same plane as the initial ions. As a result, two-dimensional structures are generated which are periodically repeated (and are therefore pseudo-infinite) in one direction of a varying width perpendicular to the major axis. As the number of layers added becomes large, then these structures tend to infinite square net or hexagonal net sheets. The hexagon structure b appears to undergo a much greater stabilisation as the layers are added in comparison to the structure consisting of square nets. This stabilisation effect appears most significant for the linear structure of hexagons (the structure shown in figure 5.10b).

The energy of the structures containing m layers can be thought of in terms of ions residing in a chain at the edge of the structure (U_{out}) and the energy of the ions residing in chains in the central region of the structure (U_{in}). The partitioning of these energies is dependent on the number of ions residing at the edge of the structure a, b or c. For structure a, consisting of square nets we have

$$U^a = \frac{1}{m}[U^a_{out} - U^a_{in}] + U^a_{in} \tag{5.7}$$

where there are $2m$ chains of alternating ions running down the length of the structure (see figure 5.12). Similarly, for structure b consisting of a linear arrangement

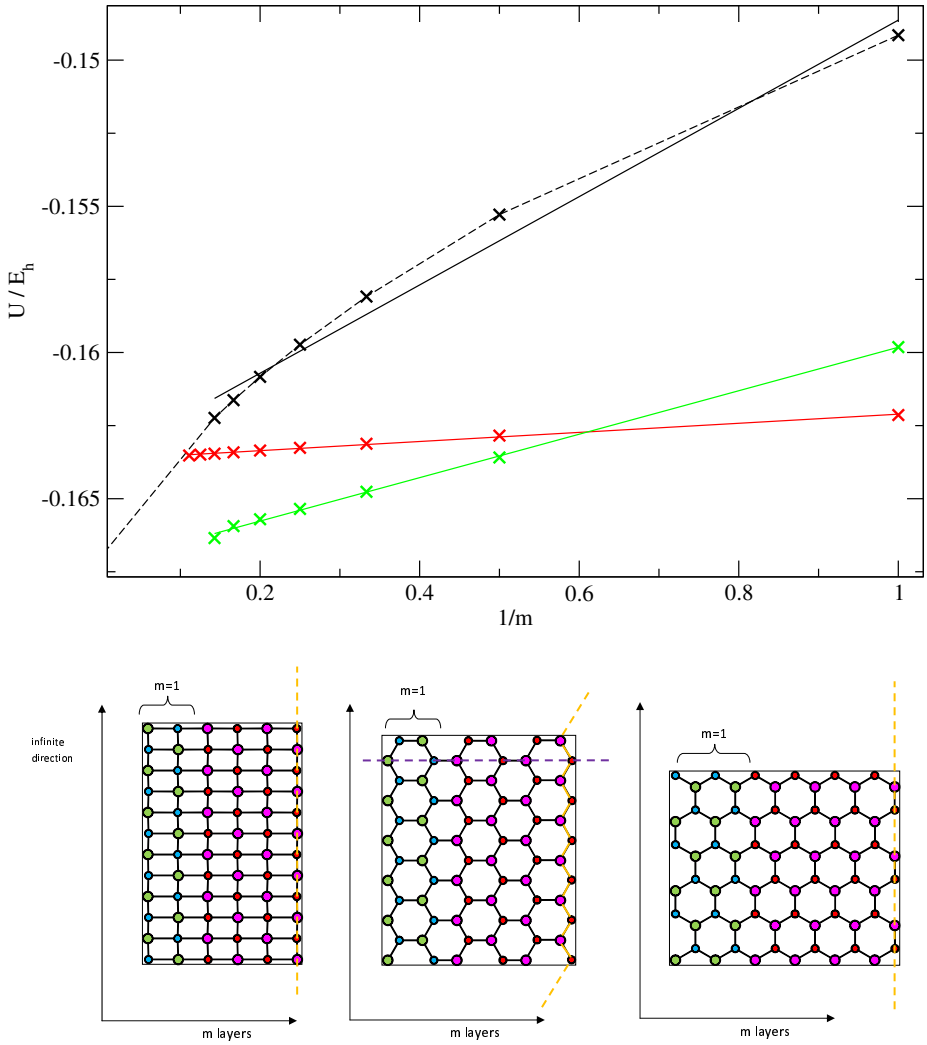

Figure 5.12: Top: How the energy of the layered structures a, b and c vary with $1/m$, where m is the number of layers. Structure a (squares, red) shows a good fit to equation 5.7 as does the fit of structure c (non-linear hexagons, green) to equation 5.9. However, although structure b is correct in the limit of large m (linear hexagons, black) it shows a very poor fit to the model described by equation 5.8. Bottom Left: Structure a built up into $m = 3$ layers, the $m = 1$ layer is shown in green and blue for clarity. The energy of this structure is partitioned along the orange dotted line, an alternating chains of cations and anions that are equally spaced. The importance of such interactions is discussed in chapter 6. Bottom Centre: Structure b built up into $m = 3$ layers, the $m = 1$ layer is shown in green and blue for clarity. The energy of this structure is partitioned along the orange "zig-zag" line of cations and anions of alternating charge in equation 5.8. However, this partitioning is unsuccessful due to the stronger interactions shown by the purple line along the finite axis of the structure. Bottom Right: Structure c built up into $m = 3$ layers, the $m = 1$ layer is shown in green and blue for clarity. The energy of this structure is successfully partitioned along the straight orange dotted line, an alternating chains of cations and anions that run along the infinite axis of the structure. There are four such chains in each layer m.

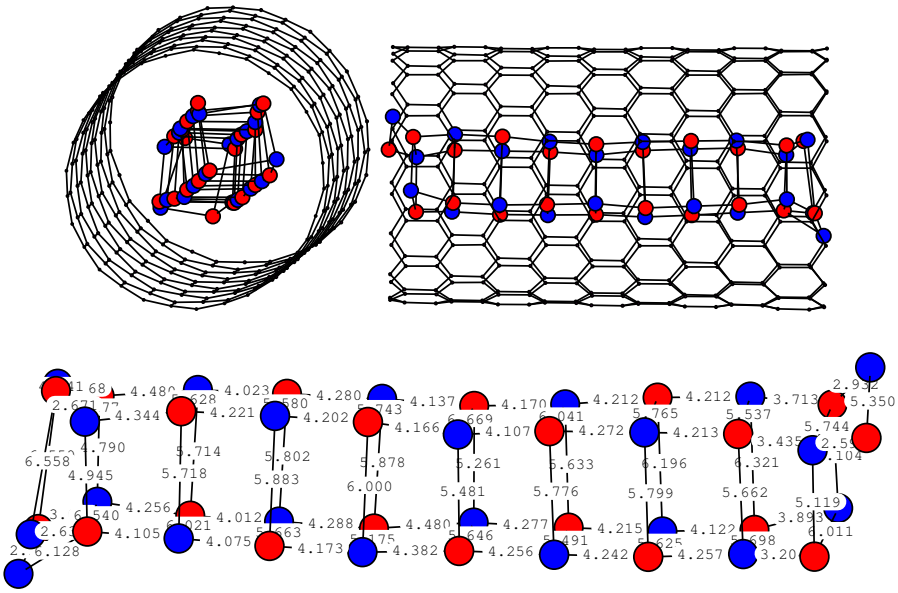

Figure 5.13: Time averaged structure (section 4.7) formed inside the (15,0) carbon nanotube using potential II. The bond lengths are shown in the $(2,2)_{sq}$ INT observed to form. This structure also forms using potential III and IV inside the (15,0) carbon nanotube. Notice the shorter cation-anion bond lengths along the nanotube axis in comparison to the longer cation-anion bond lengths perpendicular to the axis. The structure appears to contract along the alternating chains of ions.

of hexagon units, we have

$$U^b = \frac{1}{m}[U^b_{out} - U^b_{in}] + U^b_{in} \tag{5.8}$$

where the structure consists of $2m$ "zig-zag" chains of alternating ions running down the length of the structure (see figure 5.12). Finally, for structure c, consisting of a non-linear arrangement of hexagon units, we have

$$U^c = \frac{1}{m}\left[\frac{U^c_{out} - U^c_{in}}{2}\right] + U^c_{in} \tag{5.9}$$

since there are $4m$ chains of alternating charged ions running down the length of the structure, as highlighted in figure 5.12. Figure 5.12 shows a plot of the total energy as a function of $1/m$. Structure a and c conform to our model successfully by demonstrating a linear relationship, as would be expected from equations 5.7 and 5.9. The intercept of these functions are -0.163669 ± 0.00001 E_h and -0.1672537 ± 0.00005 E_h respectively, which correctly correspond to the energy of an ion residing in an infinite square net sheet and hexagon sheet. The gradients of the functions imply that the energy of an ion at the edge of the square net sheet is -0.16211 ± 0.00003 E_h and -0.1524 ± 0.0002 E_h for the layered structure c sheet. This model

is successful since the interactions of alternating chains of ions running along the infinite axis dominate. The perpendicular interactions (along the finite axis of the structure) between chains are weaker and are dominated by the nearest neighbour chains only. The energy of an ion residing in a chain more than one chain away from the edge can be considered as the same as an ion residing in a chain within an infinite sheet. The energy of an ion at the edge of the sheet U_{out} (with one nearest neighbour chain) is only slightly greater in energy than an ion in the central region of the sheet U_{in} (with two nearest neighbour chains), suggesting that the interaction energy between the chains is weak.

Structure	U_{in}	U_{out}	ΔU
a	-0.16367 ± 0.00001	-0.16211 ± 0.00003	0.00156 ± 0.00003
c	-0.16725 ± 0.00005	-0.1524 ± 0.0002	0.01486 ± 0.0003

Table 5.3: The intercept from figure 5.12 is used to determine the energy of an ion in a chain in the central region of the layered structure (U_{in}). The gradient allows us to calculate ΔU, which is the increase in energy for an ion in a chain at the edge of the sheet.The ions residing in a chain at the edge of the structure are under coordinated with respect to the ions in the central region. Finally, U_{out} is calculated by taking $U_{out} - U_{in}$ which corresponds to the energy of an ion at the edge of the layered structure. The energies are per ion and given in atomic units.

In contrast, figure 5.12 shows us that equation 5.8 gives us a very poor fit to the energies for structure *b*. We recall that the energy was partitioned into alternating "zig-zag" chains running down the length of the layered structure *b*. The non-linear dependence of the energy indicates that, unlike structures *a* and *c*, the energy of an ion is dependent on its distance from the edge of the structure. In structure *b*, the straight chain of alternating ions shown by the purple dashed line in figure 5.12 runs along the finite axis of the layered structure. This is equivalent to the interaction shown in orange running along the infinite axis in structure *c*.

Although, the energy of structure *b* cannot be partitioned successfully as described in equation 5.8 to give a linear function, the limit of $m = \infty$ layers in figure 5.12 does tend to that of the infinite hexagonal sheet (shown with a black dashed line). The intercept of this non-linear function appears to tend to that of the linear function of structure *c* (shown in green). At this limit, the straight chain of alternating ions (which run perpendicular to the "zig-zag chains") also becomes infinitely long.

The interaction along the alternating ion chains shown in figure 5.12 (shown in purple for structure *b* and orange for structure *c*) provides a rationale for the greater energetic stability of the non-linear arrangement with respect to the linear

arrangement of hexagons. In the former the chain runs down the infinite length of the structure and in the latter, the interaction runs along the finite axis.

5.2.2 Potentials II, III and IV

Potentials II, III and IV all filled to give the $(2,2)_{sq}$ INT on application of pressure to the system (figure 5.13). This corresponds in all cases to the lowest energy structure in the preferred region of the energy landscape. Again, we find that there is a contraction of anion-cation separations parallel to the nanotube axis as can be seen by monitoring the mean separations in the time-averaged structures (see table 5.4. This is due to the favouring of alternating ion chains that is explained using the theory derived in chapter 6.

Potential	**a** (a_0)	**b** (a_0)	$x = a/b$
II	5.9	3.9	1.50
III	6.5	6.1	1.07
IV	5.7	4.6	1.24

Table 5.4: The mean time averaged anion-cation separations perpendicular to the nanotube axis (a) and (b) parallel to the nanotube axis (b) for the $(2,2)_{sq}$ INTs formed inside the (15,0) carbon nanotube. The ratio x is given by a/b and shows that there is a contraction of anion-cation separations along the alternating ion chains that run down the length of the nanotube.

5.3 The (9,9) carbon nanotube

The next smallest carbon nanotube after the (15,0) is the comparably sized (9,9) carbon nanotube (diameters of 22.9 a_0 and 23.8 a_0 respectively). These nanotubes lie in the "small radius" regime. Both potentials model I and II were successful in filling the (9,9) carbon nanotube without the application of pressure. Potential III and IV required a small external pressure to instigate filling (0.00002 atomic units, 0.58 GPa).

It was found that the final structures that formed inside the nanotube pore were all based on the folding of a sheet of square nets. This is because the diameter of the carbon nanotube (23.76 a_0) and the ion-carbon equilibrium separation (6.84 a_0) give a preferred INT radius of the order of 5 a_0. At this radius, the INT is still in the small radii regime and the energy landscape predicts structures based on the folding of square net sheet for all four ionic systems (see figures 5.6 and 5.7).

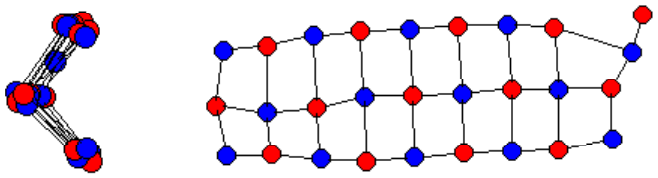

Figure 5.14: Average final structure in the (9,9) carbon nanotube with potential I. The subsection of the square net infinite sheet consists of three chains of alternating ions which bends into a "hinge" shape. This three chain structure does not belong to either the INT_{sq} or INT_{hex} morphology since the unit cell cannot be constructed by folding an infinite sheet along along chiral vector to form a cylinder However, it is most closely related to the former morphology as it consists of tessellating square nets.

5.3.1 Potential I

On examining the filling evolutions of the (9,9) carbon nanotube we can see that the number of ions in the nanotube plateaued at various stages of the filling (figure 4.19). Examination of the average internal structure at each of these plateaus gives us an insight as to the filling mechanism. For potential I it was found that the

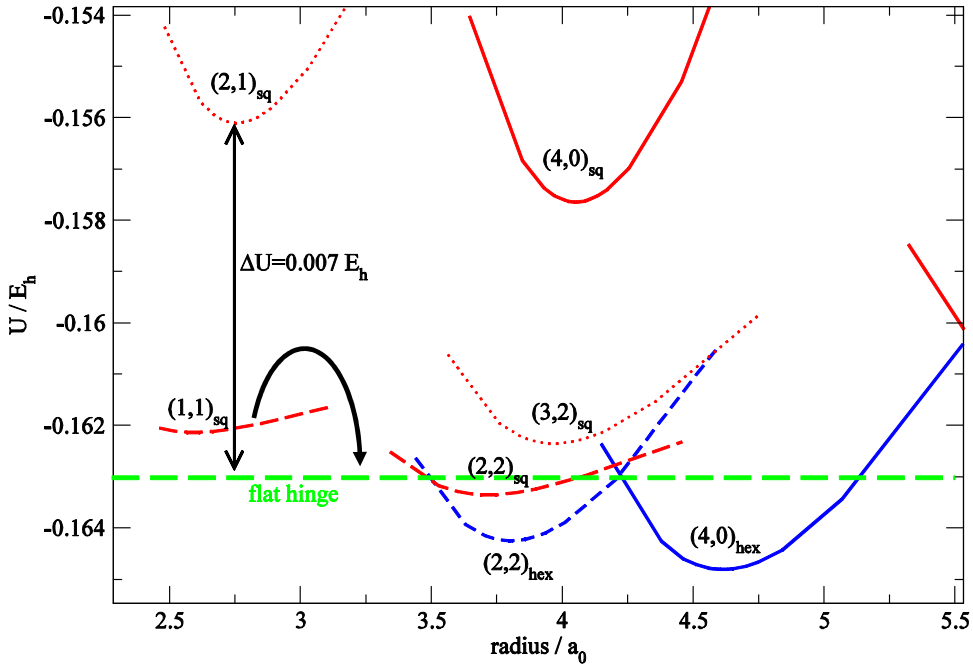

Figure 5.15: The energy landscape of potential I in the area of interest (5 a_0). The green dashed line corresponds to the energy of the flat hinge shape and is a guide only since a parabola cannot be defined for this structure which has infinite conformers (the hinge angle can theoretically take any value). The hinge structure is the observed final structure for this ionic system in the (15,0) carbon nanotube.

tube filling proceeded via a "ladder-like structure" or using our nomenclature the $(1,1)_{sq}$ INT. We recall this structure was also observed as both intermediate and final

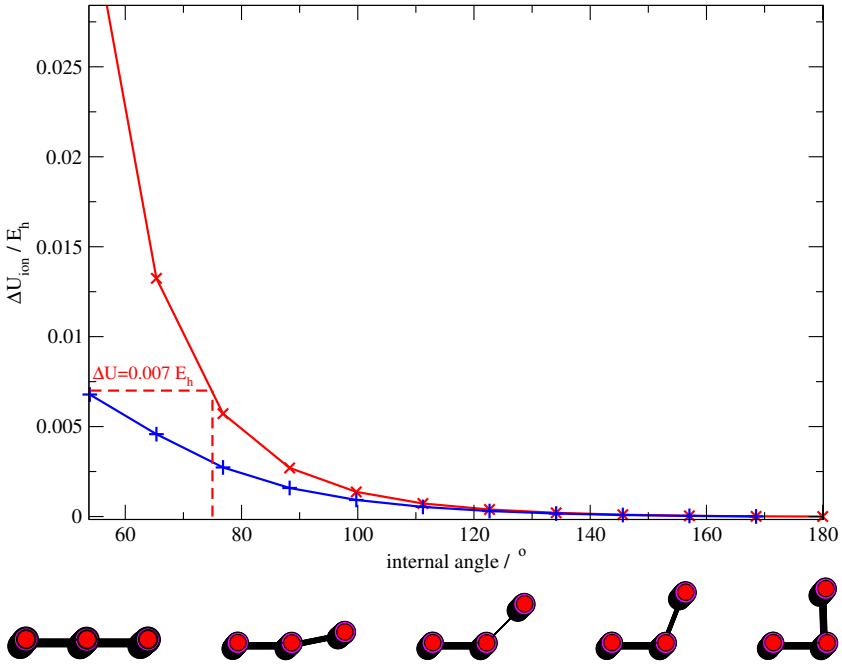

Figure 5.16: Top: How the energy of the "hinge" structure increases above that of the planar structure (180°) as it bends and the internal angle decreases. The red line shows the total energy per ion of the structure and the blue line shows only the coulombic contributions to the energy. The highlighted point shows that for a structure $0.007E_h$ over the planar structure energy (the point at which the $(2,1)_{sq}$ INT becomes more favourable) an internal angle of 75° is required. Below: Snapshots from the single point energy calculations. Left to right depicts internal angles of 180°, 157°, 135°, 111° and 88°.

structures in the (15,0) carbon nanotube. It is noted that this structure consists of two alternating chains of cations and anions. The next plateau (and the final structure for potential I) consists of a square net structure of three alternating ion chains. This "hinge" shaped structure can be considered a sub-section of the square net sheet consisting of three rows of alternating ions (figure 5.14).

The energy of the flat conformer of the hinge structure can be included in the energy landscape (figure 5.15, shown as a green dashed line) and we see that this structure appears energetically favourable for radii less than 3.5 a_0. However, as indicated in figure 5.14, the observed structures of this type appear bent into a "v-shape" cross section (or "hinged" about the central ion chain). The formation of such a bent structure can readily be rationalised as an effect of the confining carbon nanotube as the cylindrical geometry of the carbon nanotube will be expected to favour internal structures with a more circular cross section.

The bending of the hinge structure about the central ion chain increases the potential energy since the distance between ions of like charge along the two outer chains is decreased. As a result, the stability of such "hinged" structures within the carbon nanotubes must represent a subtle balance between this repulsive energy and a favourable change in the carbon nanotube-INT interaction. To quantify this effect, figure 5.16 shows the energy associated with the bending mode. The single point energy calculation is performed with all the anion-cation separations fixed to $a = 4.25\ a_0$, (the lowest energy anion-cation separation from the infinite square sheet in figure 5.2). The bending energy is defined as the difference in energy between the planar structure (where the internal angle $\theta = 180°$) and the bent "hinged" structure (where the internal angle $\theta < 180°$). The total energy increase above the planar structure is shown in red in figure 5.16 and the coulombic interactions which are seen to dominate for internal angles greater than 100° are shown in blue.

This hinged subsection of the square net sheet cannot be considered to be a true tubular structure as it cannot be created by rolling the infinite sheet along a chiral vector. In fact, there are only two alternative nanotube structures consisting of three alternating chains of ions based on the INT_{sq} morphology which can be rationalised in this manner, the $(3,0)_{sq}$ and $(2,1)_{sq}$ INTs. It can be seen from the energy landscape in figure 5.15 that these alternative tubular $(3,0)_{sq}$ and $(2,1)_{sq}$ structures are energetically unfavourable in comparison to the planar "hinged" structure. We can further rationalise our observations on examination of figures 5.15 and 5.16. The energy difference between the planar "hinge" and $(2,1)_{sq}$ INT structures is of the order of 0.007 a_0. Thus in order for the $(2,1)_{sq}$ INT to be energetically stable over the "hinged" structure, the bending would have to exceed an internal angle

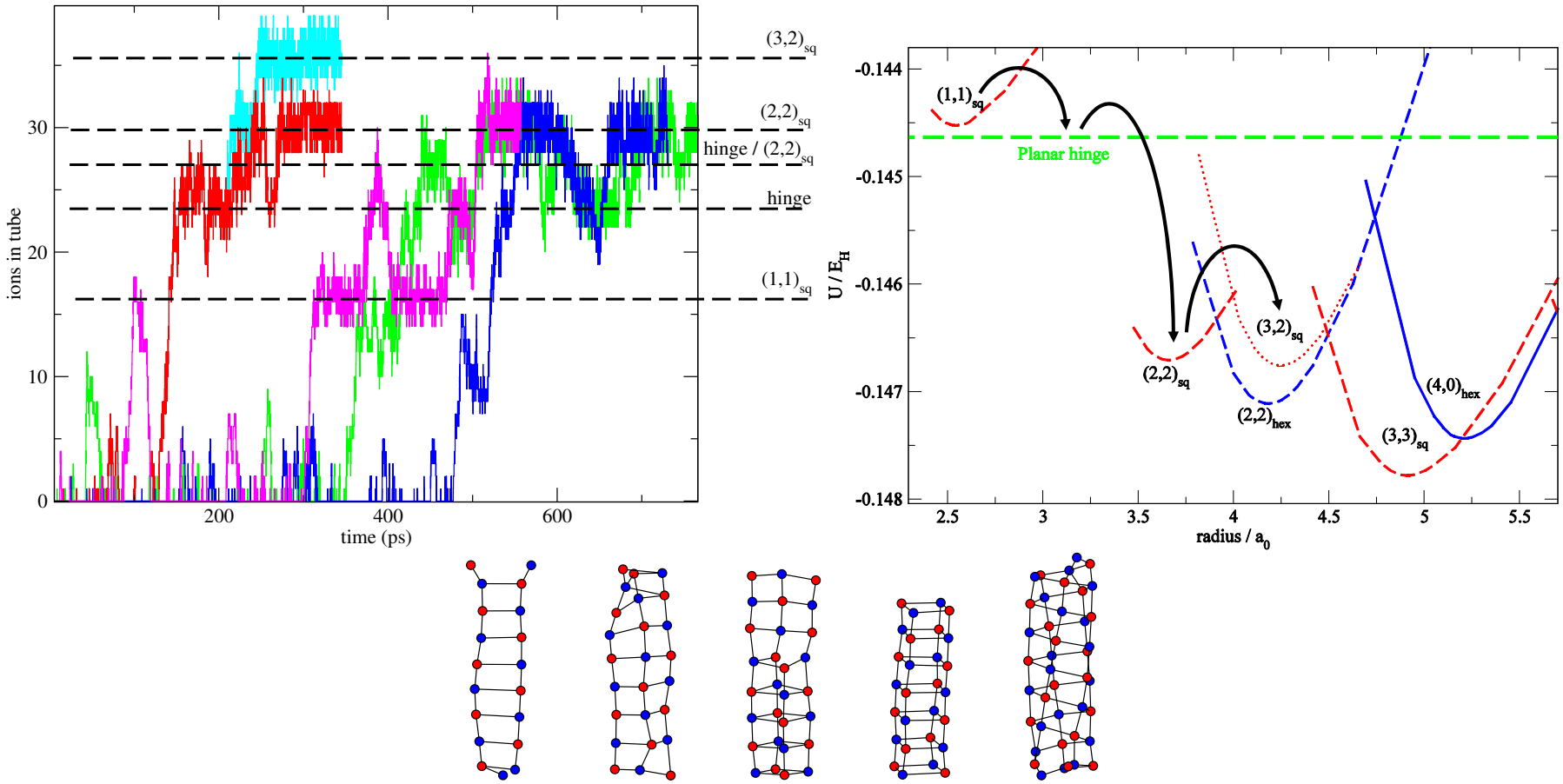

Figure 5.17: Top Left: Time evolution for the tube filling of the (9,9) carbon nanotube using potential II. Five filling simulations were analysed. The plateaus indicate the various square net intermediate structures. Right: The energy landscape of potential II in the area of interest (up to 5 a_0). The mechanism of filling proceeds by crossing the energy landscape from left to right. The final structures observed are the $(2,2)_{sq}$ INT in four out of five simulations and the $(3,2)_{sq}$ INT in one simulation. Bottom: Time averaged (section 4.7 structures of the various INTs that were observed to form during the filling process. Each structure corresponds to a different plateau in the time evolution of the filling simulations above. The filling appears to proceed via a "chain by chain" mechanism. From left to right: $(1,1)_{sq}$ INT, two chains. The bent hinge structure, three chains. The $(2,2)_{sq}$ INT/hinge intermediate structure, three/four chains. $(2,2)_{sq}$ INT, four chains. $(3,2)_{sq}$ INT, five chains.

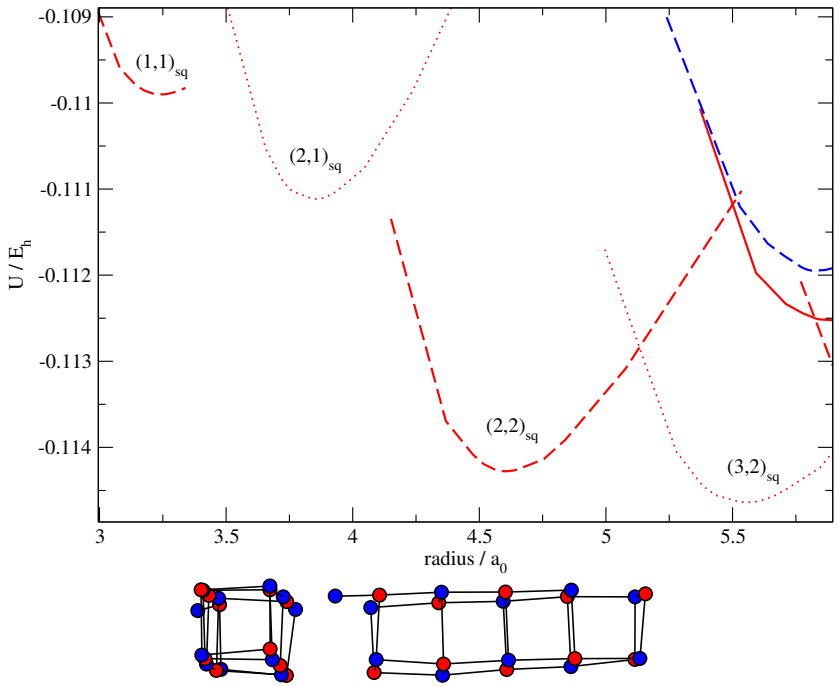

Figure 5.18: The energy landscape of potential III in the area of interest (5 a_0). The final structure observed is the the $(2,2)_{sq}$ INT as is to be expected from the energy landscape.

of 80° (as indicated in figure 5.15). The observed bond angle in the time-averaged structure in figure 5.16 is approximately 100°.

Finally, we note that the structure does not transform to either the $(2,2)_{sq}$ INT or any INT_{hex} on the timescale of the simulation. Such transformations might be expected as these INTS are the lower energy structures in the preferred region of the energy landscape (up to 5 a_o). There may be an activation barrier to this transition preventing its occurrence on the timescale of the simulation.

5.3.2 Potential II

For the (9,9) carbon nanotube filled using potential II, a similar "chain-by-chain" mechanism was observed (figure 5.17). In order to probe the reproducibility, five different filling simulations were performed for this system, using different starting liquid configurations. In four of the simulations the final time-averaged structure (section 4.7) was found to be the $(2,2)_{sq}$ INT which consists of four chains of alternating ions. In the other filling simulation this then transformed once again to give the denser $(3,2)_{sq}$ INT.

The mechanism of formation can be rationalised by reference to the filling profiles (figure 5.17). Firstly, the INT_{sq} or "ladder" consisting of two alternating chains of ions was the first structure observed as a plateau in the filling profile. The next

plateau in the filling profile corresponds to the "hinge" structure (figure 5.14) and consists of three chains of alternating ions. The carbon nanotube continues to fill and a plateau corresponding to the $(2,2)_{sq}$ INT is observed at longer times. This can be considered a structure of four alternating ion chains and is the final structure in four of the five filling events observed. In the other filling event (shown in cyan in figure 5.17), the inorganic structure further transformed to the even denser $(3,2)_{sq}$ INT which is a structure consisting of five alternating chains of ions.

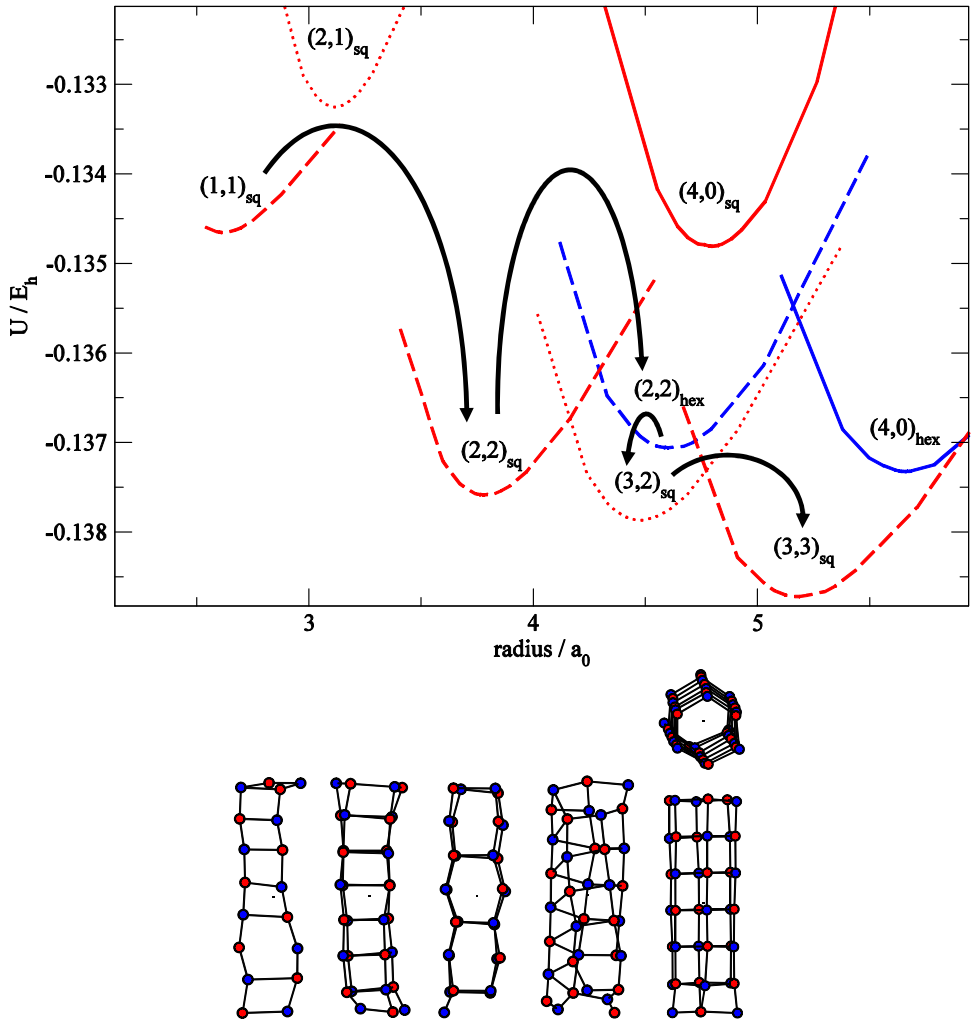

Figure 5.19: Top:The energy landscape of potential IV in the area of interest (5 a_0). Bottom: The various INTs that were observed to form during the filling process, from left to right, they are shown in order of appearance. Firstly, the $(1,1)_{sq}$, two chains. Secondly, the $(2,2)_{sq}$ structure, four chains. This transforms to the INT_{hex} morphology, the first example of such a transformation in the form of the $(2,2)_{hex}$. Penultimately, we have the lower energy, denser $(3,2)_{sq}$ formed of five chains. The final structure observed is the the $(3,3)_{sq}$ INT formed of six chains, as is to be expected since it is the lowest energy structure in the "preferred region" of the energy landscape.

In the filling simulation shown in green in figure 5.17, we see another clear plateau

between that of the $(2,2)_{sq}$ INT and the $(3,2)_{sq}$ INT structures. This is a truly intermediate structure in the sense that it occurs when half the carbon nanotube contains the hinge structure (three chains) and half contains the $(2,2)_{sq}$ INT (four chains). The molecular graphics snapshot of this intermediate structure is shown in figure 5.17.

The mechanism can be further understood on examination of the energy landscape, in the preferred region of up to 5 a_0 (figure 5.17). The structures formed correspond to "hops" from one energy minimum to another, travelling to larger radii across the landscape. The lowest energy structure at small radii is the $(1,1)_{sq}$ INT so it is the first INT to form during the filling process. As more ions enter the nanotube and the structure becomes denser, we are forced to higher radii INTs. The hinge structure, which forms next, lies somewhere between the $(1,1)_{sq}$ INT formed of two chains and the $(2,2)_{sq}$ INT formed of four chains in the energy landscape. The dashed green line indicates a possible location of the "hinge structure" on the energy landscape. However, as with potential I, the energy of this structure is sensitive to various contributing factors. As the internal angle of the "hinged structure" decreases the repulsion between ions of like charge increases. Additionally, the anion-cation separations (which are fixed to the infinite square net plane value of 4.70 a_0 in this calculation) can adjust to lower the energy by contacting along the anion-cation chains running parallel to the nanotube axis (see chapter 6). Finally, in one of the five simulations, there is a further push to higher radii, with a "hop" to the $(3,2)_{sq}$ INT.

These final two INTs are not the lowest energy INTs in the landscape, the $(2,2)_{hex}$ INT is actually lower in energy at equivalent radii (as can be seen in figure 5.17). This might be explained as one might expect a higher activation barrier between a transformation from a INT_{sq} to a INT_{hex} morphology. On the timescale of the simulation, such a transformation is not observed. In contrast, we will see the exact reverse transition does occur in the latter stages of the mechanism of potential IV filling the (9,9) carbon nanotube. Either, the reverse transition (determined for the $(2,2)_{hex}$ to the $(3,2)_{sq}$ INT) has a lower activation barrier in the reverse or the larger anion of that potential facilitates the transition in that system.

Once again, we find that chains of alternating ions are playing an important role in the INT energetics. This is both in regards to the INTs formed and the energy pathway of the filling mechanism which proceeds by the addition of an increasing number of chains of alternating ions.

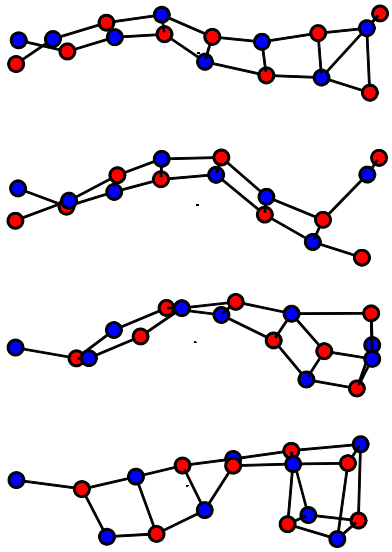

Figure 5.20: Evidence of the "folding mechanism" [113] is observed by monitoring the molecular graphics during the transformation from the $(1,1)_{sq}$ to the $(2,2)_{sq}$ INT. (See also figure 1.5). There is no evidence of the "hinge structure" forming during this transformation unlike potentials I and II where the "hinge" was observed. Top to Bottom: (a) The $(1,1)_{sq}$ INT formed of two alternating chains. (b) The folding mechanism commences at the right hand side of the INT structure by the concerted movement of an ion pair. (c) The folding mechanism continues as one cation interacts with an anion at the entrance of the carbon nanotube pore. (d) The formation of a section of the $(2,2)_{sq}$ is observed at the entrance of the carbon nanotube.

5.3.3 Potential III

The filling mechanism of potential III is rapid and no intermediate structures, not even the $(1,1)_{sq}$ INT, are observed during the filling process. The final structure is the $(2,2)_{sq}$ INT formed of four chains which is the expected low energy structure in the "preferred region" of the energy landscape (shown in figure 5.18). The landscape of this potential appears not as rich as the other potentials at these small radii, with fewer available INTs to "hop" between as it travels across the landscape, which may explain the lack of intermediate INTs being observed in this system.

5.3.4 Potential IV

The landscape of potential IV is much richer than that of potential III (see figure 5.19) with plenty of low energy small radii INTs present up to and in the "preferred region" (up to 5 a_0). The mechanism of filling appears to follow the "chain by chain" mechanism that was observed for both potentials I and II. Again, we can clearly see that the inorganic structure is crossing the energy landscape from left to right, "hopping" from one energy minima to another, approaching increasingly large radii. Firstly, the $(1,1)_{sq}$ INT consisting of two ion chains, is observed to form within the nanotube pore. Unlike potential I and II the hinge 3 chain structure is not the next observed INT. In contrast to those ionic systems there is evidence from viewing molecular graphics snapshots (figure 5.20) of the "folding mechanism" that has been observed in previous work with rigid nanotubes [113] (see also figure 1.5). This results in a direct transformation from the $(1,1)_{sq}$ INT formed of two chains to the $(2,2)_{sq}$ INT which is formed of four chains of alternating ions. Unlike, potential I and II, this then undergoes a transformation to the $(2,2)_{hex}$ INT, which is slightly more dense than the $(2,2)_{sq}$ INT. This is the first example of a transition between the INT_{sq} and INT_{hex} morphologies. The transition involves only a lengthening of alternate bonds running perpendicular to the nanotube axis. In this way, the higher energy $(2,2)_{hex}$ INT has provided an accessible pathway to the lower energy $(3,2)_{sq}$ INT which is of a similar radius (see the close proximity of the parabolas in figure 5.19). (We recall that the reverse $(3,2)_{sq}$ to $(2,2)_{hex}$ INT transition was not observed using potential II.) After this transition, the structure increases in density by forming the lower energy $(3,2)_{sq}$ INT formed of five alternating chains of ions which is of similar diameter to the $(2,2)_{hex}$ INT. Finally, the structure forms the six chain $(3,3)_{sq}$ INT which is the lowest energy INT in the "preferred region" of the energy landscape.

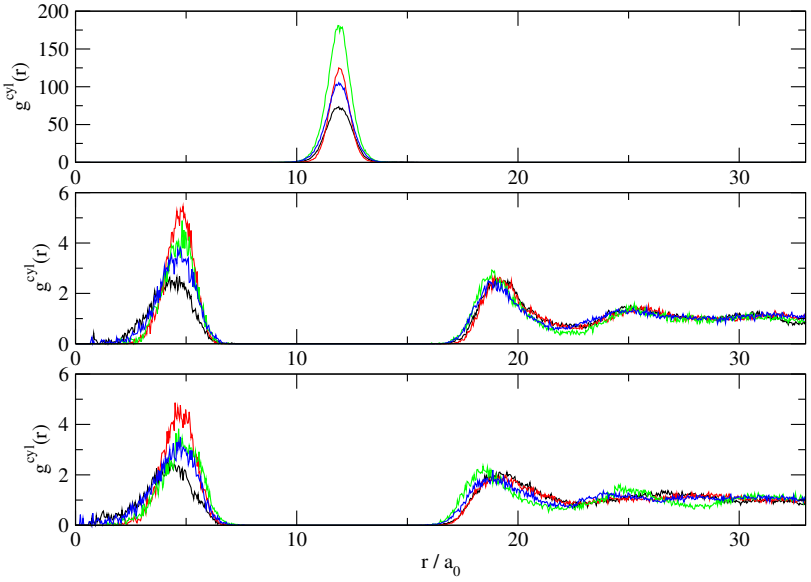

Figure 5.21: The cylindrical radial distribution functions $g^{cyl}(r)$ for the (9,9) carbon nanotube using potential I (black), potential II (red), potential III (green) and potential IV (blue). The top panel shows the distribution for the carbon atoms, the centre and bottom panels show the distributions for the cations and anions respectively.Potential I shows an INT with a smaller radii than that of the other potentials. This is explained as it is of the "hinge" morphology for which the cross sectional size varies over time due to fluctuations in the internal angle θ. The mean distance between the ions and the carbon nanotube is 7.2 a_0.

5.3.5 General Observations

Figure 5.21 shows the cylindrical radial distribution function (see section 4.8) for all four potentials calculated during the time of the final filling plateau. The mean distance between the final INTs and the enclosing carbon nanotube can be determined by subtracting the position of the lower peak in the anion/cation function (which corresponds to the ions forming the internal INT structure) from the position of the carbon peak. For potentials II-IV the INTs all have comparable radii of 4.7 a_0, therefore the distance between the INTs and the carbon nanotube is 7.2 a_0. For potential I the mean distance between the carbon nanotube and the INT is slightly larger at 7.6 a_0. This is because the INT did not transform to a larger radius structure on the timescale of the simulation.

The observed mean distances for all potential models are larger than calculations predicted (6.84 a_0 for the flat infinite sheets in section 4.4). However, in that calculation the change in curvature on deforming a graphene sheet to give the carbon nanotube was neglected. The curvature of the sheets increases the repulsion between a given ion and the non-nearest carbon atoms in the nanotube giving rise to

longer ion sheet-graphene sheet separations. The presence of the molten ionic liquid around the nanotube will also contribute to the preferred INT-nanotube distance. The separation is decreased due to the long range attraction between the INT and the molten salts counteracting the curvature effect. Overall, the curvature effect appears to dominate since the separation is greater than that calculated for the flat infinite sheets without the presence of molten liquid.

5.4 The (22,0) carbon nanotube

The (22,0) carbon nanotube was successfully filled using all four potential models. The average radius of the carbon nanotube is 16.8 a_0 which suggests that an inorganic nanotube of radius of the order of 10 a_0 may be formed.

5.4.1 Potential I

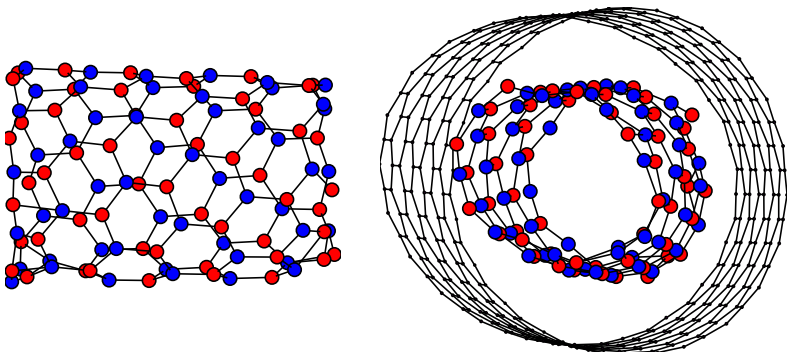

Figure 5.22: Two views of the (22,0) carbon nanotube filled with the potential I ionic salt. The average structure of the inorganic nanotube formed is the $(8,0)_{hex}$ INT.

We can see from figure 5.6 that a radius of the order of 10 a_0 lies in the regime where the hexagon net nanotubes are significantly lower in energy than the square net analogues for potential I. We can now be considered to be in the "large radius" regime for the filling process. It is found that the nanotube fills with a $(8,0)_{hex}$ INT (figure 5.22) whose energy minimum lies at a radius of 8.75 a_0 on the energy landscape.

In this larger carbon nanotube radius regime the filling mechanism appears to differ from the smaller (15,0) and (9,9) carbon nanotubes in which the structure evolved in a manner that could be considered as "hopping" across the energy landscape to INTs having increasingly large radii and lower energy. However, the mechanism again appears to depend on the formation of chains of ions forming along

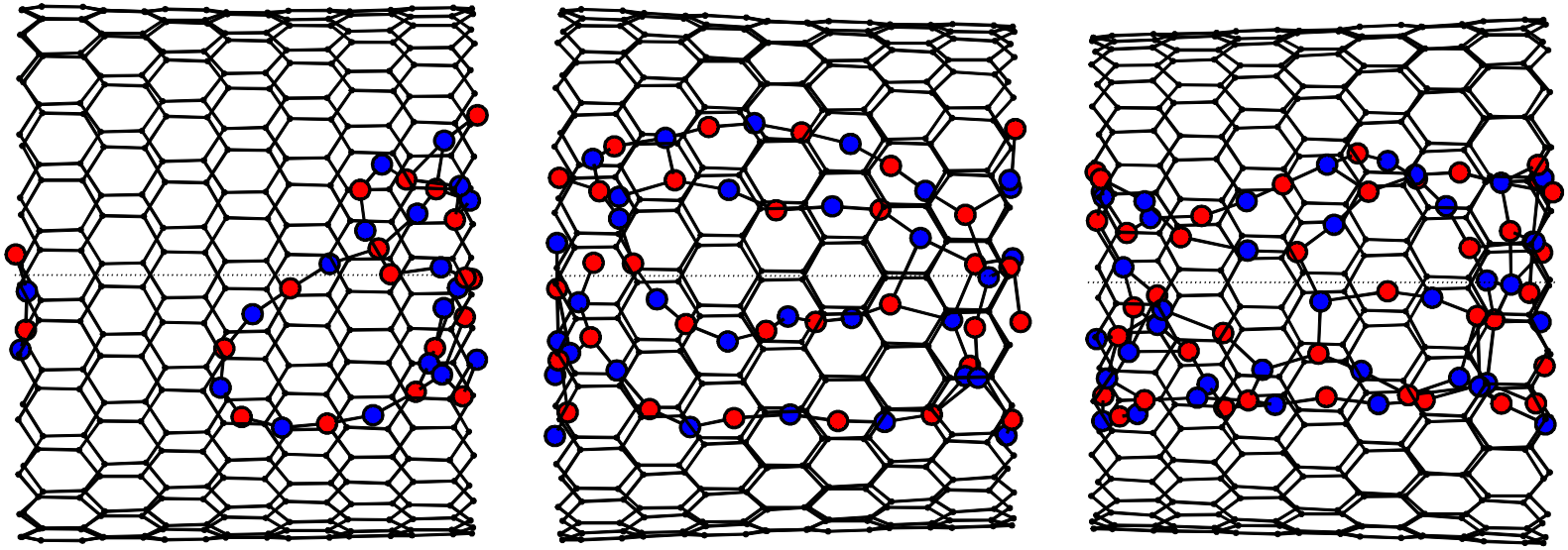

Figure 5.23: The mechanism of filling for the formation of the $(8,0)_{hex}$ INT inside the (22,0) carbon nanotube using potential I. Left: Firstly, an exploratory loop of alternating ions enters the carbon nanotube. Centre: Chains of alternating ions are observed to form down the length of the pore. Right: Interactions between adjoining chains form to give local environments consisting of hexagon loops.

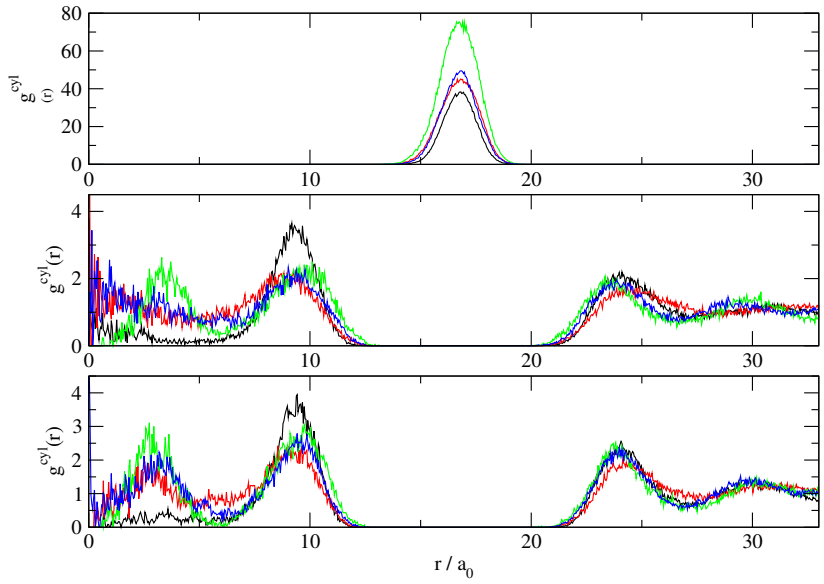

Figure 5.24: The cylindrical radial distribution functions $g^{cyl}(r)$ for the (22,0) carbon nanotube using potential I (black) , potential II (red), potential III (green) and potential IV (blue). The top panel shows the distribution for the carbon atoms, the centre and bottom panels show the distributions for the cation and anions respectively. Potentials II, III and IV show INTs that consist of two distinct cylindrical structures or "double-walled" INTs. The average distance between the ions and the nanotube is 7.4 a_0.

the nanotube pore. This is consistent with the chain theory that is developed in chapter 6. The rate of filling for potential I allows us to analyse the filling mechanism as it proceeds. Figure 5.23 shows time-averaged structures (section 4.7) from various points in the filling process of the (22,0) carbon nanotube. We find the the filling commences with a single "exploratory chain" of alternating ions that forms an increasingly large ion loop that travels down the carbon nanotube pore. This is analogous to the $(1,1)_{sq}$ exploratory ladder structure that was observed in the small radii carbon nanotubes. The filling proceeds via the formation of an increasing number of chains that lie parallel to the carbon nanotube axis (see the centre structure in figure 5.23). Connections between adjoining chains begin to form as the number of ions inside the nanotube increases (see the final structure in figure 5.23). Finally, the connections between the ion chains mean that local environments consisting of loops containing six ions or "hexagons" develop and the lowest energy INT structure in the "preferred region" of the energy landscape, the $(8,0)_{hex}$ INT is formed.

5.4.2 Potential II

The (22,0) carbon nanotube was also successfully filled with an inorganic structure using potential II. However, the final INT is highly defective and cannot be characterised by the folding of a pure tessellating hexagon or pure square net sheet.

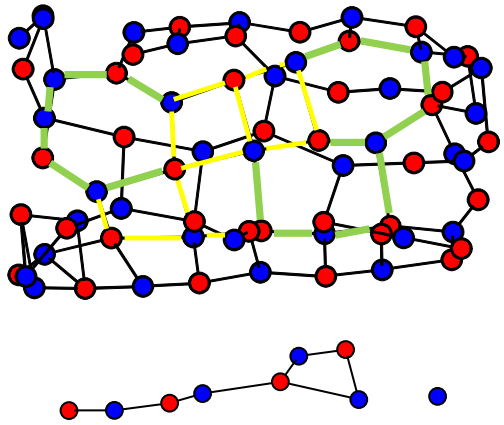

Figure 5.25: Top: The outer INT formed inside the (22,0) carbon nanotube using potential II. Both three coordinate environments (highlighted green) and two coordinate environments (highlighted yellow) are visible. This is due to the parametrisation of this potential which means that both tetrahedral and octahedral crystal systems are equally favoured in the bulk. Bottom: The inner INT formed inside the (22,0) carbon nanotube using potential II. It consists of a defective single chain of alternating ions.

The energy landscape (figure 5.6) would suggest that the lowest energy structure is an INT based on the folding of a hexagon sheet. However, the cylindrical distribution function indicates that the final structure is a double walled nanotube (figure 5.24). A double-walled INT (DWINT) consists of two distinct shell structures as can be seen clearly in figure 5.24. As a result it is useful to attempt to break down the total internal structure into the structures of the two distinct shells. The time-averaged structure (section 4.7) can be seen in figure 5.25 for both the inner and outer structures, in the latter there are clearly both four and three coordinate ions present. The square nets and hexagons are highlighted in yellow and green respectively in this figure. The defective structure might be explained due to the small energy difference between the hexagon and square net nanotubes for this potential. We recall that that the parameters for potential II were chosen to make the four and six coordinate structures equally favourable in the bulk. The INT$_{sq}$s and INT$_{hex}$s are very close in energy in the energy landscape for potential II (figure 5.6). Since the perfect structures are quantised to give certain radii INTs only, it is conceivable that an INT formed of both hexagons and squares are favourable at

some radii. In addition, since the energies of the INT_{hex}s and INT_{sq}s are so close, at this temperature we would expect to see a significant amount of both morphologies if a Boltzmann distribution is adhered to. The internal structure of the DWINT is a simple chain of alternating ions. The formation of chains of alternating ions is energetically favourable, as we will see in chapter 6.

5.4.3 Potential III

Potential III was also found to fill with ions when a pressure was applied to the system ($P = 0.00002\ a_0$, 0.58 GPa). Again, a double-walled INT was found to

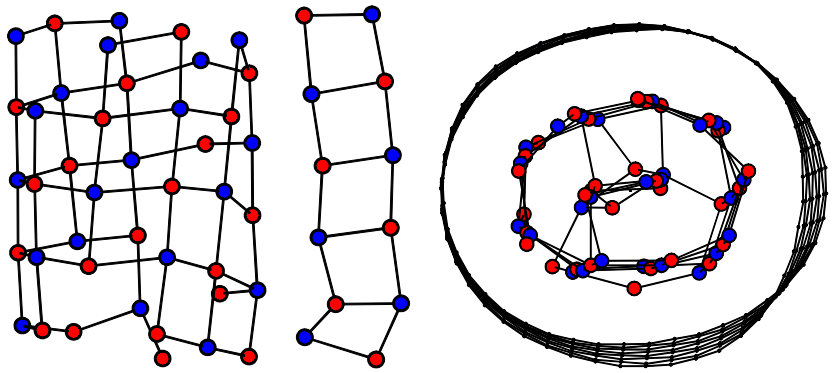

Figure 5.26: Left: The outer structure formed inside the (22,0) carbon nanotube using potential III based on the folding of an infinite square net sheet. The morphology of this structure is the $(5,4)_{sq}$ INT consisting of nine chains of alternating ions. Centre: The internal INT structure is the $(1,1)_{sq}$ INT or a "ladder" like structure. This is formed of an additional two alternating chains of ions. Right: The complete time averaged structure for the (22,0) carbon nanotube (section 4.7). The carbon nanotube is filled with a double-walled INT. Both structures are based on chains of alternating anions and cations. There appears to be significant elliptical deformation in the carbon nanotube and the outer INT_{sq}.

form and both the inner and outer structures were of the INT_{sq} morphology (see figure 5.26). The internal INT_{sq} consists of the $(1,1)_{sq}$ INT or the "ladder" structure which has been observed in isolation in some of the smaller carbon nanotubes. The external INT_{sq} is formed in the $(5,4)_{sq}$ INT morphology which consists of nine chains of alternating ions. These alternating chains twist around the nanotube axis but have a much larger component that runs parallel to the nanotube axis and only a small component that runs to perpendicular to it.

The time-averaged structure shown in figure 5.26 shows evidence of a significant elliptical deformation being present in the carbon nanotube itself. We note that such a deformation would be impossible to observe without the inclusion of the carbon nanotube flexibility introduced in our model. This deformation is different to the

instantaneous elliptical defect noted to appear at random during the filling events (figure 4.18, section 4.9). This is because it is not a short-lived deformation and it remains as a feature in the final structure. We note that the internal structure $(1,1)_{sq}$ INT is an anisotropic structure which may be the cause of the anisotropy in the templating carbon nanotube itself. Pressure was applied in this filling simulation to instigate the filling event and this may exacerbate the anisotropic elliptical deformation.

5.4.4 Potential IV

The ionic salt described by potential IV was also observed to fill the (22,0) carbon nanotube with the application of a small amount of pressure (0.00002 atomic units, 0.58 GPa). The resulting final structure appears highly defective, consisting of

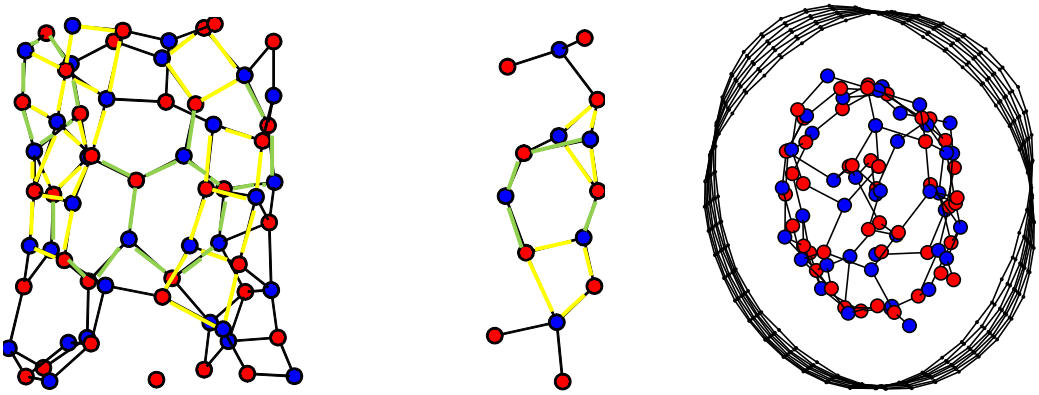

Figure 5.27: The time averaged structure (section 4.7) of the filled (22,0) carbon nanotube using potential IV. Left: The outer cylindrical INT structure is highly defective and consists of both three and four coordinate ions. Centre: The internal cylindrical INT structure consists of both three and four coordinate ions in a chain structure. Right: The entire structure viewed from the end. An elliptical deformation is observed in the time-averaged structure of the external INT and the carbon nanotube itself.

both three and four coordinate ions within the inner and outer INTs of the double walled structure (figure 5.27). The mixture of three and four coordinate ions is a product of the close energy of the hexagons and square net sheets is this potential model, which only slightly favours the square nets at this radius. Once again, an elliptical deformation is observed in the time-averaged structure (section 4.7). As with potential III, both the anisotropy of the double-walled INT in its cross section and the applied pressure to the system are possible origins of this deformation.

5.4.5 General Observations

Once again, the INT-nanotube separation is comparable for all four potential models. This is expected since the same ion-carbon potential Lennard-Jones potential is used for all four systems. The average separation in figure 5.24 is 7.4 a_0 which is greater than the ideal separation predicted for the flat infinite sheets (6.84 a_0). As with the smaller radii INTs this difference may be attributed to the combined yet opposite effects of the curvature and the presence of the molten ions outside the nanotube. The curvature of the (22,0) carbon nanotube is less than the smaller (15,0) and (9,9) carbon nanotubes and so the effects of curvature may have diminished some what. However, with the larger (22,0) carbon nanotube we have the additional effect of the presence of the internal structures in the DWINTs which will also interact with the outer inorganic structures. Clearly the separation depends on a subtle balance of all these various contributing factors.

5.5 The (13,13) carbon nanotube

5.5.1 Potential I

Potential I fills the (13,13) carbon nanotube of diameter 34.3 a_0 (which is slightly larger but of comparable size to the (22,0) carbon nanotube which has a diameter of 33.5 a_0). The final structure is a double-walled INT, with the external wall being of the $(8,2)_{hex}$ morphology (figure 5.29). The structure of the outer INT is consistent with the lowest energy INTs in the energy landscape (figure 5.6) at this radius. The internal INT is a chain of alternating ions, the importance of which is discussed in chapter 6. The isotropic nature of this double-walled INT means that no elliptical distortion is observed in the final time-averaged structure.

The mechanism for filling the (13,13) carbon nanotube has been analysed by viewing time-averaged structures obtained during the process of filling. Example, "snapshots" are shown in figure 5.28. The mechanism of INT formation appears similar to that observed for the (22,0) carbon nanotube (which is of comparable diameter) using potential I. Firstly, exploratory loops of alternating ions enter the nanotube and start the filling event. These form largely non-interacting chains of alternating ions that run down the central pore. Finally connections between adjoining chains begin to form, creating loops of alternating ions, often consisting of six or eight ions. Previously, during filling simulations of rigid nanotubes, formation of octagon and squares have been observed at low ion densities at the early stages of the filling process [112]. The formation of octagon-square net motif is observed

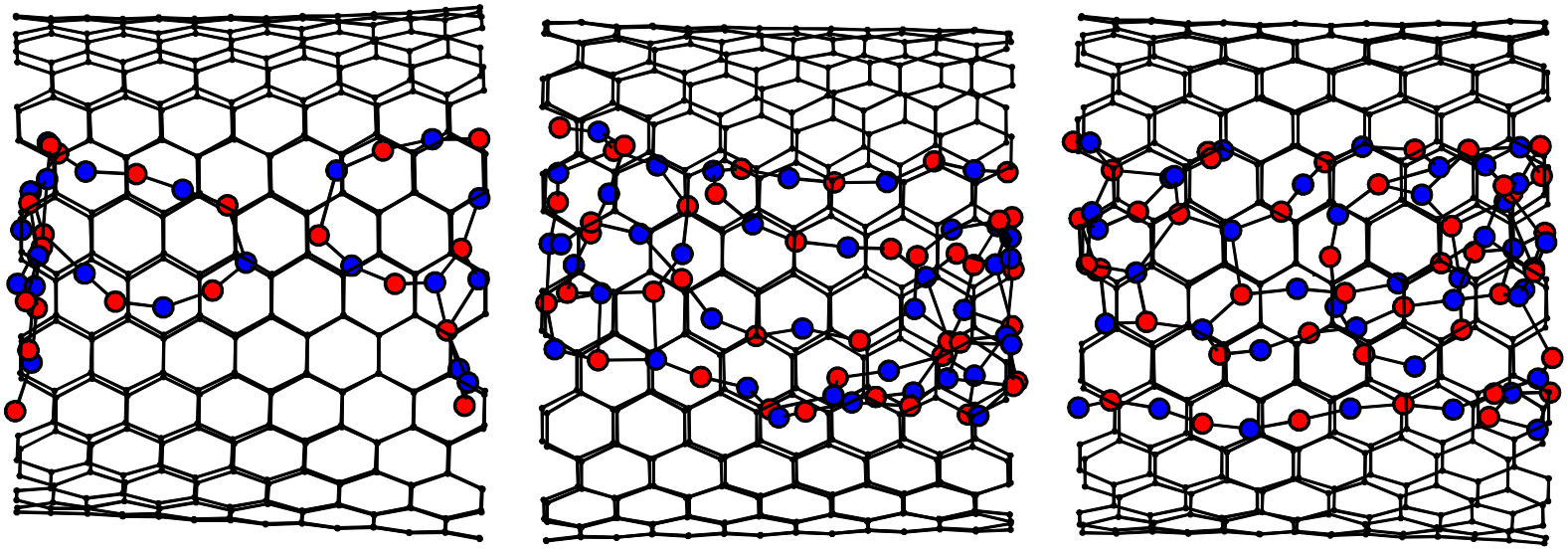

Figure 5.28: Various time averaged structures (section 4.7) from the filling of the (13,13) carbon nanotube with potential I. The mechanism of filling is similar to that of the (22,0) carbon nanotube using potential I also. The (22,0) carbon nanotube is of a similar size pore and had a comparable filling rate. Left: Exploratory loops enter the nanotube and consist of chains of alternating ions. Centre: Chains of alternating ions form down the length of the nanotube. A new exploratory loop can be seen entering the nanotube. Right: Connections begin to form between adjoining chains. These cause looped environments consisting of hexagons and octagons to be formed. Eventually, all the connections will take the form of three coordinate environments in the form of hexagons to form the $(8,2)_{hex}$ INT.

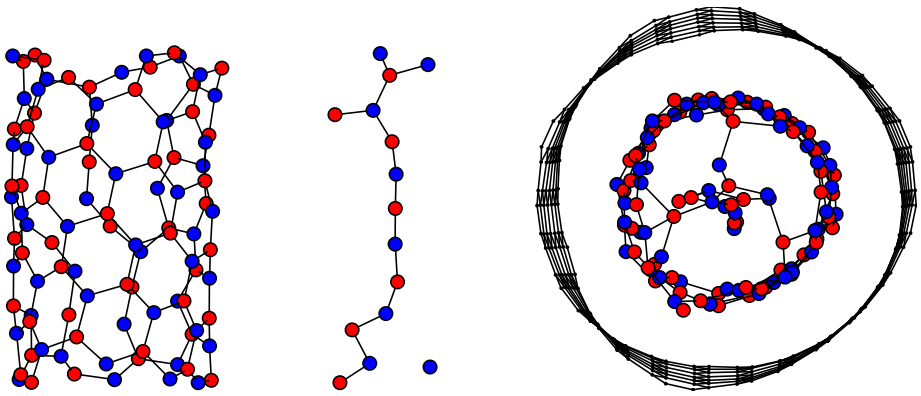

Figure 5.29: The structure formed inside the (13,13) carbon nanotube using potential I. Left: The outer INT is of the $(8,2)_{hex}$ INT morphology. The ionic system described by potential I predicts low energy structures of the INT_{hex} morphology. Centre: The internal structure is a chain of alternating ions, the importance of which is discussed in chapter 6. Right: The entire time-averaged structure (section 4.7) consists of a double-walled INT. There is no elliptical deformation as the cross section of this structure is isotropic.

in this work during the filling stage in which the alternating ion chains of connect together. The mechanism in which the octagon-square nets transform to tessellating hexagons is described by Wilson [112]. Eventually, all the ions participate in "six ion loops" (hexagons), so that they all reside in the energetically favourable three coordinate environments of the INT_{hex}.

5.5.2 Potential II

The ionic system described by potential II also filled the carbon nanotube but, as with the similar sized (22,0) carbon nanotube, the result is highly defective (see figure 5.30). The final INT is double-walled with both the inner and outer structures consisting of a mixture of hexagons and squares. We recall that this potential equally favours the tetrahedral and octahedral environments in the bulk due to the anion-cation radius ratio controlled through the potential parameters. As a result, the INT_{hex}s and the INT_{sq}s lie very close in energy producing defective structures such as this. There is an elliptical deformation in the time-averaged structure due to the anisotropic cross section of the INT. This simulation was performed at zero pressure and so the deformation is not a result of applied pressure.

5.5.3 Potential III

Potential III filled the (13,13) carbon nanotube with the application of pressure ($P = 0.00002\ a_0$, 0.58 GPa). As we would expect from the energy landscape (figure

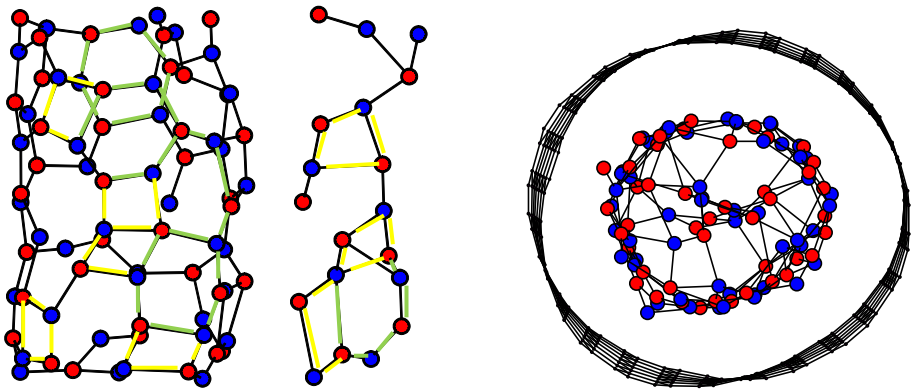

Figure 5.30: The structure formed inside the (13,13) carbon nanotube using potential II. Left: The outer INT is highly defective with both three coordinate (green) and four coordinate (yellow) environments. Centre: The internal structure is also highly defective. Right: The entire time-averaged structure (section 4.7) consists of a double-walled INT. There is an elliptical deformation in the cross section since this structure is anisotropic.

5.7) the INT formed is of the INT_{sq} morphology. The structure is a double-walled with the outer structure consisting of the $(6,2)_{sq}$ INT formed of eight chains of alternating ions. The internal structure consists of the $(1,1)_{sq}$ INT or "ladder" structure formed of two alternating chains of ions. Both the inner and outer structure are shown in figure 5.31. An elliptical deformation is again observed due to the anisotropic cross section of the double-walled structure.

5.5.4 Potential IV

Potential IV also showed successful filling with the same application of pressure as potential III. The formation of a defective double-walled INT_{sq} with several hexagon defects in the external INT was observed (figure 5.32). Although this potential model predicts INT_{sq} as the favoured morphology (figure 5.7), the INT_{hex}s lie only slightly higher in energy at this radius, which is the origin of the hexagon defects in this structure. Again, an elliptical deformation is observed in the INT and the carbon nanotube itself due to the anisotropic cross section of the INT.

5.5.5 General Observations

Figure 5.33 shows the cylindrical radial distribution function $g^{cyl}(r)$ for all four potentials. In each case the INT-nanotube separation averages at 7.7 a_0, which is slightly larger than for the (9,9) and (22,0) carbon nanotubes. With less curvature, the INT-nanotube separation might be expected to approach the ideal separation of 6.84 a_0 of the flat infinite sheets calculated in section 4.4. The differing behaviour

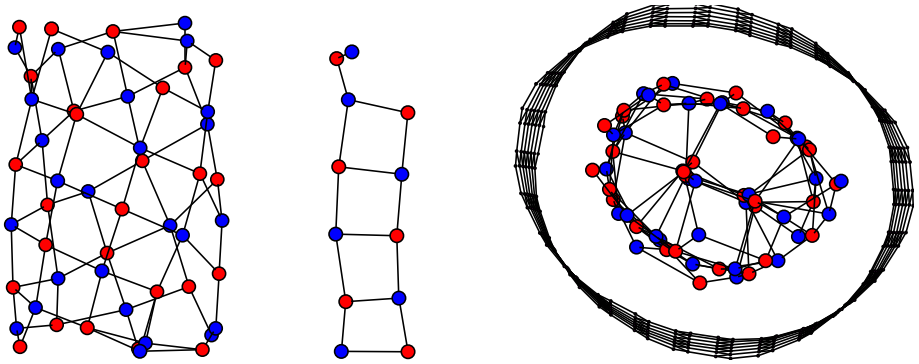

Figure 5.31: The structure formed inside the (13,13) carbon nanotube using potential III. Left: The outer INT is of the $(6,2)_{sq}$ INT morphology, which consists of eight chains of alternating ions. The ionic system described by potential III predicts low energy structures of the INT_{sq} morphology. Centre: The internal structure is the $(1,1)_{sq}$ INT. Right: The entire time-averaged structure (section 4.7) consists of a double-walled INT. There is an elliptical defect due to the anisotropic cross section of this structure. The applied pressure may exacerbate this deformation further.

of the four potentials is evident from the cylindrical distributions. The first peak in $g^{cyl}(r)$ corresponds to the internal INT and differs for all four systems due to the differing ideal cation-anion separations of each of the potentials.

5.6 The (25,0) carbon nanotube

The diameter of the (25,0) carbon nanotube (38.1 a_0) is significantly larger than that of the (22,0) and (13,13) carbon nanotubes. All, four potential models filled with double-walled INTs. At this larger radius, the morphology of all of the external INTs was determined simply by the radius ratio of the ionic system modelled. However, the internal INTs are in the small radius INT regime and so INTs containing chains of ions are dominant (see chapter 6).

5.6.1 Potential I

Potential I filled the (25,0) carbon nanotube with a double-walled INT consisting of an INT_{hex} in the external structure and a chain of three alternating ions forming the internal INT (see figure 5.35). The internal structure consists of chains of alternating ions, which in the small radii regime is the dominant structure for all potential models (see chapter 6). The external structure of the INT is generally based on the folding of an infinite hexagon sheet into a cylinder which is expected from this potential since the tetrahedral environment dominates in the bulk. However, the structure is highly defective with only a portion of the structure that consists

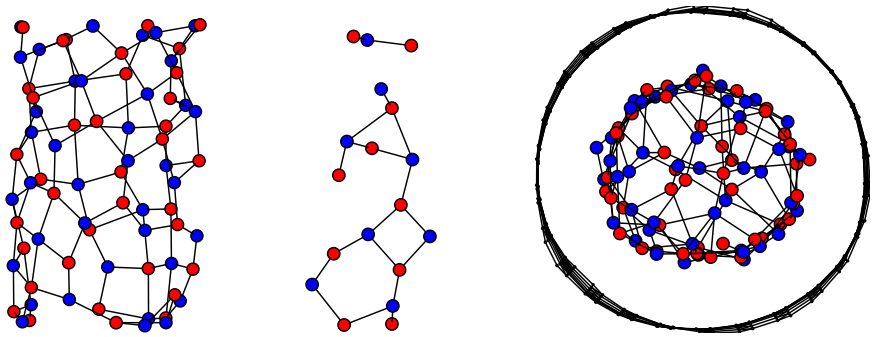

Figure 5.32: The structure formed inside the (13,13) carbon nanotube using potential IV. Left: The outer INT is highly defective but is most closely related to the INT_{sq} morphology. However, the structure contains several hexagon defects. The ionic system described by potential IV predicts low energy structures of the INT_{sq} morphology but the INT_{hex} lay only slightly higher in energy. Centre: The internal structure is defective. Right: The entire time-averaged structure (section 4.7) consists of a double-walled INT. There is an elliptical defect due to the anisotropic cross section of this structure. The applied pressure may exacerbate this deformation further.

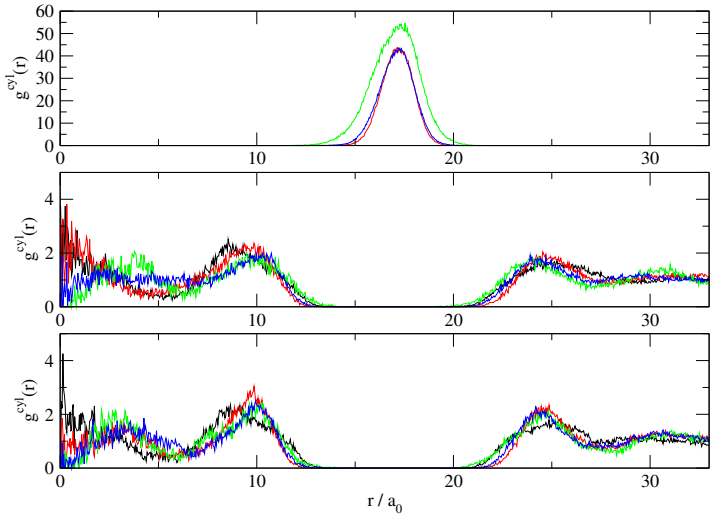

Figure 5.33: The cylindrical radial distribution functions $g^{cyl}(r)$ for the (13,13) carbon nanotube using potential I (black), potential II (red), potential III (green) and potential IV (blue). The top panel shows the distribution for the carbon atoms, the centre and bottom panels show the distributions for the cation and anions respectively. All potentials show an average INT-nanotube distance of 7.7 a_0 with the external INT in each case lying at 9.7 a_0, the same Lennard-Jones ion-carbon potential is used for all systems. The INT-INT distance varies for each potential due to the different ion-ion potentials used for each system.

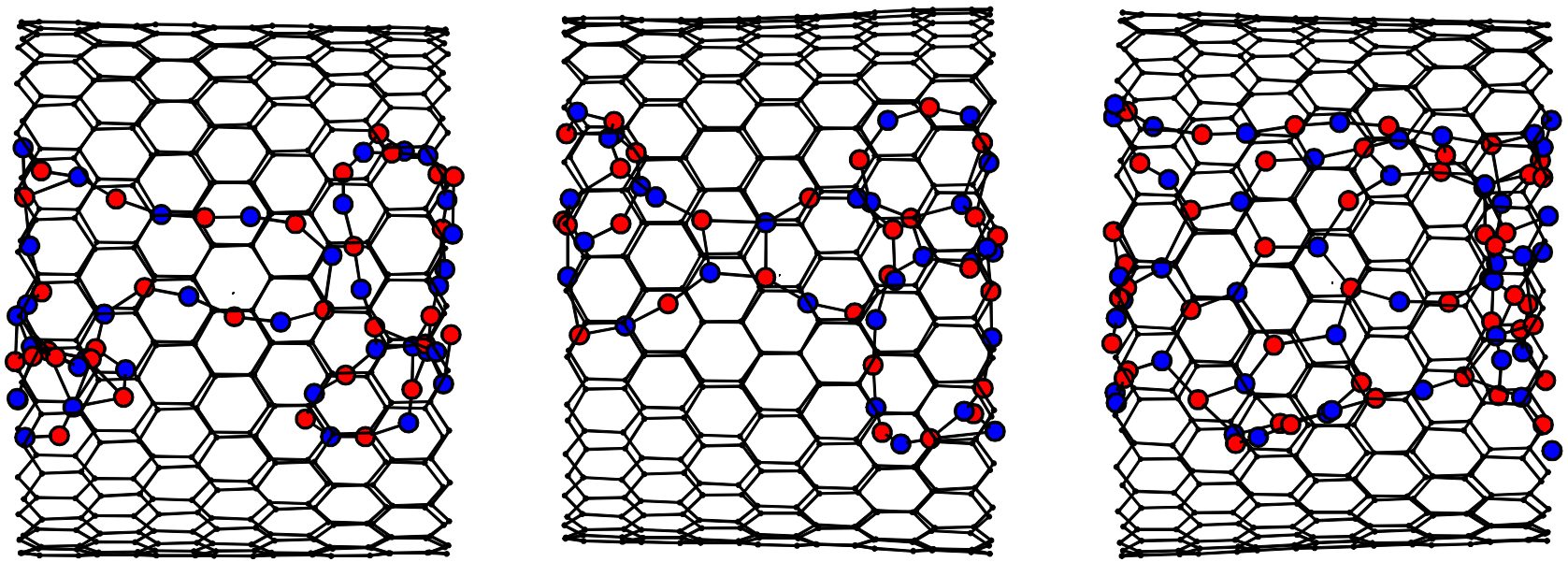

Figure 5.34: The mechanism of filling the (25,0) carbon nanotube using potential I. Left: Exploratory loops of alternating ions enter the nanotube. Centre: Two chains of alternating ions run along the length of the nanotube. Two further exploratory loops enter the pore. Right: Connections form between adjoining chains, which forms loops of ions. We can see the formation of several loops of six ions or hexagons in this figure. Formation of larger loops results in defects in the final structure (figure 5.35).

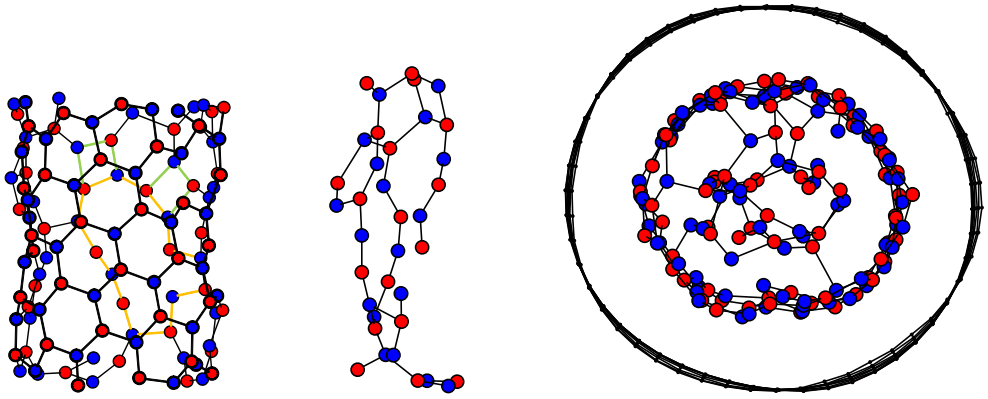

Figure 5.35: The double-walled structure formed inside the (25,0) carbon nanotube using potential I. Left: The external wall of the INT is of the INT_{hex} morphology but some square defects (highlighted in green) and larger loop defects are present (highlighted in orange). Centre: The internal structure is defective but consists of three chains of alternating ions. Right: The entire time-averaged (section 4.7) which consists of a double-walled INT. The structure is isotopic in the cross section and so no elliptical deformation is observed.

purely of percolating hexagons corresponding to a section of the $(8,5)_{hex}$ INT. The remainder of the structure consists of many defects which take the form of large loops of alternating ions (for example, the loop highlighted in orange in figure 5.35) and smaller square net defects (highlighted in green). Such defects provide evidence that the structure is unable to reach its equilibrium INT_{hex} structure on the timescale of the simulation.

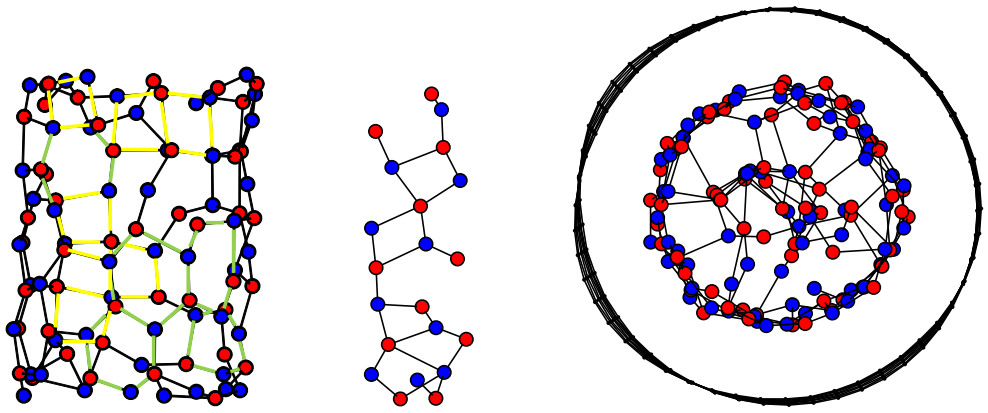

Figure 5.36: The double-walled structure formed inside the (25,0) carbon nanotube using potential II. Left: The external wall of the INT is highly defective and formed both of hexagons (green) and squares (yellow). Centre: The internal structure is formed of square nets but is defective. This is consistent with the small radius INT regime for all potentials. Right: The entire time-averaged (section 4.7) which consists of a double-walled INT.

The analysis of the mechanism (figure 5.34) gives us further insight to the source

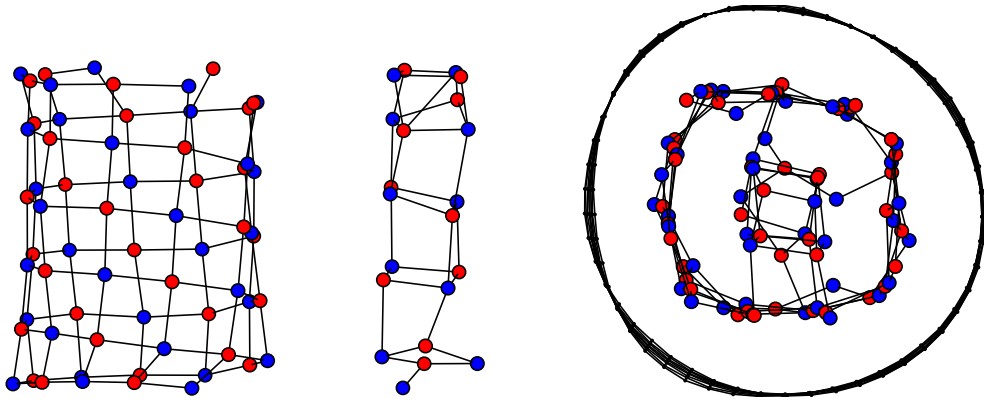

Figure 5.37: The double-walled structure formed inside the (25,0) carbon nanotube using potential III. Left: The external wall of the INT is the $(5,6)_{sq}$ morphology formed of eleven alternating chains of ions. Centre: The internal structure is the $(2,2)_{sq}$ INT. Right: The entire time-averaged (section 4.7) which consists of a double-walled INT of the INT_{sq} morphology. The structure is isotopic in the cross section and so no elliptical deformation is observed.

of such defects as we recall that it proceeds via the formation of chains along the nanotube pore and then interactions between adjoining chains. The last stage of this mechanism can result in larger loops than the "six-loop" hexagons residing in the INT_{hex} structure since the rearrangement of the ions into the perfect structure requires a cooperative rearrangement of ions in the local environment.

5.6.2 Potential II

Potential II also fills the (25,0) carbon nanotube with a double-walled INT (see figure 5.36). The external INT is highly defective which is a consequence of potential II being parametrised to favour both the tetrahedral and octahedral environments equally in the bulk crystals. The internal structure is also defective but is of the INT_{sq} which is consistent with the small radius regime for all four potentials (see chapter 5.36).

5.6.3 Potential III

With the addition of a small amount of pressure to the system modelled using potential III ($P = 0.00002\ a_0$, 0.58 GPa), the (25,0) carbon nanotube was filled with an isotropic double-walled structure (see figure 5.37). The morphology of the external INT was the $(6,5)_{sq}$ INT, consisting of eleven chains of alternating ions. The internal INT was also formed of square nets and took the form of the $(2,2)_{sq}$ INT. This potential clearly favours the INT_{sq} morphology over the INT_{hex} for this potential, giving rise to these two well-characterised INT_{sq}s.

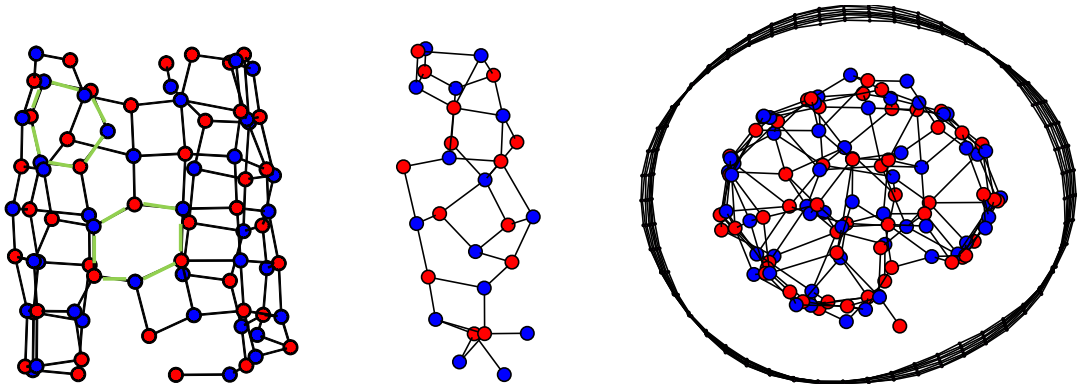

Figure 5.38: The double-walled structure formed inside the (25,0) carbon nanotube using potential IV. Left: The external wall of the INT a defective $(6,6)_{sq}$ morphology, the perfect structure of which contains twelve alternating chains of ions. The defects are in the form of hexagons (green) which is due small difference in energy between the INT$_{hex}$s and the INT$_{sq}$s for large radii INTs at this large radius (see figure 5.7). Centre: The internal structure is highly defective. Right: The entire time-averaged (section 4.7) which consists of a double-walled INT of the INT$_{sq}$ morphology. The structure is anisotropic in the cross section and so an elliptical deformation is observed.

5.6.4 Potential IV

Figure 5.38 shows the structure formed inside the (25,0) carbon nanotube which consists of a double-walled INT. The outer INT structure is very closely related to the $(6,6)_{sq}$ INT formed of twelve alternating chains of ions. However, the INT possesses some defects in the form of hexagons which is due to the small difference in energy between the INT$_{hex}$s and the INT$_{sq}$s for this potential model (see figure 5.7). The internal structure is highly defective and cannot be characterised. However, the result is that the cross section of this INT is anisotropic, giving rise to an elliptical defect.

5.6.5 General Observations

The cylindrical radial distribution g^{cyl} was calculated for all four ionic salts and is shown in figure 5.39. The external INT-nanotube separation averages at 7.7 a_0 which is longer than the separation predicted for the flat, infinite sheets. The balance of curvature effects, the presence of the molten liquid and internal INTs explain the deviation from that value. The deviation in radii of the internal INTs is observable since this separation is dominated by the differing potential parameters for all four ionic systems.

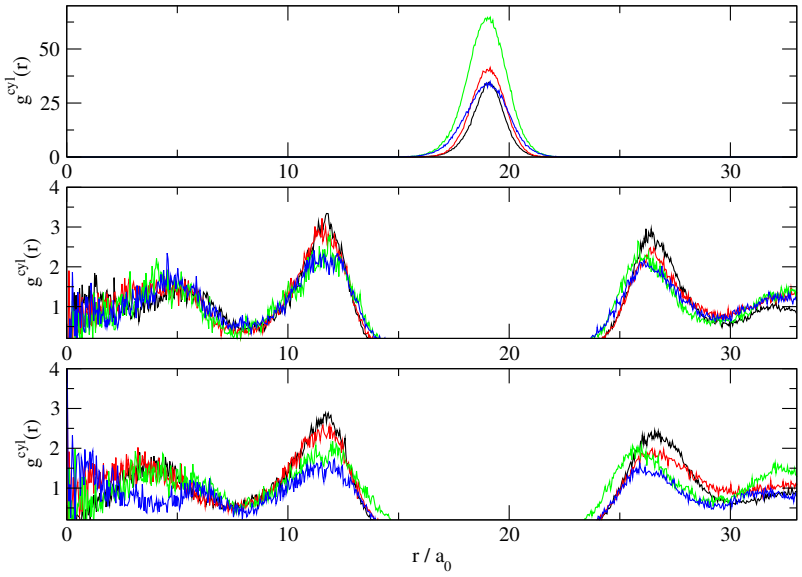

Figure 5.39: The cylindrical radial distribution functions $g^{cyl}(r)$ for the (25,0) carbon nanotube using potential I (black) , potential II (red), potential III (green) and potential IV (blue). The top panel shows the distribution for the carbon atoms, the centre and bottom panels show the distributions for the cation and anions respectively. All potentials show an average INT-nanotube distance of 7.7 a_0 with the external INT. The INT-INT distance varies for each potential due to the different ion-ion potentials used for each system.

5.7 The (15,15) carbon nanotube

5.7.1 Potentials I, II, III and IV

All four potential models filled the largest of all the carbon nanotubes, the (15,15) carbon nanotube with the ionic salts. As before, potentials III and IV required a small amount of pressure to instigate filling.

The very large diameter of the (15,15) carbon nanotube (39.6 a_0) appears to give rise to a different family of inorganic structures in comparison to the INTs formed in the small ((15,0) and (9,9) nanotubes) and large regime nanotubes ((22,0), (13,13) and (25,0) nanotubes). We recall, that the structures inside all those carbon nanotubes consisted of one cylindrical (INT) or two concentric cylindrical inorganic nanotubes (DWINTs). As the diameter of the carbon nanotube increases, the enclosed volume increases and so the limiting behaviour of the ions inside the cavity is expected to tend to that of ions in the liquid phase.

We appear to be at the limit of this behaviour with the (15,15) carbon nanotube, as the structures no longer consist of distinct concentric cylindrical INTs, as can be observed by monitoring the cylindrical radial distribution function $g^{cyl}(r)$ in figure 5.40. As with the smaller carbon nanotubes, we have an excluded volume between

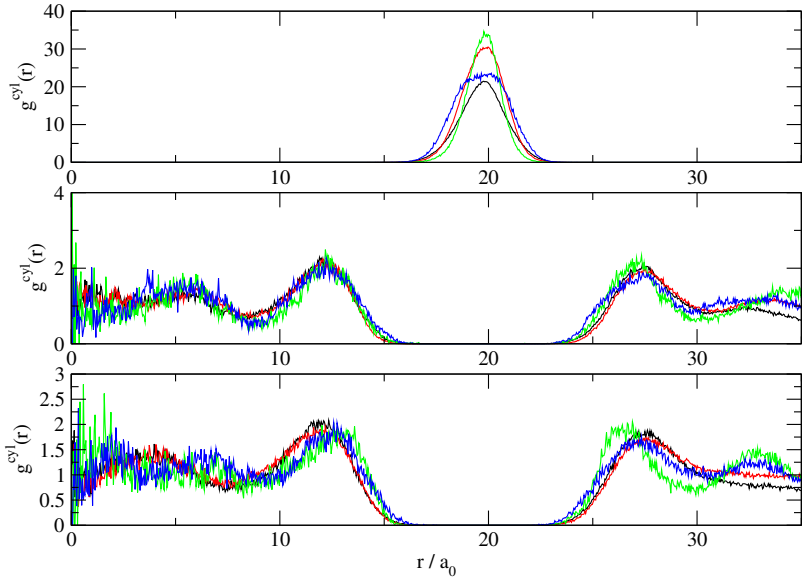

Figure 5.40: The cylindrical radial distribution functions $g^{cyl}(r)$ for the (15,15) carbon nanotube using potential I (black) , potential II (red), potential III (green) and potential IV (blue). The top panel shows the distribution for the carbon atoms, the centre and bottom panels show the distributions for the cation and anions respectively. We can see that for this very large carbon nanotube, distinct cylindrical INTs are no longer observed. We still have an excluded volume between the carbon nanotube and the enclosed ions but the function oscillates about one at small values of r.

the enclosed ions and the carbon nanotube and the confined ions due to the short-range Lennard-Jones repulsion between the species. However, at smaller values of r (i.e. the more central ions in the structure), the distribution is smooth, oscillating around $g^{cyl}(r) = 1$. This indicates a more uniform ion density towards the centre of the nanotube, which we also observe for the ions outside of the nanotube in the liquid phase. The presence of the carbon nanotube wall and the excluded volume give rise to short-range ordering reflected by the peak in $g^{cyl}(r)$ at 12.2 a_0. As we observed for the large carbon nanotube radius regime, the short range ordering in this outer volume of the internal structure is determined by the potential parameters used. The local environments of potentials I and II are dominated by hexagon units and the local environments using potentials III and IV are dominated by square nets.

Figure 5.41 is typical of the structures formed inside the (15,15) carbon nanotube. The structure shown is for potential II and we see from the end view that it does not consist of concentric cylinders and appears liquid-like. The outer most layer of this structure shows some short-range ordering and we see both square net and hexagon motifs in this volume.

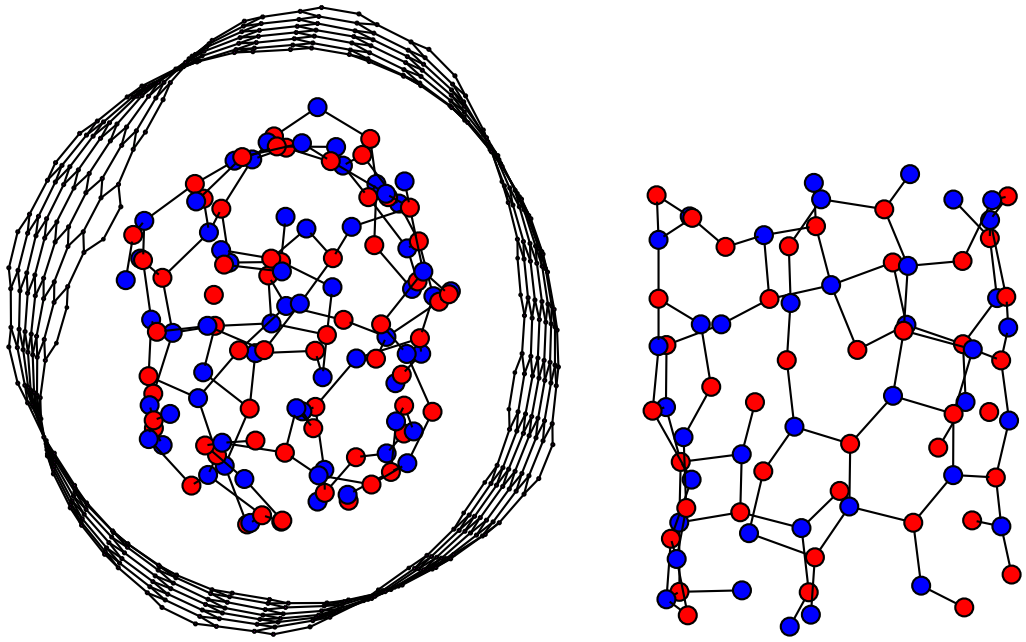

Figure 5.41: Left: A time-averaged snapshot from the molecular graphics of the filled (15,15) carbon nanotube using potential II. At this very large radius, we find that the confined ions do not form concentric cylindrical INTs as with the smaller carbon nanotubes. Instead the density is more uniform resembling the liquid phase outside of the nanotube walls. Right: The side view of the structure showing only the ions residing between 9 a_0 and 15 a_0 from the central axis. These are the ions in the outermost layer of the internal structure corresponding to the largest peak in figure 5.40. There appears to be some short range ordering and we observe the presence of the hexagon motif.

5.8 Long-lived Elliptical Deformations

The introduction of carbon-carbon interactions into the model means that the carbon nanotube can undergo deformations from the cylindrical geometry in which the cross section of the nanotube has an aspect ratio of unity. During the process of filling, some instantaneous elliptical deformations were observed (see figure 4.18, section 4.9). These were relatively short-lived distortions that occurred in some, but not all, of the filling events. Once the filling process had completed, the structures

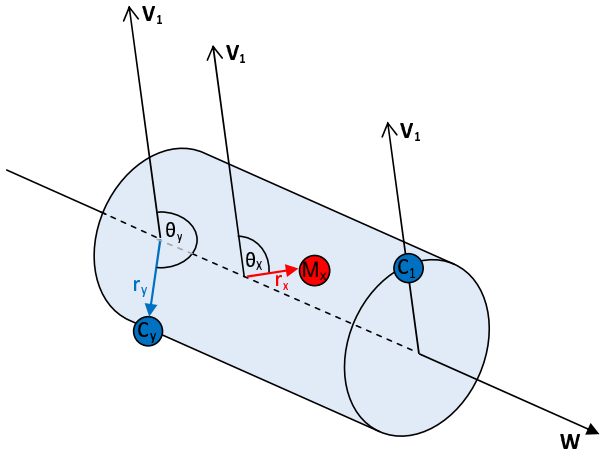

Figure 5.42: The function $g_i(\theta)$ can be calculated for the confined ions (M_x) and the carbon atoms (C_y) to monitor the correlation between the eccentricity and the anisotropic INTs. The vector $\mathbf{v_1}$ is first defined by the shortest separation between the central carbon nanotube axis **W** and the carbon atom C_1. For the i^{th} particle (ion M_x or atom C_y), the vector $\mathbf{r_i}$ can also be defined as the shortest separation between the central carbon nanotube axis **W** and particle i (for example, the vectors $\mathbf{r_x}$ and $\mathbf{r_y}$). The angle θ_i is the angle between the vectors $\mathbf{r_i}$ and $\mathbf{v_1}$ (travelling clockwise) and the distance $g_i(\theta)$ is given by $|\mathbf{r_i}|$.

of the INTs were probed via a time-averaging of the Cartesian coordinates of the nanotube and its contents (section 4.7). On examination of these structures, it is evident that many display a longer lived elliptical deformation in which the aspect ratio of the cross section of both the carbon nanotube and its ionic salt contents have deviated from unity. It is found that the INTs that cause the elliptical defect in the templating nanotube are those that are anisotropic in the cross section.

One such anisotropic structure which occurred frequently during the filling was the $(1,1)_{sq}$ INT found either as a transition state INT during the mechanism of filling or as the complete time-averaged final structure in a small radius nanotube or as the internal structure within a double walled INT. The $(1,1)_{sq}$ causes an elliptical defect in the carbon nanotube in all these cases.

We can define a function $g(\theta)$ in order to monitor the correlation between the

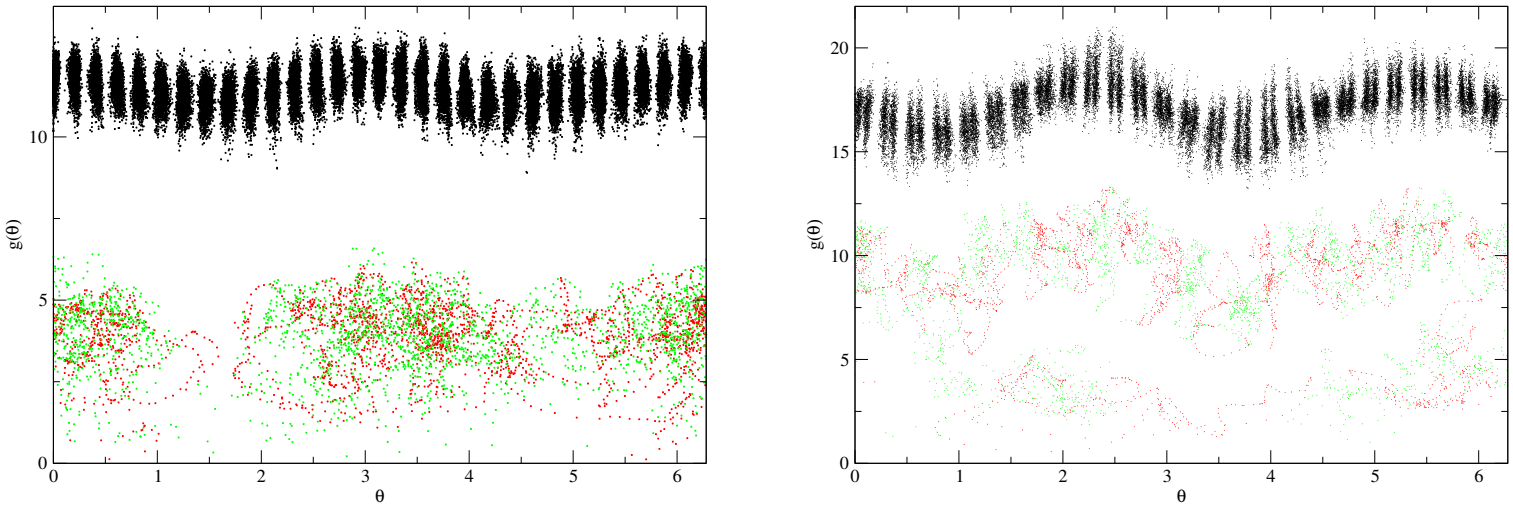

Figure 5.43: The instantaneous perpendicular separation of the carbon atoms (black), cations (red) and anions (green) from the nanotube axis as a function of angle θ about the axis. Left: The (15,0) carbon nanotube filled with the ionic salt described by potential I to form the $(1,1)_{sq}$ INT. The high ion density correlates with the larger carbon-nanotube axis separations. The aspect ratio of the nanotube is approximately 0.8 (eccentricity of 0.6), corresponding to an increase of 0.00005 a_0 per carbon atom above that of a perfect cylinder. Right: The (13,13) carbon nanotube filled with the ionic salt described by potential III to form the double-walled INT. The $(1,1)_{sq}$ INT is surrounded by the $(6,2)_{sq}$ INT which displays larger ion-axis separations at the angles at which the ions forming the $(1,1)_{sq}$ INT reside. Larger carbon-nanotube axis separations are also visible at these values of θ. The aspect ratio of the nanotube is approximately 0.85 (eccentricity of 0.5), corresponding to an increase of 0.00002 a_0 per carbon atom above that of a perfect cylinder.

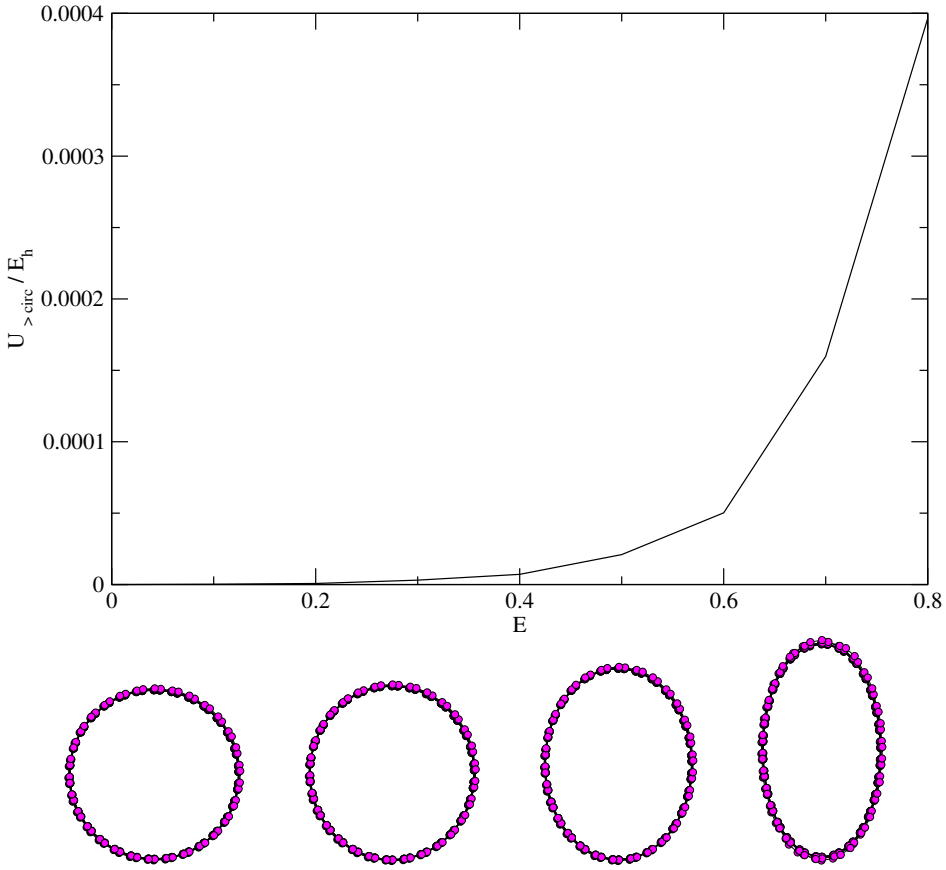

Figure 5.44: Top: How the potential energy (per carbon atom) of a nanotube varies as a function of the nanotube eccentricity. Bottom: Snapshots of the cross section of the relaxed nanotube at varying values of eccentricity. From left to right: Eccentricity of 0.0, 0.4, 0.7 and 0.9.

elliptical deformation of the carbon nanotube and the anisotropic structures formed inside. A carbon atom is arbitrarily selected as C_1 and the vector $\mathbf{v_1}$ is defined by the shortest separation between the central axis $\mathbf{W}$ and the atom C_1, as can be seen in figure 5.42. For any other carbon atom C_y or ion confined within the nanotube M_x, the respective vectors $\mathbf{r_y}$ and $\mathbf{r_x}$ are defined to describe the shortest separations between them and the central axis $\mathbf{W}$. The angle θ_i, which describes the angle between $\mathbf{r_i}$ and v_1, can calculated by taking the dot product of these vectors. The value of $g_i(\theta)$ for the i^{th} confined ion (or carbon atom) is the length of the vector $\mathbf{r_i}$,

$$g_i(\theta) = |\mathbf{r_i}|. \tag{5.10}$$

To investigate any correlation between the internal INT structure and the deformations in the confining carbon nanotube, figure 5.43 shows the instantaneous (not time-averaged) perpendicular distance of the ions and carbon atoms $g(\theta)$ from the central nanotube axis as a function of the angle θ. The example shown is for the (15,0) carbon nanotube filled with the salt described by potential I (section 5.2). We recall that the final internal structure in that case consisted of the $(1,1)_{sq}$ INT or "ladder-like" structure. As we circumvent the central axis we observe a deviation of the perpendicular separation of the carbon atoms (black) from the central axis. There is a clear correlation between the angle at which the largest carbon-nanotube axis separations occur and the angle at which there is the greatest density of ions residing inside the carbon nanotube.

Many of the INT structures observed in sections 5.2 to 5.7 possess anisotropic cross sections which give rise to elliptical deformations in the carbon nanotube. A further example is the double-walled INT formed in the (13,13) carbon nanotube using potential III (see figure 5.43, right). The internal INT is the anisotropic $(1,1)_{sq}$ INT which gives rise to larger ion-nanotube axis separations in the external $(6,2)_{sq}$ INT. The carbon-nanotube axis separations are also increased at values of θ at which the largest ion densities of the internal INT occur. There is a strong correlation between the $(1,1)_{sq}$ INT ion densities and the carbon nanotube deformation.

In order to further understand the energetics of the formation of such non-circular cross section structures, calculations were performed to evaluate the energy cost of deformations from an aspect ratio of unity. As an example, figure 5.44 shows the energy of a (15,15) carbon nanotube as a function of elliptical deformation. The coordinates of nanotubes of varying eccentricity were generated with a cross-sectional perimeter equal to that of the circumference of the perfect cylinder. The

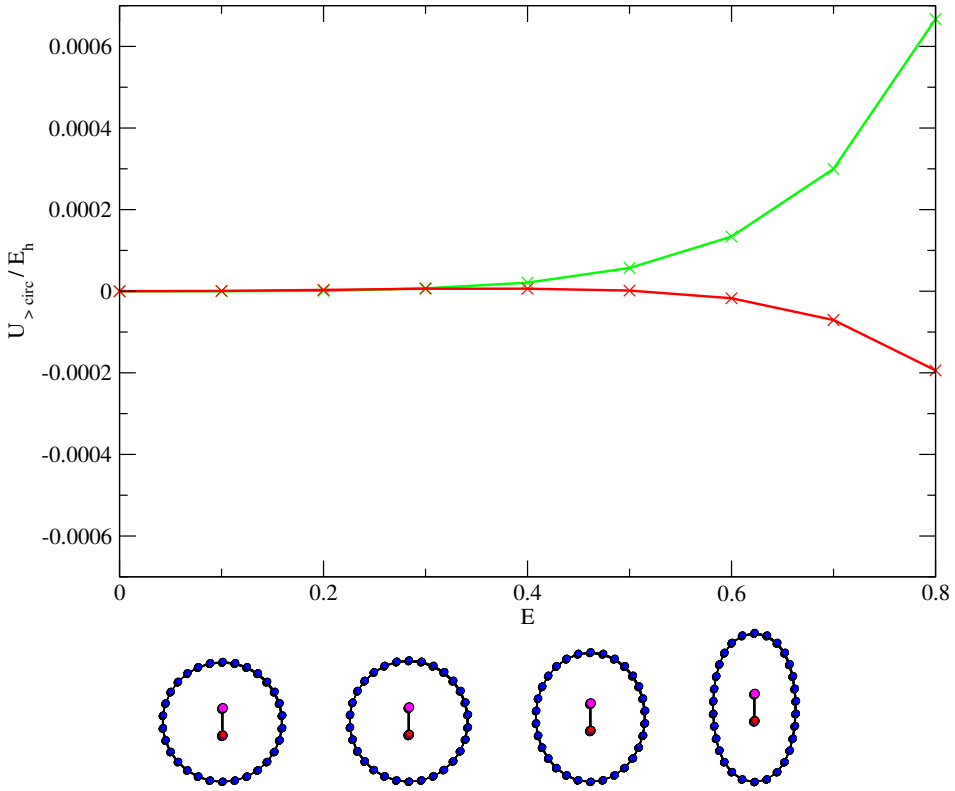

Figure 5.45: Top: How the potential energy (per carbon atom) varies as a function of the nanotube eccentricity. The elliptical defect causes an increase in the Tersoff potential energy (shown in green). Concurrently, there is a decrease in the ion-carbon energy which arises from the Lennard-Jones expression of the potential energy (red). Bottom: Snapshots of the cross section of the relaxed nanotube containing a ladder, at varying values of eccentricity. From left to right: Eccentricity of 0.0, 0.3, 0.6 and 0.8.

eccentricity is defined by

$$E = \sqrt{1 - (\frac{b^2}{a^2})}, \tag{5.11}$$

where a and b are the radii of the ellipse along the major and minor axes of the cross section respectively. For a circle, with an aspect ratio of unity, the eccentricity therefore takes a value of zero.

The perimeter of the ellipse can be obtained by using Ramanujan's first approximation [107] as follows;

$$C = \pi\Big[3(a+b) - \sqrt{(a+3b)(3a+b)}\Big]. \tag{5.12}$$

A steepest descent minimisation (see Appendix A-3) was performed so that the bond lengths of the elliptical nanotube could adjust to the equilibrium separation with the elliptical geometry fixed. Figure 5.44 shows that the energy required to deform the nanotube in this way is relatively small. For example, the deformation energy represents around 0.02 % of the nanotube energy at an eccentricity of 0.6.

A similar calculation was performed for a (15,0) carbon nanotube containing an INT of the $(1,1)_{sq}$ morphology which is anisotropic in the cross section, with the average ion-ion separations observed in the molecular dynamics simulations using potential I (see 5.2). The geometry of the INT was fixed for the calculations. There are many variables in such a calculation such as the nanotube and INT length and the exact geometry of the INT in terms of the bond lengths perpendicular and parallel to the nanotube axis. However, figure 5.45 shows the general trend of how the potential energy varies as a function of eccentricity. As before, the energy of the carbon nanotube increases as it deforms from an aspect ratio of unity. Conversely, the remaining parts of the energy function decreases as the eccentricity is increased. This is because a larger number of carbon atoms approach the equilibrium ion-carbon separation once the distortion occurs. The lowering in energy is attributed to the Lennard-Jones part of the potential energy calculation. Although, the effect does not totally compensate the energy gain in the defective nanotube in this particular calculation, it is conceivable that at a differing INT geometry, carbon nanotube diameter or morphology, an elliptical geometry of the nanotube does become more favourable by lowering the energy of the Lennard-Jones function. The figure certainly highlights the subtle energetic balance between the deformed carbon nanotubes confining anisotropic INTs.

In summary, the low-energy anisotropic INTs that form inside the carbon nanotubes are accommodated more easily by an elliptical deformation in the encasing

carbon nanotube. Such elliptical deformations in the carbon nanotube are driven by the ion-carbon interactions. These distortions are only observed in this work due to the introduction of the carbon-carbon interactions into the model. As a result, the inclusion of flexibility in the confining carbon nanotube has greatly expanded the underlying/energy landscape when compared with the structures obtained using a rigid carbon nanotube description.

5.9 Summary of the INTs formed in the dynamical simulations

The flexible model that incorporates the carbon-carbon interactions within the filling simulations has been used to directly fill carbon nanotubes from four different ionic salts. In sections 5.2 to 5.7 the structures that have formed within six nanotubes of varying diameter have been surveyed. Figure 5.46 summarises the morphology of the resulting INTs that are formed in these molecular dynamics simulations.

The morphology of the INT formed depends strongly on the radius of the carbon nanotube with the structures formed appearing to lie in three regimes:

5.9.1 Small carbon nanotube radius

- In the small carbon nanotube radius regime the INT is of the INT_{sq} morphology, regardless of which potential model is used. This is because at small radii, the energetics of the INTs are dominated by the interaction of ions along a chain of alternating anions and cations. The theory that explains this favouring of the INT_{sq} morphology (in particular, the $(\text{n,n})_{sq}$ INTs) is developed in chapter 6. The energy landscapes (figures 5.6 and 5.7) confirm that the $(\text{n,n})_{sq}$ INTs are indeed favoured at small radii for all four ionic systems regardless of the relative energetics of the two dimensional hexagonal and square net sheets.

- The mechanism of filling these small radii carbon nanotubes can be understood in terms of a time evolved increase in the number of ion-chains in the INT structure. As a result, the system appears to "hop" across the energy landscape jumping between low energy INT basins of increasingly large radii.

5.9.2 Large carbon nanotube radius

- In the larger radii regime, the structure of the INT formed is determined by limiting behaviour of the potential model describing the ion-ion interac-

	Small Radius Regime		Large Radius Regime			Very large Radius Regime
	15,0	**9,9**	**22,0**	**13,13**	**25,0**	**15,15**
Nanotube Diameter (a_0)	22.87	23.76	33.54	34.33	38.11	39.61
Filled? (Pot I)	✓	✓	✓	✓	✓	✓
Filled? (Pot II)	✓ (pressure)	✓	✓	✓	✓	✓
Filled? (Pot III)	✓ (pressure)	✓ (pressure)	✓ (pressure)	✓ (pressure)	✓ (pressure)	✓ (pressure)
Filled? (Pot IV)	✓ (pressure)	✓ (pressure)	✓ (pressure)	✓ (pressure)	✓ (pressure)	✓ (pressure)
Morphology of INT (Potential I)	$(1,1)_{sq}$	Hinge	$(8,0)_{hex}$	DWINT: $(8,2)_{hex}$ / $(1,0)_{sq}$	DWINT: INT_{hex} / INT_{sq}	Liquid-like
Morphology of INT (Potential II)	$(2,2)_{sq}$	$(2,2)_{sq}$/$(3,2)_{sq}$	$INT_{sq/hex}$	DWINT: $INT_{sq/hex}$ / $INT_{sq/hex}$	DWINT: $INT_{hex/sq}$ / INT_{sq}	Liquid-like
Morphology of INT (Potential III)	$(2,2)_{sq}$	$(2,2)_{sq}$	DWINT: $(5,4)_{sq}$ / $(1,1)_{sq}$	DWINT: $(6,2)_{sq}$ / $(1,1)_{sq}$	DWINT: $(5,6)_{sq}$ / $(1,1)_{sq}$	Liquid-like
Morphology of INT (Potential IV)	$(2,2)_{sq}$	$(3,3)_{sq}$	DWINT: $INT_{sq/hex}$ / $INT_{sq/hex}$	DWINT: $INT_{sq/hex}$ / $INT_{sq/hex}$	DWINT: $(6,6)_{sq}$ / $INT_{sq/hex}$	Liquid-like
INT – Nanotube Separation (a_0)	7.3	7.2	7.4	7.7	7.7	7.7

Figure 5.46: This table summarises the resulting INTs that were formed in the carbon nanotubes of varying diameters during the molecular dynamics simulations which included the carbon-carbon interactions. Where the exact INT has been identified, the integers n and m have been given. However, identification of the more defective INTs was problematic and in these cases only the morphology is given in terms of being based on tessellating hexagons (INT_{hex}) or square nets (INT_{sq}). The colour coding is as follows; blue represents INT_{sq}, pink represents INT_{hex} and any INTs that contain both hexagons and squares are shaded in yellow. The morphology of both the internal and external INTs are given for the double-walled INTs (DWINTs). The morphology of the INT formed is dependent on whether the carbon nanotube lies in the small or large radius regime. In the very large radius regime, the structures are no longer based on the folding of infinite planar sheets of square nets or percolating hexagons.

tions. Potential I strongly favours tetrahedral crystal structures and, in two-dimensions, a sheet of tessellating hexagons is the polymorph of choice. As a result, the observed INT structures are dominated by the percolating hexagonal unit. Conversely, potential III favours the octahedral crystal systems in the bulk and an infinite sheet of square nets in two dimensions and so the observed INT structures are dominated by square nets. INTs of the $(n,n)_{sq}$ morphology (or $(n,m)_{sq}$ where $n-m$ is very small) seem to be favoured consistent with the underlying energy landscape. A simple model which explains the energy difference between the $(n,n)_{sq}$ INTs and the $(n,0)_{sq}$ INTs will be developed in chapter 6.

- The INTs for potentials II and IV also conform to the details of the ionic system determining the morphology. However, the small energy differences between the INT_{sq} and INT_{hex} morphologies mean that the INTs are often highly defective and we are often unable to define the exact chiral vector that describes the INT morphology. Potential II equally favours the octahedral and tetrahedral coordination environments in the bulk, but very slightly favours the tessellating hexagons in two dimensions. Therefore, large radii INTs are generally of the INT_{hex} morphology but are often very defective, with the square net motif present in the final structures. Conversely, potential IV favours the octahedral coordination environment in the bulk but in two-dimensions this difference is only very slight. Therefore, large radii INTs are of the square net morphology but hexagon defects are often observed in the final structures. The mechanism of filling the larger radii INTs appears to proceed as follows. Exploratory loops of chains of alternating ions enter the nanotube and as a result chains form down the length of the nanotube pore. Eventually interactions between ion chains cause small loops of ions to form. These often consist of squares, hexagons or octagons, depending on where the adjoining chains interact. As the number of ions in the nanotube reaches the preferred density for the given potential model, there is some local rearrangement of the ions and an INT of the hexagon or square morphology is formed.

- Finally, we note that, the internal INTs within the double-walled INTs lie within the small radius regime. Therefore, they generally favour INTs consisting of the square net morphology in which the interactions along chains of alternating ions can dominate. The structures of the inner INTs can be considered as confined both by the carbon nanotube and the outer INT.

5.9.3 Very large carbon nanotube radius

- For very large radii carbon nanotube, the structure formed within the nanotube pore do not consist of concentric cylindrical INTs. There is some short-range ordering in the outer confined ions which is imposed by the carbon nanotube whose local environment is determined by the potential model of choice. The ion density becomes increasingly uniform as we approach the most central ions within the nanotube, corresponding to a liquid like phase.

Chapter 6

The Energetics of Inorganic Nanotubes

In the previous chapter we established that the underlying INT energetics appear more complex than is the case for the carbon nanotubes themselves. For example, the energetics of the square net based structures appears heavily dependent upon the final morphology, whilst those for the hexagonal based structures appear near morphology independent. As a result, it is important to attempt to understand these energetics in terms of the fundamental atomistic interactions. The theory developed in this chapter appears to explain the following experimental observations:

- The rock salt structure is preferred for the nanocrystallites of the MX stoichiometry [37, 91].
- The growth of the observed rock salt nanocrystallite tends to be parallel to the crystalline $\langle 110 \rangle$ direction [37, 91].
- The nearest neighbour anion-cation separations running parallel to the nanotube major axis are contracted with respect to those running perpendicular to the same nanotube axis [87].

Furthermore, the following observations from the molecular dynamics simulations performed in chapter 5 are also explained:

- The calculated energy landscape of the INTs is complex, with a preference for the $(n,n)_{sq}$ morphology at low radii.
- The INTs observed to form dynamically within the carbon nanotubes in the small radius regime are generally of the $(n,n)_{sq}$ morphology, regardless of the potential model used.

6.1 Curvature effects

On rolling an infinite square net sheet (with nearest neighbour bond length a) along a chiral vector into a cylinder, the component of the bond lengths that are perpendicular to the INT axis are reduced. This is because the new bond lengths are the shortest distance between two ions on the surface of the cylinder and they do not correspond to the curved distance on the surface of the cylinder (which remains of length a, equal to the distance in the infinite plane). This reduction in bond length a is more pronounced as the curvature of the cylinder surface is increased. Therefore, the smaller the INT (with greater curvature), the greater the reduction in bond length we observe (see figure 6.1).

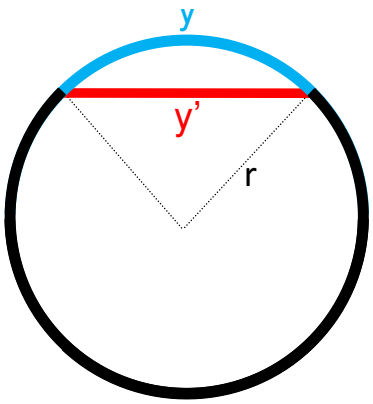

Figure 6.1: On rolling a sheet into a cylinder, there is a difference between the distances y and y'. These distances are equal in the plane (where there is no curvature). The curved distance y (blue) is the distance between two points on the surface of the cylinder, the same distance as in the plane. The distance y' (red) is the shortest distance between two points and is reduced on folding the sheet into the plane to a value less than that of y. The reduction in the distance y' is proportional to the curvature in the cylinder surface.

Let us take a cross section of the cylinder such as the one in figure 6.1. It is noted that any curved distance y in the circumference of the cross section is related to the shortest straight distance y' (between the two ends of y) by the following relation;

$$y' = 2rsin\Big(\frac{y}{2r}\Big). \tag{6.1}$$

The radius of a $(n,m)_{sq}$ INT (and therefore the curvature of the surface) is a function of n and m;

$$r_{sq} = \frac{\sqrt{2}a\sqrt{n^2+m^2}}{2\pi}. \tag{6.2}$$

Substituting this expression into equation 6.1, we have

$$y' = \frac{\sqrt{2}a\sqrt{n^2+m^2}}{\pi}\sin\left(\frac{y\pi}{\sqrt{2}a\sqrt{n^2+m^2}}\right). \tag{6.3}$$

Therefore, equation 6.3 evaluates the shortest distance between two points on the surface of an INT$_{sq}$, if the integers n and m and the equivalent curved distance between the two points on the cylinder surface are known.

Let us take a vector $\mathbf{V}$ within the INT unit cell before it is rolled into a cylinder, it is therefore is lying in the infinite plane. $\mathbf{V}$ can be defined in terms of two component vectors, one which lies perpendicular to the nanotube axis $\mathbf{v}_\perp$ and one that lies parallel to it $\mathbf{v}_\parallel$. On rolling into the INT, the length of $\mathbf{v}_\parallel$ remains unchanged yet the length of $\mathbf{v}_\perp$ is reduced. The ratio of the length of $\mathbf{v}_\perp$ before (y) and after the rolling (y') of the unit cell into a cylinder, can be determined.

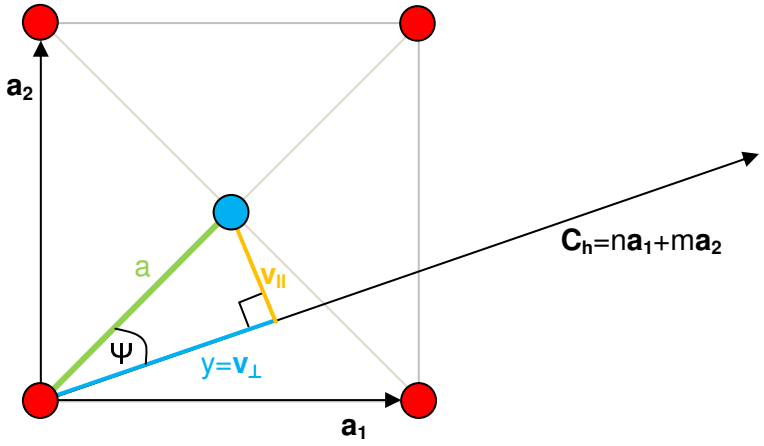

Figure 6.2: The bond between the anion and cation is shown in green and has a component parallel to the INT axis ($\mathbf{v}_\parallel$, in orange). The length of this component remains unchanged on folding the sheet into the INT. The other component runs perpendicular to the INT axis ($\mathbf{v}_\perp$, in blue) and the length of this component is reduced from y to y' on rolling the sheet into an INT. The length of $\mathbf{v}_\perp$ is calculated in terms of the angle ψ which is enclosed between the vector $\mathbf{C_h^{sq}} = n\mathbf{a_1} + m\mathbf{a_2}$ and the cation-anion bond (a,in green).

When generating the INT coordinates these curvature effects are not accounted for. This means that the nearest neighbour anion-cation distances vary within the same INT depending on the component of the bonds that are perpendicular to the INT axis. The bond lengths that have a large component perpendicular to the INT axis are significantly reduced in relation to their equilibrium separation found in the infinite plane. In small radii INTs, where the curvature effects are greatest, the generated structures become unfavourable.

In order that the coordinates of the INT$_{sq}$s have equal nearest neighbour bond lengths equal to that in the infinite plane, the nanotube must be enlarged in the

circular cross section by a factor of y/y'. In the case of the $(n,0)_{sq}$ INTS, all nearest neighbour bond lengths will be lengthened when this correction factor is applied as they all have a component perpendicular to the nanotube axis. Only half the bonds in the $(n,n)_{sq}$ INTS are affected. This is because exactly half lie parallel to the INT axis (and are therefore unaffected by the process of rolling into a cylinder). However, the other half lie perpendicular to the INT axis and must be lengthened to give bond lengths equal to the equilibrium values of the infinite square-net plane.

The length of the perpendicular component of the bond length $\mathbf{v}_\perp$ (shown in blue in figure 6.2) is a function of the integers n and m that define the chiral vector of the INT. The modulus of this component in the infinite plane (y) can be evaluated by taking the dot product of the chiral vector and the vector corresponding to the anion-cation bond (shown in green in figure 6.2) to determine the cosine of the angle ψ;

$$\cos\psi = \frac{\sqrt{2}}{2}\frac{(n+m)}{\sqrt{n^2+m^2}} \tag{6.4}$$

$$= \frac{|\mathbf{v}_\perp|}{a}. \tag{6.5}$$

If we wish to evaluate the reduction in the nearest neighbour bond length a on rolling into a cylinder, we take $|\mathbf{v}_\perp| = y$ so that

$$y = \frac{a\sqrt{2}}{2}\frac{(n+m)}{\sqrt{n^2+m^2}}. \tag{6.6}$$

This can be combined with equation 6.3 to obtain the scale factor of enlargement y/y' which can be used to correct the nearest neighbour bond lengths back to a, after folding the infinite plane into a cylinder;

$$\frac{y'}{y} = \frac{2}{\pi}\frac{(n^2+m^2)}{(n+m)}\sin\Big[\frac{\pi}{2}\frac{(n+m)}{(n^2+m^2)}\Big]. \tag{6.7}$$

In the particular special cases of an $(n,n)_{sq}$ INT (where $y = a$) or an $(n,0)_{sq}$ INT (where $y = a/\sqrt{2}$), this simplifies to

$$\frac{y'}{y} = \frac{2n}{\pi}sin\Big(\frac{\pi}{2n}\Big). \tag{6.8}$$

6.2 The difference in energy between the $(n,0)_{sq}$ and the $(n,n)_{sq}$ INTs

The coordinates of several $(n,n)_{sq}$ and $(n,0)_{sq}$ INTs were generated by the rolling up of an infinite sheet of square nets with nearest neighbour bond distances $a = 4.25$ a_0. The coordinates of the generated INTs were then corrected by the scale factor y/y' as described in section 6.1, so that the nearest neighbour bond lengths were all equal to $a = 4.25$ a_0. The single-point potential energy was calculated using potential I for all of these nanotubes where the nearest neighbour bond length was fixed to the bond length $a = 4.25$ a_0. The potential energies of the $(n,0)_{sq}$ INTs were found to be less negative than those of the $(n,n)_{sq}$ morphology at all radii. The functional form of the strain energy appears to differ significantly between the two chiralities. This preference for the $(n,n)_{sq}$ INTs is consistent with several previous results.

Firstly, the energy landscapes in figures 5.6 and 5.7 show that the $(n,n)_{sq}$ INTs are always favoured over the $(n,0)_{sq}$ INTs and this effect is most pronounced at small radii. (Those energy landscape calculations differed from the present calculations only in that the calculation was performed at varying diameters and that the bond lengths were allowed to "relax" via a steepest descent algorithm prior to the single point energy calculations.) Secondly, there was a strong preference for the formation of the $(n,n)_{sq}$ INTS during the molecular dynamics simulations (see figure 5.46), particularly at small radii. The $(n,n)_{sq}$ morphology dominated due to the lower potential energy of these structures in comparison to other INT morphologies. In addition, the formation of a $(n,n)_{sq}$ INT was frequently observed as a transition state structure during the filling process.

The preference for the $(n,n)_{sq}$ INTs is somewhat surprising. We recall that the potential energy of the templating carbon nanotubes was rationalised in terms of the elastic continuum theory (section 4.2). As with the carbon nanotubes, the structures of the INTs are rationalised in terms of the folding of an infinite sheet into a cylinder. The INT_{hex} morphology in particular can be thought of as a binary form of the carbon nanotubes themselves. We might therefore expect the potential energy of the INTs to be rationalised via the elastic continuum theory too, in an analogous way to the carbon nanotubes.

The elastic continuum theory takes the energy of the rolled cylinder to be equal to that of the infinite sheet plus the strain energy required to roll the sheet. As the infinite sheet is approximated as a continuous entity of a specified thickness, the strain energy is found to have a power law dependence of the form $\frac{1}{r^2}$ (equation 4.12).

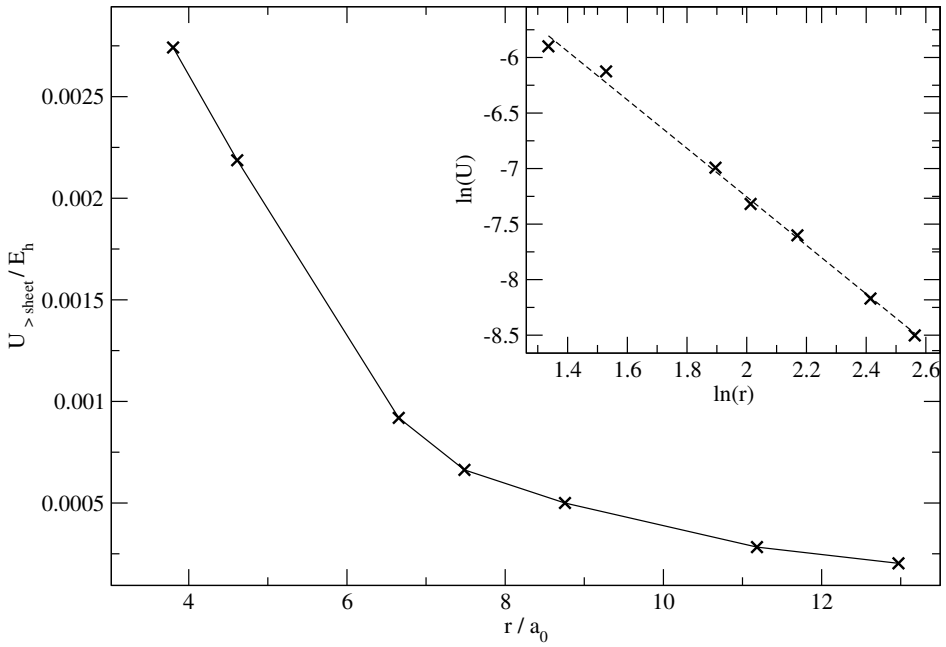

Figure 6.3: The strain energy of the INT$_{hex}$s for potential I above that of an infinite sheet (-0.167 a_0 per ion). Both the (n,n)$_{hex}$ and the (n,0)$_{hex}$ are shown and both morphologies follow the $\frac{1}{r^2}$ dependence predicted by the elastic continuum theory. The inset show a linear regression for the $\ln U$ versus $\ln r$ plot.

For the carbon nanotubes this relationship means that the amount of strain energy is independent of the nanotube chirality or in other words, the direction of folding as determined by the chiral vector. Figure 4.4 showed that the functional form of the strain energy of the carbon nanotubes conforms to the $\frac{1}{r^2}$ dependence and that the elastic modulus is the same for all morphologies of nanotube. We confirm that the strain energy is independent of the direction of folding of the graphene sheet.

Likewise, the strain energy of the INT$_{hex}$ appears to follow the $\frac{1}{r^2}$ relationship with the minima from the energy diameter calculations in section 5.1 all adhering to the same functional form, regardless of the INT morphology. Figure 6.3 presents the minima from those calculations and the inset shows a linear regression analysis of the strain energy of a range of (n,0)$_{hex}$ and (n,n)$_{hex}$ INTs. The strain energy is taken to be the energy of the INT$_{hex}$ above that of the infinite hexagon sheet (-0.167 a_0 per ion for potential I). The plot of $\ln U$ versus $\ln r$ has a slope of 2.2 ± 0.1 in agreement with the $\frac{1}{r^2}$ dependence. The intercept of the data is 2.9 ± 0.1 E_h ${a_0}^2$ for all the INT$_{hex}$ analysed. Once again, we find that the strain energy is independent of the direction of folding of the planar sheet.

In clear contrast, the differing functional forms of the strain energy in figure 6.4 of the INT$_{sq}$s means that one or both of the following hypotheses are true. The elastic modulus of the (n,n)$_{sq}$ differs from that of the (n,0)$_{sq}$ and/or they do not conform

to the $\frac{1}{r^2}$ dependence of the elastic continuum model. In order to see if either

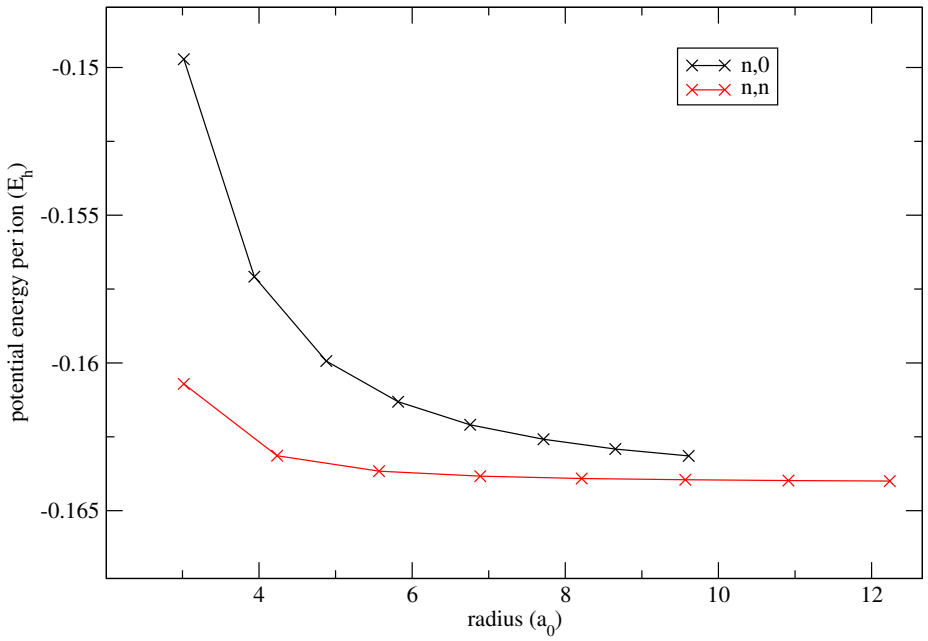

Figure 6.4: The energy of various $(n,0)_{sq}$ INTs and $(n,0)_{sq}$ INTs as a function of radius. Single point calculations were performed for INT_{sq}s in which the nearest neighbour separations had been corrected by the enlargement scale factor y/y' in the INT cross section, to be equal to their planar values $a = 4.25$ a_0. The $(n,n)_{sq}$ INTs are favoured at all radii which is consistent with the results obtained in chapter 5.

the $(n,0)_{sq}$ or the $(n,n)_{sq}$ morphology of INT fits the elastic continuum model, a regression analysis was performed (figure 6.5). The natural logarithm of the energy above that of an infinite sheet of square nets (-0.165 a_0) was plotted against the natural logarithm of the INT_{sq} radius. The $(n,0)_{sq}$ INTs give a reasonably good straight line fit to the model with gradient of -1.99 ± 0.08. However, the fit was extremely poor for the $(n,n)_{sq}$ INTs with a gradient -1.25 ± 0.2. This suggests that there is an additional favourable contribution to the energy of the $(n,n)_{sq}$ INTs, in addition to the energy of the infinite sheet and the strain energy. The infinite sheet of ionic square nets cannot be considered an infinite continuum of defined thickness, unlike a graphene sheet or an ionic sheet of tessellating hexagons which are approximated quite well by such a model.

6.3 The contributions to the INT_{sq} energies

We have determined that the INT_{sq} single point energies are dependent on the direction of the chiral vector which defines the INT morphology. The potential energy of the inorganic structures are defined by the potential energy function given

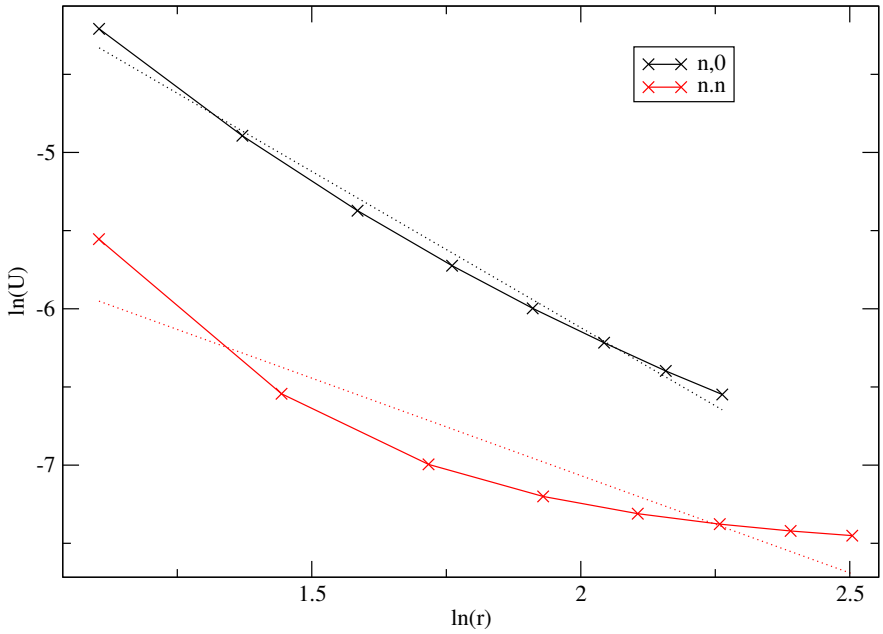

Figure 6.5: Linear regression of the natural log of the energy of the $(n,n)_{sq}$ and $(n,0)_{sq}$ INTs. The $(n,n)_{sq}$ INTs show a poor fit to an elastic continuum model.

in equation 2.43, which splits the energy into short-range repulsion (the Born-Mayer term), dispersion and the long range coulombic contributions (calculated via an Ewald summation). These various contributions to the single point energies of the $(n,n)_{sq}$ and the $(n,0)_{sq}$ INTs were separated out and then plotted as a function of nanotube radius in order that the source of the differing single-point energies could be determined (figure 6.6).

Figure 6.6 shows that the lower $(n,n)_{sq}$ total energy is a result of two of the energy contributions. Firstly there is less repulsion in the $(n,n)_{sq}$ INTs and secondly there is a more favourable coulombic interaction in the $(n,n)_{sq}$ INTs (specifically in the real part of the Ewald summation). These lower energies of the $(n,n)_{sq}$ INTs contribute equally to the overall favouring in the energies of the $(n,n)_{sq}$ INTs. There is a small favouring of the $(n,0)_{sq}$ INTs within the dispersion contribution but this small difference is overpowered by the repulsion and coulombic contributions. We note that there is no difference in the reciprocal coulombic term for the two classes of INTs. Therefore, we must look more closely at both the repulsion and coulombic terms in turn in order that we can determine the cause of the lower energy of the $(n,n)_{sq}$ INTs.

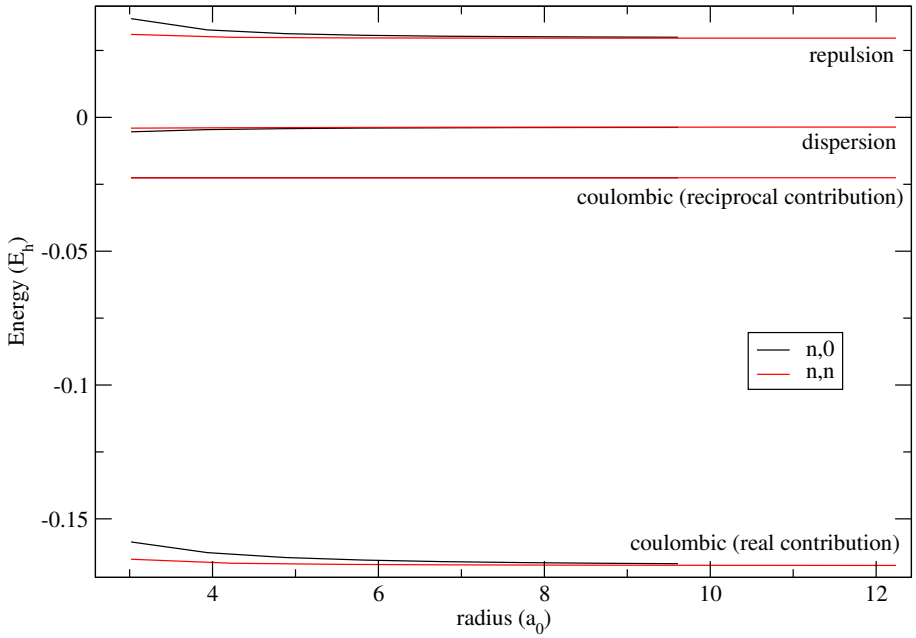

Figure 6.6: Various contributions to the potential energy of $(n,n)_{sq}$ and $(n,0)_{sq}$ INTs as a function of radius.

6.4 Repulsion energy of the INT$_{sq}$s

The short range repulsion of the ions is described by the Born-Mayer term in the potential energy function;

$$U(r) = B_{ij}e^{-a_{ij}r}. \tag{6.9}$$

There is less repulsion in the $(n,n)_{sq}$ than in the $(n,0)_{sq}$ INTs. This difference persists at large radii and since repulsion is a relatively short range interaction, it suggests that it is not entirely due to cross tube interactions. We can break down the repulsion energy terms further into cation-cation, anion-anion and cation-anion contributions. Figure 6.7 shows that the most repulsion occurs from the anion-cation interactions. This is to be expected as these are the nearest neighbour interactions. However, any difference between the anion-cation repulsion is negligible between the two morphologies of INT due to the fixed nearest neighbour separation of $a = 4.25a_0$.

The cation-cation repulsion is eliminated in this model where we are using the parameters for potential I. In that potential model, the B_{ij} parameter is equal to zero which physically corresponds to an ionic salt in which the cations are very small with minimum repulsion between them.

As a result, the only remaining contribution which can give rise to the difference between the two models is the repulsions between the anions. The anion-anion interactions are indeed where the difference in repulsion energy lies. We can explain

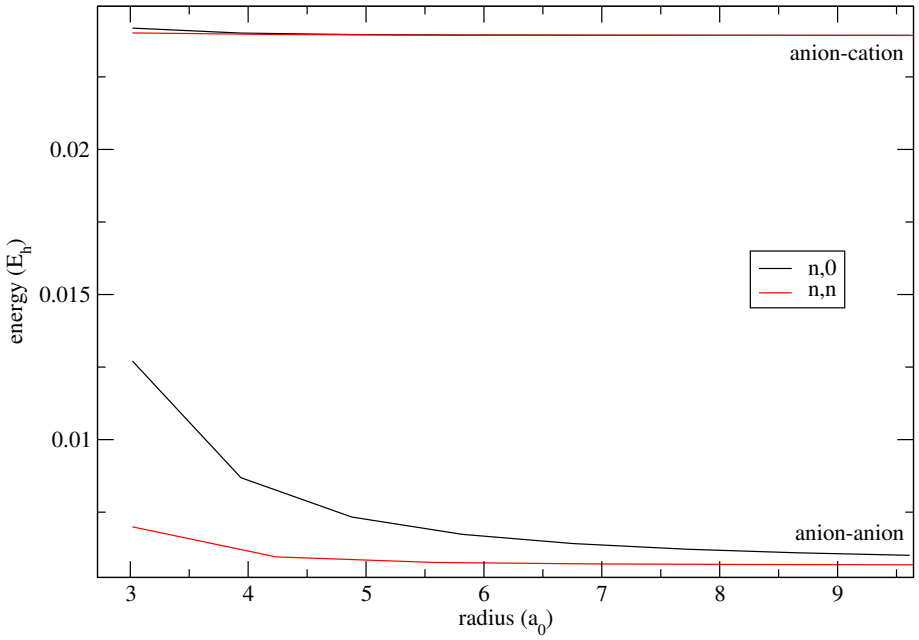

Figure 6.7: The repulsion energies as a function of radius. The most significant contribution to the repulsion of both INTs is the anion-cation repulsion which is due to their small separation. However, this contribution is comparable for both morphologies where the nearest neighbour is $a = 4.25\ a_0$. Although a less significant contribution to the overall repulsion, the anion-anion repulsion is much higher in the $(n,0)_{sq}$ INTs than in the $(n,n)_{sq}$ INTs and this gives rise to the difference in overall repulsion.

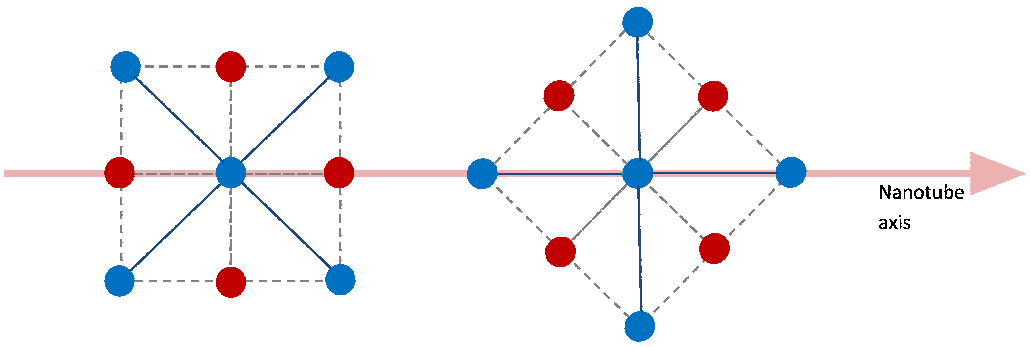

Figure 6.8: Left: The $(n,n)_{sq}$ INT alignment. The four anion-anion distances are equal in length with a value of $a\sqrt{2}$, even after folding into a cylinder. Right: The $(n,0)_{sq}$ INT alignment. The two anion-anion separations along the axis remain at $a\sqrt{2}$ on folding but the other two anion-anion distances are reduced on creation of the cylinder. The shorter separations cause greater repulsion in the $(n,0)_{sq}$ morphology.

this difference in energy by looking at the nearest neighbour anion-anion separations. Let us consider an anion in the infinite square net sheet. There are four surrounding anions at a distance of $\sqrt{2}a$ away from the central anion. Figure 6.8 shows how the anion-anion separations are affected depending on the relative direction of the chiral vector which defines the INT morphology.

When the sheet is rolled into a cylinder along the chiral vector and the correction in the xy plane is applied, all the nearest neighbour cation-anion separations are equal to $a = 4.25\ a_0$. The next nearest neighbours are anions which remain at a distance of $\sqrt{2}a$ from the central anion in the $(n,n)_{sq}$ INTs on folding of the sheet into the cylinder. In contrast, only the two anions which lie parallel to the INT axis in the $(n,0)_{sq}$ INT remain at a distance of $\sqrt{2}a$ on folding of the infinite sheet. The other two anions that lie perpendicular to the nanotube axis have their separations reduced on rolling into the cylinder. This means that the repulsion of the central anion with these two anions is increased in comparison to the infinite sheet on creation of the cylindrical INT. The new anion-anion separation perpendicular to the axis when the sheet is rolled and corrected for the nearest neighbour separation is calculated by taking $y = a\sqrt{2}$ in equation 6.3. The correction scale factor of y/y' must also be accounted for, as this was applied to ensure that the nearest neighbour anion-cations remained at $a = 4.25\ a_0$ (equation 6.8). Therefore the new anion-anion distance perpendicular to the INT axis is given by

$$r_{anion,anion} = \frac{a\sqrt{2}sin\left[\frac{\pi}{n}\right]}{2sin\left[\frac{\pi}{2n}\right]}. \tag{6.10}$$

The reduction factor in the two anion-anion separations perpendicular to the axis was calculated using equation 6.10 for various $(n,0)_{sq}$ INTs and is shown in table 6.4. The repulsion energy is increased significantly due to the reduction in the nearest neighbour anion-anion separations perpendicular to the INT axis within the $(n,0)_{sq}$ INTs. This increase in nearest neighbour anion-anion energy is calculated in the fifth column of table 6.4.

In summary, the repulsion energy of the $(n,0)_{sq}$ INTs is greater than that of the $(n,n)_{sq}$ INTs. This is due to the reduction of two of the anion-anion separations perpendicular to the INT axis on folding the infinite square net sheet into a cylindrical $(n,0)_{sq}$ INT. The respective anion-anion separations remain unaltered from the length in the infinite sheet in the $(n,n)_{sq}$ INTs (once the correction scale factor y/y' is applied).

n,0	$\frac{2r_{anion,anion}}{a\sqrt{2}}$	E_{rep}(n,n)	E_{rep}(n,0)	ΔE_{rep} **per anion**
3	0.866	0.0111	0.0249	0.0138
4	0.924	0.0111	0.0168	0.0057
5	0.951	0.0111	0.0143	0.0032
6	0.966	0.0111	0.0132	0.0021
7	0.975	0.0111	0.0126	0.0015
8	0.981	0.0111	0.0122	0.0011
9	0.985	0.0111	0.0119	0.0008
10	0.988	0.0111	0.0118	0.0007
11	0.990	0.0111	0.0116	0.0006

Table 6.1: The factor that the anion-anion nearest neighbour distance perpendicular to the nanotube axis is reduced by on creation of a $(n,0)_{sq}$ INT is given in column two (equation 6.4). ΔE_{rep} is the difference in repulsion energy (using the parameters from potential I) between a central anion surrounded by four anions at a distance $a\sqrt{2}$ (the $(n,n)_{sq}$ INT or indeed the flat infinite sheet, column three) and the energy of a central anion surrounded by two anions at a distance $a\sqrt{2}$ and two at the distance reduced by the factor in column 2 (the $(n,0)_{sq}$ INT, column four).

6.5 Coulombic energy of the INT$_{sq}$s

The coulombic energy makes a contribution to the favouring of the $(n,n)_{sq}$ INTs over the $(n,0)_{sq}$ INTs equal to that of the repulsive interactions. As with the difference in the repulsion energy (attributed to anion-anion interactions) we can break down the coulombic energy into smaller contributions in order to determine the source of this difference in energy of the two morphologies of INT$_{sq}$. The coulombic energy was calculated using an Ewald summation and therefore has both a contribution calculated in real space and reciprocal space. We recall from section 6.3 that the difference in energy occurs only in the real part of the summation. Figure 6.9 shows that there is a difference in energy in both the repulsive interactions (anion-anion and cation-cation) and in the attractive interactions (cation-anion). The repulsive interactions favour the $(n,n)_{sq}$ INTs which shows less coulombic repulsion at all radii. However, the $(n,0)_{sq}$ INTs are favoured by the attractive interactions. On balance, the difference between the repulsive interactions is larger and therefore the overall coulombic energy favours the $(n,n)_{sq}$ INTs since they act to minimise the like charge repulsions.

The difference in the short range repulsion energy in section 6.4 was understood in terms of the reduced separations of the anion-anion distances on the folding of the infinite square net sheet. This interaction is short-ranged so a localised explanation such as that suffices for explaining the minimised repulsion in the $(n,n)_{sq}$ INTs. However, the coulombic interactions are much more long ranged and must be

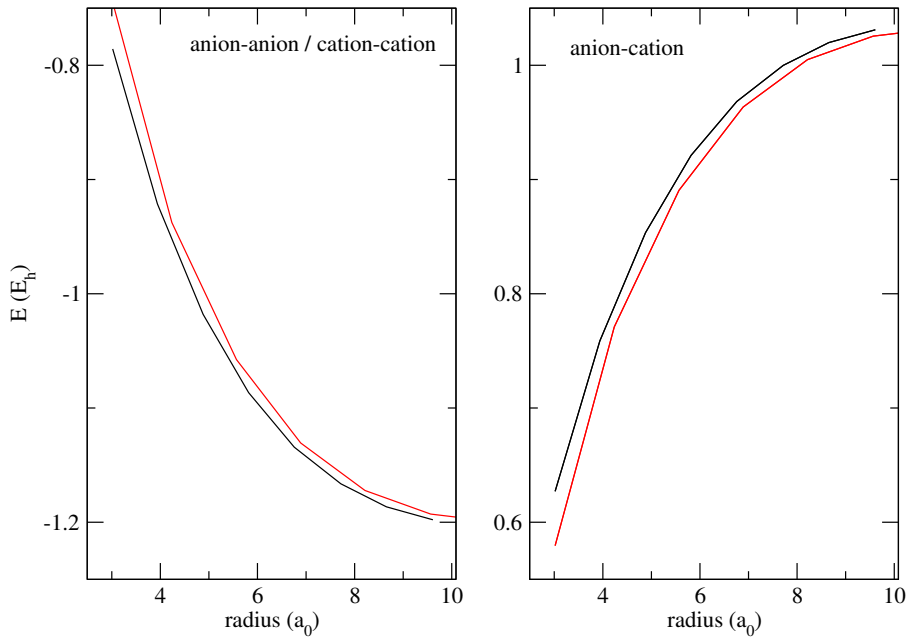

Figure 6.9: The contributions to the real part of the coulomb energy. Left: Unlike (anion-cation), attractive contribution which favours the $(n,0)_{sq}$ INTs (black). Right: Like (anion-anion/cation-cation), repulsive contribution which favours the $(n,n)_{sq}$ INTs (red).

calculated via a summation. Therefore, a more complex model is needed in order to determine the source of the difference in the coulombic energy between the $(n,n)_{sq}$ INTs and the $(n,0)_{sq}$ INTs.

6.6 "Chain" calculations for the $(m_1 \times m_2 \times \infty)$ nanocrystallites

In section 6.5 we arbitrarily deconstructed the coulombic long-range energy contributions into anion-cation interactions and the like-charge interactions (cation-cation or anion-anion). Clearly, we can seek some alternative partitioning of the coulombic interactions, which may further our understanding of the energetics of the INT$_{sq}$s.

Bichoutskaia and Pyper [7] develop such a model for the "nanocrystalline ionic solids" or pseudo one-dimensional crystallites which relate to small but infinitely long sections of the rock-salt bulk material. These nanocrystallites have a cross section which is formed of the square net structure with m_1 rows and m_2 columns of ions. The $(2 \times 1 \times \infty)$ consisting of two rows and one column of ions in the cross section corresponds to our $(1,1)_{sq}$ INT and the $(2 \times 2 \times \infty)$ nanocrystallite containing two rows and one columns of ions in the cross section is our $(2,2)_{sq}$ INT. It will be helpful for the later derivation to note the bond lengths a and b which run

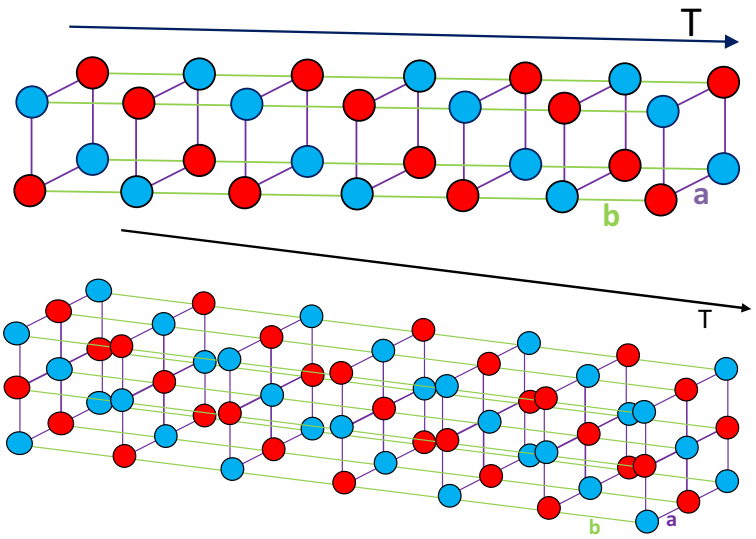

Figure 6.10: Top: The $(2 \times 2 \times \infty)$ nanocrystallite corresponds to the $(2,2)_{sq}$ INT in our nomenclature. The cation-anion separations perpendicular to the nanotube axis shown in purple are defined as a and the cation-anion separations running parallel to the nanotube axis are shown in green. Bottom: The $(3 \times 3 \times \infty)$ nanocrystallite does not correspond to any $(n,m)_{sq}$ SWINTs in our nomenclature. The structure is rationalised in terms of a section of the bulk rock salt crystal.

perpendicular and parallel receptively to the chiral vector of the enclosing carbon nanotube. However, for nanocrystallites with m_1 and m_2 values larger than two, there are no corresponding $(n,n)_{sq}$ SWINTs. This is to be expected as the former are considered as long sections of the bulk rock-salt crystal and the latter are cylindrical by definition being formed from the rolling of the infinite square net sheet.

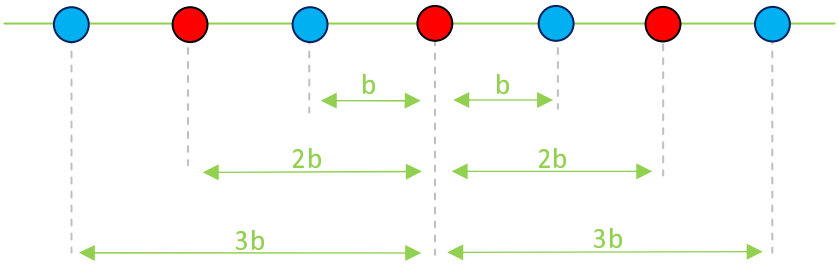

Figure 6.11: A one dimensional chain of alternating cations and anions. The power series for $\ln(1+x)$ enables us to evaluate the Madelung constant as $2\ln(2)$. The factor of two arises as the separations are summed to infinity both left and right of the central ion.

In the model that describes the energetics of these $(m_1 \times m_2 \times \infty)$ nanocrystallites, the energy is arbitrarily partitioned into the interaction energy of an ion residing in an infinite chain of alternating cations and anions and the interaction energy of an ion with cations and anions in adjoining ion chains. This is a convenient way of partitioning the energy as the one-dimensional Madelung constant of a chain of

alternating ions is well defined (see, for example, Kittel and McEuen [42]). As the ions are equally spaced at a distance b from one another we can sum over all the separations r_{ij} within the chain in order to evaluate the coulombic energy (see figure 6.11).

$$U_{chain}(b) = \frac{1}{2}\sum_{j=1,i\neq j}^{N}\sum_{i=1}^{N}\frac{z_i z_j}{r_{ij}} \tag{6.11}$$

$$= 2\Big[-\frac{1}{b}+\frac{1}{2b}-\frac{1}{3b}+\frac{1}{4b}-...\Big] \tag{6.12}$$

$$= \frac{2}{b}\Big[-1+\frac{1}{2}-\frac{1}{3}+\frac{1}{4}-...\Big]. \tag{6.13}$$

The separations occur at integer values of b and the alternating sign represents the alternating cation-cation and cation-anion interactions. The factor of two arises due to the interactions to the left and right of the central cation. If we take $x = 1$ in the power series

$$\ln(1+x) = x-\frac{x^2}{2}+\frac{x^3}{3}-\frac{x^4}{4}+...\frac{(-1)^{n+1}x^n}{n}+..., \tag{6.14}$$

equation 6.13 simplifies to

$$U_{chain}(b) = -\frac{2}{b}\ln(2) \tag{6.15}$$

or

$$U_{chain}(b) = -\frac{1}{b}M_{1D}, \tag{6.16}$$

where M_{1D} is given by

$$M_{1D} = 2\ln(2), \tag{6.17}$$

the Madelung constant for a one-dimensional chain of alternating ions.

Since the energy of an ion residing in the infinite chain has been established ($-\frac{2}{b}\ln(2)$), only the energy of an ion interaction with adjoining chains remains to be quantified.

Bichoutskaia and Pyper [7] define the energy of an ion in the $(m_1 \times m_2 \times \infty)$ nanocrystallite as

$$U^{nano}(a,b) = U^{nano}_{chain}(b)+U^{nano}_{inter}(a,b)+\frac{2A}{b^n}+\frac{CA}{a^n} \tag{6.18}$$

$$U^{nano}(a,b) = -\frac{2}{b}\ln(2)+U^{nano}_{inter}(a,b)+\frac{2A}{b^n}+\frac{CA}{a^n}, \tag{6.19}$$

where the second term is the interaction energy between adjoining chains and the third and fourth terms are the short range repulsions evaluated via the Born model (rather than a Born-Mayer expression that has been used in this work). The short range repulsion only applies to nearest neighbour interactions in a chain (the third term) and inter-chain nearest neighbours (fourth term) and are functions of the nearest neighbour separations b and a respectively (defined in figure 6.10). From our calculations in section 6.4 (where we found the inclusion of the second nearest neighbour anion-anion repulsions of utmost importance to determining the energies of our cylindrical crystallites), this omission of anion-anion repulsion is clearly an over simplification.

It is helpful to introduce the definition of the ratio $x = a/b$ to obtain

$$U^{nano}(a,b) = \frac{-2ln2 - M_b(x)}{b} + \frac{2A}{b^n} + \frac{CA}{a^n}, \tag{6.20}$$

where $M_b(x)$ is an effective Madelung constant for the inter-chain ion interactions and the constant C depends on the coordination numbers of the ions in the nanocrystallite. The effective Madelung constant (and in turn, the inter-chain energy) can be evaluated by summing over all the inter-chain ion interactions as follows

$$U^{nano}_{inter} = -\frac{M_b(x)}{b} \tag{6.21}$$

$$= -\frac{1}{b}\Big[\frac{2}{n_c}\sum_q (-1)^{q+1} n^q_{cp}\Big(\frac{1}{x\sqrt{q}} - 2\sum_{m=1}^{\infty}\frac{(-1)^{m+1}}{(qx^2+m^2)^{1/2}}\Big)\Big], \tag{6.22}$$

where n_c is the number of chains in the nanocrystallite, q indicates the position of the chain within the crystallite and n^q_{cp} is the number of pairs of chains of type q.

The Madelung energies of the various nanocrystallites were determined by Bichoutskaia and Pyper [7] and it was found that the energy of interaction between adjoining chains (U^{nano}_{inter}) is significantly weaker than the energy of the single chain itself ($U^{nano}_{chain} = -\frac{2}{b}ln(2)$). This results in a contraction of cation-anion separations along the chain so that the ratio x is greater than 1, consistent with the experimental observation of the KI crystallites encapsulated within carbon nanotubes [87]. Values of the ratio x for which U^{nano} was minimised were then determined by numerical methods. The ratio x is found to be dependent on the Born exponent n of the short-range repulsion terms in equation 6.19 but independent of the parameter A (in other words the ratio x is dependent on the rate of decay rather than the strength of the short-range repulsion).

Clearly, the $(m_1 \times m_2 \times \infty)$ nanocrystallites examined in this model are closely related to the $(n,n)_{sq}$ INTs of our work. Both are infinite pseudo one-dimensional

structures consisting of chains of alternating ions running along the length of the carbon nanotube. In the nanocrystallite the chains are arranged to form small subsections of the bulk rock salt with a square net cross section. In the $(n,n)_{sq}$ INTs the chains are arranged to form the surface of a cylinder. In this work, the model of Pyper and Bichoutskaia will be adapted to describe the energetics of the $(n,n)_{sq}$ INTs. This explains the contraction of the cation-anion distances that was observed in the $(n,n)_{sq}$ INT structures produced in the molecular dynamics simulations of chapter 5. Furthermore, it is extended to describe the $(n,0)_{sq}$ INT morphology and thus explains the discrimination towards the $(n,n)_{sq}$ INTs observed in simulation, in terms of the coulombic interactions.

6.7 A "chain model" for the $(n,n)_{sq}$ INTs

In this section we will derive a "chain model" for the $(n,n)_{sq}$ INTs in the spirit of the Bichoutskaia and Pyper method for the "bulk-like" $(m_1 \times m_2 \times \infty)$ nanocrystallites.

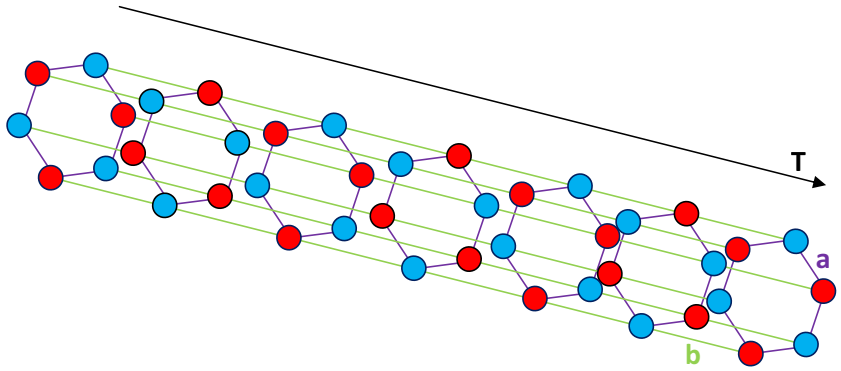

Figure 6.12: The $(3,3)_{sq}$ INT consists of six straight chains of alternating cations-anions that are arranged in a cylindrical geometry. We define the nearest neighbour separations as b running parallel to the nanotube axis (green) and a for the separations perpendicular to the nanotube axis (purple).

6.7.1 The $(n,n)_{sq}$ INT, where $n \geq 2$

Once again we define the ratio $x = a/b$ for the INT$_{sq}$s where a is the nearest neighbour separation running perpendicular to the nanotube axis and b is the separation that lies parallel with respect to the nanotube axis, as can be seen in figure 6.12.

For $n \geq 2$, the energy is given by the following expression which is equivalent to Bichoutskaia and Pyper's equation 6.19 with the Born-Mayer expression for the

nearest neighbour repulsions (instead of the Born model):

$$U^{n,n}(a,b) = U^{n,n}_{chain}(b) + U^{n,n}_{inter}(a,b) + 2\beta e^{-\alpha a} + 2\beta e^{-\alpha b} \quad (6.23)$$

$$U^{n,n}(a,b) = -\frac{2}{b}\ln(2) + U^{n,n}_{inter}(a,b) + 2\beta e^{-\alpha a} + 2\beta e^{-\alpha b}. \quad (6.24)$$

We note that once again, the term $U^{n,n}_{chain}$ takes the value of $-\frac{2}{b}\ln(2)$ since the structure consists of straight chains of alternating cations and anions as with the nanocrystallites. As we observed with the $(m_1 \times m_2 \times \infty)$ nanocrystallites, the short range repulsion is only accounted for in the nearest neighbour cation-anion interactions. This is clearly an over simplification, as the short range repulsion of the anion-anions are significant (section 6.4).

It is helpful to write the expression as a function of x and b.

$$U^{n,n}(a,b) = \frac{-2\ln(2) - M_b(x)}{b} + 2\beta e^{-\alpha x b} + 2\beta e^{-\alpha b}. \quad (6.25)$$

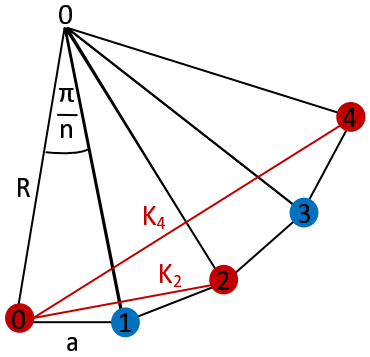

Figure 6.13: For a (n,n)$_{sq}$ INT, the value K_i is the shortest distance between an ion in the 0^{th} chain and the i^{th} chain. By definition K_i lies perpendicular to the nanotube axis.

Aside from the alternative approach to the short range repulsion, this expression differs in the definition of $M_b(x)$. We recall that this term accounts for the inter-chain interactions and therefore depends on the inter-chain separations. The effective Madelung constant $M_b(x)$ differs from the $(m_1 \times m_2 \times \infty)$ nanocrystallites as the structures are now cylindrical in geometry. The new effective Madelung constant for the inter-chain interactions is given by:

$$M_b(x) = -\sum_{i=1}^{2n}\left(\frac{(-1)^i}{K_i x} + 2\sum_{j=1}^{\infty}\frac{(-1)^{i+j}}{(K_i^2x^2 + j^2)^{\frac{1}{2}}}\right). \quad (6.26)$$

Equation 6.26 is a summation over the i adjoining chains. The first term in this summation corresponds to the interaction of an ion in the 0^{th} chain with its nearest neighbour in the i^{th} adjoining chain. This is a function of K_i where aK_i corresponds

to the shortest distance between the two ion chains (see figure 6.13). For a $(n,n)_{sq}$ INT, the value of K_i in terms of i and n can be derived as follows. The radius of the $(n,n)_{sq}$ INT R is

$$R = \frac{a}{2\sin(\frac{\pi}{2n})} \tag{6.27}$$

and therefore the distance K_i (the shortest distance between an ion and the i^{th} adjoining chain) is given by

$$K_i = 2R\sin(\frac{i\pi}{2n}) \tag{6.28}$$

$$= a\frac{\sin(\frac{i\pi}{2n})}{\sin(\frac{\pi}{2n})}. \tag{6.29}$$

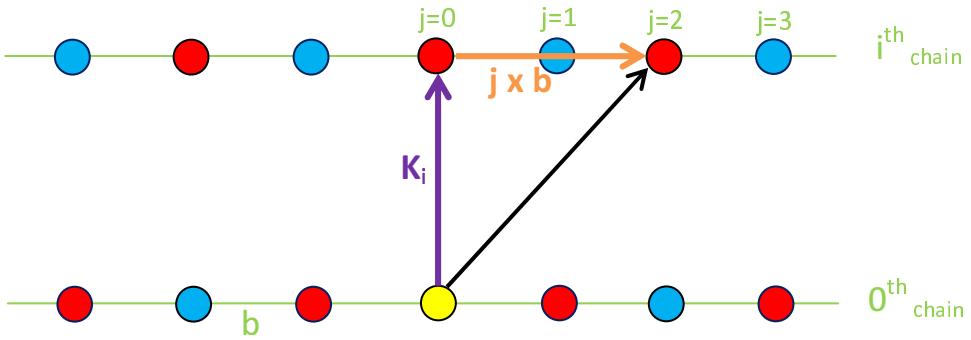

Figure 6.14: In order to evaluate $U^{n,n}_{inter}$, a summation is required over the distance from the yellow ion to every other ion in the i^{th} adjoining chain. This diagram shows the distance between the yellow ion and the $j = 2$ ion in the adjoining i^{th} chain. This is composed of a the shortest distance between the two chains perpendicular to the nanotube axis, K_i (equation 6.29) and a distance along the i^{th} chain (in this case $2b$) which lies parallel to the nanotube axis. The factor two in the summation over j in equation 6.26 is due to the interactions both left and right of the $j = 0$ ion in the i^{th} chain.

The second term in equation 6.26, which is a summation over j is the interaction of an ion with the j^{th} ion in the adjoining chain which resides at successively larger separations, see figure 6.14. Hence, the alternating sign of this expression arises from the alternating charges on the ions as we travel further down the i^{th} adjoining chain. This separation between an ion and an ion in the i^{th} adjoining chain can be described by two components. Firstly, a component perpendicular to the nanotube axis K_i which is the shortest distance between the two chains in question (see figure 6.13). Secondly, a component that runs parallel to the nanotube axis which is an integer multiple of the nearest neighbour separations b.

The energy of the $(n,n)_{sq}$ INT is therefore rationalised in terms of the intra-chain interactions ($U^{n,n}_{chain}$) which is well defined by the one-dimensional Madelung

constant M_{1D} and the inter-chain interactions in which an ion interacts with every other ion in each of the other i^{th} chains in the structure. We will examine the relative strengths of these terms in a later section (section 6.8) but firstly we will examine how the energy of the $(\mathrm{n,n})_{sq}$ INT varies with the ratio x.

6.7.2 Variation of the energy of the $(\mathrm{n,n})_{sq}$ INTs with the ratio x

During the molecular dynamics simulations, $(\mathrm{n,n})_{sq}$ INT structures were observed in which the nearest neighbour separations parallel to the nanotube axis (b) were shorter than the separation perpendicular to the nanotube axis (a), see for example figure 5.8. This is consistent with a more attractive $U^{n,n}_{chain}$ energy than $U^{n,n}_{inter}$ energy. This phenomenon was most pronounced for potentials with a smaller amount of short-range repulsion (i.e potentials I and II).

We will see how the overall $(\mathrm{n,n})_{sq}$ INT energy $U^{n,n}(b,x)$ varies with the ratio x and b by determining the partial derivatives $\left[\frac{\partial U^{n,n}}{\partial x}\right]_b$ and $\left[\frac{\partial U^{n,n}}{\partial b}\right]_x$. The global minimum will occur when both these quantities are equal to zero. The first partial derivative at constant b is

$$\left[\frac{\partial U^{n,n}(x,b)}{\partial b}\right]_x = \frac{2ln2 + M_b(x)}{b^2} - 2\beta\alpha[xe^{-\alpha bx} + e^{-\alpha b}] \tag{6.30}$$

and the second partial derivative at constant x is

$$\left[\frac{\partial U^{n,n}(x,b)}{\partial x}\right]_b = -\frac{1}{b}\frac{dM(x)}{dx} - 2\beta\alpha be^{-\alpha bx}. \tag{6.31}$$

We have two equations in x and b; if we set them each to zero we can solve for both and locate the global minimum. From equation 6.31 we have

$$2\beta\alpha = -\frac{1}{b^2}\frac{dM(x)}{dx}e^{\alpha bx} \tag{6.32}$$

and

$$2\beta\alpha e^{-\alpha bx} = -\frac{1}{b^2}\frac{dM(x)}{dx}. \tag{6.33}$$

Substitute equations 6.32 and 6.33 into equation 6.30 and we have

$$\frac{2ln2 + M_b(x)}{b^2} + \frac{x}{b^2}\frac{dM(x)}{dx} + \frac{1}{b^2}\frac{dM(x)}{dx}e^{-\alpha b}e^{\alpha bx} = 0. \tag{6.34}$$

We can rearrange this for $b(x)$

$$b(x) = \frac{1}{\alpha(x-1)} ln\Big[-[\frac{2ln2 + M_b(x)}{\frac{dM(x)}{dx}}] - x\Big]. \tag{6.35}$$

In order to evaluate $b(x)$ we need $\frac{dM(x)}{dx}$ given by

$$\frac{dM_b(x)}{dx} \quad = \quad M_b(x) = -\sum_{i=1}^{2n}\left(\frac{(-1)^{i+1}}{K_i x^2} - 2\sum_{j=1}^{\infty}(-1)^{i+j}\frac{K_i^2 x}{(K_i^2x^2 + j^2)^{\frac{3}{2}}}\right). \tag{6.36}$$

If we substitute $b(x)$ into equation 6.31, we have a function $\big[\frac{\partial U^{n,n}(x)}{\partial x}\big]_b$ which is only a function of x. If the function $\big[\frac{\partial U^{n,n}(x)}{\partial x}\big]_b$ is evaluated for various values of x then we can determine for what value of x (and therefore b) the partial derivatives 6.32 and 6.33 are equal to zero. We note that equation 6.35 is not defined for $x = 1$. As a result, the nearest neighbour separations perpendicular to the nanotube axis (a) can never be equal to the separations lying parallel to the nanotube axis (b), for any $(n,n)_{sq}$ INT of finite radius.

6.7.3 The $(1,1)_{sq}$ INT

For $(n,n)_{sq}$ INTs with $n = 1$ then the energy expression differs in the repulsion terms. Since the $(1,1)_{sq}$ INT corresponds to a "ladder-like" structure, each ion experiences only one repulsion perpendicular to the nanotube axis at a distance a (instead of two nearest neighbour repulsions in $(n,n)_{sq}$ INTS where $n > 1$). The energy expression for the $(1,1)_{sq}$ INT becomes

$$U^{n,n}(x,b) = (\frac{-2ln2 - M_b(x)}{b} + \beta e^{-\alpha x b} + 2\beta e^{-\alpha b}). \tag{6.37}$$

Therefore, the force with respect to b becomes

$$\Big[\frac{\partial U(x,b)}{\partial b}\Big]_x = \frac{2ln2 + M_b(x)}{b^2} - \beta\alpha[xe^{-\alpha bx} + 2e^{-\alpha b}] = 0 \tag{6.38}$$

and the force with respect to x becomes

$$\Big[\frac{\partial U(x,b)}{\partial x}\Big]_b = -\frac{1}{b}\frac{dM(x)}{dx} - \beta\alpha b e^{-\alpha bx} = 0. \tag{6.39}$$

By following the same procedure for $(n,n)_{sq}$ INTs with $n \geq 2$, we find that $b(x)$ is given by:

$$b(x) = \frac{1}{\alpha(x-1)} ln\Big[-\frac{1}{2}[\frac{2ln2 + M_b(x)}{\frac{dM(x)}{dx}}] - \frac{x}{2}\Big]. \tag{6.40}$$

6.7.4 Calculated ratios

The partial derivatives 6.32 and 6.33 are plotted for various $(n,n)_{sq}$ INTs as a function of the ratio x in figure 6.15 using the repulsive anion-cation Born-Mayer parameters from potential I. The partial derivatives are both equal to zero at the global minimum which is identified as where the function crosses the x-axis in this figure. As we increase the value of n (or the radius of the INT), the ratio x approaches unity. This is to be expected as at a value of $n = \infty$ (an infinitely large INT with zero curvature) we have an infinite square net planar sheet where the two lengths a and b become equivalent.

Figure 6.16 shows the predicted values of a and b using the short range anion-cation repulsion from each of the four potentials. As expected, the potential I values tend to the shortest separations in the infinite plane and potential III the largest. Potential II and IV are intermediate between these length scales. This is due to their respective anion-cation radius ratios which also give rise to their preferred crystal morphology in the bulk. Deviations from these calculated values of a and b may be observed in the molecular dynamics simulations due to several contributing factors. Firstly, only the nearest neighbour cation-anion repulsions have been accounted for which is clearly a simplification. For example, the anion-anion repulsions have been found to play an important role in discriminating between the two INT_{sq} morphologies (section 6.4). The presence of the carbon nanotube, interactions with the surrounding molten salts and thermal fluctuations will also cause deviations from these calculated values during the simulations. Indeed, the ratios observed in the molecular dynamics simulations are consistently larger than those predicted from these results. For example, a small sample of bond lengths from the molecular dynamics simulations have been surveyed. These were from the $(1,1)_{sq}$ INT within the (15,0) carbon nanotube using potential I and the $(2,2)_{sq}$ INT within the (15,0) carbon nanotube using potentials II, III and IV. The ratio x was found to be 1.76, 1.50, 1.07 and 1.24 respectively which compares qualitatively with the calculated ratios of 1.16, 1.09, 1.04 and 1.07.

6.8 A "chain model" for the $(n,0)_{sq}$ INTs

In the previous section a chain model was developed for quantifying the coulombic energy of the $(n,n)_{sq}$ INTs. The same approach can be utilised for determining the coulombic energy of the $(n,0)_{sq}$ INTs by stating the energy in terms of a sum of the interaction along a chain of alternating ions and the energy of interaction between

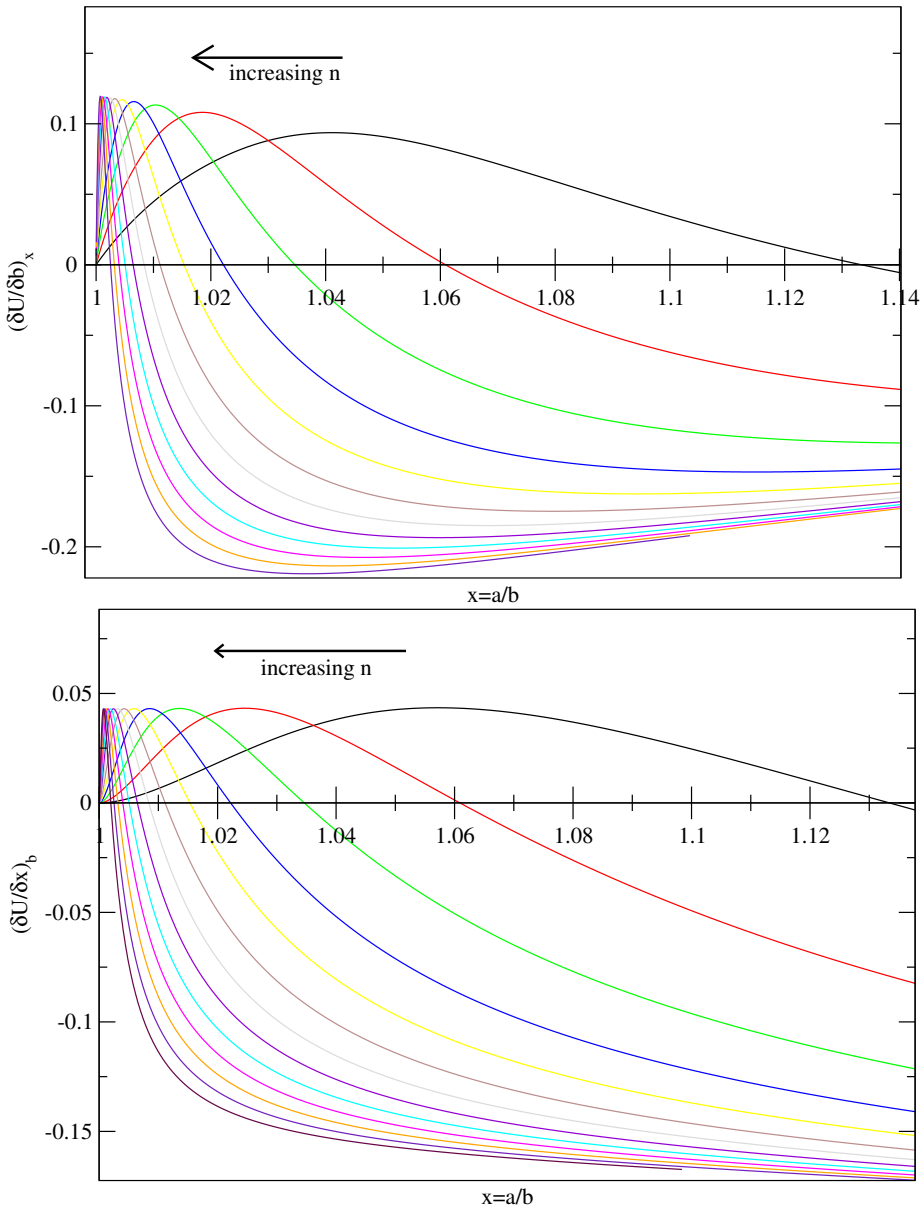

Figure 6.15: The partial derivatives as a function of x. Where the functions cross the x axis, both partials are equal to zero and they are at the global minimum. As the value of n increases (from 1 to 10) the global minimum occurs at a smaller ratio of x.

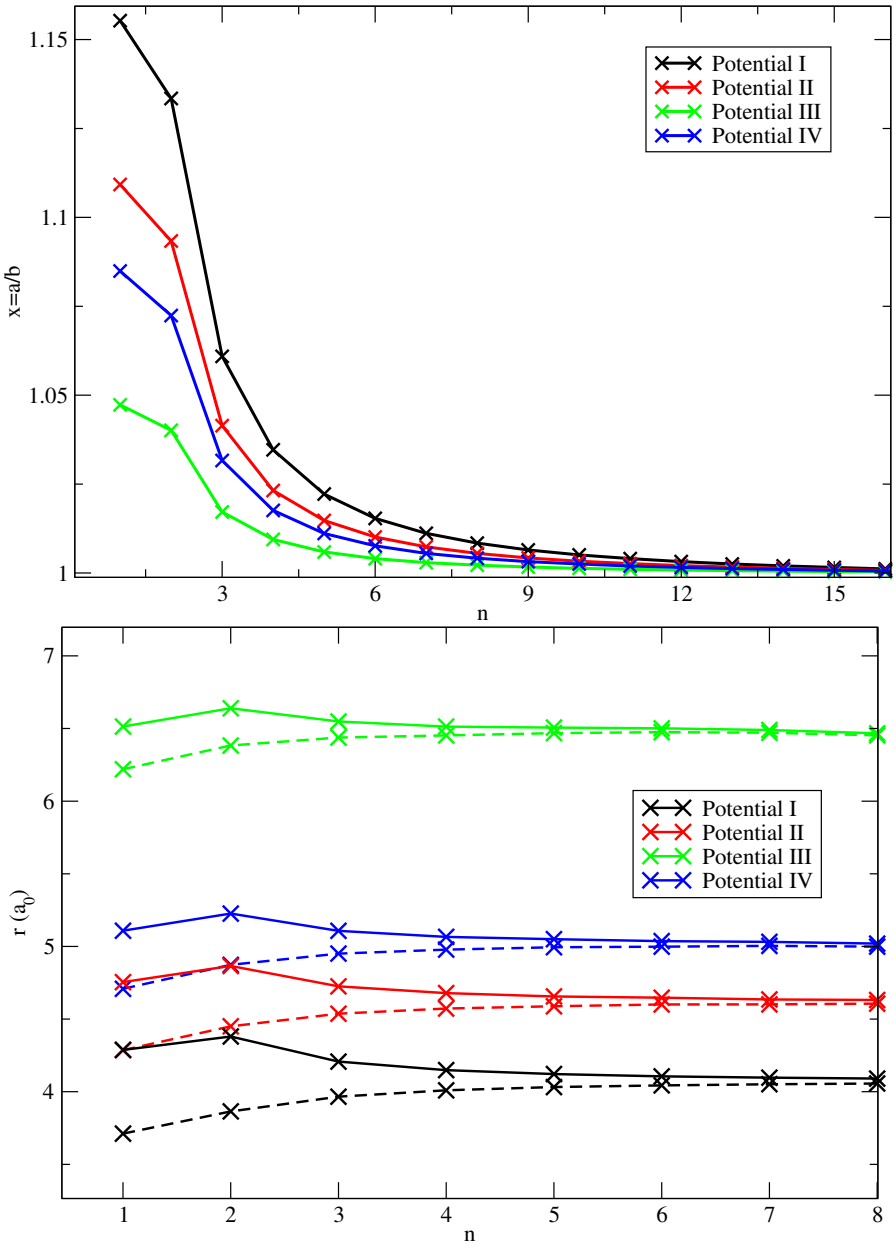

Figure 6.16: Calculations to locate the global minimum for the $(n,n)_{sq}$ INTs. Top: The ratio $x = a/b$ as a function of n. As the INT increases in size, the contraction along the chains becomes less pronounced. The contraction is greatest for potential I, due to the weaker anion-cation repulsion in this model. Bottom: The lengths a (solid lines) and b (dashed lines) are plotted as a function of n. As the radius of the $(n,n)_{sq}$ INT increases, the two anion-cation separations approach that of the infinite square net plane. The value of a is smaller than expected for the $(1,1)_{sq}$ INT due to there only being one nearest neighbour short range repulsion perpendicular to the nanotube axis. For $n \geq 2$ there are two nearest neighbour short range repulsions both perpendicular and parallel to the nanotube axis.

adjoining alternating chains;

$$U^{n,0} = U^{n,0}_{chain} + U^{n,0}_{inter}. \tag{6.41}$$

There is a fundamental difference when comparing the $(n,0)_{sq}$ INTs with both the $(m_1 \times m_2 \times \infty)$ nanocrystallites and the $(n,n)_{sq}$ INTs. The latter two both consist

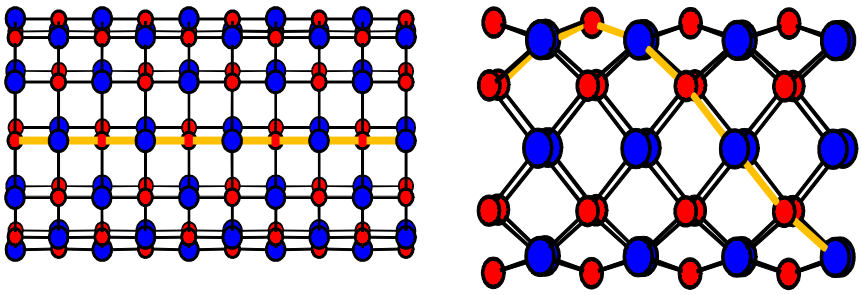

Figure 6.17: Two classes of INT_{sq} with a chain of alternating cation and anions highlighted in orange. Left: The $(n,n)_{sq}$ INT which is formed of straight chains of alternating actions and anions arranged into a cylinder. Right: The $(n,0)_{sq}$ INT which is formed of twisted chains of alternating cations and anions arranged into a cylinder.

of straight chains of alternating ions running down the length of the structure, these are then arranged into a bulk-like crystallite or a cylinder respectively. In the case of the $(n,0)_{sq}$ INTs however, the alternating chains of ions do not lie parallel to the nanotube axis and instead spiral around the cylinder surface as can be seen in figure 6.17. We can still consider the energy of a sum of the energy of an ion in a chain plus the interaction energy of the ion with the other chains. However, the energy of an ion in a spiralling chain $U^{n,0}_{chain}$ is no longer equal to $-2ln2$ and must be determined by a new expression.

A summation is required in which a central ion interacts with all other ions in the spiralling chain. The distance between the central ion and an ion further down the chain can be calculated by considering the sum of a vector parallel to the nanotube axis and a vector perpendicular to the axis. The parallel component of the m^{th} ion in a chain is

$$D^m_{\parallel} = \frac{m\sqrt{2}}{2.} \tag{6.42}$$

The perpendicular component is derived from equation 6.3 to give

$$D^m_{\perp} = \frac{2n}{\pi} sin\Big(\frac{m\pi}{2n}\Big). \tag{6.43}$$

For a $(n,0)_{sq}$ INT, with bond lengths corrected by the factor y'/y, so that they are

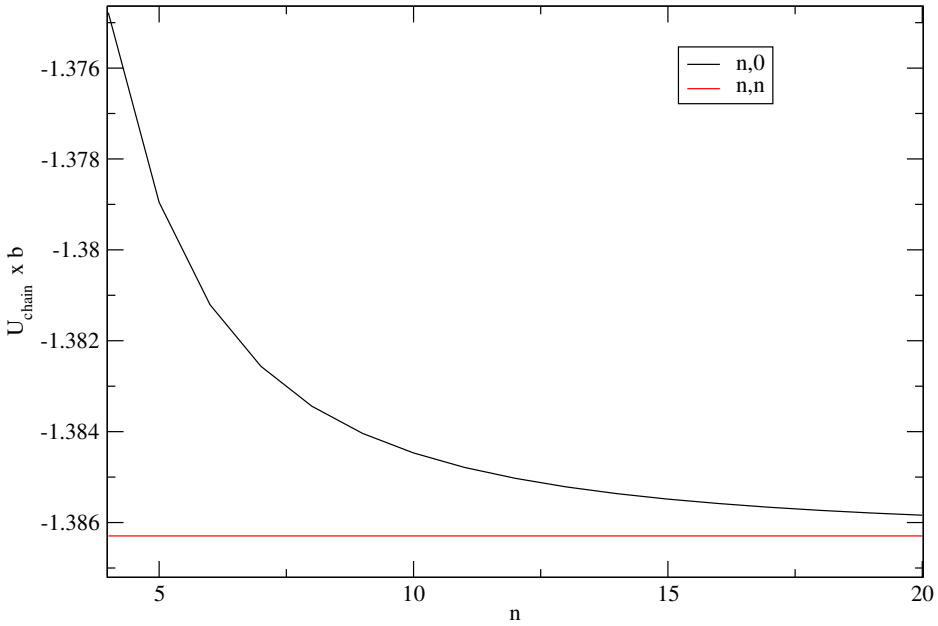

Figure 6.18: The energy of a chain of alternating ions in a $(n,0)_{sq}$ and $(n,n)_{sq}$ INT as a function of n. $U^{n,0}_{chain}$ is calculated from equation 6.46 and $U^{n,n}_{chain}$ is equal to $-2\ln 2$ at all radii since the chain is always straight for all $(n,n)_{sq}$ INTs.

equal to those in the infinite sheet (as described in 6.1), this then becomes

$$D^m_\perp = \frac{2n}{\pi} sin\Big(\frac{m\pi}{2n}\Big)\Big[\frac{y}{y'}\Big]^{-1} \tag{6.44}$$

$$D^m_\perp = \frac{2n}{\pi} sin\Big(\frac{m\pi}{2n}\Big)\Big[\frac{2n}{\pi} sin\Big(\frac{\pi}{2n}\Big)\Big]^{-1}. \tag{6.45}$$

The summation over the ions in the same chain is therefore

$$U^{n,0}_{chain} = -\frac{2}{b}\sum_{m=1}^{m=\infty} \frac{(-1)^{m+1}}{\Big[(D^m_\perp)^2 + (D^m_\parallel)^2\Big]^{\frac{1}{2}}}. \tag{6.46}$$

Such an interaction is shown in figure 6.20, where the orange central ion is shown to interact with all other ions in the same chain which is highlighted with a black-dashed line. A sum over all these interactions to the left and right of the central ion gives $U^{5,0}_{chain}$.

The energy of an infinite chain ($U^{n,0}_{chain}$) was calculated for various $(n,0)_{sq}$ INTs using equation 6.46. This contribution becomes more negative at larger values of n, indicating the energy of the chain is more favourable as the curvature of the INT decreases. Figure 6.18 shows $U^{n,0}_{chain}$ in comparison to the energy of an infinite straight chain of alternating ions which is in fact $U^{n,n}_{chain}$ or $-2\ln(2)$. At very large values of n corresponding to large radii $(n,0)_{sq}$ INTs with low curvature, the chain

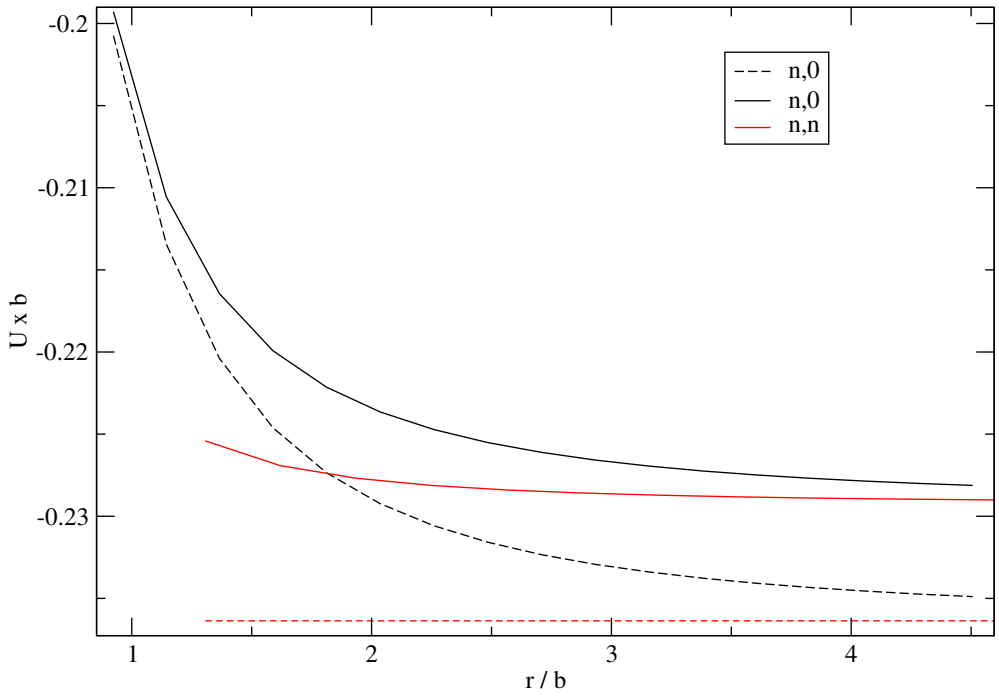

Figure 6.19: The energy of interaction of an ion with neighbouring chains ($U_{inter}^{n,n}$ and $U_{inter}^{n,0}$). The interaction energy is shown for $(n,0)_{sq}$ INTs and $(n,n)_{sq}$ INTs (with corrected nearest neighbour bond lengths to the planar values) as a function of radii (solid lines). The dashed lines show the energy of the two nearest neighbour chains. As expected these are attractive interactions since the nearest neighbours in adjoining chains are of opposite charge. We see that the nearest neighbour chains dominate the overall U_{inter} terms in both morphologies. The nearest neighbour $U_{inter}^{n,n}$ is constant due to the chain-chain separation being a constant distance of a apart for all $(n,n)_{sq}$ INTs.

energy $U^{n,0}_{chain}$ approaches $U^{n,n}_{chain}$.

The interaction energy of an ion with ions in neighbouring chains $U^{n,0}_{inter}$ can also be calculated in a similar manner for the $(n,0)_{sq}$ INT by considering a perpendicular ($D_\perp$) and parallel ($D_\parallel$) component to the cylinder axis. Unlike the $(n,n)_{sq}$ INTs the distance of ions in neighbouring chains is not symmetrical about the central ion and so must be made up of two separate summations, as can be seen in the second part of equation 6.47. This is because only the perpendicular component is reduced from the planar value on folding the INT into a cylinder and not the parallel component. The energy of interaction is given by

$$\begin{aligned} U^{n,0}_{inter} &= -\frac{1}{b}\sum_{q=2}^{n}\frac{(-1)^q}{\left[\left(D_\perp^{q-1}\right)^2+\left(D_\parallel^{q-1}\right)^2\right]^{\frac{1}{2}}} \\ &- \frac{1}{b}\sum_{q=2}^{n}\sum_{p=q}^{\infty}\frac{(-1)^{p+1}}{\left[\left(D_\perp^{p}\right)^2+\left(D_\parallel^{p+2(1-q)}\right)^2\right]^{\frac{1}{2}}}+\frac{(-1)^{p+1}}{\left[\left(D_\perp^{p+2(1-q)}\right)^2+\left(D_\parallel^{p}\right)^2\right]^{\frac{1}{2}}}. \end{aligned} \quad (6.47)$$

The first summation in equation 6.47 represents the closest ion-ion interaction in the chain, as shown in orange in figure 6.20. The second two summations represented by the blue and red parts of the $q = 3$ chain can also be seen in this diagram.

We can compare the interaction of the chains in the $(n,0)_{sq}$ INTs calculated by this "chain model" with that of the $(n,n)_{sq}$ INTs, as shown in figure 6.19. We find that $U^{n,0}_{inter}$ is higher in energy than the $U^{n,n}_{inter}$ nanotube at all radii. Therefore it is both the energy of the alternating ion chain and the interaction between the chains that are unfavourable in the $(n,0)_{sq}$ INTs.

In order to understand the difference in the U_{inter} we can split the energy into both repulsive and attractive interactions. The interaction energy between chains is overall repulsive if the nearest neighbour interactions between ions in the differing chains is repulsive. Conversely, if the nearest neighbours are attractive the overall interaction is also attractive. Figure 6.21 shows that the attractive interactions dominate the interaction energy and that they favour the $(n,n)_{sq}$ INTs. This is to be expected as the nearest neighbour chain interactions are attractive. The repulsive interactions are much smaller and actually favour the $(n,0)_{sq}$ INTs. This is consistent with the results shown in figure 6.9 in which the INT_{sq} energies were broken down into the anion-anion and anion-cation contributions.

In a $(n,0)_{sq}$ INT there are n chains of alternating ions that make up the INT and in the $(n,n)_{sq}$ INT there are $2n$ chains interacting. We can look at the energies of the individual chains to see if the lower energy is simply due to an increase in the number of attractive interactions (due to the larger number of chains) or if it is due

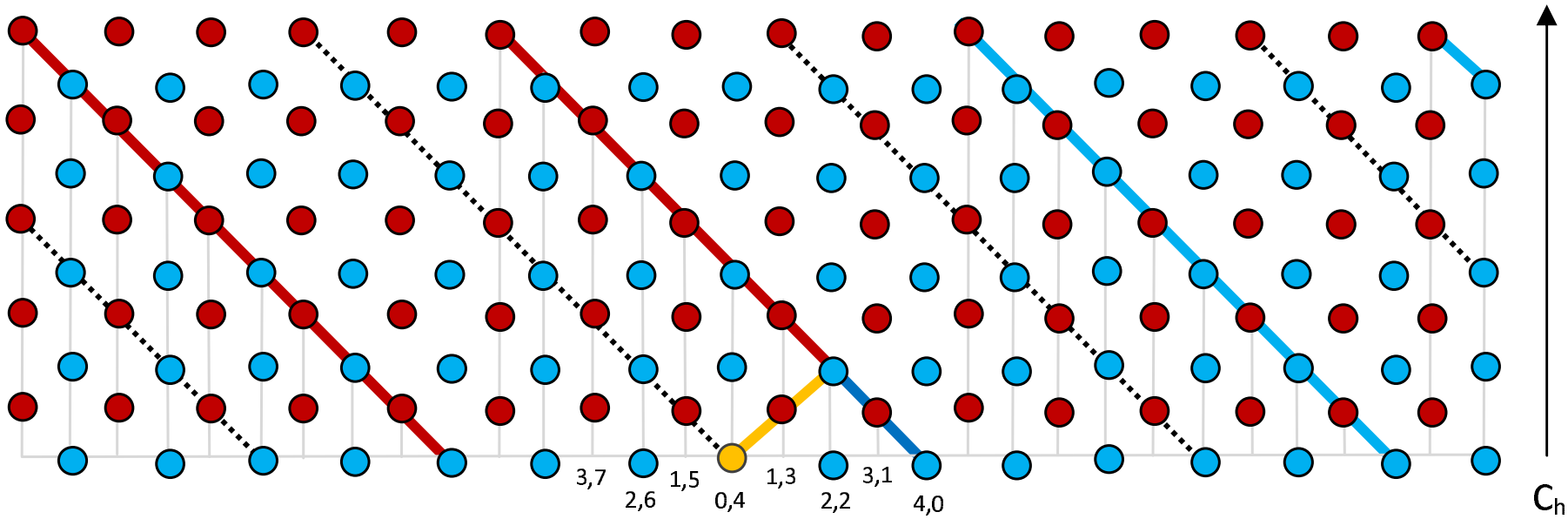

Figure 6.20: The square net sheet that can be rolled to form the $(5,0)_{sq}$ INT with the vector C_h forming the circumference. Before the sheet is rolled, the perpendicular and parallel components of the distance between neighbouring ions are both equal to $a\sqrt{2}/2$. The diagram shows the interaction of a central ion (orange) residing in the $q = 1$ chain (black dashed line) with all the ions in the $q = 3$ chain (red and blue lines). The first part of the sum in equation 6.47 accounts for the closest interaction in that chain (shown in orange). The second part of equation accounts for all the other ions in the chain and is therefore made up of two summations. These correspond to the ions in the red and blue parts of the chain respectively. We note that the perpendicular components of the nanotube are reduced by the act of rolling the sheet and can be calculated using equation 6.43. The parallel components remain unchanged on folding the sheet and therefore the summation corresponding to the red part of the chain differs from the summation corresponding to the blue part of the chain. This is because the interaction with ion (3,1) in the red part of the chain is not equal to the interaction with (1,3) ion in the blue part of the chain, for example.

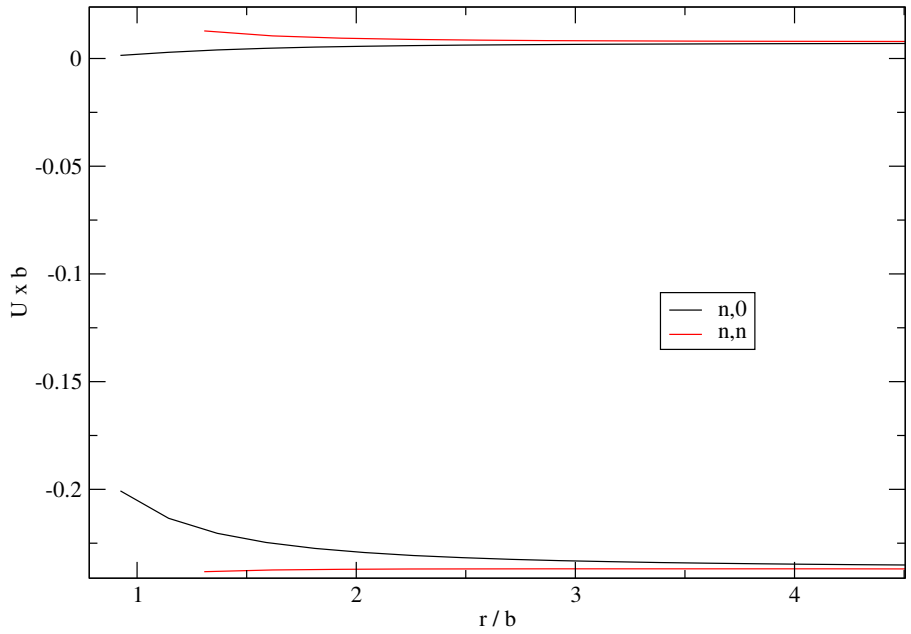

Figure 6.21: The repulsive and attractive interactions of an ion with neighbouring chains in a $(n,0)_{sq}$ INT and a $(n,n)_{sq}$ INT (with corrected nearest neighbour bond lengths to the planar value) as a function of INT_{sq} radii. The interaction is overall "repulsive" if the central ion is of like charge to its nearest neighbour in the adjoining chain. Conversely, the interaction is overall "attractive" if the central ion is of a different charge to its nearest neighbour in the adjoining chain.

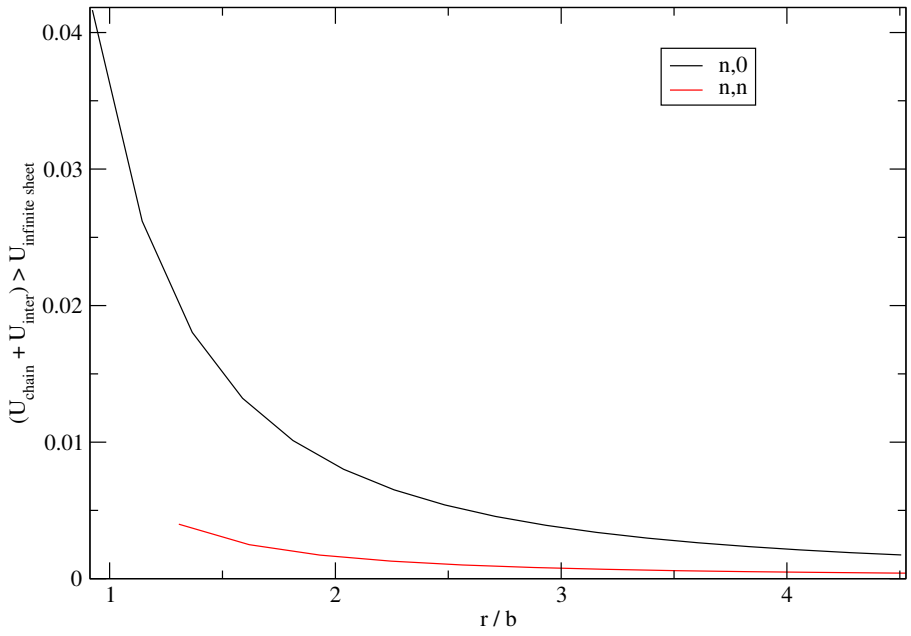

Figure 6.22: The total coulombic energy of the nanotubes (above that of an infinite square net sheet) as a function of nanotube radius as calculated by summing the U_{inter} and U_{chain} terms.

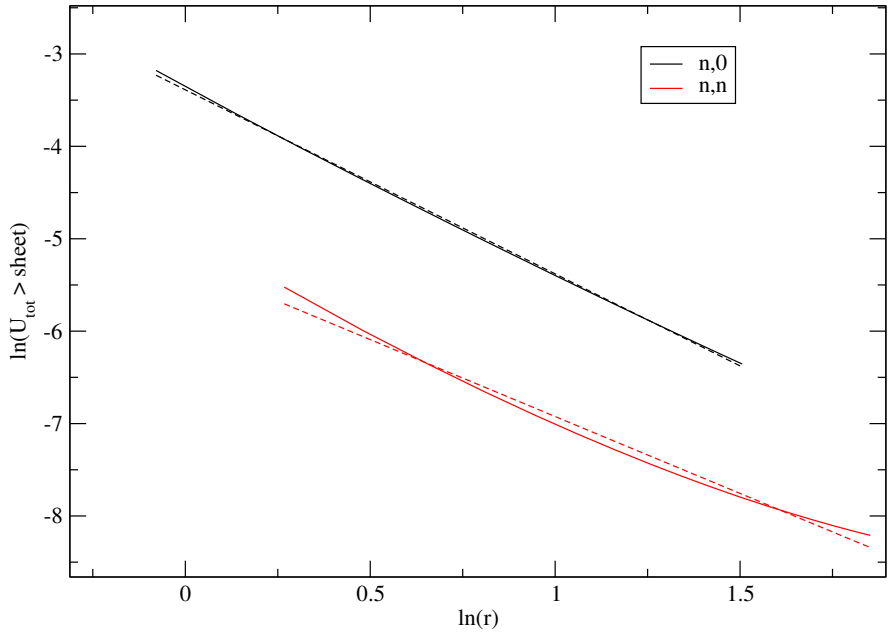

Figure 6.23: Linear regression analysis of the total coulombic energy of the nanotube. The $(n,0)_{sq}$ INTs provide a good fit for the elastic continuum model with a slope of -1.99 ± 0.01. In contrast, the $(n,n)_{sq}$ INTs demonstrate a poor fit, with a slope of -1.66 ± 0.04. However, if we were to assume a good fit to the model in both cases, the intercepts are also very different, indicating different elastic moduli. This suggests the ease of folding the nanotube is dependent on the angle at which the nanotube sheet is folded.

to the strength of a particular interaction of an individual chain (or chains). The solid lines in figure 6.19 show U_{inter} for both morphologies of the INT_{sq}. The dashed lines in that figure are the contribution from the two nearest neighbour chains. This confirms that it is the nearest neighbour chain interactions that dominate the U_{inter} term due to the close proximity of the chains in the INT_{sq}s. As expected, the nearest neighbour chain contribution is constant for the $(n,n)_{sq}$ INT where the chains lie parallel to the nanotube axis at a constant distance b apart.

The total coulombic energies of the two INT_{sq} morphologies can be calculated by summing the U_{inter} and U_{chain} terms, as can be seen in figure 6.22. The calculations confirm that the coulombic energy $U^{n,n}$ is indeed lower in energy than the coulombic energy $U^{n,0}$ at all radii. The natural logarithm of the energies was plotted versus the natural logarithm of the radius and a linear regression was then performed and can be seen in figure 6.23. The coulombic energy of the $(n,0)_{sq}$ INTs give a good fit to the elastic continuum model but the $(n,n)_{sq}$ INTs do not. The slope of the linear regression of this plot is -1.66 ± 0.04 for the $(n,n)_{sq}$ INTs and -1.99 ± 0.01 for the $(n,0)_{sq}$ INTs. We recall that the same trend was observed when this analysis was performed for all the contributions to the INT_{sq} energies in figure 6.5 where the repulsive and dispersion terms were also accounted for. By limiting the analysis to the coulombic energy only, the $(n,n)_{sq}$ shows less deviation from the elastic continuum theory. The excellent fit for the $(n,0)_{sq}$ INTs remains but with an improved standard deviation for the regression when the dipersion and repulsion are neglected.

These calculations were performed for INT_{sq}s in which all the bond lengths have been fixed to the same value. However, we learnt in section 6.7.4 that the energy of the $(n,n)_{sq}$ INTs can be lowered further by a contraction along the alternating ion chains. The bond lengths in the $(n,0)_{sq}$ structure are all equivalent and therefore, there is no equivalent contraction in the $(n,0)_{sq}$ INTs. As a result, the inclusion of this contraction in this comparison of the two morphologies would only act to strengthen the discrimination towards the $(n,n)_{sq}$ through the lowering of the $(n,n)_{sq}$ energies.

6.9 Summary of coulombic interactions

In summary the $(n,n)_{sq}$ INTs are favoured by the coulombic interactions in both the U_{chain} and U_{inter} terms. The U_{inter} term is dominated by the favourable interactions of the nearest neighbour chains. The nearest neighbour chain interaction is constant and lower in energy in the $(n,n)_{sq}$ INTs as the chains are straight and at a constant

separation of b from each other for all radii INTs. In the $(n,0)_{sq}$ INTs the U_{chain}

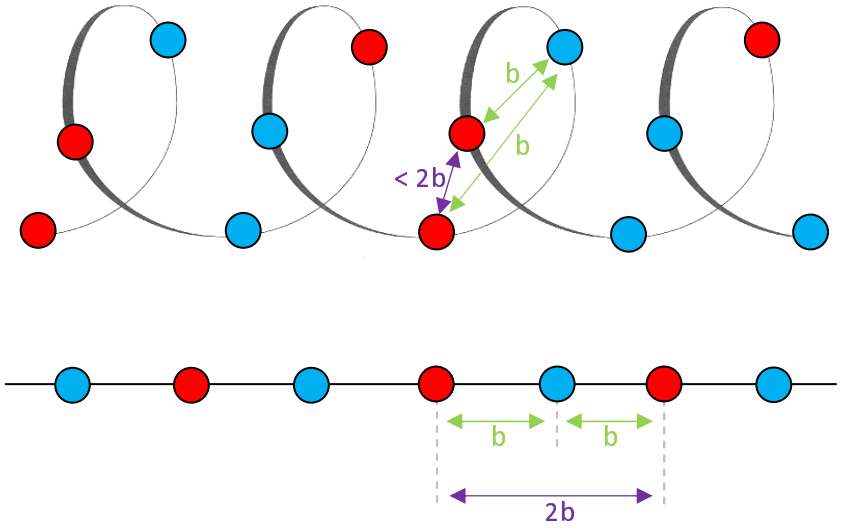

Figure 6.24: The nearest neighbour distances are fixed to b, the separation in the planar square net sheet. Top: A twisted chain of ions such as one observed in the $(n,0)_{sq}$ INT. The nearest neighbour separation in b but due to the twist of the chain, the second nearest neighbour is less than $2b$. Bottom: The distance between the ions in a straight chain is always b. Therefore, there is less repulsion between like charged ions in a straight chain, than in the twisted chain.

term is higher in energy at all radii but approaches that of the $(n,n)_{sq}$ INTs as the radius increases and the spiralling chain becomes more linear in nature. Similarly, the nearest neighbour dominating interaction of the $U_{inter}^{n,0}$ term approaches the more favourable $U_{inter}^{n,n}$ nearest neighbour interaction at large radii as the chains become more linear. Only one interaction favours the $(n,0)_{sq}$ INTs and that is the interaction between chains with like nearest neighbours. However, this effect is overpowered by all other interactions which favour the $(n,n)_{sq}$ INTs.

We can explain both these differences by considering the difference between a spiralling and linear chain. The m^{th} ion in a spiralling chain is closer to the central ion than the m^{th} ion in a linear chain (see figure 6.24). Since the nearest neighbour interactions have been fixed to be at a distance b in both classes of nanotube the difference in the Madelung summation will be dominated by the second nearest neighbour. This is a repulsive interaction and suggests that the coulombic energy of the spiralling chain will always be higher in energy of that in the linear chain.

Chapter 7

Conclusions

In this thesis, the systematic filling of carbon nanotubes has been investigated using molecular dynamics computer simulation. The carbon nanotubes have been modelled as flexible, deformable entities (using the established many body Tersoff II potential model [99, 100]) which advances significantly on previous work in which the tubes were held rigid.

7.0.1 New salt model

We have constructed a simple potential model in which the underlying bulk four coordinate and six coordinate based crystal environments have minima at the same energies. This allows us to investigate the relationship between the formed INT structures and the underlying potential model.

- The new salt model has been characterised in both the molten and crystal phases. The melting point of the system has been determined for both the rock salt (B1) and zinc blende (B3) crystal phases. The difference in melting temperatures between the two crystals is purely entropic in origin.

- The novel thermodynamic properties of the new potential mean that, theoretically, the B3 to B1 pressure-driven phase transition can take place at zero pressure. To further understand the relationships between the different ion coordination environments this transition has been studied directly. The mechanism of the transition appears to include the d-β-Sn intermediate, the observation of which is extremely rare in the literature (see section 1.5.1). However, the mechanism is dependent on both the relaxation time of the thermostat/barostats and whether the anisotropic cell fluctuations are permitted.

- The molten salts have been modelled by four potential models of the MX

stoichiometry, the properties of which are highly dependent on the radius ratio of the ions. As a result, the the potentials can be "fine tuned" by modification of the parameters (e.g. B_{ij}) in order to gain further insight into the physical properties of the system.

7.0.2 Carbon nanotubes

A Tersoff II potential model [99, 100] has been employed to model the carbon nanotubes as flexible entities.

- In order to allow comparison with the formed INTs the key properties of the carbon nanotubes have been determined. Most significantly, in our context, the energetics of a carbon nanotube of radius r appears to demonstrate a simple r^{-2} power law dependence, consistent with an elastic continuum model. As a result, the strain energy of the nanotube appears independent of the nanotube morphology.

- The use of a flexible model allows the carbon nanotube to both rotate and translate during the direct filling simulations requiring the development of additional analysis techniques. A method of analysis has been developed to fit the carbon nanotube coordinates to those of a perfect cylinder and to determine if an ion is encapsulated within the carbon nanotube pore.

7.0.3 Direct filling simulations

The application of the developed model within molecular dynamics simulation models has led to the following conclusions:

- All four potential models have been shown to fill the carbon nanotube with inorganic structures of the MX stoichiometry. The structure of the INT formed can be characterised in terms of whether the carbon nanotube radius falls into the small, large or very large regime. In the small radius regime, the $(n,n)_{sq}$ INTs are the favoured morphology, regardless of the radius ratio of the ionic salt. In the large radius regime, the morphology of the cylindrical INT is determined by the radius ratio of the potential model used.

- The mechanism of filling the carbon nanotubes appears to be based on an increasing number of M-X-M-X... chains within the nanotube pore. The observation of long-lived plateau in the filling profiles are indicative of relatively stable intermediate structures each consisting of an integral number of such alternating ion chains.

- A new intermediate structure, the bent "hinge", is observed which is formed of three chains of alternating ions. In addition, INTs with an anisotropic cross section have been observed to fill the nanotube pore, giving rise to elliptical deformations in the carbon nanotube walls. This new observation is a direct consequence of incorporating the carbon carbon interactions into the model. For example, the three chain "hinge" structure is strongly favoured by the elliptical deformations of carbon nanotube which would not be possible for the rigid representation.

7.0.4 The INT energy landscape

The construction of the underlying potential simulation model determines the underlying INT energy landscape. The application of the model to the direct filling of carbon nanotubes within molecular dynamics simulations reveals the complex nature of these energy landscapes.

- The energy landscape of the INTs appears more complex than that of the carbon nanotubes and does not always conform to the elastic continuum model. For example, the $(n,n)_{sq}$ INTs are the favoured morphology at low radii. The mechanism of filling appears to show the structures "hopping" to successively lower energy basins at increasingly larger radii until the repulsion of the carbon nanotube wall prevents any further "hops".

- The energetics of the $(n,n)_{sq}$ and the $(n,0)_{sq}$ INTs have been decomposed in terms of the energy required to form a M-X-M-X... chain and the energy of interaction between these chains. The energy of interaction energy between chains is shown to be weaker than the individual chain energy. The energy of a straight chain of alternating anions and cations is always lower in energy than a twisted chain of alternating ions and therefore, the $(n,n)_{sq}$ INTs are the favoured morphology. The experimentally observed preference for the rock salt structure nanocrystallites with growth along the $\langle 110 \rangle$ direction within the MX stoichiometry [57, 87] is consistent with this observation that the $(n,n)_{sq}$ INTs are the favoured morphology at low radii.

7.1 Future work

The development and successful application of the flexible model to the salts of the MX stoichiometry paves the way for the application to the direct filling by other molten systems. For example, systems of other stoichiometry that have been

observed experimentally in the filling of carbon nanotubes (MX_2, MX_3 and MX_4) or any alternative MX system which is described by potential models other than the Born-Mayer [36] type. Preliminary investigations in which the flexible model has been applied to the filling of the carbon nanotube with AgI are very encouraging. The model has been constructed using the Rahman, Vashishta and Parrinello (RVP) potential [69] and a more rapid filling rate has been observed than for the current MX systems. The energy landscape of this potential model is expected to be of interest due to the super ionic conducting properties of this system. In addition, the rapidity of the filling will accommodate more simulations from different liquid configurations enabling greater statistical analysis. In this way phenomena, such as the correlation between the carbon nanotube and inorganic nanotube morphologies, can be probed.

Further development of the current model utilising the Born-Mayer potentials [36] is certainly possible. For example, in the current model the ions within the nanotube pore can interact directly with the ions in the surrounding molten liquid. In reality, the electronic properties of the carbon nanotube probably act to alter such interactions. In future, we might consider incorporating a screening charge on the carbon nanotube itself in order to modify the interactions between the internal and external ions. Recent theoretical calculations have shown that charge transfer and dispersive interactions should be incorporated into the model for a realistic description of the ion-carbon interactions [10]. In particular, these interactions are shown to be responsible for the increased inter chain separation observed experimentally (above that of the increased separation that we predict from our calculations in chapter 6). Bichoutskaia *et al* have developed a new potential model for the absorption of noble gases on a graphite surface which accounts for dispersive interactions [9] and this could be used to replace the current Lennard-Jones description of the current model.

In addition to the possible model developments, there are further applications of the current model that can be undertaken. For example, the role that the ubiquitous $(1,1)_{sq}$ or "ladder" structure has in producing elliptical deformations in outer INTs and the carbon nanotube itself will be further investigated. The mechanism of filling the small radius nanotube has been shown to consist of "hops" across the energy landscape to INTs of successively lower energy and large radii. The transitions between these INTs of different morphology will be investigated to gain understanding of the transition mechanism and the energy barriers to such transformations.

APPENDIX

A-1 Atomic Units

In this thesis we refer to length, time, pressure and energy in atomic units. The conversion to SI units is as follows:

length	1 a_0	5.29×10^{-11} m
time	1 au	2.42×10^{-17} s
energy	1 E_h	4.36×10^{-18} J
pressure	1 au	2.94×10^{13} Pa

Table 7.1: Atomic unit conversions.

.

A-2 The Tersoff forces

As part of this work the Tersoff II potential was incorporated into the molecular dynamics code. In the velocity verlet algorithm (section 2.6), the forces on the atoms must be calculated and they are derived here for the Tersoff II potential.

We recall that the Tersoff II energy function is a three-body potential model and is a function of $\mathbf{r_{ij}}$,$\mathbf{r_{ik}}$ and $\mathbf{r_{jk}}$:

$$U_{ij:k} = \sum_i U_i = \frac{1}{2} \sum_{i,j \neq i} f_c(\mathbf{r_{ij}}) \Big[f_R(\mathbf{r_{ij}}) + b_{ij} f_A(\mathbf{r_{ij}}) \Big]. \tag{A-1}$$

The forces are therefore are calculated with respect to $\mathbf{r_{ij}}$,$\mathbf{r_{ik}}$ and $\mathbf{r_{jk}}$.

Firstly, with respect to $\mathbf{r_{ij}} = (r_{ij}^x, r_{ij}^y, r_{ij}^z)$ of length $|\mathbf{r_{ij}}|$:

$$\begin{aligned}\frac{\partial U}{\partial r_{ij}^x} &= \frac{1}{2}\sum_{i,j\neq i}\frac{\partial f_c(\mathbf{r_{ij}})}{\partial r_{ij}^x}\Big[f_R(\mathbf{r_{ij}}) + b_{ij}f_A(\mathbf{r_{ij}})\Big] \\ &\quad + f_c(\mathbf{r_{ij}})\Big[\frac{\partial f_R(\mathbf{r_{ij}})}{\partial r_{ij}^x} + b_{ij}\frac{\partial f_A(\mathbf{r_{ij}})}{\partial r_{ij}^x} + \frac{\partial b_{ij}}{\partial r_{ij}^x}f_A(\mathbf{r_{ij}})\Big], \qquad \text{(A-2)}\end{aligned}$$

where

$$\frac{\partial f_c(\mathbf{r_{ij}})}{\partial r_{ij}^x} = \begin{cases} 0, & r < R-D \\ -\frac{\pi r_{ij}^x}{4|\mathbf{r_{ij}}|D}cos[\frac{\pi}{2D}(|\mathbf{r_{ij}}| - R)], & R-D < r < R+D \\ 0, & r > R+D \end{cases} \qquad \text{(A-3)}$$

$$\frac{\partial f_R(|\mathbf{r_{ij}}|)}{\partial r_{ij}^x} = -A\lambda_1\frac{r_{ij}^x}{|\mathbf{r_{ij}}|}\exp(-\lambda_1|\mathbf{r_{ij}}|) \qquad \text{(A-4)}$$

$$\frac{\partial f_A(\mathbf{r_{ij}})}{\partial r_{ij}^x} = B\lambda_2\frac{r_{ij}^x}{|\mathbf{r_{ij}}|}\exp(-\lambda_2|\mathbf{r_{ij}}|). \qquad \text{(A-5)}$$

We have used

$$\begin{aligned}\frac{\partial|\mathbf{r_{ij}}|}{\partial r_{ij}^x} &= \frac{\partial[{r_{ij}^x}^2 + {r_{ij}^y}^2 + {r_{ij}^z}^2]^{1/2}}{\partial r_{ij}^x} \\ &= \frac{r_{ij}^x}{|\mathbf{r_{ij}}|}. \qquad \text{(A-6)}\end{aligned}$$

The differential of b_{ij} is given by:

$$\frac{\partial b_{ij}}{\partial r_{ij}^x} = -\frac{1}{2n}(1+\beta^n\xi^n)^{\frac{-1-2n}{2n}}\beta^n n\xi^{n-1}\frac{\partial\xi}{\partial r_{ij}^x}, \qquad \text{(A-7)}$$

where

$$\frac{\partial\xi}{\partial r_{ij}^x} = \sum_{k\neq i,j} f_C\mathbf{r_{ik}}\frac{\partial g(\theta)}{\partial r_{ij}^x} \qquad \text{(A-8)}$$

and

$$\frac{\partial g(\theta)}{\partial r_{ij}^x} = \frac{2c^2(h-cos(\theta))}{\Big[d^2 + [h-cos(\theta)]^2\Big]^2}\Big[-\frac{r_{ik}^x}{|\mathbf{r_{ij}}||\mathbf{r_{ik}}|} + \frac{r_{ij}^x}{|\mathbf{r_{ik}}|}\frac{(\mathbf{r_{ij}}\cdot\mathbf{r_{ik}})}{|\mathbf{r_{ij}}|^3}\Big]. \qquad \text{(A-9)}$$

Secondly, with respect to $\mathbf{r_{ik}} = (r_{ik}^x, r_{ik}^y, r_{ik}^z)$ of length $|\mathbf{r_{ik}}|$:

$$\frac{\partial U}{\partial r_{ij}^x} = \frac{1}{2}\sum_{i,j\neq i} f_C(\mathbf{r_{ij}})f_A(\mathbf{r_{ij}})\frac{\partial b_{ij}}{\partial r_{ik}^x}. \qquad \text{(A-10)}$$

The differential of b_{ij} is given by:

$$\frac{\partial b_{ij}}{\partial r_{ik}^x} = -\frac{1}{2n}(1+\beta^n\xi^n)^{\frac{-1-2n}{2n}}\beta^n n\xi^{n-1}\frac{\partial \xi}{\partial r_{ik}^x}, \tag{A-11}$$

where

$$\frac{\partial \xi}{\partial r_{ik}^x} = \sum_{k\neq i,j}\frac{\partial f_C(\mathbf{r_{ik}})}{\partial r_{ik}^x}g(\theta) + f_C(\mathbf{r_{ik}})\frac{\partial g(\theta)}{\partial r_{ik}^x} \tag{A-12}$$

$$\frac{\partial f_c(\mathbf{r_{ik}})}{\partial r_{ik}^x} = \begin{cases} 0, & r < R-D \\ -\frac{\pi r_{ik}^x}{4|\mathbf{r_{ik}}|D}cos[\frac{\pi}{2D}(|\mathbf{r_{ik}}|-R)], & R-D < r < R+D \\ 0, & r > R+D \end{cases} \tag{A-13}$$

$$\frac{\partial g(\theta)}{\partial r_{ik}^x} = \frac{2c^2(h-cos(\theta))}{\left[d^2+[h-cos(\theta)]^2\right]^2}\Big[-\frac{r_{ij}^x}{|\mathbf{r_{ik}}||\mathbf{r_{ij}}|}+\frac{r_{ik}^x}{|\mathbf{r_{ij}}|}\frac{(\mathbf{r_{ik}}\cdot\mathbf{r_{ij}})}{|\mathbf{r_{ik}}|^3}\Big]. \tag{A-14}$$

Finally,with respect to $\mathbf{r_{jk}} = (r_{jk}^x, r_{jk}^y, r_{jk}^z)$ of length $|\mathbf{r_{jk}}|$:

$$\frac{\partial U}{\partial r_{ij}^x} = 0. \tag{A-15}$$

A-3 Steepest Descent Fitting

The coordinates of the carbon nanotube were fitted to that of a perfect cylinder by minimising the error function $E(C, \mathbf{W}, r)$ via a steepest decent algorithm. In addition, system configurations were "relaxed" by minimising the energy via a steepest descent algorithm effectively removing any kinetic energy from the system and preventing it from mounting any activation barriers.

The method of steepest descent is a first order minimisation method because the gradient of the function is utilised to determine the next set of coordinates in the iteration. The iterative process is as follows [45]. Firstly, an initial set of coordinates $\mathbf{x_0}$ is required to begin the minimisation which is close to the global minimum. Therefore, the process converges to the global minimum rather than a local minimum. In the fitting of the carbon atoms to the surface of a cylinder the parameters from the previous available time step are utilised as a suitable starting point and in a system relaxation the coordinates from the molecular dynamics simulation are utilised. If the system is equilibrated this should be near the thermodynamic minimum energy configuration. The next set of coordinates are given by

$$\mathbf{x_{n+1}} = \mathbf{x_n} + \lambda_n \mathbf{s_n}, \tag{A-16}$$

where $\mathbf{s_n}$ is a unit vector corresponding to the gradient at $\mathbf{x_n}$ and λ_n determines

the distance travelled along the line of force for the n^{th} step. Each successive vector $\mathbf{s_{n+1}}$ is orthogonal to the previous line of force $\mathbf{s_n}$. The value of λ_n is increased at each step that the function $f(\mathbf{x_n})$ decreases in value *i.e.* the error function decreases for the cylinder fitting of the carbon coordinates or the potential energy decreases for the system "relaxation". If the value of $f(\mathbf{x_n})$ is found to increase then we assume that the function has crossed to the opposite side of the potential energy well, travelling past the local minimum and the magnitude of λ_n is reduced.

Eventually, the values of $\mathbf{x_n}$ are found to converge and the local minimum of the function $f(\mathbf{x})$ has been located.

Bibliography

[1] Ajayan, P., Ebbesen, T., Ichihashi, T., Iijima, S., Tanigaki, K. & Hiura, H. (1993). Opening carbon nanotubes with oxygen and implications for filling. *Nature*, **362**, 522–525.

[2] Ajayan, P., Stephan, O., Redlich, P. & Colliex, C. (1995). Carbon nanotubes as removeable templates for metal-oxide nanocomposites and nanostructures. *Nature*, **375**, 564–567.

[3] Allen, M.P. & Tildesley, D.J. (1987). *Computer Simulation of Liquids*. Oxford Science Publications.

[4] Baldoni, M., Leoni, S., Sgamellotti, A., Seifert, G. & Mercuri, F. (2007). Formation, structure, and polymorphism of novel lowest-dimensional Agl nanoaggregates by encapsulation in carbon nanotubes. *Small*, **3**, 1730–1734.

[5] Bar-Sadan, M., Kaplan-Ashiri, I. & Tenne, R. (2007). Inorganic fullerenes and nanotubes: Wealth of materials and morphologies. *Eur Phys J-Spec Top*, **149**, 71–101.

[6] Bethune, D., Kiang, C., Devries, M., Gorman, G., Savoy, R., Vazquez, J. & Beyers, R. (1993). Cobalt-catalyzed growth of carbon nanotubes with single-atomic-layerwalls. *Nature*, **363**, 605–607.

[7] Bichoutskaia, E. & Pyper, N. (2006). Fundamental global model for the structures and energetics of nanocrystalline ionic solids. *Journal of Physical Chemistry B*, **110**, 5936–5949.

[8] Bichoutskaia, E. & Pyper, N. (2006). Structure and energetics of LiF chains as a model for low dimensional alkali halide nanocrystals. *Chem Phys Lett*, **423**, 234–239.

[9] Bichoutskaia, E. & Pyper, N. (2008). A theoretical study of the cohesion of noble gases on graphite. *J Chem Phys*, **128**.

[10] Bichoutskaia, E. & Pyper, N.C. (2008). Theoretical study of the structures and electronic properties of all-surface KI and CsI nanocrystals encapsulated in single walled carbon nanotubes. *J Chem Phys*, **129**, 154701–15.

[11] Bishop, C.L. & Wilson, M. (2008). The energetics of inorganic nanotubes. *Molecular Physics*, **106**, 1665 – 1674.

[12] Bray, J. (2001). http://www.biochem.ucl.ac.uk/∼james/latex/. *James Bray's Latex Help*.

[13] Campos, C., Lima, J., Grandi, T., Itié, J., Polian, A., Chervin, J., Pizani, P.S. & Saitovich, E. (2008). The pressure-induced phase transition of mechanically alloyed nanocrystalline GaSb. *Journal of Physics: Condensed Matter*, **20**, 275212.

[14] Chen, J., Li, S. & Tao, Z. (2003). Novel hydrogen storage properties of MoS_2 nanotubes. *J Alloys Compounds*, **356**, 413–417.

[15] Chen, J., Li, S., Tao, Z., Shen, Y. & Cui, C. (2003). Titanium disulfide nanotubes as hydrogen-storage materials. *J Am Chem Soc*, **125**, 5284–5285.

[16] Chen, Y., Green, M. & Tsang, S. (1996). Synthesis of carbon nanotubes filled with long continuous crystals of molybdenum oxides. *Chem Commun*, 2489–2490.

[17] Dominko, R., Arcon, D., Mrzel, A., Zorko, A., Cevc, P., Venturini, P., Gaberscek, M., Remskar, M. & Mihailovic, D. (2002). Dichalcogenide nanotube electrodes for Li-ion batteries. *Advan Mater*, **14**, 1531.

[18] Eberly, D. (2007). *3D Game Engine Design: 3D Game Engine Design, Second Edition*. Morgan Kaufmann.

[19] Erkoc, S. (1997). Empirical many-body potential energy functions used in computer simulations of condensed matter properties. *Physics Reports-Review Section of Physics Letters*, **278**, 80–105.

[20] Ewald, P. (1921). Die Berechnung optischer und elektrostatischer gitterpotentiale. *Annalen der Physik*, **369(3)**, 253–287.

[21] Fan, R., Karnik, R., Yue, M., Li, D., Majumdar, A. & Yang, P. (2005). DNA translocation in inorganic nanotubes. *Nano Lett*, **5**, 1633–1637.

[22] Flahaut, E., Sloan, J., Friedrichs, S., Kirkland, A., Coleman, K., Williams, V., Hanson, N., Hutchison, J. & Green, M. (2006). Crystallization of 2H and 4H PbI_2 in carbon nanotubes of varying diameters and morphologies. *Chem Mater*, **18**, 2059–2069.

[23] Frenkel, D. & Smit, B. (1996). *Understanding Molecular Simulation from Algorithms to Applications*. Academic Press.

[24] Friedrichs, S., Meyer, R., Sloan, J., Kirkland, A., Hutchison, J. & Green, M. (2001). Complete characterisation of a Sb_2O_3/(21,8)SWNT inclusion composite. *Chem Commun*, 929–930.

[25] Friedrichs, S., Falke, U. & Green, M. (2005). Phase separation of LaI_3 inside single-walled carbon nanotubes. *Chemphyschem*, **6**, 300–305.

[26] Fumi, F.G. & Tosi, M.P. (1964). Ionic sizes + Born repulsive parameters in NaCl-type alkali halides I. Huggins-Mayer + Pauling forms. *Journal of Physics and Chemistry of Solids*, **25**, 31–43.

[27] Geng, B., Zhan, F., Jiang, H., Guo, Y. & Xing, Z. (2008). Egg albumin as a nanoreactor for growing single-crystalline Fe_3O_4 nanotubes with high yields. *Chemical Communications*, advanced Article on the Web.

[28] Goldberger, J., He, R., Zhang, Y., Lee, S., Yan, H., Choi, H. & Yang, P. (2003). Single-crystal gallium nitride nanotubes. *Nature*, **422**, 599–602.

[29] Grimes, C. (2007). Synthesis and application of highly ordered arrays of TiO_2 nanotubes. *J Mater Chem*, **17**, 1451–1457.

[30] Guan, L., Suenaga, K., Shi, Z., Gu, Z. & Iijima, S. (2007). Polymorphic structures of iodine and their phase transition in confined nanospace. *Nano Lett*, **7**, 1532–1535.

[31] Hemmati, M., Wilson, M. & Madden, P. (1999). Structure of liquid Al_2O_3 from a computer simulation model. *J Phys Chem B*, **103**, 4023–4028.

[32] Holloway, A., Toghill, K., Wildgoose, G., Compton, R., Ward, M., Tobias, G., Llewellyn, S., Ballesteros, B., Green, M. & Crossley, A. (2008). Electrochemical opening of single-walled carbon nanotubes filled with metal halides and with closed ends. *J Phys Chem C*, **112**, 10389–10397.

[33] Hoover, W.G. (1985). Canonical dynamics - equilibrium phase-space distributions. *Physical Review A*, **31**, 1695–1697.

[34] Hoover, W.G. (1986). Constant-pressure equations of motion. *Physical Review A*, **34**, 2499–2500.

[35] Huber, K. & Herzberg, G. (1979). *Molecular Spectra and Molecular Structure. IV. Constants of Diatomic Molecules*. Van Nostrand Reinhold Co.

[36] Huggins, M. & Mayer, J. (1933). Interatomic distances in crystals of the alkali halides. *Journal of Chemical Physics*, **1**, 643–646.

[37] Hutchison, J., Sloan, J., Kirkland, A., Green, M. & Green, M. (2004). Growing and characterizing one-dimensional crystals within single-walled carbon nanotubes. *J Electron Microsc*, **53**, 101–106.

[38] Iijima, S. (1991). Helical microtubules of graphitic carbon. *Nature*, **354**, 56–58.

[39] Iijima, S. & Ichihashi, T. (1993). Single-shell carbon nanotubes of 1 nm diameter. *Nature*, **364**, 737–737.

[40] Joselevich, E., Dai, H., Liu, J., Hata, K. & Windle, A. (2008). Carbon nanotube synthesis and organization. *Top Appl Phys*, **111**, 101–164.

[41] Kavan, L. & Dunsch, L. (2007). Spectroelectrochemistry of carbon nanostructures. *Chemphyschem*, **8**, 974–98.

[42] Kittel, C. & McEuen, P. (2004). *Introduction to Solid State Physics*. Wiley.

[43] Kukovecz, A., Pichler, T., Pfeiffer, R., Kramberger, C. & Kuzmany, H. (2003). Diameter selective doping of single wall carbon nanotubes. *Physical Chemistry Chemical Physics*, **5**, 582–587.

[44] Kurti, J., Zolyomi, V., Kertesz, M. & Sun, G. (2003). The geometry and the radial breathing mode of carbon nanotubes: beyond the ideal behaviour. *New J Phys*, **5**.

[45] Leach, A. (2001). *Molecular Modelling: Principles and Applications*. Pearson Education.

[46] Lin, H., Mou, C. & Liu, S. (2000). Formation of mesoporous silica nanotubes. *Advan Mater*, **12**, 103–106.

[47] Ma, R., Bando, Y., Zhu, H., Sato, T., Xu, C. & Wu, D. (2002). Hydrogen uptake in boron nitride nanotubes at room temperature. *J Am Chem Soc*, **124**, 7672–7673.

[48] Madden, P.A. & Wilson, M. (1996). 'Covalent' effects in 'ionic' systems. *Chemical Society Reviews*, **25**, 339–350.

[49] Marinkovic, S. (2004). Diamond synthesized at low pressure. *Chemistry and Physics of Carbon*, **29**, 71–208.

[50] Martyna, G., Tobias, D. & Klein, M.L. (1994). Constant-pressure molecular dynamics algorithms. *Journal of Chemical Physics*, **101**, 4177–4189.

[51] Martyna, G.J., Klein, M.L. & Tuckerman, M. (1992). Nosé-Hoover chains - the canonical ensemble via continuous dynamics. *Journal of Chemical Physics*, **97**, 2635–2643.

[52] Mayer, J. (1933). Dispersion and polarizability and the van der Waals potential in the alkali halides. *Journal of Chemical Physics*, **1**, 270–279.

[53] McMahon, M., Nelmes, R., Wright, N. & Allan, D. (1994). Pressure-dependence of the Imma phase of silicon. *Phys Rev B*, **50**, 739–743.

[54] McMillan, P.F. (2002). *Liquid State Polymorphism*, 511–543. IOS Press, Amsterdam.

[55] Melchionna, S., Ciccotti, G. & Holian, B.L. (1993). Hoover NPT dynamics for systems varying in shape and size. *Molecular Physics*, **78**, 533 – 544.

[56] Menoni, C., Hu, J. & Spain, I. (1986). Germanium at high-pressures. *Phys Rev B*, **34**, 362–368.

[57] Meyer, R., Sloan, J., Dunin-Borkowski, R., Kirkland, A., Novotny, M., Bailey, S., Hutchison, J. & Green, M. (2000). Discrete atom imaging of one-dimensional crystals formed within single-walled carbon nanotubes. *Science*, **289**, 1324–1326.

[58] Mezoua, M., Libotte, H., Dputier, S., Le Bihan, T. & Husermann, D. (1999). The effect of micro-strain and pressure medium on the high-pressure phase of GaSb. *physica status solidi (b)*, **211**, 395–400.

[59] Mintmire, J. & White, C. (1996). *Carbon Nanotubes: Preparation and Properties*, chap. Properties: Theoretical Predictions. CRC Press.

[60] Monthioux, M. & Kuznetsov, V. (2006). Who should be given the credit for the discovery of carbon nanotubes? *Carbon*, **44**, 1621–1623.

[61] Mujica, A. (2003). High-pressure phases of group-IV, III-V, and II-VI compounds. *Rev Mod Phys*, **75**, 863.

[62] Mujica, A. & Needs, R. (1997). Theoretical study of the high-pressure phase stability of GaP, InP, and InAs. *Phys Rev B*, **55**, 9659–9670.

[63] Nelmes, R., McMahon, M. & Belmonte, S. (1997). Nonexistence of the diatomic beta-tin structure. *Phys Rev Lett*, **79**, 3668–3671.

[64] Nelmes, R.J. & McMahon, M.I. (1998). Structural transitions in the group IV, III-V, and II-VI semiconductors under pressure. *High Pressure in Semiconductor Physics 1*, **54**, 145–246.

[65] Nosé, S. (1984). A molecular-dynamics method for simulations in the canonical ensemble. *Molecular Physics*, **52**, 255–268.

[66] Nosé, S. (1984). A unified formulation of the constant temperature molecular-dynamics methods. *Journal of Chemical Physics*, **81**, 511–519.

[67] Oberlin, A., Endo, M. & Koyama, T. (1976). Filamentous growth of carbon through benzene decomposition. *J Cryst Growth*, **32**, 335–349.

[68] Ozolins, V. & Zunger, A. (1999). Theory of systematic absence of NaCl-type (beta-Sn-type) high pressure phases in covalent (ionic) semiconductors. *Phys Rev Lett*, **82**, 767–770.

[69] Parrinello, M., Rahman, A. & Vashishta, P. (1983). Structural transitions in superionic conductors. *Physical Review Letters*, **50**, 1073–1076.

[70] Pauling, L. (1929). The principles determining the structure of complex ionic crystals. *J Am Chem Soc*, **51**, 1010–1026.

[71] Peralta-Inga, Z., Boyd, S., Murray, J., O'Connor, C. & Politzer, P. (2003). Density functional tight-binding studies of carbon nanotube structures. *Struct Chem*, **14**, 431–443.

[72] Philp, E., Sloan, J., Kirkland, A., Meyer, R., Friedrichs, S., Hutchison, J. & Green, M. (2003). An encapsulated helical one-dimensional cobalt iodide nanostructure. *Nat Mater*, **2**, 788–791.

[73] Pyper, N. (1986). Relativistic ab initio calculations of the properties of ionic solids. *Royal Society of London Philosophical Transactions Series A*, **320**, 107–158.

[74] Pyper, N. (1994). The relative stability of the 6-fold and 8-fold coordinated structures of cesium chloride. *Chem Phys Lett*, **220**, 70–76.

[75] Robertson, D.H. (1992). Energetics of nanoscale graphitic tubules. *Phys Rev B*, **45**, 12592.

[76] Sadus, R.J. (2002). *Molecular Simulations of Fluids. Theory, Algorithms and Object-Orientation*. Elsevier.

[77] Saito, R., Dresselhaus, G. & Dresselhaus, M. (1998). *Physical Properties of Carbon Nanotubes*. Imperial College Press.

[78] Sangster, M.J.L. & Dixon, M. (1976). Interionic potentials in alkali-halides and their use in simulations of molten-salts. *Advances in Physics*, **25**, 247–342.

[79] Sceats, E. (2007). *Theoretical Investigations into the molecular and electronic structure of filled single-walled carbon nanotubes*. Ph.D. thesis, St Hugh's College, University of Oxford.

[80] Sceats, E., Green, J. & Reich, S. (2006). Theoretical study of the molecular and electronic structure of one-dimensional crystals of potassium iodide and composites formed upon intercalation in single-walled carbon nanotubes. *Phys Rev B*, **73**.

[81] Shankar, K., Mor, G., Prakasam, H., Yoriya, S., Paulose, M., Varghese, O. & Grimes, C. (2007). Highly-ordered TiO_2 nanotube arrays up to 220 μm in length: use in water photoelectrolysis and dye-sensitized solar cells. *Nanotechnol*, **18**.

[82] Shao, L., Tobias, G., Huh, Y. & Green, M.L. (2006). Reversible filling of single walled carbon nanotubes opened by alkali hydroxides. *Carbon*, **44**, 2855–2858.

[83] Slater, J. (1931). The van der Waals forces in gases. *Phys Rev*, **37**, 682.

[84] Sloan, J., Cook, J., Chu, A., Zwiefka-Sibley, M., Green, M. & Hutchison, J. (1998). Selective deposition of UCl_4 and $(KCl)_x(UCl_4)_y$ inside carbon nanotubes using eutectic and noneutectic mixtures of UCl_4 with KCl. *J Solid State Chem*, **140**, 83–90.

[85] Sloan, J., Hammer, J., Zwiefka-Sibley, M. & Green, M. (1998). The opening and filling of single walled carbon nanotubes (SWTs). *Chem Commun*, 347–348.

[86] Sloan, J., Wright, D., Woo, H., Bailey, S., Brown, G., York, A., Coleman, K., Hutchison, J. & Green, M. (1999). Capillarity and silver nanowire formation observed in single walled carbon nanotubes. *Chem Commun*, 699–700.

[87] Sloan, J., Novotny, M., Bailey, S., Brown, G., Xu, C., Williams, V., Friedrichs, S., Flahaut, E., Callender, R., York, A., Coleman, K., Green, M., Dunin-Borkowski, R. & Hutchison, J. (2000). Two layer $4:4$ co-ordinated KI crystals grown within single walled carbon nanotubes. *Chem Phys Lett*, **329**, 61–65.

[88] Sloan, J., Friedrichs, S., Meyer, R., Kirkland, A., Hutchison, J. & Green, M. (2002). Structural changes induced in nanocrystals of binary compounds confined within single walled carbon nanotubes: A brief review. *Inorg Chim Acta*, **330**, 1–12.

[89] Sloan, J., Grosvenor, S., Friedrichs, S., Kirkland, A., Hutchison, J. & Green, M. (2002). A one-dimensional BaI_2 chain with five- and six-coordination, formed within a single-walled carbon nanotube. *Angew Chem Int Ed*, **41**, 1156.

[90] Sloan, J., Terrones, M., Nufer, S., Friedrichs, S., Bailey, S., Woo, H., Ruhle, M., Hutchison, J. & Green, M. (2002). Metastable one-dimensional $AgCl_{(1-x)}I_x$ solid-solution wurzite "tunnel" crystals formed within single-walled carbon nanotubes. *J Am Chem Soc*, **124**, 2116–2117.

[91] Sloan, J., Kirkland, A., Hutchison, J. & Green, M. (2003). Aspects of crystal growth within carbon nanotubes. *C R Phys*, **4**, 1063–1074.

[92] Sloan, J., Luzzi, D., Kirkland, A., Hutchison, J. & Green, M. (2004). Imaging and characterization of molecules and one-dimensional crystals formed within carbon nanotubes. *Mrs Bull*, **29**, 265–271.

[93] Spahr, M., Bitterli, P., Nesper, R., Muller, M., Krumeich, F. & Nissen, H. (1998). Redox-active nanotubes of vanadium oxide. *Angew Chem Int Ed*, **37**, 1263–1265.

[94] Steele, W.A. (1978). Interaction of rare-gas atoms with graphitized carbon-black. *Journal of Physical Chemistry*, **82**, 817–821.

[95] Swope, W.C., Andersen, H.C., Berens, P.H. & Wilson, K.R. (1982). A computer-simulation method for the calculation of equilibrium-constants for the formation of physical clusters of molecules- application to small water clusters. *Journal of Chemical Physics*, **76**, 637–649.

[96] Tang, K.T. & Toennies, J.P. (1984). An improved simple-model for the van der Waals potential based on universal damping functions or the dispersion coefficients. *Journal of Chemical Physics*, **80**, 3726–3741.

[97] Tenne, R. & Rao, C. (2004). Inorganic nanotubes. *Phil Trans Roy Soc London A*, **362**, 2099–2125.

[98] Tenne, R., Margulis, L., Genut, M. & Hodes, G. (1992). Polyhedral and cylindrical structures of tungsten disulfide. *Nature*, **360**, 444–446.

[99] Tersoff, J. (1988). Empirical interatomic potential for carbon, with applications to amorphous carbon. *Physical Review Letters*, **61**, 2879–2882.

[100] Tersoff, J. (1988). New empirical approach for the structure and energy of covalent systems. *Physical Review B*, **37**, 6991–7000.

[101] Thamavaranukup, N., Hoppe, H., Ruiz-Gonzalez, L., Costa, P., Sloan, J., Kirkland, A. & Green, M. (2004). Single-walled carbon nanotubes filled with MOH (M = K, Cs) and then washed and refilled with clusters and molecules. *Chem Commun*, 1686–1687.

[102] Tibbetts, G. (1984). Why are carbon filaments tubular? *J Cryst Growth*, **66**, 632–638.

[103] Tobias, G., Shao, L., Salzmann, C., Huh, Y. & Green, M. (2006). Purification and opening of carbon nanotubes using steam. *J Phys Chem B*, **110**, 22318–22322.

[104] Tsang, S., Chen, Y., Harris, P. & Green, M. (1994). A simple chemical method of opening and filling carbon nanotubes. *Nature*, **372**, 159–162.

[105] Vanpeteghem, C., Nelmes, R., Allan, D. & McMahon, M. (2002). New high-pressure phase of GaSb. *Phys Rev B*, **65**.

[106] Warner, J., Ito, Y., Zaka, M., Ge, L., Akachi, T., Okimoto, H., Porfyrakis, K., Watt, A., Shinohara, H. & Briggs, G. (2008). Rotating fullerene chains in carbon nanopeapods. *Nano Lett*, **8**, 2328–2335.

[107] Weisstein, E.W. (2003). *CRC Concise Encyclopedia of Mathematics*. CRC Press.

[108] Wilson, M. (2002). The formation of low-dimensional ionic crystallites in carbon nanotubes. *J Chem Phys*, **116**, 3027–3041.

[109] Wilson, M. (2002). Structure and phase stability of novel 'twisted' crystal structures in carbon nanotubes. *Chemical Physics Letters*, **366**, 504–509.

[110] Wilson, M. (2004). The formation of inorganic nanotubular structures in carbon nanotubes. *Nano Letters*, **4**, 299–302.

[111] Wilson, M. (2004). The formation of low-dimensional chiral inorganic nanotubes by filling single-walled carbon nanotubes. *Chemical Physics Letters*, **397**, 340–343.

[112] Wilson, M. (2006). The formation of low-dimensional inorganic nanotube crystallites in carbon nanotubes. *Journal of Chemical Physics*, **124**, 124706.

[113] Wilson, M. (2007). Formation of, and ion-transport in, low-dimensional crystallites in carbon nanotubes. *Faraday Discussions*, **134**, 283–295.

[114] Wilson, M. & Friedrichs, S. (2006). The formation of low-dimensional metal trihalide crystals in carbon nanotubes. *Acta Crystallogr A*, **62**, 287–295.

[115] Wilson, M. & Madden, P. (2001). Growth of ionic crystals in carbon nanotubes. *J Am Chem Soc*, **123**, 2101–2102.

[116] Wilson, M., Madden, P.A., Pyper, N.C. & Harding, J.H. (1996). Molecular dynamics simulations of compressible ions. *Journal of Chemical Physics*, **104**, 8068–8081.

[117] Wilson, M., Hutchinson, F. & Madden, P.A. (2002). Simulation of pressure-driven phase transitions from tetrahedral crystal structures. *Physical Review B*, **65**.

[118] Xu, C., Sloan, J., Brown, G., Bailey, S., Williams, V., Friedrichs, S., Coleman, K., Flahaut, E., Hutchison, J., Dunin-Borkowski, R. & Green, M. (2000). 1D lanthanide halide crystals inserted into single-walled carbon nanotubes. *Chem Commun*, 2427–2428.

[119] Yam, C., Ma, C., Wang, X. & Chen, G. (2004). Electronic structure and charge distribution of potassium iodide intercalated single-walled carbon nanotubes. *Appl Phys Lett*, **85**, 4484–4486.

[120] Zhang, J., Sun, L., Liao, C. & Yan, C. (2002). A simple route towards tubular ZnO. *Chem Commun*, 262–263.

[121] Zheng, L., O'Connell, M., Doorn, S., Liao, X., Zhao, Y., Akhadov, E., Hoffbauer, M., Roop, B., Jia, Q., Dye, R., Peterson, D., Huang, S., Liu, J. & Zhu, Y. (2004). Ultralong single-wall carbon nanotubes. *Nat Mater*, **3**, 673–676.